Dissertation

submitted to the

Combined Faculties for the Natural Sciences and for Mathematics

of the Ruperta-Carola University of Heidelberg, Germany

for the degree of

Doctor of Natural Sciences

presented by

Dipl.-Phys. Christian Linn

born in Zweibrücken, Germany

Oral examination: May 15th, 2013

Measurement of the CP-violating phase ϕ_s using $B_s^0 \to J/\psi\phi$ and $B_s^0 \to J/\psi\pi^+\pi^-$ decays with the LHCb experiment

Referees:

Prof. Dr. Ulrich Uwer

Prof. Dr. Tilman Plehn

Abstract

This thesis presents a measurement of the CP-violating phase ϕ_s, arising in the interference of B_s^0 mixing and the amplitudes of $B_s^0 \to J/\psi\phi$ and $B_s^0 \to J/\psi\pi^+\pi^-$ decays. The phase ϕ_s is an observable with very high sensitivity for physics phenomena beyond the Standard Model. New, heavy particles could contribute to the mixing process and influence the measured value of ϕ_s. As the prediction for ϕ_s is very precise, already small deviations of the measured value would be a hint for new physics effects.
The presented measurement is done with a data set corresponding to an integrated luminosity of $\mathcal{L} = 1.0\,\text{fb}^{-1}$, collected during 2011 with the LHCb experiment. The determination of ϕ_s with $B_s^0 \to J/\psi\phi$ decays requires a time-dependent analysis, depending also on the decay angles of the B_s^0 to separate the CP-eigenstates of the decay. A four-dimensional maximum likelihood fit, including as well information of the B_s^0 production flavour, is used to determine ϕ_s from the corresponding measured time and angular distributions. The measurement of the strong phase difference between K^+K^- P-wave and S-wave amplitudes, as a function of the invariant K^+K^- mass, allows to resolve a twofold ambiguity ($\phi_s \leftrightarrow \pi - \phi_s$) in the differential $B_s^0 \to J/\psi\phi$ decay rate. The measured value is $\phi_s = 0.069 \pm 0.091\,(\text{stat.}) \pm 0.014\,(\text{syst.})\,\text{rad}$. Performing a combined analysis of $B_s^0 \to J/\psi\phi$ and $B_s^0 \to J/\psi\pi^+\pi^-$ decays a value of $\phi_s = 0.043 \pm 0.076\,(\text{stat.}) \pm 0.014\,(\text{syst.})\,\text{rad}$ is determined. The obtained results are in agreement with the prediction.

Kurzfassung

In der vorliegenden Arbeit wird eine Messung der CP-verletzenden Phase ϕ_s vorgestellt, die in der Interferenz von B_s^0 Mischung und $B_s^0 \to J/\psi\phi$ oder $B_s^0 \to J/\psi\pi^+\pi^-$ Zerfallsamplituden auftritt. Die Phase ϕ_s ist eine Observable mit hoher Sensitivität für physikalische Phänomene jenseits des Standard Modells. Neue, schwere Teilchen können zu der Mischung beitragen und so den gemessenen Wert von ϕ_s beeinflussen. Da die Vorhersage für ϕ_s sehr präzise ist, sind bereits geringe Abweichungen in der Messung Anzeichen für neue physikalische Effekte.
Die vorgestellte Messung benutzt einen Datensatz, der einer integrierten Luminosität von $\mathcal{L} = 1.0\,\text{fb}^{-1}$ entspricht und während 2011 mit dem LHCb Experiment aufgenommen wurde. Zur Bestimmung von ϕ_s mit Hilfe von $B_s^0 \to J/\psi\phi$ Zerfällen ist eine zeitabhängige Analyse notwendig, die auch von den Zerfallswinkeln des B_s^0 abhängen muss, um die CP Eigenzustände des Zerfalls zu separieren. Um ϕ_s von den gemessenen Zeit- und Winkelverteilungen zu bestimmen, wird ein vierdimensionaler Maximum Likelihood Fit benutzt, der Informationen über den B_s^0 Produktionszustand beinhaltet. Die Messung der Phasendifferenz von K^+K^- P- und S-Wellen Amplituden als Funktion der K^+K^- Masse wird benutzt um eine Ambiguität ($\phi_s \leftrightarrow \pi - \phi_s$) in der $B_s^0 \to J/\psi\phi$ Zerfallsrate aufzulösen. Der gemessene Wert ist $\phi_s = 0.069 \pm 0.091\,(\text{stat.}) \pm 0.014\,(\text{syst.})\,\text{rad}$. In einer kombinierten Analyse von $B_s^0 \to J/\psi\phi$ und $B_s^0 \to J/\psi\pi^+\pi^-$ Zerfällen wird ein Wert von $\phi_s = 0.043 \pm 0.076\,(\text{stat.}) \pm 0.014\,(\text{syst.})\,\text{rad}$ bestimmt. Die gemessenen Ergebnisse sind in Übereinstimmung mit der Vorhersage.

Contents

CHAPTER 1

Introduction

The current knowledge of the fundamental particles and their interactions is described by a single theory, the Standard Model of Particle Physics [1] [2] [3]. It was extensively tested during the last decades and, although it is very succesful in describing the observations of particle physics experiments, some hints appeared that it cannot explain all aspects of nature:

- Cosmological observation showed that only $\sim 5\%$ of the energy density of the universe is explained by the matter described in the Standard Model. The remaining part is so called *Dark Matter* with $\sim 22\%$ and *Dark Energy* with $\sim 73\%$ of the energy density [4] [5]. Both components do not exist in the theoretical framework of the Standard Model.

- Matter and Antimatter were produced in equal amounts in the Big Bang. Nevertheless, today the universe is dominated by matter. This asymmetry cannot be explained by the mechanisms in the Standard Model[6] [7].

To address these and other open questions in particle physics, and to confirm the existence of the Higgs-boson, a fundamental particle in the Standard Model, the Large Hadron Collider (LHC) was built. It is located at CERN near Geneva and is the most powerful particle accelerator today, colliding protons with center-of-mass energies up to $\sqrt{s} = 14\,\text{TeV}$. Four large particle detectors are located at the collision points, following different approaches to search for physics effects beyond the Standard Model (*New Physics*). ATLAS and CMS are general purpose detectors to perform direct searches

for new particles. ALICE is a detector designed for heavy-ion collisions. LHCb is a specialised detector for precision measurements of b- and $_s$hadron decays, searching for indirect effects of new virtual particles in quantum loops.
The LHCb detector profits from the large production cross section of $b\bar{b}$ quark pairs at the LHC. In 2011 at a center-of-mass energy of $\sqrt{s} = 7\,\text{TeV}$ and an integrated luminosity of $\mathcal{L} = 1.0\,\text{fb}^{-1}$, approximately $3 \cdot 10^{11}$ $b\bar{b}$ pairs were produced. This allows for a huge variety of precision measurements of b-hadron decays. The most sensitive processes for indirect searches for New Physics are so called flavour changing neutral currents (FCNC). In the Standard Model these transitions are only allowed in loop processes. An example for FCNC in the Standard Model is the mixing of neutral B-mesons, transitions between B and anti-B, that is only possible through suppressed box diagrams. Potential new particles can contribute to the mixing diagram and change both the absolute value and the phase of the mixing amplitude. The phase in loop process is experimental accesible via the measurement of time-dependent CP violation. CP violation arises when the symmetry of the combined charge (C) and parity (P) transformation of a process is violated.
This thesis presents a measurement of the CP-violating mixing phase ϕ_s that arises in the interference of B_s^0 mixing and decay amplitudes to final states as $J/\psi\phi$. The prediction for ϕ_s is very precise, $\phi_s = -0.0364 \pm 0.0016\,\text{rad}$ [8]. This makes ϕ_s to an excellent observable for New Physics effects, as already small deviations from the prediction can be interpreted as New Physics. The currently available measurements of this phase still allow for large deviations from the Standard Model values.
The measurement of ϕ_s using $B_s^0 \to J/\psi\phi$ decays requires a four-dimensional fitting technique, based on the maximisation of a likelihood function, to determine ϕ_s from a flavour dependent analysis of the decay time and angular distributions of the decay. This technique relies on the correct description of detector acceptance and resolution effects. To perform the analysis flavour dependent, the production flavour of the B_s^0 mesons must be determined.
The measurement is performed with the data sample collected during the 2011 run of the LHC, using reconstruted $B_s^0 \to J/\psi\phi$ decays as well as $B_s^0 \to J/\psi\pi^+\pi^-$ decays to determine ϕ_s.
The following thesis presents the analysis techniques and results of this measurement. It is organised as follow: Chapter 2 discusses the theoretical background, starting from a general introduction of the Standard Model and the phenomenological description of B mixing, followed by to the derivation of the equations describing the $B_s^0 \to J/\psi\phi$ and $B_s^0 \to J/\psi\pi^+\pi^-$ decay. Chapter 3 introduces the LHCb experiment by explaining the working principle and performance of the subdetector components. In chapter 4, a short introduction to the analysis strategy will be given. Chapter 5 describes the data taking conditions as well as the reconstruction and selection process of the used data sample. Chapter 6 disusses the algorithms and methods used to determine the production flavour of the B_s^0 mesons. The determination of the decay time resolution of the detector is presented in chapter 7. The detector acceptances that incluence the measured distribtuions are discussed in chapter 8. The fitting technique used to determine ϕ_s is

explained in chapter 9 with a detailed discussion of the functions describing the signal and background components. Chapter 10 and 11 present the results for the physics parameters extracted first in a simplified and then in an extended fit of $B_s^0 \to J/\psi\phi$ decays. In chapter 12 the systematic uncertainties of the measurement are evaluated, before, in chapter 13 a combined result of ϕ_s using $B_s^0 \to J/\psi\phi$ and $B_s^0 \to J/\psi\pi^+\pi^-$ decays is presented. Finnaly, chapter 14 summarises the measurement and gives a short outlook in the future prospects.

CHAPTER 2

B_s^0 mixing and CP violation

In this chapter the theoretical background of the presented measurement will be given. The Standard Model of particle physics ([1], [2], [3]) will be introduced shortly, followed by a phenomenological discussion of B meson mixing and CP violation. The decay $B_s^0 \to J/\psi\phi$ will be discussed in detail with its possible impact on physics beyond the Standard Model.

2.1 The Standard Model of Particle Physics

The Standard Model of Particle Physics is a renormalisable field theory, describing the fundamental particles of nature and the interactions between them ([10], [11]). The particles that construct the known matter are described by fermion fields with half-integer spin. They can be divided in quarks and leptons and are grouped in three generations as shown in Table 2.1. Each generation contains a lepton with electric charge (e, μ, τ), one lepton without electric charge, called neutrino (ν_e, ν_μ, ν_τ), one *up-type* quark (u, c, t) and one *down-type* quark (d, s, b). For each fermion f exists an anti-fermion $\bar{f}$ with opposite quantum numbers.
The interactions between the fermions are mediated by integer-spin gauge bosons. They are introduced in the Standard Model by transforming the global symmetries of the Standard Model Lagrangian to local gauge symmetries that are separately valid at each space-time point. The gauge bosons, listed in Table 2.2 carry the three fundamental forces: The massless photon (γ) mediates the electromagnetic force, the massless

gluons (g) the strong force and the massive $W^{\pm}$ and Z^0 bosons mediate the weak force. The gravitational force is not described in the Standard Model. The Higgs-boson H is not related to a fundamental force but its existence is a consequence of the mass mechanism of the Standard Model and will be discussed later.
The gauge symmetry group of the Standard Model is $\mathrm{SU(3)_C} \otimes \mathrm{SU(2)_L} \otimes \mathrm{U(1)_Y}$. Each symmetry implies a quantum number that is conserved in the related interaction. In the following the different fundamental interactions and their relation to the Standard Model gauge symmetry group will be discussed:

The theory of the **strong interaction** (QCD) is based on the $\mathrm{SU(3)_C}$ gauge group and defines the interactions and couplings of the quarks. C denotes the quantum number related to the symmetry, called *colour*. The strong force acts on all fermions with *colour* quantum number. The quarks can have the quantum numbers *red, green, blue* and the corresponding anti-colours. The gauge bosons of the strong interaction, the gluons, have colour quantum number as well and can therefore self-interact. Leptons do not have colour and thus do not take part in strong interactions. A special feature of the strong interaction is that quarks can only exist in bound states, a phenomena referred to as *confinement*. The bound states are called hadrons. There are two types of hadrons: the *mesons* consisting of a quark anti-quark pair and the *baryons* consisting of three quarks of different type.

In the Standard Model the electromagnetic interaction and the weak interaction are unified to a common theoretical description, the **electroweak interaction** with gauge group $\mathrm{SU(2)_L} \otimes \mathrm{U(1)_Y}$. The $\mathrm{SU(2)_L}$ symmetry introduces three gauge bosons W_i. The related conserved quantum number is the weak isospin T with third component T_3. Only left-handed fermions and right-handed anti-fermions have $T \neq 0$ and couple to the W_i bosons. The symmetry of the $\mathrm{U(1)_Y}$ gauge group implies the hypercharge quantum number Y and introduces a gauge boson A. The hypercharge of a fermion is given by $Y = Q - T_3$ where Q is the electric charge. The exchange bosons of the electromagnetic and weak interactions are given by linear combinations of the gauge bosons W_i and A:
The exchange boson of the electromagnetic interaction, the photon, is a combination of the W_3 and A gauge bosons. It couples to the electric charge Q of the fermions. All fermions except the neutrinos have an electric charge and take therefore part in electromagnetic interaction processes.
The weak interaction processes can be classified by two different types: The *neutral current* is mediated by the Z^0 boson that is similar to the photon a combination of the W_3 and A gauge bosons. Due to charge conservation, it couples only to fermion anti-fermion pairs. The *charged current* is carried by the charged $W^{\pm}$ bosons that are linear combinations of the W_1 and W_2 gauge bosons. The charged current is the only process in the Standard Model where fermions of different generations can take part. Flavour changing neutral currents (FCNC) are not allowed in the Standard Model in tree-level processes.

Experiments have demonstrated that the $W^{\pm}$ and Z^0 gauge bosons have masses. Separate mass terms in the Standard Model Lagrangian however would violate the local gauge symmetry. By introducing a scalar Higgs-field with non-zero vacuum expectation value, the electroweak symmetry is spontaneously broken and the bosons gain masses. A consequence of the Higgs-mechanism is the existence of an additional scalar Higgs-boson H. A first observation of a Standard Model H-like particle was made by the ATLAS and CMS collaborations [12] [13]. Similar to the boson masses, the masses of the fermions are introduced by their coupling to the Higgs-field (Yukawa-coupling).

	quarks		leptons	
generation	type	mass	type	mass
1	u	1.7 – 3.3 MeV	ν_e	< 2 eV
	d	4.1 – 5.8 MeV	e	0.511 MeV
2	c	1.27 GeV	ν_μ	< 2 eV
	s	101 MeV	μ	105.7 MeV
3	t	172 GeV	ν_τ	< 2 eV
	b	4.19 GeV	τ	1.78 GeV

Table 2.1: Fermions in the Standard Model, grouped in three generations. The mass values are taken from [9].

interaction	gauge boson	mass
electromagnetic	γ	0
strong	g	0
weak	$W^{\pm}$	80.4 GeV
	Z^0	91.2 GeV
-	H	~ 125 GeV

Table 2.2: Bosons and fundamental forces in the Standard Model. The mass values are taken from [9].

2.2 The CKM formalism

A result of the electroweak symmetry breaking is additional mass terms for the fermions (Yukawa terms) in the Standard Model Lagrangian. The Yukawa terms of the quark fields can be expressed as [14]

$$\mathcal{L}_{\mathrm{Y}}^{q} = -\frac{v}{\sqrt{2}}(\bar{d}'_{\mathrm{L}} Y_d d'_{\mathrm{R}} + \bar{u}'_{\mathrm{L}} Y_u u'_{\mathrm{R}}) + h.c.\,, \tag{2.1}$$

where the quark fields $u'_{\mathrm{L/R}}$ denote the weak eigenstates of the left-handed and right-handed up-type quarks and the quark fields $d'_{\mathrm{L/R}}$ denote the weak eigenstates of the left- and right-handed down-type quarks. $\bar{u}'_{\mathrm{L/R}}$ and $\bar{d}'_{\mathrm{L/R}}$ are the corresponding fields describing the anti-quarks. The Yukawa matrices Y_u and Y_d are 3×3 complex matrices. They have non-zero off-diagonal elements which leads to the fact that the weak eigenstates of the quarks are not equal to their mass eigenstates.

The mass eigenstates $u_{\mathrm{L/R}}$ and $d_{\mathrm{L/R}}$ are obtained by unitary basis transformations $u_{\mathrm{L/R}} = V^u_{\mathrm{L/R}} u'_{\mathrm{L/R}}$ and $d_{\mathrm{L/R}} = V^d_{\mathrm{L/R}} d'_{\mathrm{L/R}}$ with unitary matrices $V^u_{\mathrm{L/R}}$ and $V^d_{\mathrm{L/R}}$ that must be constructed such that the Yukawa matrices are diagonalised.

If both Yukawa matrices can not be diagonalised simultaneously by the same matrices ($V^u_{\mathrm{L/R}} \neq V^d_{\mathrm{L/R}}$), the basis transformation leads to a remaining factor $V_{\mathrm{CKM}} = V^u_{\mathrm{L}} V^{d\,\dagger}_{\mathrm{L}}$ in the term of the Lagrangian describing the charged weak current $\mathcal{L}_{\mathrm{cc}}$ [14]:

$$\mathcal{L}_{\mathrm{cc}} = -\frac{g}{\sqrt{2}} (\bar{u}_{\mathrm{L}} \gamma^\mu W^+_\mu V_{\mathrm{CKM}} d_{\mathrm{L}} + \bar{d}_{\mathrm{L}} \gamma^\mu W^-_\mu V^\dagger_{\mathrm{CKM}} u_{\mathrm{L}}) \,. \tag{2.2}$$

V_{CKM} is the unitary 3×3 Cabbibo-Kobayashi-Maskawa matrix [15] connecting left-handed down-type quarks to left-handed up-type quarks. In particular, the off-diagonal elements of the CKM-matrix allow for transitions between quarks of different generations.
Using a notation with quark flavour indices, the CKM-matrix can be written as

$$V_{\mathrm{CKM}} = \begin{pmatrix} V_{ud} & V_{us} & V_{ub} \\ V_{cd} & V_{cs} & V_{cb} \\ V_{td} & V_{ts} & V_{tb} \end{pmatrix} . \tag{2.3}$$

with complex matrix elements V_{ij} and thus in total 18 parameters. They can be reduced by taking into account the unitary relation of the CKM-matrix $V_{\mathrm{CKM}} V^\dagger_{\mathrm{CKM}} = 1$ and redefining the quark-fields by absorbing 5 unobservable phases. Four free parameters are left, three real mixing angles ($\theta_{12}, \theta_{13}, \theta_{23}$) and one complex phase (δ_{13}).
Due to the remaining complex phase, the Lagrangian is not invariant under CP transformation. CP means a combined parity (P) transformation, inverting the space coordinates of the fields, and a charge (C) conjugation, transforming particles to anti-particles. Applying the CP transformation to the charged current leads to [14]:

$$\mathcal{L}^{CP}_{\mathrm{cc}} = -\frac{g}{\sqrt{2}} (\bar{d}_{\mathrm{L}} \gamma^\mu W^-_\mu V^{\mathrm{T}}_{\mathrm{CKM}} u_{\mathrm{L}} + \bar{u}_{\mathrm{L}} \gamma^\mu W^+_\mu V^*_{\mathrm{CKM}} d_{\mathrm{L}}) \,. \tag{2.4}$$

The complex phase in the CKM-matrix implies $V_{\mathrm{CKM}} \neq V^*_{\mathrm{CKM}}$ and results in different complex couplings for quarks in weak transitions. The CP symmetry of the charged current Lagrangian is broken (CP violation). In fact the complex phase in the CKM-matrix is the unique source of CP violation in the Standard Model.

To better reflect the hierarchical order of the matrix elements, V_{CKM} is often expressed in the Wolfenstein parameterisation [16]

$$V_{CKM} = \begin{pmatrix} 1-\frac{\lambda^2}{2} & \lambda & A\lambda^3(\rho - i\eta) \\ -\lambda & 1-\frac{\lambda^2}{2} & A\lambda^2 \\ A\lambda^3(1-\rho-i\eta) & -A\lambda^2 & 1 \end{pmatrix} + O(\lambda^4) \tag{2.5}$$

as an expansion in $\lambda = \sin\theta_{12}$, with $A = \frac{\sin\theta_{23}}{\lambda^2}$ and $\rho + i\eta = \sin\theta_{13}e^{i\delta_{13}}/A\lambda^3$. The values of the parameters are obtained from global fits using experimental data to [9]:

$$\begin{aligned} \lambda &\approx 0.23\,, \qquad & A &\approx 0.81\,, \\ \bar{\rho} = \rho(1-\frac{\lambda^2}{2}) &= 0.13\,, \qquad & \bar{\eta} = \eta(1-\frac{\lambda^2}{2}) &= 0.35\,. \end{aligned} \tag{2.6}$$

The diagonal elements of the CKM-matrix are ~ 1 and transitions between quarks of the same generation are therefore preferred. Transitions between the generations, described by the off-diagonal elements, are suppressed (up to λ^3 for V_{ub} and V_{td}). The parameter η in V_{ub} and V_{tb} defines the imaginary parts of the CKM-matrix elements that can lead to CP violation in the corresponding quark transition processes.

From the unitarity condition of the CKM-matrix ($V_{\mathrm{CKM}}V^{\dagger}_{\mathrm{CKM}} = 1$), one can derive six relations of the form

$$V_{ud}V^*_{ub} + V_{cd}V^*_{cb} + V_{td}V^*_{tb} = 0\,, \tag{2.7}$$

which can be interpreted as triangles in the complex plane with the related angles

$$\alpha \equiv \arg\left(-\frac{V_{td}V^*_{tb}}{V_{ud}V^*_{ub}}\right), \quad \beta \equiv \arg\left(-\frac{V_{cd}V^*_{cb}}{V_{td}V^*_{tb}}\right), \quad \gamma \equiv \arg\left(-\frac{V_{ud}V^*_{ub}}{V_{cd}V^*_{cb}}\right). \tag{2.8}$$

Figure 2.1 shows the corresponding triangle with sides normalised to $V_{\mathrm{cd}}V^*_{\mathrm{cb}}$.

The unitarity triangle in Equation 2.7 is often called the "B^0_d triangle" because the related CKM-matrix elements are accessible via measurements of B^0_d meson decays. Similarly, there is a second triangle that can be constrained using B^0_s meson decays ("B^0_s triangle"). It is given by the relation

$$V_{us}V^*_{ub} + V_{cs}V^*_{cb} + V_{ts}V^*_{tb} = 0\,. \tag{2.9}$$

Of particular interest for this thesis is the small angle

$$\beta_{\mathrm{s}} \equiv \arg\left(-\frac{V_{ts}V^*_{tb}}{V_{cs}V^*_{cb}}\right), \tag{2.10}$$

which is, via the complex matrix elements V_{ts} (at $O(\lambda^4)$), sensitive to CP violation.

The CKM-matrix elements are not predicted by the Standard Model. Many measurements have been performed to determine the CKM-matrix elements and test the unitarity of the CKM-matrix. Figure 2.2 summarises the current experimental status of the "B^0_d triangle" and the "B^0_s triangle":

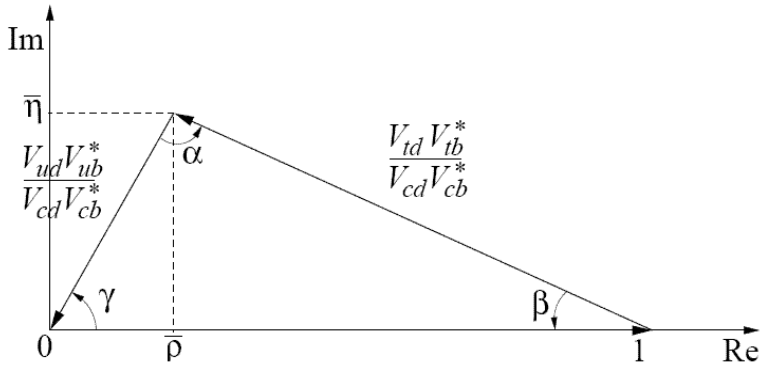

Figure 2.1: Unitarity triangle, corresponding to Equation 2.7, with side lengths normalised to $V_{cd}V_{cb}^*$. The figure is taken from [17].

- The length of the left side of the triangles is constrained by branching ratio measurements of semileptonic B decays. The branching ratio of $B \to Xl\nu$ decays is proportional to the CKM-matrix element $|V_{ub}|^2$ or $|V_{cb}|^2$, if X contains a u or a c quark, respectively.

- The right side of the triangles is constrained by measurements of B_d^0-$\overline{B}^0$ and B_s^0-$\overline{B}_s^0$ mixing.

- The angles of the unitarity triangles can be determined by precision measurements of CP violation in B meson decays. Currently, the strongest constraint for the "B_d^0 triangle" is given by measurements of $\sin 2\beta$ using $B_d^0 \to J/\psi K_S^0$ decays. For the "B_s^0 triangle" the angle β_s can be measured with $B_s^0 \to J/\psi\phi$ decays.

- Additional constraints are given on the position of the apex of the triangles by neutral kaon physics.

2.3 B_s^0–$\overline{B}_s^0$ mixing

The charged current in the Standard Model (Equation 2.2) allows for interactions between up-type and down-type quarks. As a consequence, transitions between the flavour eigenstates of neutral B mesons are possible. This process is called B-$\overline{B}$ mixing. The theoretical description of B-$\overline{B}$ mixing is identical for B_d^0 and B_s^0 mesons. In the following, they will simply be denoted as B_q. The leading-order mixing process can be described by a box-diagram shown in Figure 2.3. The dominant contribution to

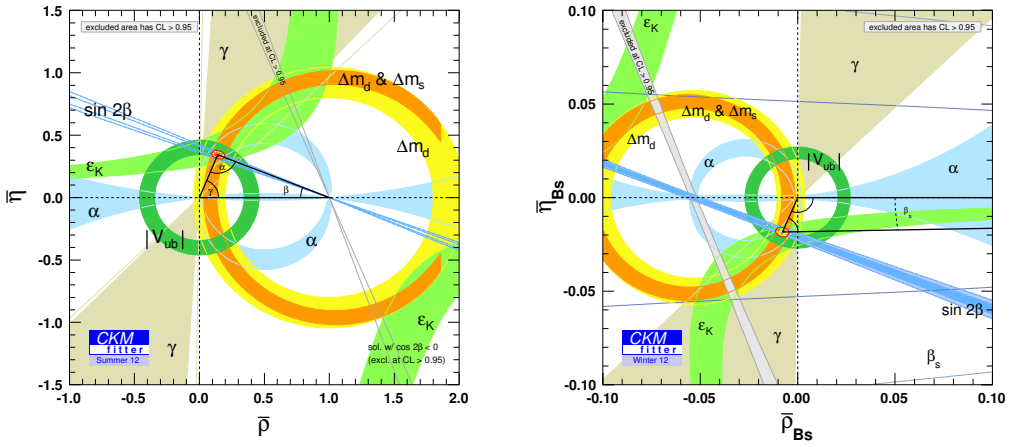

(a) "B_d^0 triangle" (b) "B_s^0 triangle"

Figure 2.2: Current experimental status of the unitarity triangles defined in equations 2.7 and 2.9. The single measurements limit the apex of the triangles to 95% confidence intervals indicated by the red dashed regions. Both figures are taken from [18].

the mixing amplitude is the process with a t-quark in the internal loop.

The phenomenology of B_q-$\overline{B}_q$ mixing is discussed in several documents and will only be briefly summarised here. The following details are extracted from References [19], [20] and [21].
The state vectors of flavour eigenstates at $t = 0$ can be denoted as $|B_q\rangle = |\bar{b}q\rangle$ and $|\overline{B}_q\rangle = |b\bar{q}\rangle$. They behave under a CP transformation as

$$CP|B_q\rangle = -|\overline{B}_q\rangle\,, \quad CP|\overline{B}_q\rangle = -|B_q\rangle\,. \tag{2.11}$$

The time evolution of these states $|B_q(t)\rangle$ and $|\overline{B}_q(t)\rangle$ is given by the phenomenological Schroedinger equation for the 2-state system:

$$i\frac{\mathrm{d}}{\mathrm{d}t}\begin{pmatrix} |B_q(t)\rangle \\ |\overline{B}_q(t)\rangle \end{pmatrix} = \left(M - i\frac{\Gamma}{2}\right)\begin{pmatrix} |B_q(t)\rangle \\ |\overline{B}_q(t)\rangle \end{pmatrix}\,. \tag{2.12}$$

The mass matrix M and the decay width matrix Γ are 2×2 hermitian matrices. Due to the CPT invariance theorem, their diagonal elements are identical:

$$M_{11} = M_{22}\,, \quad \Gamma_{11} = \Gamma_{22}\,. \tag{2.13}$$

The off-diagonal elements $M_{12} = M_{21}^*$ and $\Gamma_{12} = \Gamma_{21}^*$ are responsible for the B_q-$\overline{B}_q$ mixing. M_{12} represents short-distance effects where the mixing is processed via virtual

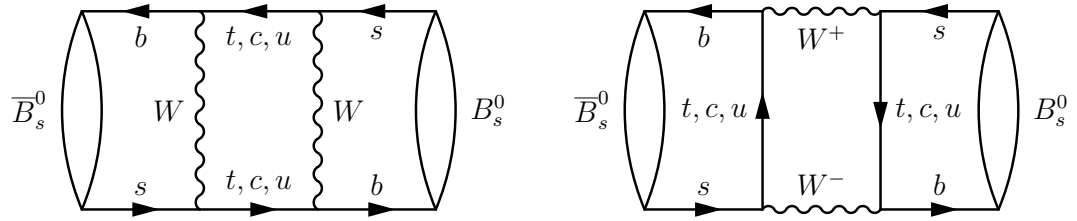

Figure 2.3: Leading-order diagrams contributing to B_q-$\overline{B}_q$ mixing (shown for B_s^0 mesons). The figure is taken from [22].

heavy states as shown in Figure 2.3. Γ_{12} represents the long-distance mixing via real on-shell particles such as an intermediate $\pi^+\pi^-$ state. For B_q-$\overline{B}_q$ mixing, the short-distance effects are dominant and therefore $|M_{12}| >> |\Gamma_{12}|$.
The non-zero off diagonal elements also imply that the mass eigenstates of the B_q mesons are not identical to the flavour eigenstates. The mass eigenstates at $t = 0$, represented by the state vectors $|B_L\rangle$ and $|B_H\rangle$, can be obtained by diagonalising the matrix $(M - i\frac{\Gamma}{2})$ and can be related to the flavour eigenstates via:

$$\begin{aligned} |B_L\rangle &= p|B_q\rangle + q|\overline{B}_q\rangle\,, \\ |B_H\rangle &= p|B_q\rangle - q|\overline{B}_q\rangle\,, \end{aligned} \tag{2.14}$$

where $|p|^2 + |q|^2 = 1$. The corresponding mass eigenvalues $(M_{\mathrm{H}} - i\Gamma_{\mathrm{H}}/2)$ and $(M_{\mathrm{L}} - i\Gamma_{\mathrm{L}}/2)$ lead to the time evolution of the mass eigenstates such that

$$\begin{aligned} |B_H(t)\rangle &= e^{-(iM_{\mathrm{H}}+\Gamma_{\mathrm{H}}/2)t}|B_H\rangle\,, \\ |B_L(t)\rangle &= e^{-(iM_{\mathrm{L}}+\Gamma_{\mathrm{L}}/2)t}|B_L\rangle\,. \end{aligned} \tag{2.15}$$

M_{H} and M_{L} are the masses and Γ_{H}, Γ_{L} the decay widths of the corresponding mass eigenstates. It is possible to relate these parameters to the parameters in the flavour eigenbasis by defining the variables

$$\begin{aligned} m &= \frac{M_{\mathrm{H}} + M_{\mathrm{L}}}{2}\,, \qquad & \Gamma &= \frac{\Gamma_{\mathrm{L}} + \Gamma_{\mathrm{H}}}{2}\,, \\ \Delta m &= M_{\mathrm{H}} - M_{\mathrm{L}}\,, \qquad & \Delta\Gamma &= \Gamma_{\mathrm{L}} - \Gamma_{\mathrm{H}}\,, \end{aligned} \tag{2.16}$$

where Δm is the mass difference, often called mixing frequency, and $\Delta\Gamma$ is the decay width difference of the states $|B_H\rangle$ and $|B_L\rangle$. The mixing frequency in the B_d^0 system, in the following denoted as Δm_{d}, was first measured by the ARGUS collaboration [23]. The current world average is $\Delta m_{\mathrm{d}} = 0.507 \pm 0.004\,\mathrm{ps}^{-1}$ [9]. The B_s^0 meson oscillates much faster and the mixing was first observed by the CDF collaboration [24]. The currently best value of the mixing frequency was measured by LHCb with

$\Delta m_s = 17.63 \pm 0.11\,\text{ps}^{-1}$ [25].
The variables in Equation 2.16 are related to M_{12} and Γ_{12} by

$$(\Delta m)^2 - \frac{1}{4}(\Delta\Gamma)^2 = 4|M_{12}|^2 - |\Gamma_{12}|^2\,, \qquad \Delta m\Delta\Gamma = -4\Re(M_{12}\Gamma_{12}^*)\,. \tag{2.17}$$

Similarly, one can relate q/p to the off-diagonal matrix elements by

$$\frac{q}{p} = -\frac{\Delta m + i\Delta\Gamma/2}{2M_{12} - i\Gamma_{12}} = -\frac{2M_{12}^* - i\Gamma_{12}^*}{\Delta m + i\Delta\Gamma/2}\,. \tag{2.18}$$

As $|\Gamma_{12}| << |M_{12}|$ in the B_q-$\overline{B}_q$ mixing, the above expressions can be expanded in $\frac{\Gamma_{12}}{M_{12}}$, leading to

$$\begin{aligned} \Delta m = 2|M_{12}|\,, \quad \Delta\Gamma = 2|\Gamma_{12}|\cos\phi_{M_{12}/\Gamma_{12}}\,, \\ \frac{q}{p} = -e^{-i\phi_\text{M}}(1 - \frac{1}{2}\frac{|\Gamma_{12}|}{|M_{12}|}\sin\phi_{M_{12}/\Gamma_{12}})\,, \end{aligned} \tag{2.19}$$

with $\phi_{M_{12}/\Gamma_{12}} = \arg(-\frac{M_{12}}{\Gamma_{12}})$ and $\phi_\text{M} = \arg(M_{12})$. It is possible to approximate q/p even further to $q/p = -e^{-i\phi_\text{M}}$.

Given the relations of flavour and mass eigenstates in Equation 2.14, the time evolution of the flavour eigenstates can be calculated from Equation 2.15 as

$$\begin{aligned} |B_q(t)\rangle &= g_+(t)|B_q\rangle + \frac{q}{p}g_-(t)|\overline{B}_q\rangle\,, \\ |\overline{B}_q(t)\rangle &= \frac{p}{q}g_-(t)|B_q\rangle + g_+(t)|\overline{B}_q\rangle\,, \end{aligned} \tag{2.20}$$

The functions $g_\pm(t)$ contain the full time-dependence and are given by

$$\begin{aligned} g_+(t) &= e^{-imt}e^{-\Gamma t/2}\left(\cosh\frac{\Delta\Gamma}{4}\cos\frac{\Delta m t}{2} - i\sinh\frac{\Delta\Gamma t}{4}\sin\frac{\Delta m t}{2}\right)\,, \\ g_-(t) &= e^{-imt}e^{-\Gamma t/2}\left(-\sinh\frac{\Delta\Gamma}{4}\cos\frac{\Delta m t}{2} + i\cosh\frac{\Delta\Gamma t}{4}\sin\frac{\Delta m t}{2}\right)\,. \end{aligned} \tag{2.21}$$

The time dependent decay rate of a produced B_q meson decaying into some final state f is given by

$$\frac{\Gamma(B_q(t) \to f)(t)}{\mathrm{d}t} = \frac{1}{N_B}\frac{\mathrm{d}N(B_q(t) \to f)}{\mathrm{d}t} \propto |\langle f|B_q(t)\rangle|^2\,, \tag{2.22}$$

where N_B is a normalisation factor giving the total number of produced B_q mesons. $N(B_q(t) \to f)$ is the number of initially produced B_q mesons decaying to the final state f at time t. For simplification of the further expressions, the decay amplitudes at $t = 0$ will be denoted as:

$$A_f = \langle f|B_q\rangle\,, \quad \overline{A}_f = \langle f|\overline{B}_q\rangle \tag{2.23}$$

In addition, the complex parameter λ_f is introduced, defined as

$$\lambda_f = \frac{q}{p}\frac{\overline{A}_f}{A_f}\,. \tag{2.24}$$

λ_f will play an important role in the discussion of CP violation in the next section.

Using Equation 2.20 and the above notations, the differential decay rates for at time $t = 0$ produced B_q and $\overline{B}_q$ mesons into the final state f can be written as

$$\begin{aligned}\frac{\Gamma(B_q(t) \to f)}{\mathrm{d}t} \;\propto\; |A_f|^2 e^{-\Gamma t}\Bigg[&\frac{1+|\lambda_f|^2}{2}\cosh\frac{\Delta\Gamma t}{2} + \frac{1-|\lambda_f|^2}{2}\cos(\Delta m t)\\ &- \Re\lambda_f \sinh\frac{\Delta\Gamma t}{2} - \Im\lambda_f \sin(\Delta m t)\Bigg].\end{aligned} \tag{2.25}$$

$$\begin{aligned}\frac{\Gamma(\overline{B}_q(t) \to f)}{\mathrm{d}t} \;\propto\; |A_f|^2 |\frac{p}{q}|^2 e^{-\Gamma t}\Bigg[&\frac{1+|\lambda_f|^2}{2}\cosh\frac{\Delta\Gamma t}{2} - \frac{1-|\lambda_f|^2}{2}\cos(\Delta m t)\\ &- \Re\lambda_f \sinh\frac{\Delta\Gamma t}{2} + \Im\lambda_f \sin(\Delta m t)\Bigg],\end{aligned} \tag{2.26}$$

Both decay rates differ only in the sign of the oscillation terms $\sin(\Delta m t)$ and $\cos(\Delta m t)$ and in an additional factor $|\frac{p}{q}|^2$.
For the decay of the B_q mesons in the CP-conjugated final state $\bar{f}$ with $|\bar{f}\rangle = CP|f\rangle$ one can write the decay amplitudes at $t = 0$ as

$$A_{\bar{f}} = \langle \bar{f}|B_q\rangle\,, \quad \overline{A}_{\bar{f}} = \langle \bar{f}|\overline{B}_q\rangle\,. \tag{2.27}$$

The differential decay rates for at time $t = 0$ produced B_q and $\overline{B}_q$ mesons in the final state $\bar{f}$ are then given by:

$$\begin{aligned}\frac{\Gamma(B_q(t) \to \bar{f})}{\mathrm{d}t} \;\propto\; |\overline{A}_{\bar{f}}|^2 |\frac{q}{p}|^2 e^{-\Gamma t}\Bigg[&\frac{1+|\bar{\lambda}_{\bar{f}}|^2}{2}\cosh\frac{\Delta\Gamma t}{2} - \frac{1-|\bar{\lambda}_{\bar{f}}|^2}{2}\cos(\Delta m t)\\ &- \Re\bar{\lambda}_{\bar{f}} \sinh\frac{\Delta\Gamma t}{2} + \Im\bar{\lambda}_{\bar{f}} \sin(\Delta m t)\Bigg],\end{aligned} \tag{2.28}$$

$$\begin{aligned}\frac{\Gamma(\overline{B}_q(t) \to \bar{f})}{\mathrm{d}t} \;\propto\; |\overline{A}_{\bar{f}}|^2 e^{-\Gamma t}\Bigg[&\frac{1+|\bar{\lambda}_{\bar{f}}|^2}{2}\cosh\frac{\Delta\Gamma t}{2} + \frac{1-|\bar{\lambda}_{\bar{f}}|^2}{2}\cos(\Delta m t)\\ &- \Re\bar{\lambda}_{\bar{f}} \sinh\frac{\Delta\Gamma t}{2} - \Im\bar{\lambda}_{\bar{f}} \sin(\Delta m t)\Bigg],\end{aligned} \tag{2.29}$$

where $\bar{\lambda}_{\bar{f}}$ is defined as $\bar{\lambda}_{\bar{f}} = \frac{p}{q}\frac{A_{\bar{f}}}{\overline{A}_{\bar{f}}}$.

2.3.1 CP violation

From the differential decay rates described above, three different mechanisms of CP violation can be observed and will be discussed in the following. The measurement of CP violation is only possible in the interference of two amplitudes, each containing a complex phase that changes the sign under CP transformation, called *weak phase* and a phase that does not change sign under a CP transformation, called *strong phase*. The weak phase usually originates from weak interactions and is related to the complex phase in the CKM-matrix.

CP violation in decay

CP violation in decay happens when the decay amplitude of B_q decaying to the final state f is different than the decay amplitude of the CP-conjugate process, $\overline{B}_q$ decaying to $\bar{f}$. In terms of the decay rates, this is realised when $\Gamma(B_q \to f) \neq \Gamma(\overline{B}_q \to \bar{f})$ corresponding to

$$|\frac{\overline{A}_{\bar{f}}}{A_f}| \neq 1\,. \tag{2.30}$$

CP violation in decay can be observed by measuring the time-integrated asymmetry

$$a = \frac{\Gamma(B_q \to f) - \Gamma(\overline{B}_q \to \bar{f})}{\Gamma(B_q \to f) + \Gamma(\overline{B}_q \to \bar{f})}\,. \tag{2.31}$$

It can, for example, be measured in $B_d^0 \to K^+\pi^-$ decays where the CP violation is introduced by a large interference between tree and suppressed penguin amplitudes.

CP violation in mixing

CP violation in mixing occurs when the oscillation probability of $B_q \to \overline{B}_q$ is different than the probability of $\overline{B}_q \to B_q$. This is realised when $\Gamma(B_q \to \bar{f}) \neq \Gamma(\overline{B}_q \to f)$ corresponding to

$$\frac{|q|}{|p|} \neq 1\,. \tag{2.32}$$

The CP violation is introduced by the interference of two different mixing amplitudes, shown in Figure 2.3. It can be measured with the time integrated asymmetry

$$a = \frac{\Gamma(B_q \to \bar{f}) - \Gamma(\overline{B}_q \to f)}{\Gamma(B_q \to \bar{f}) + \Gamma(\overline{B}_q \to f)}\,, \tag{2.33}$$

when the process $B_q \to \bar{f}$ can only happen via an oscillation $B_q \to \overline{B}_q \to \bar{f}$ (flavour specific decay). Examples of this are semileptonic $B_d^0 \to Xl^+\nu$ decays. The Standard Model prediction for the asymmetry for $B_d^0 \to Xl^+\nu$ decays is small, $O(10^{-4})$ [14].

CP violation in interference of mixing and decay

An additional type of CP violation can occur when the final state f is a CP eigenstate f_{CP} for which $CP|f_{CP}\rangle = \eta_{CP}|f_{CP}\rangle$, where $\eta_{CP} = \pm 1$. In this case the amplitudes of B_q decaying directly to f_{CP} and the amplitude of B_q oscillating first to $\overline{B}_q$ and then decaying to f_{CP} can interfere. The process is illustrated in Figure 2.4. The relative phase between the two amplitudes can introduce CP violation in the interference of mixing and decay.
It is related to a difference in the decay rates $\Gamma(B_q \to \bar{f}_{CP})$ and $\Gamma(\overline{B}_q \to f_{CP})$ (see Equations 2.25 and 2.28) that is introduced by the complex parameter λ_f which, for a decay into a CP eigenstate f_{CP}, can be denoted as

$$\lambda_{\mathrm{CP}} = \frac{q}{p}\frac{\overline{A}_{f_{CP}}}{A_{f_{CP}}}\,. \tag{2.34}$$

The decay amplitude $A_{f_{CP}}$ of $B_q \to f_{CP}$ can be written as

$$A_{f_{CP}} = |A_{f_{CP}}|e^{i(\delta_f + \phi_{\mathrm{D}})}\,, \tag{2.35}$$

where ϕ_{D} is a weak phase that enters the decay amplitude and its CP conjugate with different signs. δ_f is a strong phases that does not change sign under a CP transformation. The decay amplitude of $\overline{B}_q \to f_{CP}$ can be related to $A_{f_{CP}}$ using the property of CP eigenstates $|f_{CP}\rangle = \eta_{CP}|\bar{f}_{CP}\rangle$, and assuming no CP violation in decay ,as

$$\overline{A}_{f_{CP}} = \eta_{CP}\overline{A}_{\bar{f}_{CP}} = \eta_{CP}|A_{f_{CP}}|e^{i(\delta_f - \phi_{\mathrm{D}})}\,, \tag{2.36}$$

The ratio of the two amplitudes is then given by

$$\frac{\overline{A}_{f_{CP}}}{A_{f_{CP}}} = \eta_{CP}e^{i2\phi_{\mathrm{D}}}\,. \tag{2.37}$$

Following equation 2.19, the ratio $\frac{q}{p}$ is approximated to $\frac{q}{p} = -e^{-i\phi_{\mathrm{M}}}$ with $\phi_{\mathrm{M}} = \arg(M_{12})$ (implying $|\frac{q}{p}| = 1$). Both phases, ϕ_{M} and ϕ_{D}, are convention dependent; the ratio λ_{CP} is not. The phase of λ_{CP}, expressed as

$$\phi = -\arg\lambda_{\mathrm{CP}} = \phi_{\mathrm{M}} - 2\phi_{\mathrm{D}} \tag{2.38}$$

is a phase difference and thus an observable. As a consequence, even if $|\frac{q}{p}| = 1$ (no CP violation in mixing) and $|\frac{\overline{A}_{f_{CP}}}{A_{f_{CP}}}| = 1$ (no CP violation in decay) the relative phase between $\frac{q}{p}$ and $\frac{\overline{A}_{f_{CP}}}{A_{f_{CP}}}$ can introduce CP violation.

CP violation in the interference of decay and mixing can be measured with the time-dependent asymmetry

$$a(t) = \frac{\Gamma(\overline{B}_q \to f)(t) - \Gamma(B_q \to f)(t)}{\Gamma(\overline{B}_q \to f)(t) + \Gamma(B_q \to f)(t)}\,. \tag{2.39}$$

If $|\lambda_{\mathrm{CP}}| = 1$, the asymmetry is given by

$$a(t) = \frac{\Im\lambda_{\mathrm{CP}} \sin(\Delta m t)}{\cosh(\Delta\Gamma t/2) - \Re\lambda_{\mathrm{CP}} \sinh(\Delta\Gamma t/2)} . \tag{2.40}$$

It was, for example, measured for the decay channel $B_d^0 \to J/\psi K_S^0$ where due to $\Delta\Gamma_{\mathrm{d}} \approx 0$ expression 2.40 simplifies to

$$a(t) = \Im\lambda_{\mathrm{CP}} \sin(\Delta m_{\mathrm{d}} t) = -\eta_{CP} \sin(\phi) \sin(\Delta m_{\mathrm{d}} t) . \tag{2.41}$$

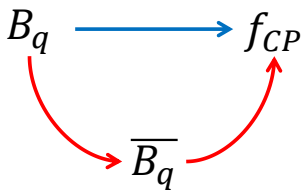

Figure 2.4: Illustration of the interfering amplitudes (red and blue) contributing to CP violation in interference of decay and mixing.

2.4 Time dependent decay rate for $B_s^0 \to J/\psi\phi$

This thesis presents a measurement of CP violation in the interference of B_s^0 mixing and decay. Two different final states $f = J/\psi K^+K^-$ and $f = J/\psi\pi^+\pi^-$ are used for this: The most important case is when the $J/\psi K^+K^-$ is reached via an intermediate ϕ resonance with $\phi \to K^+K^-$. The branching ratio for this decay is $\mathrm{BR}(\mathrm{B_s^0} \to \mathrm{J/\psi\phi}) = 1.09^{+0.28}_{-0.23} \cdot 10^{-3}$ [9]. This case is called P-wave amplitude as the ϕ is a spin-1 meson. The P-wave amplitude can interfere with a much smaller contribution of non-resonant $B_s^0 \to J/\psi K^+K^-$ decays or $B_s^0 \to J/\psi f_0(980)$ decays with $f_0(980) \to K^+K^-$, that contribute to the same final state. These are called S-wave amplitude as the non-resonant K^+K^- system as well as the $f_0(980)$ resonance are spin-0.
In addition the final state $J/\psi\pi^+\pi^-$ can be used with a branching ratio relative to $B_s^0 \to J/\psi\phi$ of $\frac{\mathrm{BR}(\mathrm{B_s^0 \to J/\psi\pi^+\pi^-})}{B_s^0 \to J/\psi\phi} = (21.28 \pm 0.51 \pm 0.56)\%$ [26]. This final state can be reached via several interfering resonances, the most important one is $J/\psi f_0(980)$ with $f_0(980) \to \pi^+\pi^-$. A detailed discussion of the $J/\psi\pi^+\pi^-$ resonance structure will be given in Chapter 13.

The dominant transition diagrams for the different final states are very similar, as shown in Figure 2.5. The total amplitude of the B_s^0 decaying to $J/\psi\phi$ is, following [27], given by

$$A_f = V_{\mathrm{cs}}V_{\mathrm{cb}}^*(T + P_c - P_t) + V_{\mathrm{us}}V_{\mathrm{ub}}^*(P_u - P_t) , \tag{2.42}$$

where T denotes the tree-level amplitude, shown in the left diagram of Figure 2.5, and the P_i with $i = u, c, t$ denote the penguin amplitudes (right diagram of Figure 2.5). $V_{\mathrm{us}}V_{\mathrm{ub}}^*$ is suppressed by a factor $\lambda^2 \approx 0.05$ compared to $V_{\mathrm{cs}}V_{\mathrm{cb}}^*$ and, with the expected precision, needs not to be considered in this analysis. For the $J/\psi\pi^+\pi^-$ final state, the quark composition of the intermediate resonances is not very well known. Therefore additional amplitudes might contribute [28], but also not relevant for the precision of this analysis. The weak phase of the decay amplitudes is then only given by $\phi_{\mathrm{D}} = \arg(V_{\mathrm{cs}}V_{\mathrm{cb}}^*)$
The weak phase of the B_s^0-$\overline{B}_s^0$ mixing amplitude, ϕ_{M}, is given by the CKM-matrix elements of the leading box-diagram (figure 2.3) $\phi_{\mathrm{M}} = -2\arg(V_{\mathrm{ts}}V_{\mathrm{tb}}^*)$. The observable phase in the interference of B_s^0 mixing and decay to the final states $f = J/\psi K^+K^-$, $J/\psi\pi^+\pi^-$ will be denoted as ϕ_{s} and is, using Equation 2.38:

$$\phi_{\mathrm{s}} = \phi_{\mathrm{M}} - 2\phi_{\mathrm{D}} = -2\arg(V_{\mathrm{ts}}V_{\mathrm{tb}}^*) - 2\arg(V_{\mathrm{cs}}V_{\mathrm{cb}}^*) = -2\arg\left(-\frac{V_{ts}V_{tb}^*}{V_{cs}V_{cb}^*}\right) = -2\beta_{\mathrm{s}}\,, \quad (2.43)$$

where β_{s} is the angle in the "B_s^0 unitarity triangle" as defined in Equation 2.9. Within the Standard Model, $2\beta_{\mathrm{s}}$ has been determined indirectly from global fits to experimental data as $2\beta_{\mathrm{s}} = 0.0364 \pm 0.0016$ rad [8]. The precise Standard Model prediction makes the measurement of ϕ_{s} an excellent test for New Physics contributions.

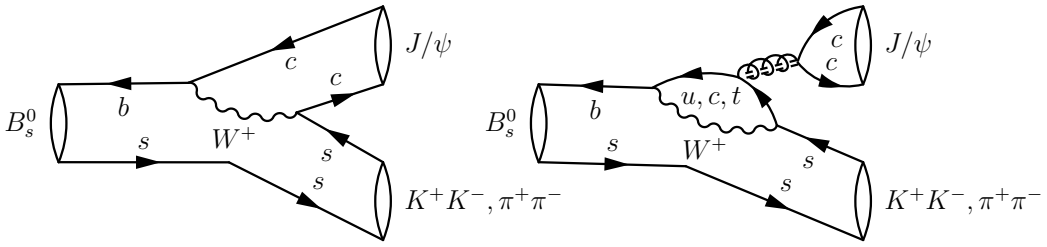

Figure 2.5: Diagrams contributing to the decay of a B_s^0 meson to the $J/\psi K^+K^-$ and $J/\psi\pi^+\pi^-$ final states. Left: tree diagram, right: penguin diagram. The figure is taken from [22].

This analysis will mainly concentrate on the measurement of ϕ_{s} with $B_s^0 \to J/\psi\phi$ decays as the most sensitive decay channel for ϕ_{s}. Nevertheless, the interference with a $J/\psi K^+K^-$ S-wave contribution needs to be taken into account. A measurement of ϕ_{s} with the $J/\psi\pi^+\pi^-$ final state will be presented in Chapter 13.
In general, the differential decay rates for B_s^0 and $\overline{B}_s^0$ decaying into a pure CP eigenstate f_{CP} are given by Equations 2.25 and 2.26 and can be expressed, assuming no CP

violation in mixing ($\frac{|q|}{|p|} = 1$), as

$$\frac{\mathrm{d}\Gamma(B_s^0 \to f_{CP})}{\mathrm{d}t} \propto |A_{CP}|^2 e^{-\Gamma_s t} \frac{1}{1+C} \Big[\cosh\left(\frac{\Delta\Gamma_s t}{2}\right) + D\eta_{CP} \sinh\left(\frac{\Delta\Gamma_s t}{2}\right) + C\cos(\Delta m_s t) - S\,\eta_{CP} \sin(\Delta m_s t)\Big], \tag{2.44}$$

$$\frac{\mathrm{d}\Gamma(\overline{B}_s^0 \to f_{CP})}{\mathrm{d}t} \propto |A_{CP}|^2 e^{-\Gamma_s t} \frac{1}{1+C} \Big[\cosh\left(\frac{\Delta\Gamma_s t}{2}\right) + D\eta_{CP} \sinh\left(\frac{\Delta\Gamma_s t}{2}\right) - C\cos(\Delta m_s t) + S\,\eta_{CP} \sin(\Delta m_s t)\Big], \tag{2.45}$$

where $|A_{CP}|^2$ is the decay amplitude and $\eta_{CP} = \pm 1$ the CP eigenvalue of f_{CP}. The terms C, D and S are defined as

$$C = \frac{1-|\lambda_{\mathrm{CP}}|^2}{1+|\lambda_{\mathrm{CP}}|^2}, \quad D = -\frac{2|\lambda_{\mathrm{CP}}|}{1+|\lambda_{\mathrm{CP}}|^2}\cos\phi_s, \quad S = -\frac{2|\lambda_{\mathrm{CP}}|}{1+|\lambda_{\mathrm{CP}}|^2}\sin\phi_s, \tag{2.46}$$

where $\phi_s = -\arg(\lambda_{CP})$ was used.

In $B_s^0 \to J/\psi\phi$ however, a pseudo-scalar meson with spin-0 decays to two vector mesons with spin-1, allowing for a relative angular momentum $l = 0, 1, 2$ between the J/ψ and ϕ meson. Thus, the final state is not a pure CP eigenstate with definite η_{CP} but a mixture of CP-even ($l = 0, 2$) and CP-odd ($l = 1$) decay amplitudes

$$CP|J/\psi\phi\rangle = (-1)^l |J/\psi\phi\rangle\,. \tag{2.47}$$

The three components with different angular momentum can be disentangled by performing an angular analysis where the final state is described in a basis of three decay angles. The measured physics observables are independent from the choice of the basis, but the basis determines the power to separate the three components. Two bases can be used for this kind of measurement: the transversity or the helicity basis.

- The transversity basis with the three transversity angles $\Omega_{\mathrm{tr}} = \{\psi, \theta, \varphi\}$ is defined in Figure 2.6. The angles θ and ϕ are defined in the rest frame of the J/ψ. The $x-y$ plane is defined by the K^+K^- plane, the x-axis by the flight direction of the ϕ and the y-axis such that $p_y(K^+) > 0$. The angle θ is then defined as the angle between the μ^+ flight direction and the z-axis. The angle φ is the angle between x-axis and the projection of the μ^+ flight direction on the $x-y$ plane. The angle ψ is defined as the angle between x-axis and the K^+ flight direction in the K^+K^- rest frame.

- The helicity basis with the three helicity angles $\Omega = \{\theta_\mu, \theta_{\mathrm{K}}, \varphi_{\mathrm{h}}\}$ is defined in Figure 2.7. θ_μ is the angle between the μ^+ and the opposite B_s^0 flight direction in the $\mu^+\mu^-$ center-of-mass frame. θ_{K} is similarly defined as the angle between the K^+ and the opposite B_s^0 flight direction direction in the K^+K^- center-of-mass frame. The relative rotation of the two decay planes is defined by φ_{h} as the angle between the K^- side of the K^+K^- plane and the μ^+ side of the $\mu^+\mu^-$ plane.

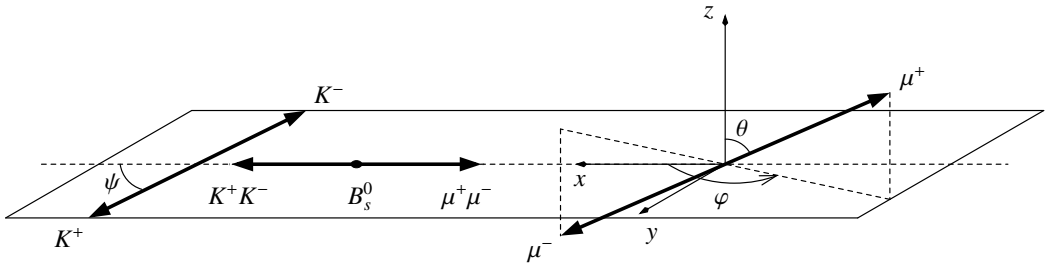

Figure 2.6: Definition of transversity angle basis. The figure is taken from [22].

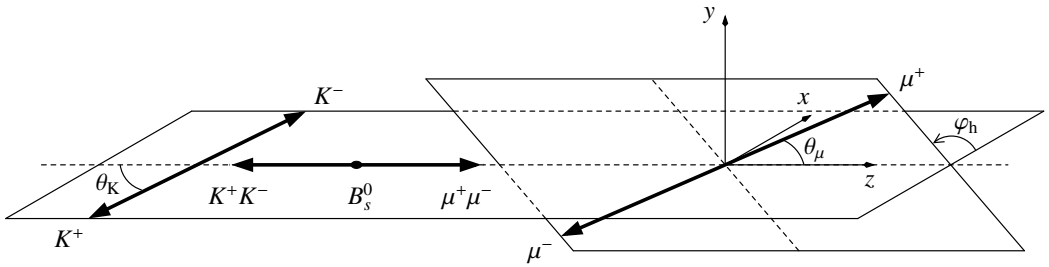

Figure 2.7: Definition of helicity angle basis used to separate the CP eigenstates of the $B_s^0 \to J/\psi\phi$ decay. The figure is taken from [22].

Both angular bases provide the same separation power for the three angular momentum states of the $B_s^0 \to J/\psi\phi$ decay and could both be chosen. While in former analysis the transversity basis was used, this analysis is performed with the helicity basis which has advantages in the description of background and detector acceptances.

The theoretical $B_s^0 \to J/\psi\phi$ decay rate is then expressed differentially in time and the three helicity angles Ω. Instead of separating the decay amplitude in three different angular momentum states, it can be decomposed in three complex polarisation amplitudes $A_0(t)$, $A_\parallel(t)$ and $A_\perp(t)$ that correspond to different polarisation states of the J/ψ and ϕ mesons. The polarisations are illustrated in Figure 2.8. $A_0(t)$ corresponds to the longitudinal polarisation of the mesons, $A_\parallel(t)$ and $A_\perp(t)$ to a transverse polarisation, where the polarisation vectors are either parallel ($A_\parallel(t)$) or perpendicular ($A_\perp(t)$). For $t = 0$, $A_0 = A_0(t = 0)$ and $A_\parallel = A_\parallel(t = 0)$ correspond to the CP-even part of the decay amplitude ($l = 0, 2$) while $A_\perp = A_\perp(t = 0)$ corresponds to the CP-odd part ($l = 1$).

Each of the amplitudes has a related strong phase $\delta_\parallel = \arg(A_\parallel)$, $\delta_\perp = \arg(A_\perp)$ and $\delta_0 = \arg(A_0)$.
Following equations 2.44 and 2.45 and accounting for interference of the single amplitudes, the time and angular dependent differential decay rate for produced B_s^0 decaying to a $J/\psi\phi$ final state can be written as [29]

$$\frac{\mathrm{d}\Gamma(B_s^0 \to J/\psi\phi)}{\mathrm{d}t\mathrm{d}\Omega} \propto \sum_{k=1}^{6} h_k(t) \cdot f_k(\Omega)\,. \tag{2.48}$$

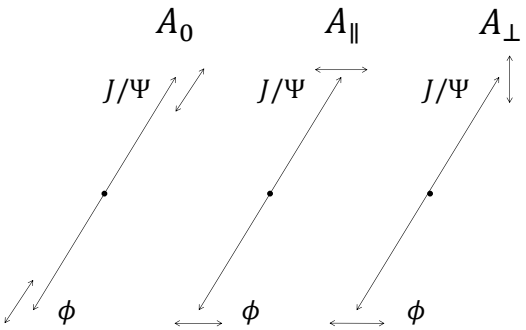

Figure 2.8: Illustration of the three polarisation amplitudes of the $B_s^0 \to J/\psi\phi$ decay. $A_0(t)$ corresponds to the longitudinal polarisation of the J/ψ and ϕ mesons, $A_\parallel(t)$ and $A_\perp(t)$ to a parallel and perpendicular transverse polarisation.

The functions $f_k(\Omega)$ depend only on the chosen angular basis Ω. For comparison, they are given in Table 2.3 for both helicity and transversity basis. The time-dependent functions $h_k(t)$ depend on the polarisation amplitudes and are defined as

$$h_k(t) = A_k e^{-\Gamma_s t} \frac{1}{1+C} \Big[a_k \cosh\left(\tfrac{1}{2}\Delta\Gamma_s t\right) + b_k \sinh\left(\tfrac{1}{2}\Delta\Gamma_s t\right) + c_k \cos(\Delta m_s t) + d_k \sin(\Delta m_s t) \Big], \tag{2.49}$$

where the coefficients A_k, a_k, b_k, c_k and d_k are given in Table 2.4. C, D and S are defined in Equation 2.46. The differential decay rate for a produced $\overline{B}_s^0$ decaying to a $J/\psi\phi$ final state is given by

$$\frac{\mathrm{d}\Gamma(\overline{B}_s^0 \to J/\psi\phi)}{\mathrm{d}t\mathrm{d}\Omega} \propto \sum_{k=1}^{6} \bar{h}_k(t) \cdot f_k(\Omega), \tag{2.50}$$

where $\bar{h}_k(t)$ can be derived from $h_k(t)$ by replacing $c_k \to -c_k$ and $d_k \to -d_k$.

2.4.1 Contribution of the $J/\psi K^+K^-$ S-wave

The decay $B_s^0 \to J/\psi\phi$ with $\phi \to K^+K^-$ can interfere with $J/\psi K^+K^-$ S-wave amplitudes, either due to non-resonant K^+K^- or an intermediate $f_0(980)$ resonance. As the K^+K^- system is spin-0 in both configurations, the S-wave amplitude is CP-odd. It can be described by the amplitude $A_s(t)$ with $A_s = A_s(t=0)$ and strong phase $\delta_s = \arg(A_s)$.

k	$f_k(\theta_\mu, \theta_K, \varphi_h)$	$f_k(\theta, \psi, \varphi)$
1	$2\cos^2\theta_K \sin^2\theta_\mu$	$2\cos^2\psi(1-\sin^2\theta\cos^2\varphi)$
2	$\sin^2\theta_K\left(1-\sin^2\theta_\mu\cos^2\varphi_h\right)$	$\sin^2\psi(1-\sin^2\theta\sin^2\varphi)$
3	$\sin^2\theta_K\left(1-\sin^2\theta_\mu\sin^2\varphi_h\right)$	$\sin^2\psi\sin^2\theta$
4	$\sin^2\theta_K\sin^2\theta_\mu\sin 2\varphi_h$	$-\sin^2\psi\sin 2\theta\sin\varphi$
5	$\frac{1}{2}\sqrt{2}\sin 2\theta_K\sin 2\theta_\mu\cos\varphi_h$	$\frac{1}{\sqrt{2}}\sin 2\psi\sin^2\theta\sin 2\varphi$
6	$-\frac{1}{2}\sqrt{2}\sin 2\theta_K\sin 2\theta_\mu\sin\varphi_h$	$\frac{1}{\sqrt{2}}\sin 2\psi\sin 2\theta\cos\varphi$

Table 2.3: Definition of angular-dependent functions f_k in the differential $B_s^0 \to J/\psi\phi$ decay rate, Equation 2.48, for helicity angles ($f_k(\theta_\mu, \theta_K, \varphi_h)$) and for transversity angles ($f_k(\theta, \psi, \varphi)$) [21], [30].

k	A_k	a_k	b_k	c_k	d_k
1	$\lvert A_0\rvert^2$	1	D	C	$-S$
2	$\lvert A_\parallel\rvert^2$	1	D	C	$-S$
3	$\lvert A_\perp\rvert^2$	1	$-D$	C	S
4	$\lvert A_\parallel A_\perp\rvert$	$C\sin(\delta_\perp-\delta_\parallel)$	$S\cos(\delta_\perp-\delta_\parallel)$	$\sin(\delta_\perp-\delta_\parallel)$	$D\cos(\delta_\perp-\delta_\parallel)$
5	$\lvert A_0 A_\parallel\rvert$	$\cos(\delta_\parallel-\delta_0)$	$D\cos(\delta_\parallel-\delta_0)$	$C\cos(\delta_\parallel-\delta_0)$	$-S\cos(\delta_\parallel-\delta_0)$
6	$\lvert A_0 A_\perp\rvert$	$C\sin(\delta_\perp-\delta_0)$	$S\cos(\delta_\perp-\delta_0)$	$\sin(\delta_\perp-\delta_0)$	$D\cos(\delta_\perp-\delta_0)$

Table 2.4: Definition of the time-dependent functions $h_k(t)$ in the differential $B_s^0 \to J/\psi\phi$ decay rate, Equation 2.48.

The differential decay rates for $B_s^0 \to J/\psi\phi$ decays in 2.48 and 2.50 need to be modified:

$$\frac{d\Gamma(B_s^0 \to J/\psi\phi)}{dt\,d\Omega} \propto \sum_{k=1}^{10} h_k(t)\cdot f_k(\Omega)\,, \tag{2.51}$$

$$\frac{d\Gamma(\overline{B}_s^0 \to J/\psi\phi)}{dt\,d\Omega} \propto \sum_{k=1}^{10} \bar{h}_k(t)\cdot f_k(\Omega)\,, \tag{2.52}$$

where the coefficients appearing in h_k (Equation 2.49) and the terms f_k with $k = 1-6$ are identical as before and given in Tables 2.4 and 2.3. The additional terms with $k = 7-10$ account for the S-wave amplitude and the interference of S-wave and P-wave amplitudes. They are introduced in Tables 2.6 and 2.5. Again, $\bar{h}_k(t)$ can be derived from $h_k(t)$ by replacing $c_k \to -c_k$ and $d_k \to -d_k$.
The differential decay rate as written in Equation 2.51-2.52 is invariant under the transformation

$$(\phi_s, \Delta\Gamma_s, \delta_\parallel, \delta_\perp, \delta_s, \delta_0) \to (\pi-\phi_s, -\Delta\Gamma_s, -\delta_\parallel, \pi-\delta_\perp, -\delta_s, -\delta_0) \tag{2.53}$$

and thus gives rise to a twofold ambiguity in the measured results.

k	$f_k(\theta_\mu, \theta_K, \varphi_h)$	$f_k(\theta, \psi, \varphi)$
7	$\frac{2}{3}\sin^2\theta_\mu$	$2(1-\sin^2\theta\cos^2\varphi)$
8	$\frac{1}{3}\sqrt{6}\sin\theta_K\sin 2\theta_\mu\cos\varphi_h$	$\sqrt{6}\sin^2\theta\sin\psi\sin 2\varphi$
9	$-\frac{1}{3}\sqrt{6}\sin\theta_K\sin 2\theta_\mu\sin\varphi_h$	$\sqrt{6}\sin 2\theta\sin\psi\cos\varphi$
10	$\frac{4}{3}\sqrt{3}\cos\theta_K\sin^2\theta_\mu$	$4\sqrt{3}\cos\psi(1-\sin^2\theta\cos^2\varphi)$

Table 2.5: Definition of angular-dependent functions f_k, that are related to the S-wave amplitudes in the differential $B_s^0 \to J/\psi\phi$ decay rate, Equation 2.51. They are given for helicity angles ($f_k(\theta_\mu, \theta_K, \varphi_h)$) and for transversity angles ($f_k(\theta, \psi, \varphi)$), [30], [31].

k	A_k	a_k	b_k	c_k	d_k
7	$\lvert A_s\rvert^2$	1	$-D$	C	S
8	$\lvert A_s A_\parallel\rvert$	$C\cos(\delta_\parallel-\delta_s)$	$S\sin(\delta_\parallel-\delta_s)$	$\cos(\delta_\parallel-\delta_s)$	$D\sin(\delta_\parallel-\delta_s)$
9	$\lvert A_s A_\perp\rvert$	$\sin(\delta_\perp-\delta_s)$	$-D\sin(\delta_\perp-\delta_s)$	$C\sin(\delta_\perp-\delta_s)$	$S\sin(\delta_\perp-\delta_s)$
10	$\lvert A_s A_0\rvert$	$C\cos(\delta_0-\delta_s)$	$S\sin(\delta_0-\delta_s)$	$\cos(\delta_0-\delta_s)$	$D\sin(\delta_0-\delta_s)$

Table 2.6: Definition of the time-dependent functions $h_k(t)$ that are related to the S-wave amplitudes in the differential $B_s^0 \to J/\psi\phi$ decay rate, Equation 2.51.

For simplicity in the rest of this thesis, the expression $B_s^0 \to J/\psi\phi$ will be used, including both the P-wave as well as the interfering $J/\psi K^+K^-$ S-wave contribution. An explicit distinction between both components will be done in case it is required.

Mass dependence of polarisation amplitudes

In general the decay amplitudes depend on the mass $m_{K^+K^-}$ of the K^+K^- final state [31]. Thus the theoretical decay rate for $B_s^0 \to J/\psi\phi$ should be a function of $m_{K^+K^-}$. The $m_{K^+K^-}$ dependence of the decay amplitudes can be expressed as

$$\begin{aligned} A_0(m_{K^+K^-}) &= A_0 g(m_{K^+K^-}), & A_\perp(m_{K^+K^-}) &= A_\perp g(m_{K^+K^-}), \\ A_\parallel(m_{K^+K^-}) &= A_\parallel g(m_{K^+K^-}), & A_s(m_{K^+K^-}) &= A_s v(m_{K^+K^-}). \end{aligned} \tag{2.54}$$

As the three P-wave amplitudes describe the $B_s^0 \to J/\psi\phi$ decay, their $m_{K^+K^-}$ dependence is defined by the ϕ meson which has a resonant structure in $m_{K^+K^-}$. Their $m_{K^+K^-}$ dependence can therefore be described by the same function $g(m_{K^+K^-})$ [31], which is usually a Breit-Wigner function. $v(m_{K^+K^-})$ describes the $m_{K^+K^-}$ dependence of the s-wave amplitude which can either be a linear function for the non-resonant $J/\psi K^+K^-$ final state or a resonant function for the case of an intermediate $f_0(980)$ resonance.
The $m_{K^+K^-}$ dependence of the decay amplitudes can be incorporated in the differential $B_s^0 \to J/\psi\phi$ decay rate. The different $m_{K^+K^-}$ dependence of P- and S-wave amplitudes

would single out one physically correct solution of Equation 2.53 and thus resolves automatically the twofold ambiguity in the differential decay rate [31].

In this measurement however a simpler strategy is used and the mass dependence of the decay amplitudes is not explicitly modeled. As a consequence additional correction factors for the amplitudes need to be introduced in the differential decay rate. The size of the correction depends on the considered $m_{K^+K^-}$ mass range $[m^1_{K^+K^-}, m^2_{K^+K^-}]$.
The decay amplitudes appear in the differential decay rate as terms $A_iA_j^*$, $A_iA_s^*$ and $A_sA_s^*$ with $i = \|, \perp, 0$. To determine the correction factors these terms are integrated over $m_{K^+K^-}$ choosing $g(m_{K^+K^-})$ and $v(m_{K^+K^-})$ to be normalised in the considered mass range [32]:

$$\begin{aligned} \int_{m^1_{K^+K^-}}^{m^2_{K^+K^-}} A_iA_j^*|g(m_{K^+K^-})|^2 = |A_i||A_j|\,, \quad \int_{m^1_{K^+K^-}}^{m^2_{K^+K^-}} A_sA_s^*|v(m_{K^+K^-})|^2 = |A_s|^2\,, \\ \int_{m^1_{K^+K^-}}^{m^2_{K^+K^-}} A_iA_s^* g(m_{K^+K^-})v^*(m_{K^+K^-}) = A_iA_s^* \cdot C_{\rm sp}e^{-i\delta_{sp}}\,, \end{aligned} \tag{2.55}$$

The terms in the differential decay rate that are proportional to $A_iA_j^*$ and A_sA_s ($k = 1-7$ in Equation 2.51-2.52) stay unchanged when integrating over $m_{K^+K^-}$. The terms describing the interference of P-wave and S-wave on the other hand ($k = 8-10$ in Equation 2.51-2.52) have to be multiplied by a correction factor $C_{\rm sp}e^{-i\delta_{sp}}$ with absolute value $C_{\rm sp}$ and phase δ_{sp}. It is given by

$$\int_{m^1_{K^+K^-}}^{m^2_{K^+K^-}} g(m_{K^+K^-})v^*(m_{K^+K^-}) = C_{\rm sp}e^{-i\delta_{sp}}\,. \tag{2.56}$$

2.5 New Physics contributions to $\phi_{\rm s}$

Physic effects beyond the Standard Model description (New Physics) can affect the B_s^0-$\overline{B}_s^0$ mixing, for example through heavy virtual particles contributing to the mixing diagram. The effect on M_{12} can be parameterised in a model-independent way by introducing a complex parameter $\Delta_{\rm s}$ [33], [34]

$$M_{12} \to M_{12}^{\rm SM}\Delta_{\rm s} = M_{12}^{\rm SM}|\Delta_{\rm s}|e^{i\phi_{\Delta_{\rm s}}}\,, \tag{2.57}$$

where $M_{12}^{\rm SM}$ corresponds to M_{12} in the Standard Model. With $\phi_{\rm M} = \arg(M_{12})$ this gives for the CP-violating phase $\phi_{\rm s}$:

$$\phi_{\rm s} = \phi_{\rm M} - 2\phi_{\rm D} \to \phi_{\rm s}^{\rm SM} + \phi_{\Delta_{\rm s}}\,. \tag{2.58}$$

$\phi_{\rm s}^{\rm SM}$ corresponds now to the Standard Model phase defined in Equation 2.38. This means that additional contributions from New Physics in M_{12} result in a change of

the mixing phase ϕ_M and thus change also the measurable phase ϕ_s. As the Standard Model prediction of ϕ_s is small and precise, already small New Physics effects can be observed in the measurement of ϕ_s in $B_s^0 \to J/\psi\phi$ decays.
Figure 2.9 shows the experimental constraints on the New Physics parameter Δ_s in summer 2011 from measurements of ϕ_s, the B_d^0 and B_s^0 mixing frequencies Δm_d and Δm_s, the decay width difference $\Delta\Gamma_s$ and the CP asymmetry in semileptonic B-decays. Δ_s is constrained to two areas in the complex plane, one of them compatible with the Standard Model prediction. Given the constraints from Δm_d and Δm_s, a precise measurement of ϕ_s will provide excellent new constraints on Δ_s.

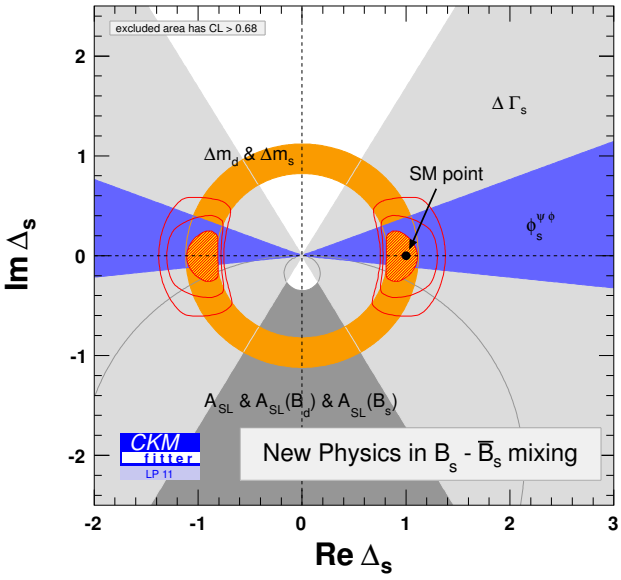

Figure 2.9: Constraints on New Physics in B_s^0-$\overline{B}_s^0$ mixing. The blue areas are constraints from measurements of ϕ_s with $B_s^0 \to J/\psi\phi$ decays. The red areas show the 68% confidence level region of Δ_s. The figure is taken from [18].

2.6 Experimental status of ϕ_s

Figure 2.10 shows the experimental status of ϕ_s and the decay width difference in the B_s^0 system, $\Delta\Gamma_s$, in spring 2012. Results from the CDF [35] and D0 [36] collaborations, as well as a previous result from the LHCb collaboration [37], are included. The figure shows the two-dimensional 68% confidence contours of the individual measurements as well as the combination of them. The uncertainties of the single measurements are still large, allowing for possible contributions of New Physics to the phase ϕ_s.

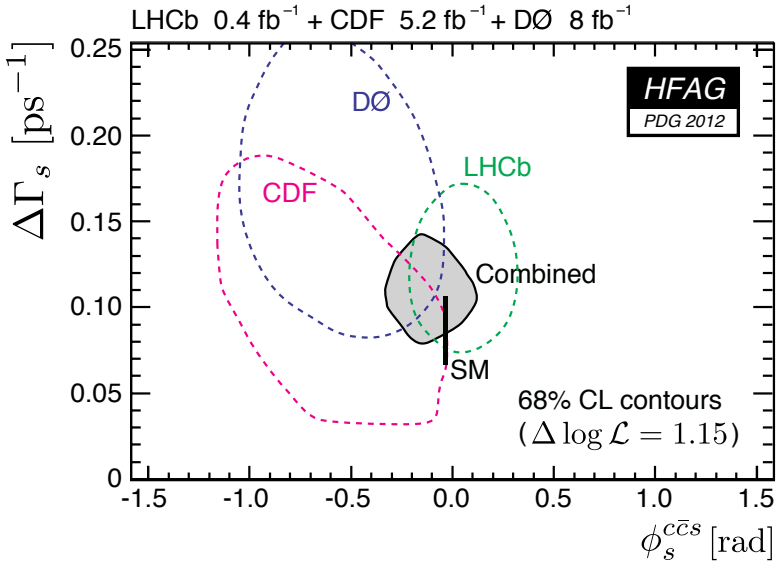

Figure 2.10: Experimental status of ϕ_s and the decay width difference in the B_s^0 system, $\Delta\Gamma_s$, in spring 2012. Shown are results from CDF [35], D0 [36] and LHCb [37]. The shaded region is the combined 68% confidence level contour. The figure is taken from [38].

CHAPTER 3

The LHCb experiment

The LHCb (Large Hadron Collider beauty) detector is one of the four large particle physics experiments at the Large Hadron Collider. It is especially designed to measure decays of b- and c-hadrons and search for CP violation and rare B meson decays. The following chapter will briefly discuss the running conditions of the Large Hadron Collider and the production mechanism of b-quarks in proton-proton collisions. The working principles and technical details of the various LHCb detector components will be summarised. At the end the measured, and simulated event samples used in this thesis are introduced.

3.1 The Large Hadron Collider

The Large Hadron Collider (LHC) [39] is a proton-proton (pp) collider located at CERN in Geneva. In a 27km long underground tunnel, two proton beams are accelerated and brought to collision at four interaction points which house the four major LHC experiments: ATLAS, CMS, ALICE and LHCb. Figure 3.1 shows the main accelerator ring with the four experiments. ATLAS and CMS are general purpose detectors, whereas ALICE is specialised for heavy ion collisions and LHCb is a experiment dedicated to measure b- and c-hadron decays.
The design energy of the LHC is $\sqrt{s} = 14\,\text{TeV}$. At a design luminosity of $\mathcal{L} = 10^{34}\,\text{cm}^{-2}\,\text{s}^{-1}$, the proton beams are separated into 2808 bunches, each containing $\sim 10^{11}$ protons. With a bunch spacing of 25 ns, this gives an interaction rate of 40 MHz.

For the LHCb experiment the design luminosity is $\mathcal{L} = 2 - 5 \cdot 10^{32}\,\mathrm{cm}^{-2}\,\mathrm{s}^{-1}$ in order to limit the number of interactions per bunch-crossing.
In the 2010 and 2011 runs of the LHC, the protons were collided with an energy of $\sqrt{s} = 7\,\mathrm{TeV}$. The instantaneous luminosity delivered to LHCb increased from $\mathcal{L} = 2 \cdot 10^{32}\,\mathrm{cm}^{-2}\,\mathrm{s}^{-1}$ in 2010 to $\mathcal{L} = 4 \cdot 10^{32}\,\mathrm{cm}^{-2}\,\mathrm{s}^{-1}$ in 2011. The collision energy was increased to $\sqrt{s} = 8\,\mathrm{TeV}$ in 2012.
The total integrated luminosity recorded by the LHCb experiment was $\mathcal{L}_{\mathrm{int}} = 0.04\,\mathrm{fb}^{-1}$ in 2010, $\mathcal{L}_{\mathrm{int}} = 1.0\,\mathrm{fb}^{-1}$ in 2011 and $\mathcal{L}_{\mathrm{int}} = 2.2\,\mathrm{fb}^{-1}$ with the higher energy in 2012. This presented analysis will focus on the data collected during the 2011 run.

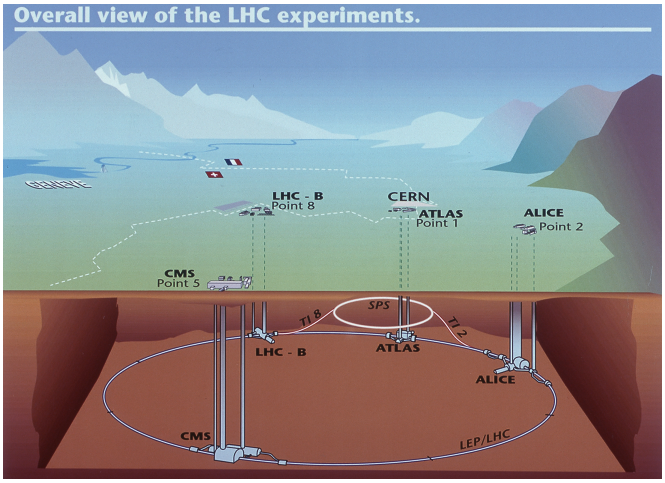

Figure 3.1: Schematic overview of the LHC accelerator ring and the location of the four particle detectors ATLAS, CMS, ALICE and LHCb. The figure is from [40].

3.2 b-hadron production at the LHC

At the LHC, b-quarks are predominantly produced in inelastic pp collisions in pairs of quark and anti-quark ($b\bar{b}$). The dominant process is the fusion of two gluons (gg) or two quarks ($q\bar{q}$). Figure 3.2 shows the leading-order Feynman diagrams of the production processes.
The cross section of producing $b\bar{b}$ pairs depends on the production angle. The momentum fraction carried by the partons of the colliding protons is defined by the parton density functions. The energy threshold to produce the $b\bar{b}$ pairs is small enough that they can also be produced by partons with very different momentum fractions. Thus it is likely that the $b\bar{b}$ system is boosted in forward or in backward direction relative to the beam line. Figure 3.3 shows the polar angle distribution of produced $b\bar{b}$ pairs, which clearly peaks at small and high polar angles. To maximise the $b\bar{b}$ production in

the detector acceptance, the LHCb detector is built as a single-arm forward spectrometer. The details of the detector will be discussed in the next section.
The total $b\bar{b}$ cross section in inelastic pp collisions at a center-of-mass energy of $\sqrt{s} = 7\,\text{TeV}$ was measured at LHCb using J/ψ from B hadron decays to be $\sigma(pp \to b\bar{b}X) = 288 \pm 4 \pm 48\,\mu\text{b}$ [41]. With a recorded integrated luminosity $\mathcal{L}_{\text{int}} = 1.1\,\text{fb}^{-1}$ in the 2011 run of the LHC, the number of produced $b\bar{b}$-pairs can be calculated to $N_{b\bar{b}} = \sigma(pp \to b\bar{b}X) \cdot \mathcal{L}_{\text{int}} \approx 3 \cdot 10^{11}$. Approximately 25% of them are produced within the LHCb detector acceptance.

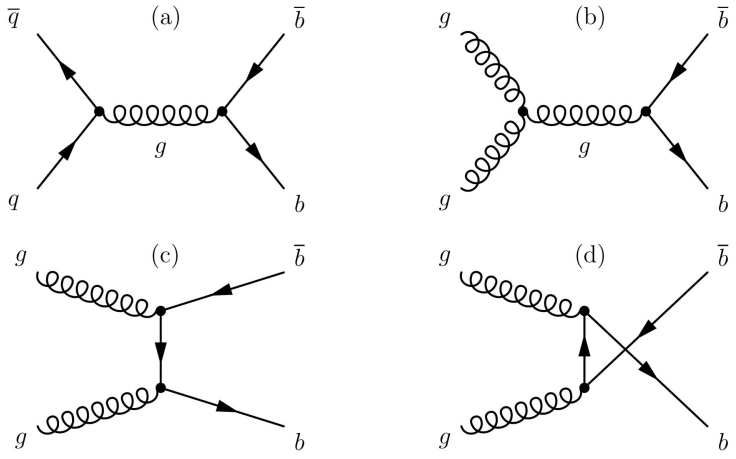

Figure 3.2: Feynman diagrams of the dominant $b\bar{b}$ production processes in pp interactions at the LHC. The figure is from [42].

3.3 The LHCb detector

The LHCb detector [43] is designed as single-arm forward spectrometer to cover the optimal acceptance for b-hadron decays. The layout of the detector is shown in figure 3.4. The coordinate system is defined by the z-axis along the beam line and the y-axis in the vertical direction. The acceptance coverage is $10-300\,\text{mrad}$ in the bending plane (x-direction) and $10-250\,\text{mrad}$ in the non-bending plane (y-direction) of the dipole magnet. It consists of several subdetectors that can be summarised in two categories:

- **Tracking detectors:** the Vertex Locator (VeLo) surrounding the pp interaction point; the Tracker Turicensis (TT) as first tracking station directly before the main dipole magnet; and three tracking stations (T1-T3) after the dipole magnet consisting of an Inner Tracker close to the beam line and an Outer Tracker covering the outside acceptance.

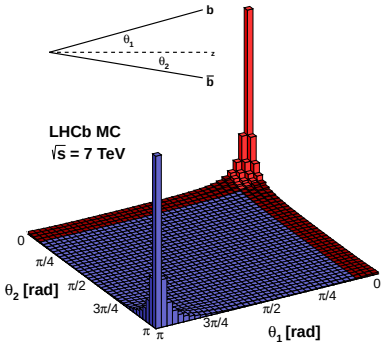

Figure 3.3: Simulated two-dimensional polar angle distribution of produced $b\bar{b}$ pairs. Both b and $\bar{b}$ quark are either produced in forward or in backward direction. The red region marks the LHCb acceptance. The figure is taken from [44].

- **Particle identification detectors:** two Cherenkov detectors (RICH1 and RICH2), one located directly after the VeLo and one located after the three tracking stations; the calorimeter system consisting of the Scintillating Pad Detector (SPD), Pre-shower Detector (PS), an electromagnetic (ECAL) and hadronic (HCAL) calorimeter, and the muon system made of 5 stations (M1-M5).

The single detector components are discussed in detail in Reference [45] and will be shortly summarised in the following sections:

3.3.1 Tracking detectors

The main purpose of the tracking system is the momentum measurement of charged particles. They are bent in the magnetic field of the dipole magnet. Their trajectories are measured before the magnet with the vertex detector and the TT and after the magnet with the three main tracking stations. The momentum can be determined from the deflection of the particle trajectory. The magnetic field is designed to be almost homogeneous, with a large component in y-direction and only small components in x- and z-direction. Particles moving in z-direction are therefore bent mainly in the (x-z) plane. Figure 3.5 shows the field strength as a function of the z-coordinate. Integrated over a length of $l = 10$ m the field strength is

$$\int B\mathrm{d}l = 4 \text{ Tm}\,. \tag{3.1}$$

As indicated in Figure 3.5, the orientation of the magnetic field can be switched, giving a powerful tool to measure charge dependent detector asymmetries.

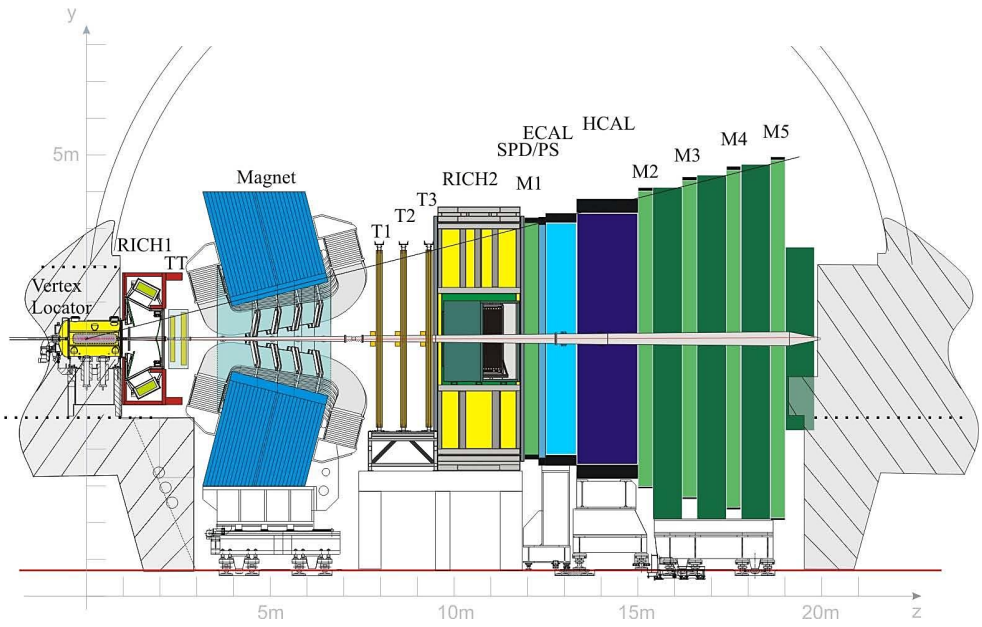

Figure 3.4: Layout of the LHCb detector showing the Vertex Locator, the two Cherenkov detectors (RICH1, RICH2), the Tracker Turicensis (TT), the tracking stations (T1-T3), the scintillating pad detector (SPD) and preshower detector (PS), the electromagnetic (ECAL) and hadronic (HCAL) calorimeters and the five muon stations (M1-M5). The figure is from [45].

Vertex detector

The Vertex Locator (VeLo) is a silicon strip detector positioned closely around the pp interaction point to measure precisely the positions of the primary interaction and secondary displaced vertices. It is built of 21 stations, as shown in Figure 3.6, with each containing a pair of silicon modules with half disk shape. The modules have an overlap in the x-direction and are mounted in 2 mm intervals in the z-direction. They consist of two different types of 300 μm thick sensors, mounted back to back. The r-sensors measure the radial distance of a particle track to the beam axis and are made of circular strips around the beam. The ϕ-sensors are made of straight radial strips and measure the polar angle of the tracks. Figure 3.7 illustrates the $r-\phi$ geometry of the sensors. To ensure a homogeneous occupancy the pitches between the strips increase with larger distance to the beam, from 38 μm to 97 μm for the ϕ-sensors and to 102 μm for the r-sensors. Additional two pile-up stations are located upstream of the VeLo consisting of two r-sensor modules. They are used in the hardware trigger to detect beam-gas interactions.
The precision of the reconstructed vertices depends on the extrapolation of the measured track positions. Therefore the VeLo modules are placed close to the interaction

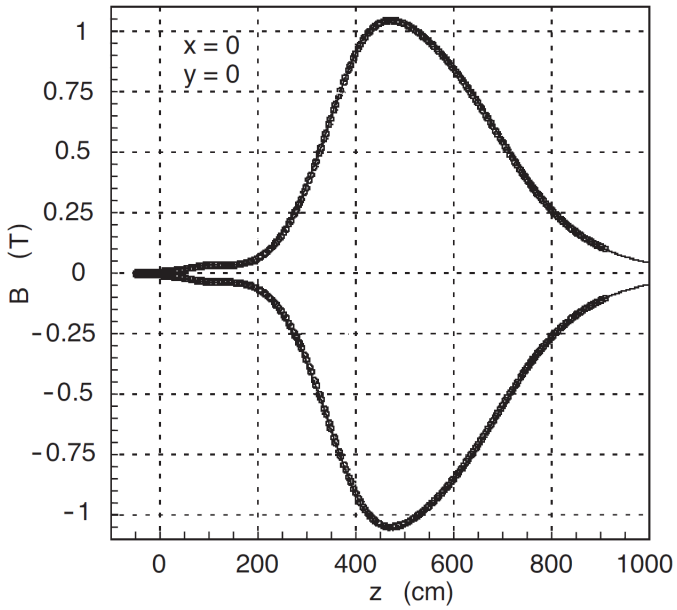

Figure 3.5: Field map of the LHCb dipole magnet. The polarity of the magnetic field can be switched from positive to negative. The figure is taken from [45].

point. The sensitive regions of the modules starts in 8 mm distance from the beam line. The sensors are separated from the beam vacuum by a thin aluminium foil at 5 mm distance to the beam. To protect the sensors during unstable beam conditions, the half modules can be moved away from the beam line.

Tracker Turicensis

The Tracker Turicensis (TT) is a silicon strip detector located upstream of the dipole magnet. It consists of two 150 cm wide and 130 cm high stations with a detection area of about 8.4m^2. The distance between the stations is 27 cm. Each station has two detection layers, where the strips are arranged in (x, u) layers for the first station, and in (v,x) layers for the second station. The x-layers have vertical strips, while they are rotated in the u- and v-layers by a stereo angle of ±5°. This allows for a three dimensional track reconstruction with the best precision in the horizontal bending-plane of the magnet. The strips are 500 μm thick with a pitch of 183 μm. Figure 3.8 shows the layout of a x- and u-layer of the TT. Depending on their distance to the beam line, a different amount of strips are connected to a single readout. The readout electronics is located at the top and the bottom of the detector. The single hit resolution of the TT is about 50 μm.

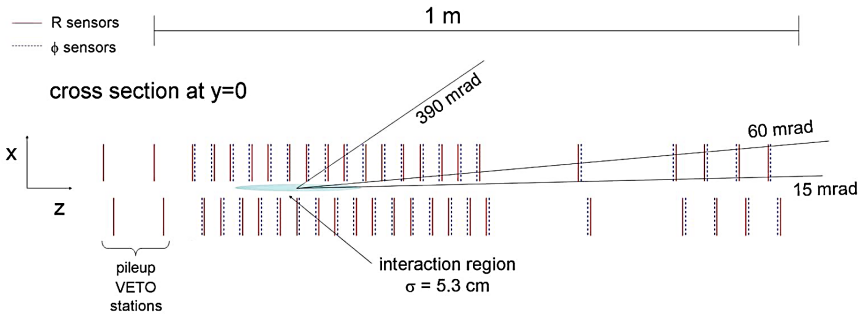

Figure 3.6: Cross section of the Vertex Locator (VeLo) in (x-z) plane showing the 21 stations with r- and ϕ-sensors. The pileup stations are only used in the trigger. The figure is from [45].

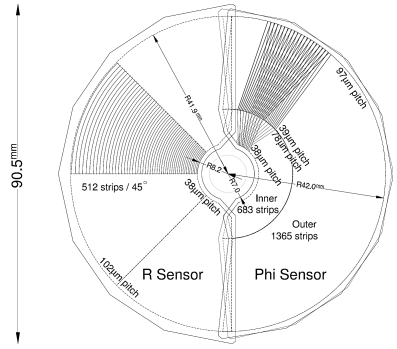

Figure 3.7: Illustration of the r- and ϕ-sensors of the VeLo modules. The figure is from [45].

Inner Tracker

The Inner Tracker (IT) is a silicon strip detector located in the center of the three tracking stations after the dipole magnet. It covers a 120 cm wide and 40 cm high cross shaped region around the beam line with an active area of about 4m^2. Each station is built of four layers where the strips are arranged in a (x, u, v, x) geometry. Similar to the TT the strips in the x-layers are vertical but rotated by $\pm 5^\circ$ in the u- and v-layers. Figure 3.9 illustrates the layout of an IT x-layer. The strip sensors are arranged in four detector boxes. They are 320 μm thick for the boxes above and below the beam line and 410 μm thick for the boxes that are placed at the sides of the beam pipe. The strip geometry was chosen to limit the maximum hit occupancy per sensor to a few percent. The pitch between the sensors is about 200 μm leading to a single hit resolution of 50 μm, similar to the TT.

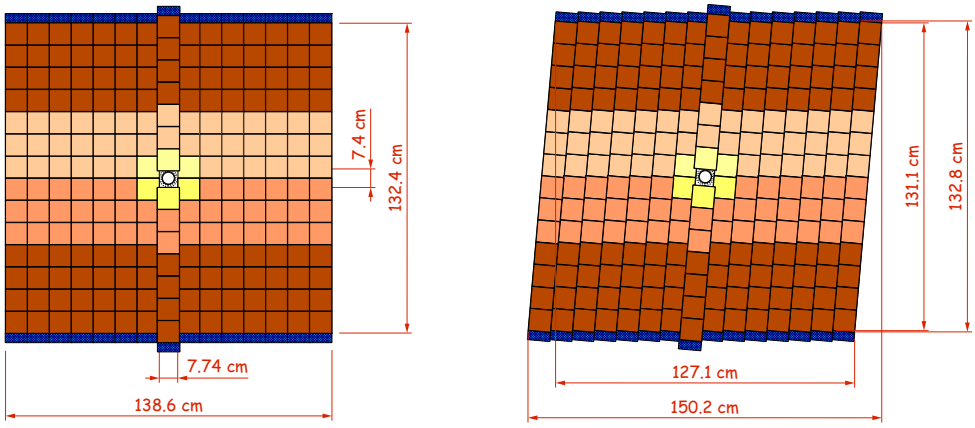

(a) x-layer of TT (b) u-layer of TT

Figure 3.8: Layout of different TT detection layers. The different colors corresponds to different readout sectors. The readout electronics is mounted at the ends of the layer. The figures are taken from [46].

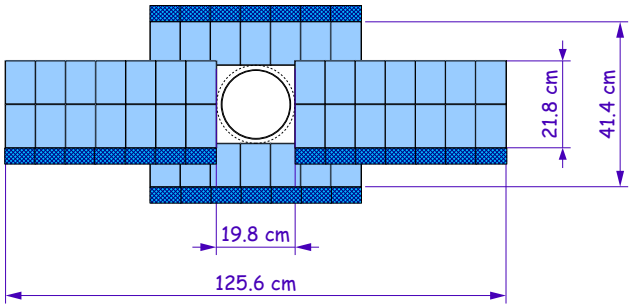

Figure 3.9: Front view of an Inner Tracker x-layer (station 2) indicating four different detector boxes. The dark blue regions mark the readout electronics. The figure is from [46].

Outer Tracker

The Outer Tracker is a straw tube drift-time detector consisting of three stations after the dipole magnet. It is located in the three tracking stations covering the large area outside the IT acceptance, as shown in figure 3.10(a). The three stations are of equal size with the outer boundary corresponding to an acceptance of 300 mrad in the horizontal and 250 mrad in the vertical plane. The stations consist of four layers in the same (x, u, v, x) layout as the Inner Tracker. The layers are built as arrays of modules, each module containing a double layer of straw tubes. The straws are filled with a mixture of Argon (70%), CO_2(28.5%) and O_2 (1.5%) as counting gas, guaranteeing a drift-time below the time of three bunch-crossings. In the center of the straws is a

24 μm thick gold coated thungsten wire, operating as anode.The inner diameter of the straws is 4.9 mm, the pitch between them is 5.25 mm. Figure 3.10(b) shows the layout of the straw tubes in a module. The spatial resolution of single straws is 200 μm. The light materials in the OT result in a radiation length below 10%.

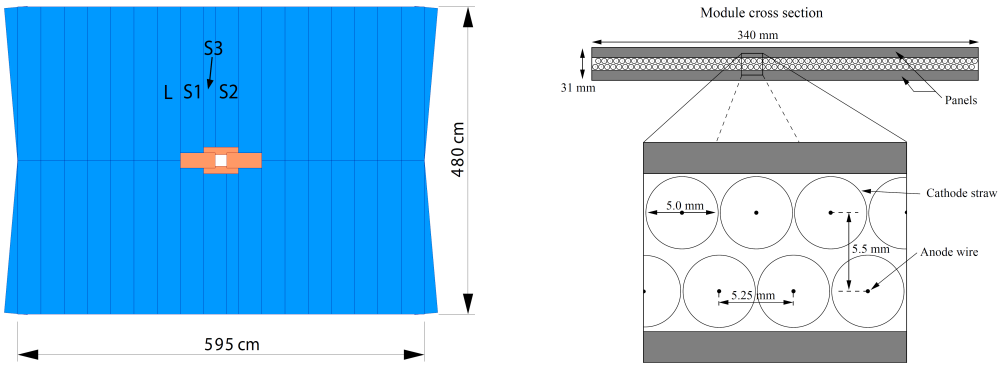

(a) Front view of OT station.

(b) Cross section of straw tube module

Figure 3.10: Outer Tracker layout: (a) front-view of an OT station, the inner (orange) part is the IT. (b) Cross section of an OT module and straw tubes. Figures are from [45].

Track reconstruction

In the track reconstruction, the hits in the tracking detectors are combined to form particle trajectories (tracks) and determine the particle momenta. Depending on the subdetectors used for this, different track types can be distinguished [45]:

- **VeLo tracks** contain only hits from the vertex detector. They are useful for the primary vertex reconstruction as they have typically a large polar angle.
- **Upstream tracks** are tracks in the Velo and TT. These are in general low momentum tracks that are bent out of the detector acceptance by the magnetic field.
- **Downstream tracks** are tracks that are only reconstructed in the TT and the tracking stations (T1-T3). They are mostly relevant for the reconstruction of long-living particles like K^0_S, that decay outside the VeLo acceptance.
- **Long tracks** traverse all tracking detectors from Velo to the tracking stations (Velo, TT, T1-T3). They have the most precise momentum resolution and are therefore the most important tracks for b-hadron reconstruction.

The first step of the track reconstruction is the pattern recognition, where the correct hits belonging to a track are searched for. The pattern recognition algorithm reconstructs track segments in the Velo and the tracking station which are used to build longtracks. Two different algorithms are applied:

- The **forward tracking** algorithm builds a track candidate from a Velo track segment and one hit in the tracking stations. Additional hits in the tracking station are assigned to the track when they are within a certain search window around the track candidate. After applying some quality criteria, the track candidate is chosen as long track and hits in the TT are added when they are close enough to the track.

- The **track matching** algorithm builds long tracks by matching track segments in the Velo and the tracking station and extrapolating them to the bending plane of the magnet. In case certain quality criteria are fulfilled, TT hits that are close to the track are added.

After remove duplicate tracks (*clone killing*), the remaining tracks are refitted using a Kalman Filter based track fit ([47]) to account for multiple scattering and energy loss. The quality of the tracks is described by the χ^2 of the track fit, divided by its degrees of freedom, $\chi^2_{\text{track}}/\text{ndf}$. The relative momentum resolution of the reconstructed longtracks depends on the track momentum and increases from $\delta p/p = 0.35\%$ for low momentum tracks ($\sim 10\,\text{GeV}$) to $\delta p/p = 0.55\%$ for high momentum tracks ($\sim 140\,\text{GeV}$).

3.3.2 Particle Identification detectors

A good particle identification is a necessary requirement to reconstruct B meson decays at the LHC. Especially in decays with hadronic final state it is important to distinguish the particle types. Several LHCb subdetectors provide information about the reconstructed particles that can be combined to a common particle hypothesis.

RICH detectors

The Ring Imaging Cherenkov (RICH) detectors are used to distinguish between different particles, especially to separate $\pi^\pm$ and $K^\pm$ over a wide momentum range. Charged particles emit photons when passing a medium with refraction index n if their velocity v is faster than the velocity of light $c\prime = \frac{c}{n}$ in this medium. The photons are emitted in a cone with opening angle θ_C given by

$$\cos\theta_\text{C} = \frac{1}{\beta n}\,, \tag{3.2}$$

where $\beta = v/c$. The RICH detectors measure the opening angles, which can be related to the mass of the traversing particle by using the momentum information of the tracking system. Two RICH detectors are installed at LHCb covering a different momentum spectrum. RICH1 identifies particles with low momenta from 1 to 60 GeV using aerogel and C_4F_{10} gas radiators. RICH2 covers the high momentum range from about 15 GeV up to 100 GeV and beyond using a CF_4 gas radiator. Figure 3.11 shows the schematic layout of the two Cherenkov detectors. RICH1 covers the full angular acceptance of the LHCb detector from 25 mrad to 300 mrad in horizontal and to 250 mrad

in vertical plane. RICH2 has a limited acceptance from ~ 15 mrad to 120 mrad in horizontal and 100 mrad in vertical plane. In both detectors, flat and spherical mirrors are used to focus and Hybrid Photo Detectors (HPDs) are used to detect the Cherenkov light. Averaged over a momentum range from 2 – 100 GeV, the kaon identification efficiency of the Cherenkov detectors is ~ 95% with a pion misidentification fraction of ~ 10% [48].

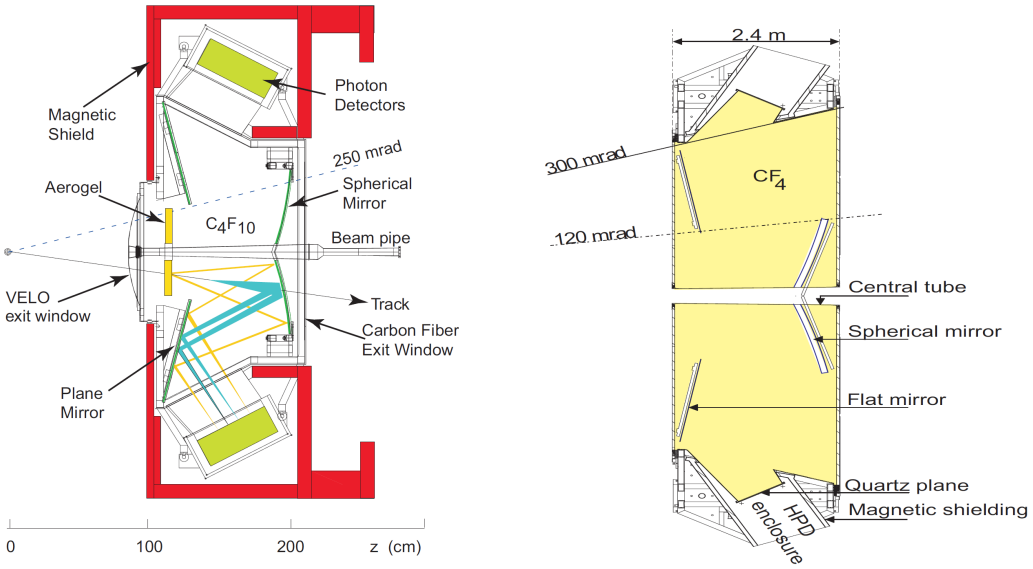

(a) Side view of RICH1 detector.

(b) Top view of RICH2 detector.

Figure 3.11: Schematic layout of the ring imaging Cherenkov detectors: (a) Side view of RICH1. (b) Top view of RICH2. The figures are from [45].

Calorimeter system

The main purpose of the calorimeter system is the identification of electrons, photons and hadrons and the measurement of their energies and positions. It also provides important input to the first trigger level. Particles interacting with the calorimeter material produce a cascade of secondary particles, called a shower. The working principle of the calorimeter system is to detect the scintillation light of the particle showers. The system is divided in several subdetectors:

- The scintillator pad detector (SPD) consists of 15 mm thick scintillating pads and is located right after the first muon station. As only charged particles are detected by the SPD, it is used to distinguish between electrons and photons.
- The preshower detector (PS) is located after the SPD and a 12 mm thick lead wall that initiates particle showers from photons or electrons. Similar to the SPD

they are detected by 15 mm thick scintillating pads. Hadronic particle showers start later and can be distinguished from electromagnetic showers.

- The electromagnetic calorimeter (ECAL) detects particle showers from electrons and photons. It is built as a sampling calorimeter with alternating layers of 2 mm thick lead plates and 4 mm thick scintillator plates for the shower detection. The energy resolution of the ECAL is given by

$$\frac{\sigma(E)}{E} = \frac{10\%}{\sqrt{E}} \oplus 1.5\% \tag{3.3}$$

  where the energy E is in GeV and $\oplus$ denotes addition in quadrature.

- The hadronic calorimeter is responsible for the detection of hadronic particle showers. It consists of alternating iron absorbers and scintillating tiles as active material. The scintillating tiles are oriented such that they run parallel to the beam axis. Figure 3.12 illustrates the structure of an HCAL module. In the longitudinal direction, the length of the iron and scintillator layers corresponds to the hadron interaction length in iron. In the transversal direction, the scintillators are intersected by 1 cm of iron. The scintillation light is collected by fibers and read out by photomultiplier tubes at the back of the HCAL. The energy resolution of the HCAL is given by

$$\frac{\sigma(E)}{E} = \frac{80\%}{\sqrt{E}} \oplus 10\% \tag{3.4}$$

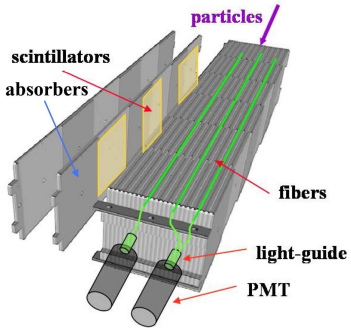

Figure 3.12: Schematic overview of the HCAL cell structure. The figure is from [45].

Muon system

The muon system consists of five stations M1-M5 and is used to reconstruct and identify muons and to provide important information to the trigger system. M2-M5 are

located at the end of the LHCb detector. They are interleaved with 80 cm thick iron layers to absorb hadronic particles. M1 is placed in front of the calorimeters to improve the momentum measurement in the trigger. The layout of the muon system is shown in figure 3.13(a). The muon system covers an angular acceptance of 20 mrad (16 mrad) to 306 mrad (258 mrad) in the bending (non-bending) plane of the dipole magnet. The thickness of the muon system corresponds to approximately 20 interaction lengths. Muons need therefore a minimum momentum of ~ 6 GeV to pass the five stations.
The muon stations consist of multiwire proportional chambers (MWPC) in the outer acceptance region and gas electron multiplier (GEM) detectors close to the beam line. Figure 3.13(b) shows the granularity of one muon station quadrant.

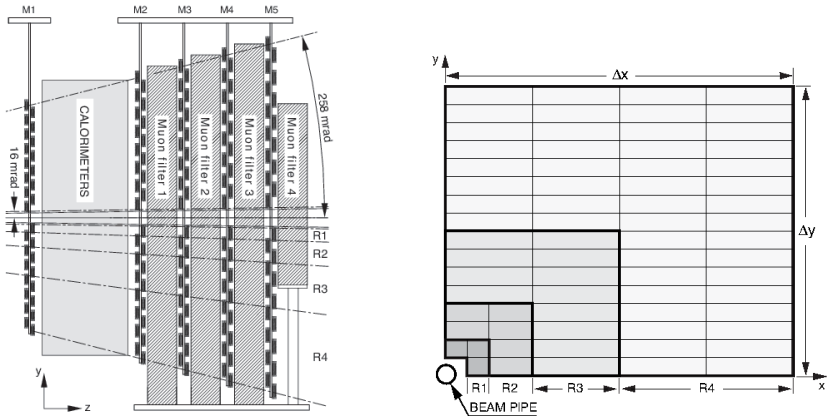

(a) Side view of the muon system

(b) Front view of a muon station.

Figure 3.13: Layout of the muon detectors: (a) side view of the five muon stations. (b) front view of a muon station with different granularity. The figures are from [45].

Relative particle hypothesis

Based on the information of the RICH detectors, the calorimeter and muon system, a likelihood value $\mathcal{L}_x$ can be created for a track, by calculating the probability of the particle hypothesis x. Usually the likelihood value is determined relative to the pion (π) hypothesis as these are the most abundant particles:

$$\Delta \ln \mathcal{L}_{x\pi} = \ln \mathcal{L}_x - \ln \mathcal{L}_\pi \,. \tag{3.5}$$

A value $\Delta \ln \mathcal{L}_{x\pi} > 0$ means that the track has a higher probability to originate from the particle x than from a pion. Especially for the identification of kaons, this variable ($\Delta \ln \mathcal{L}_{K\pi}$) is an important tool to suppress background from wrongly identified pions.

3.3.3 Trigger system

The purpose of the LHCb trigger system is to decrease the event rate of 40 MHz to approximately 3 kHz that can be written on storage for further analysis. Therefore it has to efficiently identify and select events that are interesting for the LHCb physics program. The trigger system consists of three subsequent stages: the Level-0 trigger (L0), the High Level Trigger 1 (HLT1) and the High Level Trigger 2 (HLT2). The flow diagram of the three stages is indicated in figure 3.14. The L0 trigger is a hardware trigger and reduces the event rate to < 1 MHz. HLT1 and HLT2 are software triggers running on a large computing cluster and reduce the event rate to 50 kHz and 3 kHz respectively.

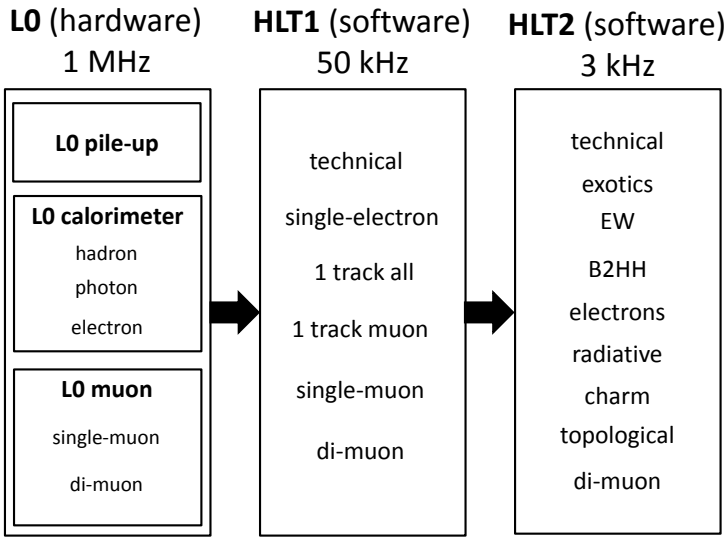

Figure 3.14: Flow diagram of the trigger steps at LHCb. The interaction rate of 40 MHz is reduced by the Level-0 (L0) and the two High Level Trigger (HLT1, HLT2) to 3 kHz event rate that is written on storage.

Level-0 trigger

The L0 trigger hardware trigger is divided in three parts: the L0 pile-up trigger, the L0 calorimeter trigger and the L0 muon trigger. Each of the parts uses informations from different detector components that are connected to a final L0 decision.
The **L0 pile-up** trigger uses the informations from the VeLo pile-up stations as shown in figure 3.6 to distinguish between events with single or multiple interactions per bunch crossing. It is not used for selecting flavour physics events.
The **L0 calorimeter** trigger forms calorimeter cluster by summing up transverse energy in 2×2 calorimeter cells. Depending on the informations of SPS, PS, ECAL

and HCAL a particle hypothesis (L0-Hadron, L0-Eectron, L0-Photon) is assigned to the clusters. An event is triggered when the transverse energy of one of the clusters is above a fixed threshold.
The **L0 muon** trigger identifies, in each quadrant of the muon stations, the two muon tracks with the highest transverse momentum by searching for straight tracks in the five muon stations pointing back to the interaction point. The event is accepted if either the largest transverse momentum of the tracks is above a fixed threshold (L0-Muon) or if the product of the two largest transverse momenta is above a threshold (L0-DiMuon).

High Level Trigger

The L0 accepted events are passed to the software based High Level Trigger. In order to cover the broad physics program, it consists of several trigger lines [49]. Each trigger line defines the executed algorithms, the basic reconstruction steps and the selection parameters that are necessary for the search for a specific event type. The trigger lines are operated independently on the L0 triggered events.
The **HLT1** lines try to confirm the L0 decision. A partial event reconstruction is done by performing fast track fits in the VeLo and tracking stations, corresponding to the L0 candidates.
In the **HLT2** a full event reconstruction is done which is as close as possible to the offline reconstruction. Several inclusive and exclusive selections are preformed reducing the event rate to the required 3 kHz.

3.4 Event samples

For this thesis, the data collected during the 2011 LHC run is used, corresponding to an integrated luminosity of $\mathcal{L} = 1.0\,\text{fb}^{-1}$ at a pp center-of-mass energy of $\sqrt{s} = 7\,\text{TeV}$ (see Section 3.1). The data taking and processing involved several steps: First, the level-0 hardware trigger and the HLT software trigger are applied to reduce the event rate. The accepted events are processed offline by the LHCb reconstruction software (*Brunel*) where pattern recognition and track fitting algorithms are executed. The LHCb Analysis software (*DaVinci*) is then used to preselect a set of $B_s^0 \to J/\psi\phi$ candidates (*stripping*). At the end a full event selection is made. The trigger and selection requirements will be discussed in the next chapter.

In addition, a sample of 10 million simulated $B_s^0 \to J/\psi\phi$ events was generated. The general purpose Monte Carlo event generator *Pythia 6* [50] was used to simulate the pp interaction together with the *EvtGen* library [51] to simulate the B-hadron decays. The sample was produced such that each event contains at least one $B_s^0 \to J/\psi\phi$ candidate. The physics parameters that were used in the simulation of the B decays are given in Table 3.1. To save CPU time, only events with $B_s^0 \to J/\psi\phi$ candidates in the region of 0 mrad − 400 mrad around the beam pipe are further processed. For these events the detector response was simulated with the *Geant4* package [52]. Based on

the simulated detector response, the trigger algorithm was applied as in data. It is especially important that all trigger and selection requirements are identical to data as the simulated sample is used to determine detector acceptance effects.

parameter	generated value
ϕ_s	-0.04 rad
$\Delta\Gamma_s$	0.06 ps^{-1}
Γ_s	0.679 ps
Δm_s	17.8 ps^{-1}
$\lvert A_\parallel \rvert^2$	0.24
$\lvert A_\perp \rvert^2$	0.16
$\lvert A_0 \rvert^2$	0.6
$\delta_\parallel$	2.5 rad
$\delta_\perp$	-0.17 rad
δ_0	0.0 rad

Table 3.1: Decay parameter values used in the generation of the simulated $B_s^0 \to J/\psi\phi$ event sample.

CHAPTER 4

Analysis Strategy

The measurement of the time-dependent CP asymmetry for the decay $B_s^0 \to J/\psi\phi$ allows for the determination of the CP-violating phase ϕ_s. This thesis presents a measurement of ϕ_s by fitting the theoretical $B_s^0 \to J/\psi\phi$ decay rates, introduced in Section 2.4, to the measured decay time and angular distributions of the reconstructed $B_s^0 \to J/\psi\phi$ decays. The fit relies on the *maximum likelihood method* that can be used to estimate parameters from a given datasample by maximising a likelihood function. The principle idea and implementation of the maximum likelihood fit will be discussed in Chapter 9. The fitting algorithm was developed in [53] and extended for the presented analysis.
Several topics have to be addressed before the CP-violating phase ϕ_s can be determined from the fit:

- The data sample of selected $B_s^0 \to J/\psi\phi$ candidates is polluted with physical and combinatorial background candidates with different decay time and angular distributions than the signal candidates. In order to get a correct measurement of ϕ_s, the background components have to be identified and modeled in the fit. Two different fitting techniques are used with different ways of treating the background component.

- The measured decay time and angular distributions are distorted by acceptance effects that can be introduced by the geometrical coverage of the detector or by trigger and selection requirements. The fit has to include corrections for these acceptance effects. The corrections of the decay time distribution are determined

by comparing the selected $B_s^0 \to J/\psi\phi$ candidates with a smaller data sample that is known to have no acceptance effects. The corrections of the angular distributions are determined from simulated $B_s^0 \to J/\psi\phi$ candidates.

- The decay time resolution of the detector influences the sensitivity on ϕ_s and is determined using a data sample of prompt $J/\psi \to \mu^+\mu^-$ decays produced directly in the primary proton-proton interaction.

- The production flavour of the B_s^0 mesons must be determined to distinguish between the decay rates of B_s^0 and $\overline{B}_s^0$ in the fit. This is done with flavour tagging algorithms that exploit either the hadronisation properties of the signal B_s^0 meson or the properties of a second b-hadron that might be produced from the $b\overline{b}$ quark pair.

As discussed in Section 2.4 the $B_s^0 \to J/\psi\phi$ P-wave amplitudes can interfere with $B_s^0 \to J/\psi K^+K^-$ S-wave amplitudes. This interference has to be considered in the determination of ϕ_s. The fraction of the S-wave component depends on the size of the K^+K^- mass interval that is used to fit the differential decay rates. Additional correction factors are needed to account for the different K^+K^- mass dependence of P- and S-wave amplitudes.
In the first step, a fit to measure ϕ_s is performed using only $B_s^0 \to J/\psi\phi$ candidates with a reconstructed K^+K^- mass in a small interval around the true mass of the ϕ resonance. By doing this, the relative fraction of the S-wave component and the corrections for the mass dependence in the differential decay rate are minimised. The performance and reliability of the likelihood fitting procedure with the given datasample are tested.
In the second step, the fitted K^+K^- mass window is enlarged. This leads to an improved sensitivity on ϕ_s due to the additional numbers of selected $B_s^0 \to J/\psi K^+K^-$ decays.
The larger mass window also allows for resolving the twofold ambiguity of the differential decay rate. As discussed in Section 2.4 the ambiguity can be resolved by measuring the K^+K^- mass dependence of the decay amplitudes. This is indirectly done by dividing the large K^+K^- mass range in several smaller intervals and measuring the difference between P- and S-wave phases for the different intervals. The trend of the phase difference can be used to single out the correct solution. For each K^+K^- mass interval, separate correction factors need to be applied.
In the end the systematic uncertainties of the measurement are determined by a number of cross-checks and pseudo-experiments simulating the real measurement conditions.
Finally, the measurement of ϕ_s is performed on a combined data sample of $B_s^0 \to J/\psi\phi$ and $B_s^0 \to J/\psi\pi^+\pi^-$ candidates, leading to a further increase in sensitivity. The $B_s^0 \to J/\psi\pi^+\pi^-$ data sample as well as the necessary acceptance and resolution corrections were the subject of a previous analysis [54] and are used for this combination here.

CHAPTER 5

Reconstruction and selection of $B_s^0 \to J/\psi\phi$ candidates

The presented thesis will mainly concentrate on the measurement of the CP-violating phase ϕ_s with reconstructed $B_s^0 \to J/\psi\phi$ decays. The sensitivity of the time and angular distributions to the physics observables increases with the number of reconstructed $B_s^0 \to J/\psi\phi$ signal decays, while it decreases with the amount of background polluting the event sample. The signal and background yields depend on the data taking conditions, the trigger and selection criteria. They will be discussed in the following chapter.

The decay topology of $B_s^0 \to J/\psi\phi$ decays is indicated in Figure 5.1. The B_s^0 meson is produced in the hadronisation of a b-quark from the pp interaction. It decays weakly, typically after a few cm of flight distance. The selected decay mode is $B_s^0 \to J/\psi[\to \mu^+\mu^-]\phi[\to K^+K^-]$ with branching ratio $\mathrm{BR}(\mathrm{B_s^0} \to \mathrm{J/\psi\phi}) = (1.09^{+0.28}_{-0.23}) \cdot 10^{-3}$ [9]. The two resonances J/ψ and ϕ decay almost instantaneously into muons and kaons with branching ratios $\mathrm{BR}(\mathrm{J/\psi} \to \mu^+\mu^-) = (5.93 \pm 0.06)\%$ and $\mathrm{BR}(\phi \to \mathrm{K^+K^-}) = (48.9 \pm 0.5)\%$ respectively [9]. The muons and kaons are stable in the sense that they usually pass the detector without decaying. The visible branching ratio for $B_s^0 \to J/\psi[\to \mu^+\mu^-]\phi[\to K^+K^-]$ is then $\mathrm{BR_{vis}}(\mathrm{B_s^0} \to \mathrm{J/\psi}[\to \mu^+\mu^-]\phi[\to \mathrm{K^+K^-}]) = 3.16 \cdot 10^{-5}$. An additional, small contribution to the same final state are non-resonant $B_s^0 \to J/\psi[\to \mu^+\mu^-]K^+K^-$ decays (S-wave).

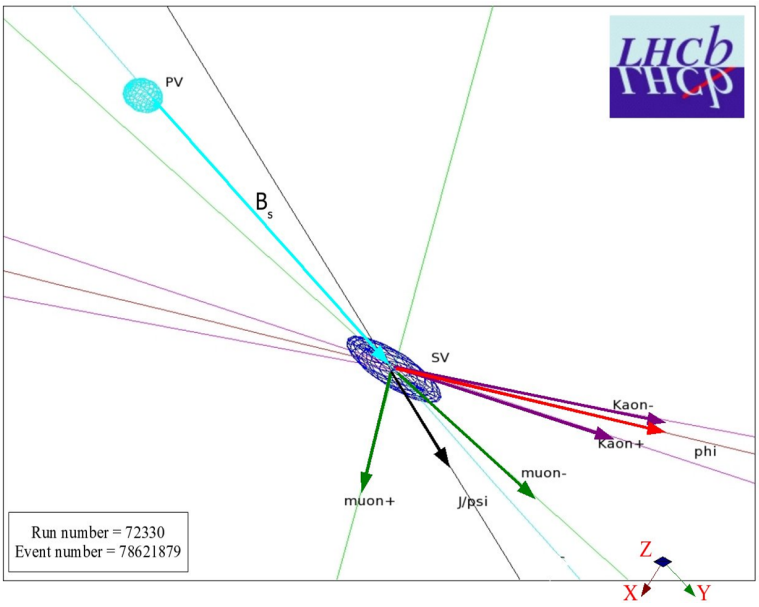

Figure 5.1: Graphical visualisation of a reconstructed $B_s^0 \to J/\psi\phi$ decay. The B_s^0 meson is produced in the pp primary interaction vertex (PV) and decays after a few cm flight distance at the secondary decay vertex (SV). The reconstructed tracks of the kaons (purple) and muons (green) are used to determine the J/ψ (black) and ϕ (red) flight direction. The figure is taken from [55].

5.1 Trigger strategy

The LHCb trigger system was discussed in detail in Section 3.3.3. To select signal events while rejecting background the trigger exploits quantities characteristic for the signal decay. Trigger lines that are suitable to select $B_s^0 \to J/\psi\phi$ decays are based on the reconstruction of muons and di-muon pairs which might form a J/ψ. Some trigger lines also put requirements on quantities that are related to the decay time of the reconstructed particle with the advantage that they are very efficient in suppressing background. The disadvantage is that they influence the observed decay time distribution.

The LHCb trigger system provides several trigger lines that can be used for the selection of $B_s^0 \to J/\psi\phi$ candidates. In principle, one would like to maximise the dataset for the analysis by using as many of them as possible. On the other hand, one has to consider that possible biases introduced by the trigger selection need to be modeled precisely. This would increase the complexity of the measurement and lead to additional potential systematic uncertainties.

The trigger strategy used in this analysis divides the data sample in two subsamples, depending whether the efficiency of the trigger selection is independent of the decay time (*unbiased*) or does depend on the decay time (*biased*) of the selected candidates:

- The **HLT1-unbiased** subsample contains all events that were triggered by a special decay time independent HLT1 trigger line, in the following denoted as *HLT1unbiased*. It requires a positive L0-Muon or L0-DiMuon decision of the hardware trigger. As discussed in section 3.3.3, this is given when the event contains one or two muon track candidates with a minimum transverse momentum relative to the beam line. In the HLT1 a full track reconstruction of the muon candidates from the L0 trigger is performed. Only events are selected where the muon track fit has a maximum χ^2_{track}. The muon candidates are required to have a minimum momentum p and transverse momentum p_{T} and a large combined invariant mass. The detailed trigger cuts are given in Table 5.1. Only events are accepted for which the trigger criterion is fulfilled by the particles used in the B^0_s reconstruction.

- The **HLT1-biased** subsample contains only events that were selected by at least one of the decay time dependent trigger lines *HLT1biasedA* and *HLT1biasedB*. The *HLT1biasedA* line requires a positive *L0-Physics* decision, meaning that either the L0 calorimeter or the L0 muon trigger (see Section 3.3.3) have selected the event. The *HLT1biasedB* line requires a positive L0-Muon or L0-DiMuon decision of the hardware trigger. Both trigger lines select events depending on the impact parameter χ^2_{IP}. It is defined as the square of the impact parameter (IP) significance $\chi^2_{\text{IP}} = (\text{IP}/\sigma_{\text{IP}})^2$, which is given by the shortest distance of the track relative to the interaction point (impact parameter), divided by its uncertainty. Tracks from decays of long-lived particles as the B^0_s have in general a higher χ^2_{IP} than tracks from the interaction point. Therefore these trigger lines are more efficient for B^0_s with a large decay time than for B^0_s with a small decay time. In addition, a minimum χ^2_{track} of the track fit is required and selection criteria on the transverse momentum p_{T} and momentum p of the tracks are applied. All selection criteria of these lines are summarised in Table 5.1.
  Again, only events are accepted for which the trigger criteria are fulfilled by the particles used in the B^0_s reconstruction. In order to avoid an overlap with the HLT1-unbiased subsample, the events must not be triggered by the *HLT1unbiased* line.

For both subsamples, HLT1-unbiased and HLT1-biased, the signal decay has to pass the decay time dependent *HLT2biased* line in the second stage of the software trigger. A first reconstruction of a J/ψ is done by combining two oppositely charged muon candidates. Signal candidates are selected by requiring a combined mass close to the J/ψ mass and a good χ^2 of the vertex fit (χ^2_{vtx}/ndf). To suppress background from prompt J/ψ from the primary vertex, candidates with a small decay length (DL) significance $\text{DL}/\sigma_{\text{DL}}$ are rejected. The requirement on the decay length significance rejects more B^0_s candidates with short decay time than with large decay time. The exact selection criteria can be found in Table 5.2.
In the end both subsamples have a distorted decay time distribution as both require the above HLT2 line. However in the rest of this document they will be classified by their

HLT1 category, HLT1-biased or HLT1-unbiased. The effect of the trigger selections and the method to correct for the decay time dependent efficiency losses will be discussed in chapter 8.
In total the HLT1-unbiased sample contains $\sim 79\%$ of the $B_s^0 \to J/\psi\phi$ candidates used in this analysis, the HLT1-biased sample contains $\sim 21\%$.

cut parameter	HLT1unbiased	HLT1biasedB	HLT1biasedA
L0	L0-Muon or L0-DiMuon	L0-Muon or L0-DiMuon	L0 Physics
p_T	> 500 MeV	> 1000 MeV	> 1700 MeV
p	> 6000 MeV	> 8000 MeV	> 10000 MeV
χ^2_{track}	< 4	< 2	< 2
di-muon mass	> 2700 MeV		
χ^2_{IP}		> 16	> 16

Table 5.1: Selection requirements of the HLT1 trigger lines used in the $B_s^0 \to J/\psi\phi$ selection.

cut parameter	HLT2biased
χ^2_{track}	< 5
$M(\mu^+\mu^-) - M(J/\psi)$	< 120 MeV
χ^2_{vtx}	< 25
$\text{DL}/\sigma_{\text{DL}}$	> 3

Table 5.2: Selection requirements of the HLT2 trigger line used in the $B_s^0 \to J/\psi\phi$ selection.

5.2 Selection criteria

After the online trigger selection, an additional offline selection is performed in order to further reduce the background contribution. The specific selection criteria are optimised to maximise the sensitivity on ϕ_s [56]. First, a loose preselection (stripping) is applied and then a tighter final selection. The detailed selection requirements are listed in Table 5.3 and documented in the following.

Reconstructed and used tracks

The tracks that are used in the reconstruction of $B_s^0 \to J/\psi\phi$ decays have to fulfill two selection criteria: In order to reject bad quality tracks, a requirement on the χ^2 of the track fit divided by the number of degrees of freedom, $\chi^2_{\text{track}}/\text{ndf}$, is made. In

some cases, two tracks are fitted from the detector hit pattern of the same real particle. These tracks are called *clones*. They are suppressed by requiring a minimum Kullback-Liebler *clone distance* [57] variable. It is a measure of the distance between the considered track and all other tracks in the event. Tracks with a small clone distance are more likely to be clones.

The J/ψ reconstruction

A J/ψ candidate is reconstructed using two muon candidates made of tracks with a positive muon probability $\Delta \ln \mathcal{L}_{\mu\pi}$ (see Section 3.3.2). In addition, a minimum muon transverse momentum p_{T} is required to suppress muons from the pp primary interaction vertex (PV). Particles produced in the proton-proton interaction have, in general, a smaller p_{T} than daughters from B-decays due to the large boost. The quality of the J/ψ vertex combination is ensured by cutting on the $\chi^2_{\mathrm{vtx}}/\mathrm{ndf}(J/\psi)$ of the J/ψ vertex fit. The invariant mass of the di-muon system $m(\mu^+\mu^-)$ should be within a certain range of the true J/ψ mass (world average: $M_{J/\psi} = 3096.916 \pm 0.011\,\mathrm{MeV}$ [9]).

The ϕ reconstruction

A ϕ candidate is reconstructed by combining two kaon candidates with a positive kaon probability $\Delta \ln \mathcal{L}_{K\pi}$. The fitted combined ϕ vertex must have a good $\chi^2_{\mathrm{vtx}}/\mathrm{ndf}(\phi)$ and the invariant mass of the combined kaons $m(K^+K^-)$ has to be in an interval around the true ϕ mass (world average: $M_\phi = 1019.455 \pm 0.02\,\mathrm{MeV}$ [9]). In addition a cut on the transverse momentum p_{T} of the ϕ candidate is placed to suppress ϕ mesons produced directly in the primary pp interaction.

The B_s^0 reconstruction

Finally a B_s^0 candidate is reconstructed from the J/ψ and the ϕ candidates, again requiring a good vertex fit $\chi^2_{\mathrm{vtx}}/\mathrm{ndf}(B_s^0)$ of the formed B_s^0 vertex.
In addition to the simple vertex fit, a kinematic fit of the full decay tree (*decay tree fit*) is performed [58]. The parameters of the fit are the vertex positions and momenta of the particles in the decay chain. They are constrained by the momentum conservation at each vertex. The input to the fit are the measured track momenta and positions. The B_s^0 candidates are required to have a good χ^2/ndf of the global kinematic fit, $\chi^2_{\mathrm{DTF}}/\mathrm{ndf}(B_s^0)$. For the determination of the reconstructed B_s^0 invariant mass $m(B_s^0)$ an additional constraint is applied in the decay tree fit, fixing the mass of the di-muon system to the true J/ψ mass. The interval of $m(B_s^0)$ is allowed to be relatively large in order to have enough events in the mass sidebands to perform background studies.
B_s^0 candidates with a large impact parameter $\chi^2_{\mathrm{IP}}(B_s^0)$ are rejected to make sure that the selected candidates originate from the primary interaction. In events with more than one pp interaction, a wrong vertex can be reconstructed as a B_s^0 production vertex, leading to a wrong measurement of the flight distance. To reject B_s^0 candidates that are close to two or more reconstructed primary vertices, a minimum impact parameter

$\chi^2_{\text{IP,next}}(B_s^0)$ of the B_s^0 to the second nearest primary vertex is required. B_s^0 candidates with a short reconstructed decay time are rejected to reduce the huge amount of background arising through wrongly combined J/ψ and ϕ particles originating from the primary vertex. In the end, in events with more than one selected B_s^0, the candidate with the best decay tree fit quality is chosen. This avoids the selection of $B_s^0 \to J/\psi\phi$ candidates with one or more tracks in common.
A more detailed description of the selection and the efficiencies of the single selection criteria can be found in [56] and [59].

Decay mode	Cut parameter	Stripping	Final selection
all tracks	$\chi^2_{\text{track}}/\text{ndf}$	< 4	< 4
	clone distance	–	> 5000
$J/\psi \to \mu^+\mu^-$	$\Delta \ln \mathcal{L}_{\mu\pi}$	> 0	> 0
	$min(p_T(\mu^+), p_T(\mu^-))$	$> 0.5\,\text{GeV}$	$> 0.5\,\text{GeV}$
	$\chi^2_{\text{vtx}}/\text{ndf}(J/\psi)$	< 16	< 16
	$\lvert m(\mu^+\mu^-) - M(J/\psi)\rvert$	$< 80\,\text{MeV}$	$\in [3030, 3150]\,\text{MeV}$
$\phi \to K^+K^-$	$\Delta \ln \mathcal{L}_{K\pi}$	> -2	> 0
	$p_T(\phi)$	$> 500\,\text{MeV}$	$> 1\,\text{GeV}$
	$m(K^+K^-)$	$\in [980, 1050]\,\text{MeV}$	$\in [1008, 1032]\,\text{MeV}$
	$\chi^2_{\text{vtx}}/\text{ndf}(\phi)$	< 16	< 16
$B_s^0 \to J/\psi\phi$	$m(B_s^0)$	$\in [5200, 5550]\,\text{MeV}$	$\in [5200, 5550]\,\text{MeV}$
	$\chi^2_{\text{vtx}}/\text{ndf}(B_s^0)$	< 10	< 10
	$\chi^2_{\text{DTF}}/\text{ndf}(B_s^0)$	–	< 5
	$\chi^2_{\text{IP}}(B_s^0)$	–	< 25
	$\chi^2_{\text{IP,next}}(B_s^0)$	–	< 50
	t	$> 0.2\,\text{ps}$	$> 0.3\,\text{ps}$

Table 5.3: Preselection (stripping) and selection requirements for the $B_s^0 \to J/\psi\phi$ decay, taken from [56] and [59].

A total number of 37361 B_s^0 candidates remain after the full selection process. Their invariant mass distribution is given in Figure 5.2. The distribution is fitted with a sum of two Gaussian functions describing the signal and a linear function describing the background component. From the fit, one can extract the number of signal $B_s^0 \to J/\psi\phi$ events to be $N_{\text{sig}} = 24989 \pm 171$. The signal to background ratio in the full B_s^0 mass interval $[5200\,\text{MeV}, 5550\,\text{MeV}]$ is $\frac{\text{S}}{\text{B}} = 2.04$ showing the low background level remaining after the selection. The composition of the background will be discussed in the next sections.

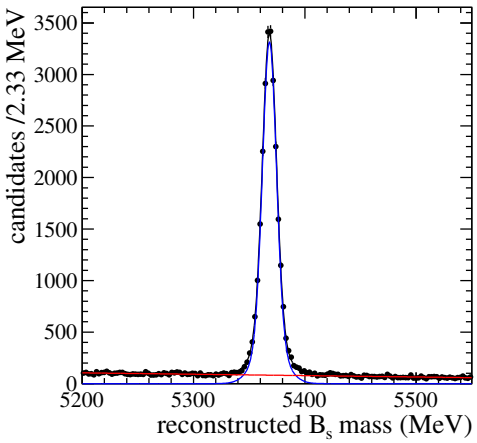

Figure 5.2: Reconstructed B_s^0 mass distribution of all selected $B_s^0 \to J/\psi\phi$ candidates, fitted with a double Gaussian function to describe the signal component (blue) and a linear function to describe the background component (red).

5.3 Signal and background distributions

The main input variables for the measurement of the time-dependent CP violation are the reconstructed B_s^0 decay time and the three helicity angles. Their distributions are shown in Figure 5.3 for background subtracted data and simulated signal decays after the full selection. The background subtraction was performed using the sideband subtraction technique. It exploits the fact that B_s^0 candidates with a reconstructed mass in the sideband regions [5200 MeV, 5320 MeV] and [5420 MeV, 5550 MeV] are known to be background events. The background contribution in the plots is then subtracted on a statistical basis.
It can be observed that the distributions of measured and simulated $B_s^0 \to J/\psi\phi$ signal candidates are not the same, especially the angular distributions are different. Their shape is mainly determined by the polarisation amplitudes of the decay. This means that the values of the polarisation amplitudes used in the simulation of $B_s^0 \to J/\psi\phi$ decays do not describe the true amplitudes. In addition there might be detector acceptance effects that are not accurate described in the simulation. The consequence of both problems will be discussed in Chapter 8 where the angular acceptances are introduced. The decay time and angular distribution of the background candidates are shown in Figure 5.4 for background candidates of the lower and upper mass sideband intervals separately. They have significantly different distributions than the signal candidates. There are especially two sharp peaks at the edges of the $\cos\theta_\mu$ spectrum visible. The shapes are identical for lower and upper sideband events, giving confidence that the background in the signal region has a similar shape and can be subtracted in the described manner.

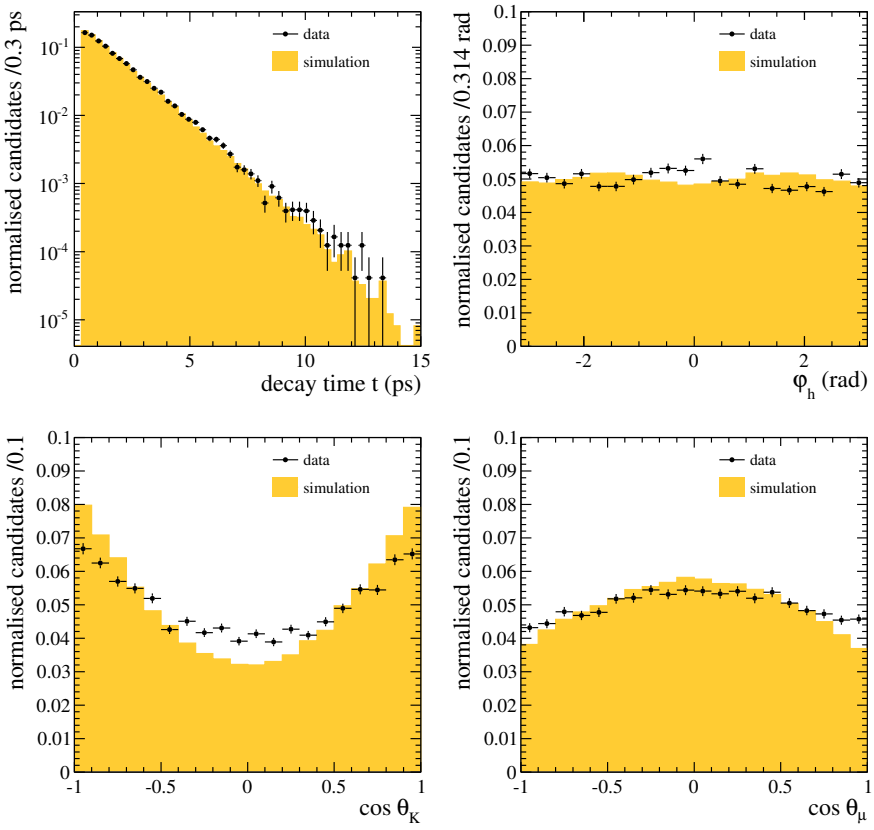

Figure 5.3: Decay time and angular distributions of selected B_s^0 decays with an invariant mass in the signal window [5320 MeV, 5420 MeV] for background subtracted data and simulation.

5.4 Background composition

As discussed, the invariant B_s^0 mass is a good variable to separate the signal and background components. In the signal region of [5320 MeV, 5420 MeV] the total background level remaining after the full selection is very low. In addition, the corresponding time and angular distributions can be easily modeled with background candidates from the B_s^0 mass sidebands. The most relevant background components have been identified:

- The largest number of the background events are candidates reconstructed from a true $J/\psi \to \mu^+\mu^-$ decay, resulting from a B decay, and two randomly picked up tracks. Their number can be extracted from a fit to the J/ψ mass distribution of the selected $B_s^0 \to J/\psi\phi$ candidates, see Figure 5.5(a). The shape of the J/ψ mass peak is determined by the detector resolution and the radiative tails of the resonance. Therefore the J/ψ component is modeled by a Crystal-Ball function [60] that consist of a Gaussian core and a polynomial to describe the tail at low masses[1].

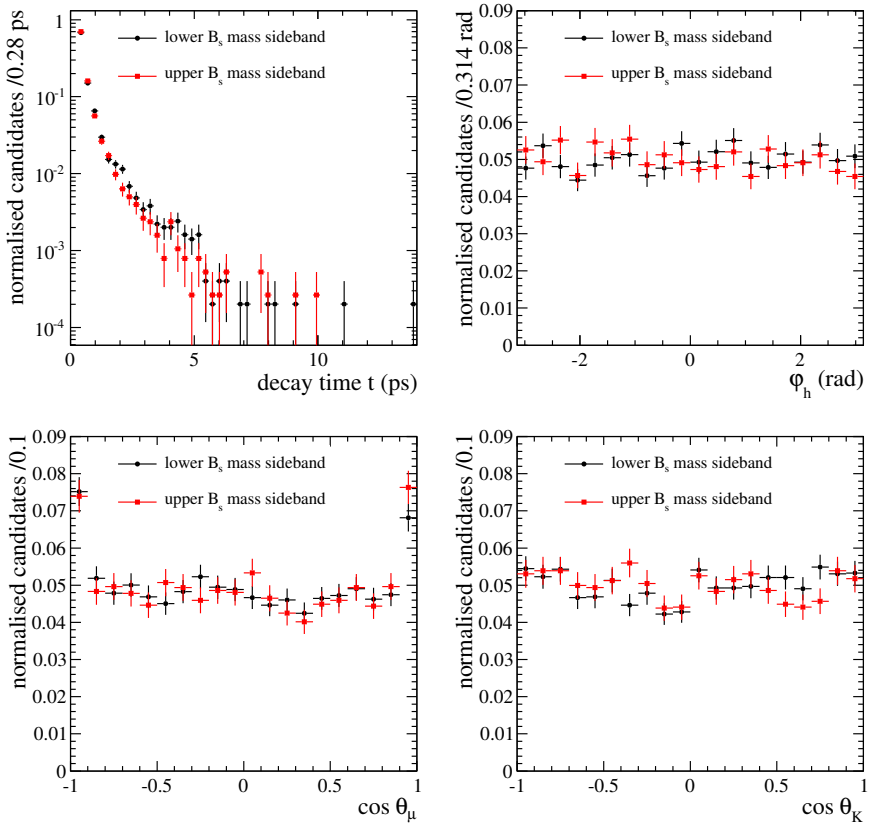

Figure 5.4: Decay time and angular distributions for $B_s^0 \to J/\psi\phi$ background candidates of the upper B_s^0 mass sideband ([5420 MeV, 5550 MeV]) and lower B_s^0 mass sidebands ([5200 MeV, 5320 MeV]).

A linear function is used to describe the non-J/ψ component. This leads to a total number of $N_{J/\psi} \approx 32600$ true J/ψ decays. The distribution in Figure 5.5(a) however contains both $B_s^0 \to J/\psi\phi$ signal and background candidates. To estimate the number of $B_s^0 \to J/\psi\phi$ background candidates reconstructed from a true J/ψ decay, the number of $B_s^0 \to J/\psi\phi$ signal candidates ($N_{\text{sig}} \approx 25000$) needs to be subtracted. This results in $N_{J/\psi}^{\text{bkg}} \approx 7600$ B_s^0 background candidates containing a true J/ψ, corresponding to a fraction of 62% of the total B_s^0 background.

[1]The Crystal-Ball function for a variable x is given by

$$CB(x|\alpha, n, \mu, \sigma) = N \cdot \begin{cases} e^{-\frac{(x-\mu)^2}{2\sigma^2}}, & \text{if } \frac{x-\mu}{\sigma} > -\alpha \\ \left(\frac{n}{|\alpha|}\right)^n e^{-\frac{|\alpha|^2}{2}} \cdot \left(\frac{n}{|\alpha|} - |\alpha| - \frac{x-\mu}{\sigma}\right)^{-n}, & \text{if } \frac{x-\mu}{\sigma} \leq -\alpha\,. \end{cases}$$

μ and σ are the mean and width of the distribution, α and n are parameters defining the starting point and order of the polynomial part of the function. N is a normalisation factor.

- A second background component are candidates reconstructed from a true $\phi \to K^+K^-$ decay. Their number can be estimated, similarly to the J/ψ background, with a fit of the ϕ mass distribution of all selected $B_s^0 \to J/\psi\phi$ candidates. It is shown in Figure 5.5(b) where a Breit-Wigner function was used to describe the ϕ resonance and a linear function for the non-ϕ component. The extracted number of true $\phi \to K^+K^-$ decays is $N_\phi \approx 28600$. As this number contains both B_s^0 signal and background candidates, the total number of B_s^0 signal candidates is subtracted to determine the number of B_s^0 background candidates containing a true ϕ decay: $N_\phi^{\text{bkg}} \approx 3600$. This corresponds to about 28% of the full $B_s^0 \to J/\psi\phi$ background.

- The remaining background consists mainly of randomly combined tracks passing the $B_s^0 \to J/\psi\phi$ selection criteria.

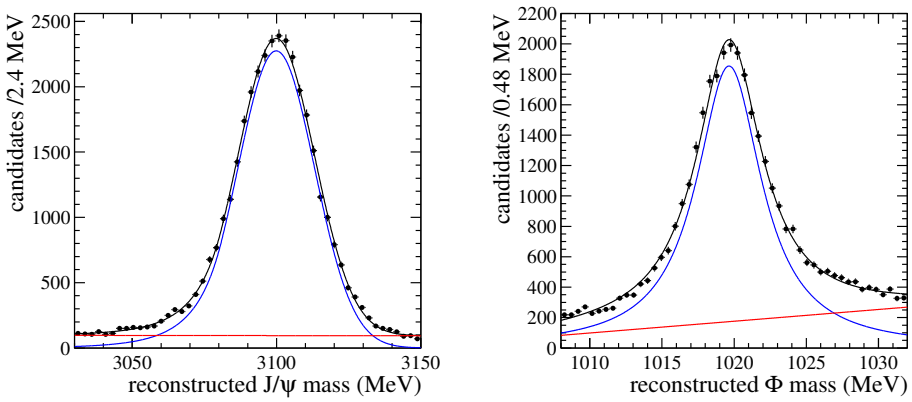

(a) J/ψ mass distribution (b) ϕ mass distribution

Figure 5.5: Reconstructed J/ψ and ϕ mass distributions of selected $B_s^0 \to J/\psi\phi$ candidates. The fitted signal components are given in blue, the fitted background components in red.

In addition to combinatorial background contributions, there could be some wrongly reconstructed physical background which is only present in the signal region of the B_s^0 mass. The only process which could lead to a significant contribution is the $B_d^0 \to J/\psi[\to \mu^+\mu^-]K^{*0}[\to K^+\mu^-]$ decay. These candidates can be falsely identified as $B_s^0 \to J/\psi\phi$ when the pion is reconstructed as a kaon and a wrong mass hypothesis is assigned. This leads to a shift of the reconstructed B_s^0 mass into the $B_s^0 \to J/\psi\phi$ signal region. To estimate the size and shape of the decay distributions of this possible background component, a sample of 10 million simulated $B_d^0 \to J/\psi K^{*0}$ decays is used. The events were processed with the full $B_s^0 \to J/\psi\phi$ selection. The B_s^0 mass distribution of the selected 735 candidates is shown in Figure 5.6. In addition to a flat component,

there is a clear peak in the B_s^0 signal region visible. This means that the decay distributions of this background component can not be modeled using events in the mass sidebands. The corresponding time and angular distributions are shown in Figure 5.7. Especially the shape of the angular distributions is clearly different from signal and from the combinatorial background components. To estimate the expected fraction of this background type relative to the number of signal decay one has to determine the integrated luminosity corresponding to the 10 million generated $B_d^0 \to J/\psi K^{*0}$ decays by using

$$\mathcal{L} = \frac{N}{\sigma_{b\bar{b}} \cdot f_{\mathrm{B}} \cdot \mathrm{BR_{vis}}(\mathrm{B_d^0} \to \mathrm{J/\psi[\to \mu^+\mu^-]K^{*0}[\to K^+\mu^-]}) \cdot \varepsilon_{\mathrm{gen}}} \,. \tag{5.1}$$

N is the number of generated decays, $\sigma_{b\bar{b}} = (288 \pm 4 \pm 48)\,\mu$b [41] the measured production cross-section of $b\bar{b}$-pairs, $\mathrm{BR_{vis}}(\mathrm{B_d^0} \to \mathrm{J/\psi[\to \mu^+\mu^-]K^{*0}[\to K^+\mu^-]}) = 7.88 \cdot 10^{-5}$ [9] the visible branching ratio and $f_{\mathrm{B}} = 0.396 \pm 0.001$ the assumed hadronisation fraction. $\varepsilon_{\mathrm{gen}} = 0.1492 \pm 0.0004$ [61] is the efficiency of the selection criteria in the event simulation, where only candidates are accepted that are generated inside the LHCb acceptance (see Section 3.4). Scaling the integrated luminosity of the 10 million simulated $B_d^0 \to J/\psi K^{*0}$ events to the 1.1 fb^{-1} used for this analysis leads to an expectation of 97 $B_d^0 \to J/\psi K^{*0}$ background candidates or a contamination of 0.3% relative to the number of $B_s^0 \to J/\psi\phi$ signal decays. This very small fraction is not expected to have a significant effect in the CP violation measurement and is therefore not separately modeled in the following analysis. However possible systematic uncertainties from ignoring this contribution will be evaluated.

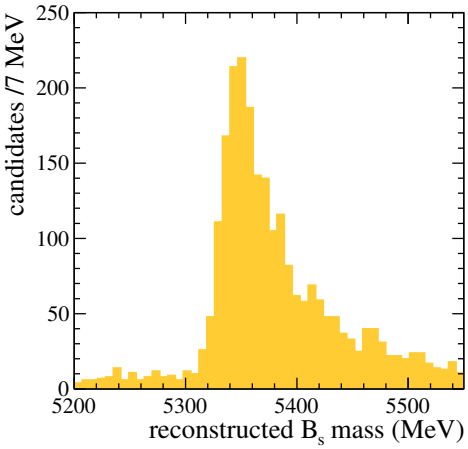

Figure 5.6: Reconstructed B_s^0 mass distribution of wrongly reconstructed, simulated $B_d^0 \to J/\psi K^{*0}$ background candidates.

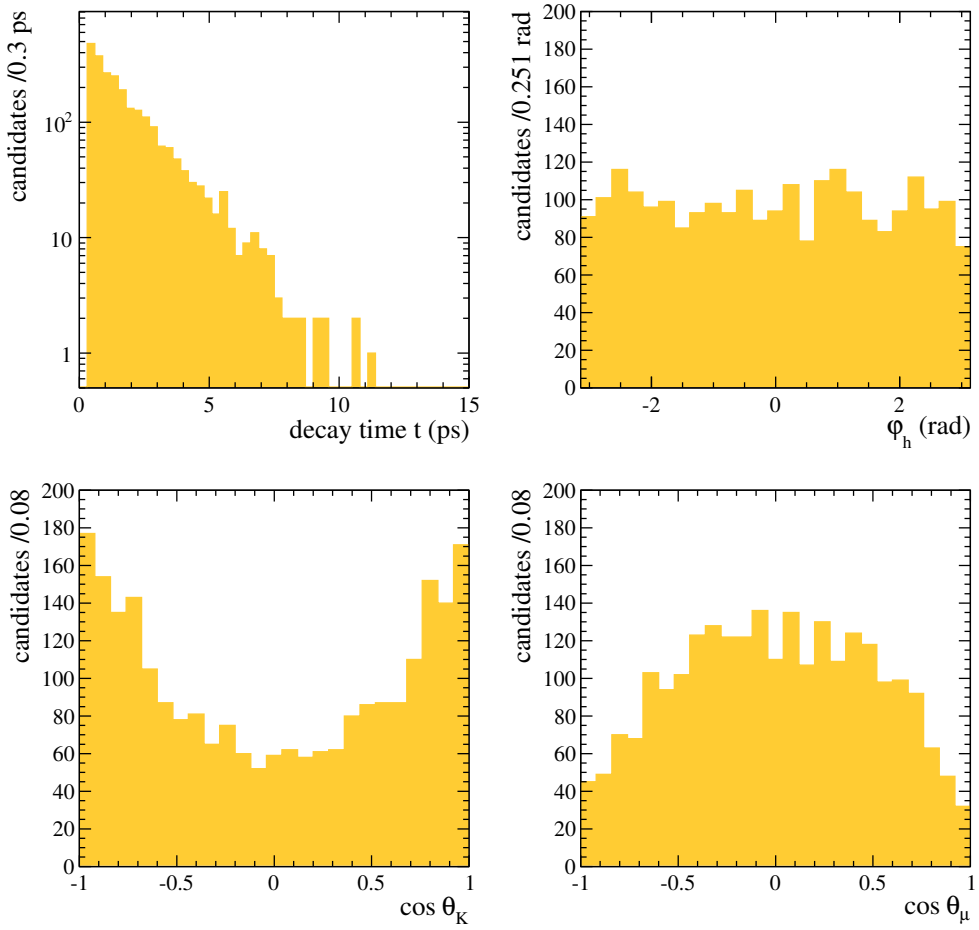

Figure 5.7: Decay time and angular distributions of wrongly reconstructed, simulated $B_d^0 \to J/\psi K^{*0}$ background candidates.

CHAPTER 6

Flavour tagging

The measurement of the CP asymmetry in the interference of mixing and decay requires the knowledge of the production flavour of the B mesons in order to distinguish the differential decay rates for B_s^0 and $\overline{B}_s^0$ mesons. The procedure to determine the production flavour is known as *flavour tagging*. Several algorithms are used in LHCb to extract the production flavour from the B meson decay kinematics and event properties. The tagging algorithms provide for each event a tagging decision q with $q = -1$ for a produced B_s^0, $q = +1$ for a produced $\overline{B}_s^0$ and $q = 0$ if no decision could be made. The tagging efficiency is defined as

$$\varepsilon_{\text{tag}} = \frac{N_{\text{tag}}}{N_{\text{all}}}\,, \tag{6.1}$$

where N_{tag} is the number of events with tagging decision $q \neq 0$ and N_{all} the number of all available events. The quality of the tagging is described by the mistag probability ω_{av} giving the fraction of wrong tagging decisions:

$$\omega_{\text{av}} = \frac{N_{\text{W}}}{N_{\text{W}} + N_{\text{R}}}\,, \tag{6.2}$$

where N_{R} is the number of events with a correct tagging decision and N_{W} the number of incorrectly tagged events. The influence of the tagging quality on the measurement of ϕ_{s} can be seen by looking at the differential decay rates. The terms providing the most information on ϕ_{s} are those proportional to $\sin\phi_{\text{s}} \cdot \sin(\Delta m_{\text{s}} t)$. These terms appear with different signs in the decay rates of B_s^0 and $\overline{B}_s^0$. A finite mistag probability for the

determination of the production flavour leads to an additional damping factor in the CP asymmetry (Equation 2.39):

$$a(t) \propto D_{\mathrm{av}} \sin\phi_{\mathrm{s}} \cdot \sin(\Delta m_{\mathrm{s}} t)\,, \tag{6.3}$$

where $D_{\mathrm{av}} = (1 - 2\omega_{\mathrm{av}})$ is the tagging dilution. The sensitivity on ϕ_{s} as the measurement of the amplitude of the CP asymmetry depends therefore directly on the mistag probability of the tagging. The effective statistical reduction of the data sample due to imperfect tagging with respect to an event sample with perfect tagging is given by the effective tagging power $\varepsilon_{\mathrm{eff}}$,

$$\varepsilon_{\mathrm{eff}} = \varepsilon_{\mathrm{tag}} D_{\mathrm{av}}^2 = \varepsilon_{\mathrm{tag}}(1 - 2\omega_{\mathrm{av}})^2\,. \tag{6.4}$$

The algorithms to determine the B_s^0 production flavour will be presented in the following chapter. The flavour tagging strategy and the achieved tagging performance for the $B_s^0 \to J/\psi\phi$ events will be discussed.

6.1 Flavour tagging at LHCb

In order to determine the production flavour of neutral B mesons two classes of algorithms are available at LHCb [62]: *Opposite-side tagging* algorithms (OST) exploit the fact that b-hadrons are always produced in pairs with opposite flavour. They use the properties of the second b-hadron in the event to determine the production flavour of the signal B_s^0 candidate. *Same-side tagging* algorithms (SST) on the other hand exploit the properties of the signal B_s^0 decay to get an estimate of the production flavour. Figure 6.1 shows a schematic overview of the different tagging algorithms. Both opposite-side and same-side tagging algorithms are used in this analysis.

6.1.1 Opposite-side flavour tagging

The opposite-side taggers use the information of the second b-hadron decay in the event to determine the flavour of the signal B_s^0 candidate [63]. There are four algorithms available, three so called *single particle tagger* using the charge information of electrons, muons and kaons from the b-hadron decay, and one *vertex charge tagger* determining the overall charge of the b-hadron decay vertex.

Single particle taggers

The single particle taggers use the charge of leptons from semi-leptonic b-hadron decays (electron- and muon-tagger) or the charge of the kaon from the $b \to c \to s$ decay chain, for example in $B_d^0 \to D^{*-}\mu^+\nu_\mu$ decays, to determine the production flavour of the signal B meson. They require the muon, electron and kaon track candidates to have a large impact parameter significance $\mathrm{IP}/\sigma_{\mathrm{IP}}$ and large transverse momentum p_{T} in order to select only candidates from long-living b-hadrons. In addition, information

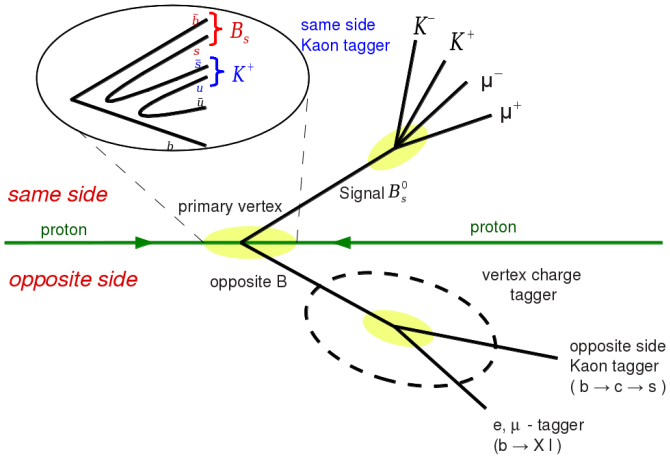

Figure 6.1: Schematic overview of tagging algorithms at LHCb. Two main types are visible: opposite-side taggers (OST) and same-side tagger (SST). The figure is taken from [62] and slightly modified.

from the particle identification detectors is used by applying $\Delta \ln \mathcal{L}$ requirements. In case a single tagger selects more than one track candidate per event, the one with the highest transverse momentum is chosen to define the tagging decision. The detailed selection for the single taggers is documented in [63].

Vertex charge tagger

The vertex charge tagger determines the overall charge associated to the decay vertex of the second b-hadron in the event. Vertex candidates are reconstructed by combining two tracks with high impact parameter significance and transverse momentum to a common vertex. For each vertex candidate, the probability to originate from a b-hadron decay is estimated, taking into account the quality of the vertex fit as well as geometric and kinematic properties of the vertex candidate. The vertex with the highest probability is chosen as decay vertex of the second b-hadron. Afterwards all tracks in the event that are compatible with originating from this vertex candidate but not from the primary vertex are assigned to the tagging vertex. After applying additional selection requirements on the sum of the associated tracks, the overall vertex charge is calculated by summing the charges of the tracks weighted by their transverse momentum. The tagging decision is made depending on the value of the overall vertex charge [63].

6.1.2 Same-side flavour tagging

In the hadronisation of a $\overline{b}$ quark to a B_s^0 meson, an $s\bar{s}$ quark pair is produced from the vacuum. The s quark forms together with the $\overline{b}$ quark the signal meson and the $\bar{s}$ quark might hadronise to a charged kaon (see Figure 6.1). In this case the charge of the kaon indirectly determines the flavour of the B_s^0 meson. To select the kaon tracks from the hadronisation, the same-side kaon tagging algorithm is used [62]. It requires the tracks to be close to the signal B_s^0 phase space by requiring a maximum polar angle difference between track and B_s^0 candidate. A maximum impact parameter significance with respect to the primary vertex is required, to ensure that the kaon candidate originates from the B_s^0 hadronisation. To reject low momentum background tracks from the primary vertex a high transverse momentum is required for the kaon candidate. The $\Delta \ln \mathcal{L}$ particle identification variable is used to distinguish kaons from pions and protons. In case more than one kaon track candidate is selected per event, the one with the highest transverse momentum is chosen to determine the tagging decision [64].

6.2 Calibration of taggers

Besides the tagging decision q, each of the single tagging algorithms provides an estimate for the mistag probability, ω_{est}, for every event. The estimated ω_{est} is determined by a neural network depending on the B_s^0 kinematic and event properties. The measurement of ϕ_s profits from the additional information provided by the estimated mistag probability because B_s^0 candidates with a more reliable tagging decision get a larger weight in the CP asymmetry. In order to use the estimated mistag probability it has to be calibrated to make sure it reflects the true mistag probability.
The performance of the tagging algorithms might in addition depend on the B_s^0 production flavour, resulting in different true mistag probabilities ω_{tag} and $\overline{\omega}_{\text{tag}}$ for produced B_s^0 and $\overline{B}_s^0$ mesons, respectively. Ignoring this difference would introduce an artificial asymmetry and lead to a wrong measurement of the CP violation. Therefore, the estimated mistag probability ω_{est} is calibrated separately for produced B_s^0 and $\overline{B}_s^0$ mesons. For the opposite side tagger, the calibration is done using $B^+ \to J/\psi K^+$ and $B^- \to J/\psi K^-$ decays. Since the charged B^+ and B^- do not oscillate, their production flavour is determined by the charge of the kaon in the decay. In the calibration procedure the estimated mistag probability ω_{est} is compared to the true mistag probabilities ω_{tag} and $\overline{\omega}_{\text{tag}}$ measured with $B^+ \to J/\psi K^+$ and $B^- \to J/\psi K^-$ decays, respectively [63].
The calibration of the same side tagger can only be done with B_s^0 decays, as a kaon needs to be produced in the hadronisation process of the B_s^0 meson (see previous section). The decay $B_s^0 \to D_s^- \pi^+$ was used for the calibration. As the B_s^0 oscillates, a time-dependent analysis is necessary to determine the production flavour [64] and measure the true mistag probabilities ω_{tag} and $\overline{\omega}_{\text{tag}}$.
In the calibration procedure a linear dependence between estimated and true mistag probabilities is assumed to derive a calibrated mistag probability ω_{C}. In order to cor-

rectly propagate the statistical and systematic uncertainties of the calibration, the true mistag probabilities ω_{tag} and $\overline{\omega}_{\text{tag}}$ are expressed as a function of the calibrated mistag probability ω_{C},

$$\begin{aligned} \omega_{\text{tag}}(\omega_{\text{C}}) &= p_0 + p_1(\omega_{\text{C}} - <\omega_{\text{C}}>) + \frac{\Delta}{2} \\ \overline{\omega}_{\text{tag}}(\omega_{\text{C}}) &= p_0 + p_1(\omega_{\text{C}} - <\omega_{\text{C}}>) - \frac{\Delta}{2}\,, \end{aligned} \tag{6.5}$$

where $<\omega_{\text{C}}>$ is the average of the calibrated mistag probabilities for all events and p_0 and p_1 are calibration parameters. For a perfectly calibrated tagger the calibration parameters are $p_0 =<\omega_{\text{C}}>$ and $p_1 = 1$ and the true mistag probabilities are identical to the calibrated mistag probability. Δ parameterises the difference between the true mistag probabilities for produced B_s^0 and $\overline{B}_s^0$ mesons. For $\Delta = 0$ the true mistag probability does not depend on the production flavour.
After the calibration of the single taggers, the tagging decisions and calibrated mistag probabilities of the opposite side taggers are combined to one single opposite side decision q^{OST} and mistag probability $\omega_{\text{est}}^{\text{OST}}$. To account for correlations between the single taggers, the calibration with $B^+ \to J/\psi K^+$ and $B^- \to J/\psi K^-$ decays has to be repeated, resulting in a single calibrated mistag probability ω_c^{OST} for the opposite side taggers.

6.3 Tagging strategy for fit

After the calibration and combination of the single opposite side taggers each B_s^0 candidate has one tagging decision and calibrated mistag probability from the opposite-side taggers q^{OST}, ω_c^{OST}, and one from the same-side tagger, q^{SST}, ω_c^{SST}. The calibrated mistag probabilities are related to the true mistag probabilities $\omega_{\text{tag}}^{\text{OST}}$ and $\omega_{\text{tag}}^{\text{SST}}$ by the parameterisation given in Equation 6.5.
For the measurement of ϕ_{s}, the $B_s^0 \to J/\psi\phi$ candidates are classified in three tagging categories, depending on the opposite and same side tagging decisions. A candidate is called *OST only* tagged when $q^{\text{SST}} = 0$ and *SST only* tagged when $q^{\text{OST}} = 0$. Candidates that have non-zero tagging decision from both kind of taggers (overlapping decisions) are called *OST+SST tagged*. For these candidates the calibrated mistag probabilities ω_{C} from the opposite side and same side taggers are combined to one single decision $q^{\text{OST+SST}}$ and mistag probability $\omega_c^{\text{OST+SST}}$:
From the decisions and mistag probabilities of OST and SST a probability $P(b)$ that the B_s^0 meson contains a b quark is calculated. The probability that the B_s^0 meson contains a $\overline{b}$ quark is given by $P(\overline{b}) = 1 - P(b)$. Depending on the value of $P(b)$, $q^{\text{OST+SST}}$ and $\omega_c^{\text{OST+SST}}$ are determined as [63]:

$$\begin{aligned} q^{\text{OST+SST}} &= -1\,,\ \omega_c^{\text{OST+SST}} = 1 - P(b) \qquad \text{if } P(b) > P(\overline{b})\,, \\ q^{\text{OST+SST}} &= +1\,,\ \omega_c^{\text{OST+SST}} = 1 - P(\overline{b}) \qquad \text{if } P(b) < P(\overline{b})\,. \end{aligned} \tag{6.6}$$

The calibration parameters p_1, p_0, Δ, relating the calibrated mistag probability ω_C to the true mistag probabilities ω_{tag} and $\overline{\omega}_{tag}$ (Equation 6.5) are given in Table 6.1 for the three different tagging categories. Both opposite and same side tagger are perfectly calibrated, resulting in $p_0 =< \omega_C >$ and $p_1 = 1$. The stated uncertainties of the calibration parameters include both statistical and systematic uncertainties from the calibration procedure. As the mistag probability of the OST+SST tagged events is already a combination of the calibrated OST and SST mistag probabilities, the calibration parameters for the OST+SST tagged category are set to $p_0 =< \omega_C >= 0$ and $p_1 = 1.0$. The uncertainties on the parameters are the propagated uncertainties from the opposite and same side tagger calibrations.
Similar to true mistag probability, the tagging efficiency can be different for produced B_s^0 and $\overline{B}_s^0$ mesons. This would as well introduce an artificial asymmetry in the CP violation measurement and influence the value of ϕ_s. The relative difference in the tagging efficiencies can be estimated in the calibration procedure and is found to be $< 0.3\%$ [65]. The expected effect of this difference on the measurement of ϕ_s is smaller than the effect from the different mistag probabilities, given by the calibration parameter Δ. It will not be directly modeled in the measurement of ϕ_s but instead used to estimate a related systematic uncertainty.

parameter	OST only	SST only	OST+SST tagged
p_0	0.392 ± 0.008	0.350 ± 0.017	0.0 ± 0.025
p_1	1.000 ± 0.023	1.000 ± 0.16	1.000
$< \omega_C >$	0.392	0.350	0.0
Δ	0.011 ± 0.0034	-0.019 ± 0.005	-0.011 ± 0.004

Table 6.1: Calibration parameters for the three tagging categories OST only, SST only and OST+SST tagged relating the calibrated mistag probabilities to the true mistag probability for each B_s^0 candidate. The uncertainties are statistical and systematic combined [22].

The quality of the tagging for the selected $B_s^0 \to J/\psi\phi$ event sample is characterised by the tagging efficiency ε_{tag}, the average mistag probabilities ω_{av} and tagging power ε_{eff} of the three tagging categories. ω_{av} and the resulting average dilution D_{av} of the CP asymmetry can be calculated following Equation 6.2 as

$$\omega_{av} = \frac{1}{N}\sum_N \omega_{tag}\,, \quad D_{av} = \frac{1}{N}\sum_N D_{tag} = \frac{1}{N}\sum_N (1 - 2\omega_{tag})\,, \tag{6.7}$$

where the sums are calculated over N selected signal $B_s^0 \to J/\psi\phi$ candidates. The distributions of the true tagging dilution $D_{tag} = (1 - 2\omega_{tag})$ in the three tagging categories are shown in Figure 6.2 for signal candidates. They are compared to the tagging dilutions of background candidates, which are very similar. Only in the SST only tagged

category, the signal candidates have in average a higher tagging dilution.
Finally, the tagging efficiency, the average dilution and the resulting tagging power

$$\varepsilon_{\text{eff}} = \varepsilon_{\text{tag}} \frac{1}{N} \sum_{N} D_{\text{tag}}^2 \tag{6.8}$$

for the selected $B_s^0 \to J/\psi\phi$ signal candidates are given in Table 6.2 for the three tagging categories. The overall tagging power is given by the sum of the tagging power in the three categories as $\varepsilon_{\text{eff}} = 3.13\%$.

	OST only	SST only	OST+SST tagged
ε_{tag}	29.10%	6.36%	3.90%
D_{av}	0.266	0.296	0.361
ε_{eff}	2.06%	0.56%	0.51%

Table 6.2: Tagging efficiency ε_{tag}, average tagging dilution D_{av} and tagging power ε_{eff} of the selected B_s^0 signal candidates in the three tagging categories OST, SST and OST+SST tagged [22].

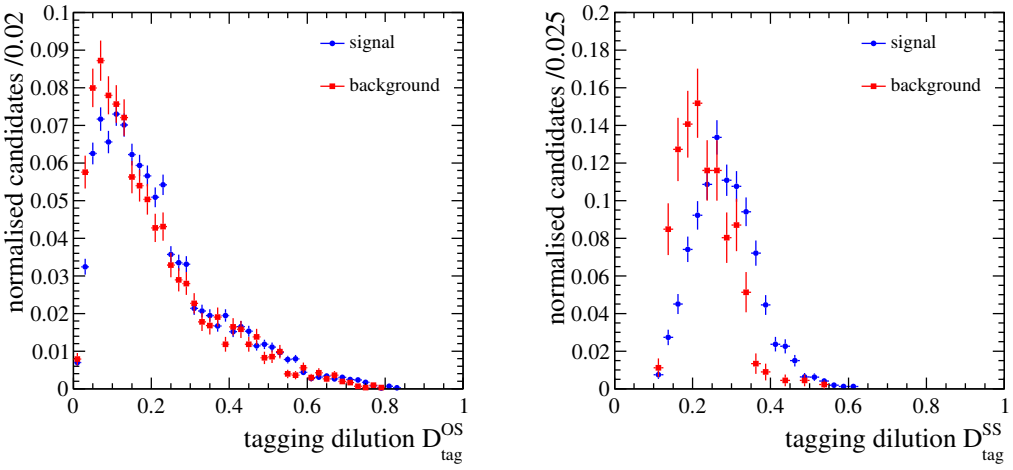

(a) OST tagged candidates

(b) SST tagged candidates

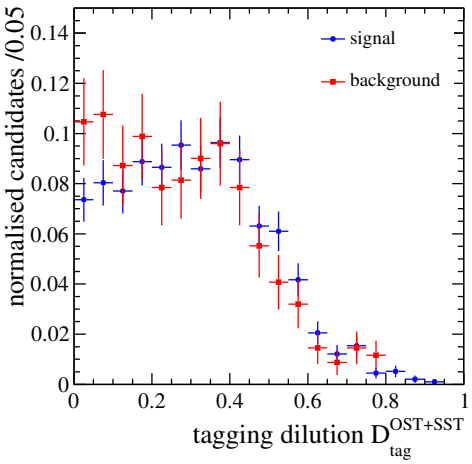

(c) OST+SST tagged candidates

Figure 6.2: Normalised distributions of true tagging dilution D_{tag} for $B^0_s \to J/\psi\phi$ sideband subtracted signal and background candidates from the three tagging categories OST only, SST only and OST+SST tagged.

CHAPTER 7

Decay time resolution

The determination of the physics parameters is done by fitting the theoretical $B_s^0 \to J/\psi\phi$ decay rate introduced in Chapter 2 to the measured data. The differential decay rate however predicts the distribution of the true B_s^0 decay time, while the measured decay time has uncertainties. The effect of a finite resolution on the measured decay time can be modeled by convoluting the underlying, theoretical, time-dependent function $p(t) = \frac{\mathrm{d}\Gamma(B_s^0 \to J/\psi\phi)}{\mathrm{d}t\mathrm{d}\Omega}$ (Equation 2.51) with a resolution model $f(t-t')$:

$$p(t) \otimes f(t) \equiv \int_{-\infty}^{\infty} p(t') f(t-t') \mathrm{d}t' \,. \tag{7.1}$$

The resolution model $f(t-t')$ must describe the decay time uncertainty introduced by the measurement process very precisely in order to not bias the determined parameter values. This is especially the case for the determination of ϕ_s. Similar to the mistag probability, a finite decay time resolution leads to an additional damping factor D_res in the measured CP asymmetry (Equation 2.40):

$$a(t) \otimes f(t) \propto D_\mathrm{res} \cdot \sin\phi_\mathrm{s} \sin(\Delta m_\mathrm{s} t) \,, \tag{7.2}$$

For a Gaussian resolution model $G(t-t'|\mu, \sigma_t^\mathrm{av})$ with mean μ and width σ_t^av, the effect on the CP asymmetry can be calculated as

$$a(t) \otimes G(t) = \int_{-\infty}^{\infty} a(t') G(t-t'|\mu, \sigma_t^\mathrm{av}) \mathrm{d}t' \quad \propto \quad \exp\left(\frac{-\Delta m_\mathrm{s}^2 \cdot \sigma_t^{\mathrm{av}2}}{2}\right) \sin\phi_\mathrm{s} \sin(\Delta m_\mathrm{s} t) \,, \tag{7.3}$$

leading to a dilution factor D_{res} of

$$D_{\text{res}} = \exp(\frac{-\Delta m_{\text{s}}^2 \cdot \sigma_t^{\text{av}\,2}}{2}) \,. \tag{7.4}$$

In the following chapter, the resolution model for the $B_s^0 \to J/\psi\phi$ candidates will be determined. The method relies on measured $B_s^0 \to J/\psi\phi$ background candidates. The simulation is used to cross-check and verify the method.

7.1 Treatment of the finite decay time resolution

The B_s^0 decay time t is determined by the flight length $\vec{d}$ and the momentum $\vec{p}$ of the B_s^0 meson, to

$$t = \gamma \frac{(\vec{d} \cdot \vec{p})m}{\vec{p}^2} \,, \tag{7.5}$$

where m is the reconstructed invariant mass. The flight length is given by the connection between B_s^0 production and decay vertex.
For each B_s^0 candidate, the decay time is determined by a global kinematic fit (decay tree fit [58]) of the momenta and vertex positions (see Section 5.2). The fit provides also an estimate for the uncertainty σ_{t} of the reconstructed decay time. The uncertainty is, following Equation 7.5, determined by the uncertainties of the B_s^0 production and decay vertex positions and the B_s^0 momentum. For $B_s^0 \to J/\psi\phi$ decays the momentum can be determined very precisely from the measured momenta of the muon and kaon tracks. The B_s^0 production vertex is the pp interaction point and the reconstruction of the produced particle tracks allows for an excellent position measurement. In contrast, the position of the B_s^0 decay vertex is only defined by the crossing point of four tracks. The uncertainty of the decay vertex position is therefore by far the largest uncertainty in the determination of the decay time.
The estimated decay time uncertainty σ_{t} of the global kinematic fit is shown in Figure 7.1 for selected, background subtracted $B_s^0 \to J/\psi\phi$ signal candidates and background candidates from the B_s^0 mass sidebands.

The modeling of the decay time resolution in the determination of ϕ_{s} can be done in two different ways. One option is an average decay time model, assuming an average uncertainty σ_t^{av} for all $B_s^0 \to J/\psi\phi$ candidates. By doing this, the decay time uncertainty is not treated in an optimal way as, for example, a dependence of the resolution on the decay time itself is not considered. A better option is an event-dependent decay time model, where the resolution for each B_s^0 candidate is given by the estimated uncertainty σ_{t} of the decay time fit. A dependence of σ_{t} on the decay time would automatically be taken into account. The absolute scale of the estimated uncertainty from the decay time fit however does not necessary correspond to the true uncertainty and must be calibrated.

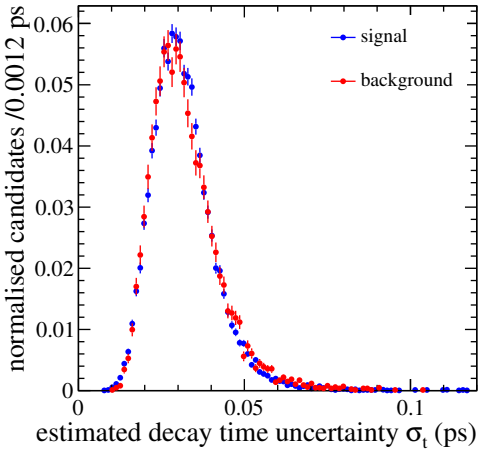

Figure 7.1: Estimated decay time uncertainty σ_t of selected $B_s^0 \to J/\psi\phi$ signal and background candidates.

For the presented thesis an event-dependent resolution model is chosen where a factor s_{σ_t} is determined to correct the absolute scale. The strategy to measure the scale factor s_{σ_t} uses $B_s^0 \to J/\psi\phi$ background candidates reconstructed from a prompt $J/\psi \to \mu^+\mu^-$ decay that is combined with two additional kaons from the primary vertex. As the J/ψ is produced directly in the pp interaction, the true decay time t_{true} of these reconstructed B_s^0 background candidates is exactly zero. However, due to the uncertainty in the reconstruction of the B_s^0 decay vertex position the measured decay time t is not exactly zero but will be distributed around $t = 0$. This distribution can be used to determine the resolution model. The width of the distribution is an estimate for the average decay time uncertainty σ_t^{av}. The deviation of the measured decay time of each candidate from zero can be used to calibrate the estimated uncertainty σ_t from the decay time fit and to determine the corresponding scale factor s_{σ_t}.
In order to select background candidates with a prompt J/ψ, the requirement of a minimum B_s^0 decay time in the selection process (Table 5.3) needs to be removed. In addition only candidates can be used that are triggered by a decay time independent trigger line to avoid distortions of the decay time distribution. Figure 7.2 shows the measured decay time distribution of the candidates that fulfill these requirements. The distribution contains a large peak around $t = 0$ which represents the prompt background candidates reconstructed from prompt J/ψ decays and a tail to longer decay times given by the $B_s^0 \to J/\psi\phi$ signal candidates and additional background from decays with long lifetimes (long-living background).

The method of calibrating the estimated decay time uncertainty σ_t with the prompt background candidates however requires that the scale factor of the calibration can be translated from the prompt background events to the signal candidates with long

lifetimes. This assumption can be checked with simulated events, where the true decay time uncertainty of signal $B_s^0 \to J/\psi\phi$ candidates is known.

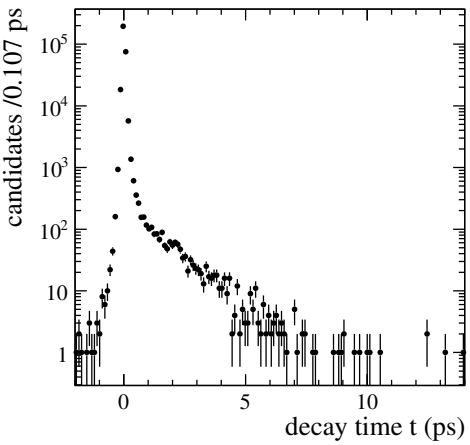

Figure 7.2: Decay time distribution for selected $B_s^0 \to J/\psi\phi$ candidates without applying decay time related cuts in selection or trigger. The large peak at $t = 0$ represents background candidates reconstructed from prompt J/ψ.

7.2 Time resolution in simulation

In order to test the assumption that background candidates reconstructed from prompt J/ψ can be used to calibrate the estimated decay time uncertainty σ_t for $B_s^0 \to J/\psi\phi$ signal candidates, the resolution model is determined with simulated events for both kind of candidates. The calibration of the estimated decay time uncertainty σ_t can be done by comparing σ_t to the true decay time uncertainty δt. For simulated events, the true decay time uncertainty for each $B_s^0 \to J/\psi\phi$ candidate can easily be determined by calculating the difference of the reconstructed decay time t and the generated, true decay time t_{true}:

$$\delta t = t - t_{\text{true}} \,. \tag{7.6}$$

Figure 7.3 shows the distribution of $\delta t/\sigma_t$ for $B_s^0 \to J/\psi\phi$ signal candidates and prompt background candidates. The width of the distribution determines the scale factor s_{σ_t} that is needed to correct the scale of the estimated decay time uncertainty σ_t. In case the true decay time uncertainty is Gaussian distributed and the estimated uncertainty is calibrated correctly, the distribution of $\delta t/\sigma_t$ should be as well Gaussian with width equal to one.
However, a Gaussian model with a single width s_{σ_t} is found to be not sufficient to describe the tails of the $\delta t/\sigma_t$ distribution. Therefore a model consisting of a sum of two

Gaussian functions with common mean μ, two widths $s_{\sigma_t,1}$, $s_{\sigma_t,2}$ and a relative fraction f_1 is used. The fit results are given in Table 7.1. For both event types the estimated decay time uncertainty seems to underestimate the true decay time uncertainty ($s_{\sigma_t,i} > 1$).

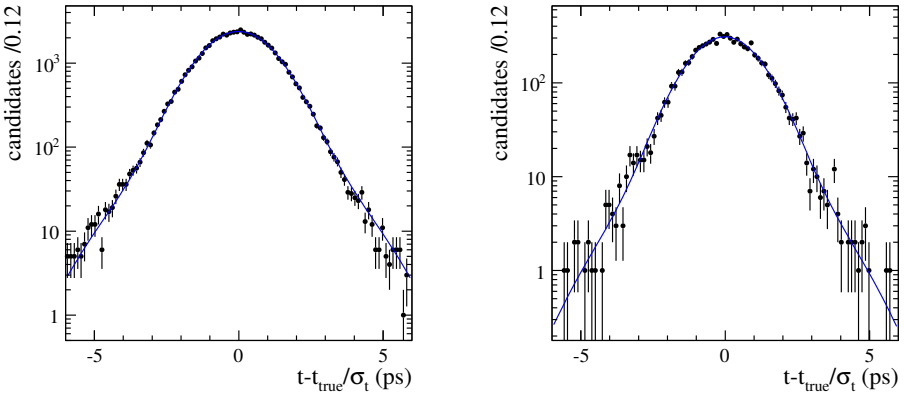

(a) $B_s^0 \to J/\psi\phi$ signal (b) prompt J/ψ background

Figure 7.3: Distribution of true decay time resolution δt divided by estimated decay time uncertainty σ_t of simulated $B_s^0 \to J/\psi\phi$ signal candidates and simulated prompt background candidates containing a true J/ψ.

parameter	$B_s^0 \to J/\psi\phi$	prompt J/ψ
$\mu(ps)$	-0.014 ± 0.005	-0.014 ± 0.014
f_1	0.877 ± 0.016	0.885 ± 0.040
$s_{\sigma_t,1}$(ps)	1.138 ± 0.010	1.102 ± 0.024
$s_{\sigma_t,2}$(ps)	2.071 ± 0.068	2.007 ± 0.179

Table 7.1: Results of fit to $\frac{\delta t}{\sigma_t}$ distribution of simulated $B_s^0 \to J/\psi\phi$ signal candidates and background candidates containing a prompt J/ψ.

To compare the effect of the two different calibration results of signal and prompt background candidates on the CP asymmetry measurement in data, the corresponding dilutions D_{res} need to be evaluated. The dilution expected from an event-dependent double Gaussian resolution model with fractions f_i and widths $s_{\sigma_t,i} \cdot \sigma_t$ is similar to Equation 7.4 given by

$$D_{\text{res}} = \frac{1}{N_{\text{ev}}} \sum_{j}^{N_{\text{ev}}} \sum_{i=1}^{2} f_i \exp\left(\frac{-\Delta m_s^2 \cdot (s_{\sigma_t,i}\, \sigma_{t,j})^2}{2}\right). \tag{7.7}$$

D_{res} is calculated by averaging over N_{ev} measured B_s^0 candidates with estimated uncertainty $\sigma_{\text{t},j}$. Using the parameters from Table 7.1, the calibration obtained from simulated signal decays gives a dilution of 0.783 ± 0.006 while the dilution obtained from the calibration with prompt background events is 0.759 ± 0.016. The small difference between the dilutions must be considered when calibrating the estimated decay time uncertainty σ_{t} of $B_s^0 \to J/\psi\phi$ signal candidates with prompt background events in data.

To quantify better the difference in the calibration of σ_{t} for signal and prompt background candidates, the determined double Gaussian models with two scale factors $s_{\sigma_{\text{t}},1}$ and $s_{\sigma_{\text{t}},2}$ can be translated to effective single Gaussian resolution models with only one scale factor $s_{\sigma_{\text{t}}}$. This is possible as, for the CP violation measurement, the actual choice of the resolution model does not matter as long as the resulting dilution D_{res} is the same. In fact, it was checked in previous studies [65], that neither of the physics parameters determined in this analysis, is biased by translating the obtained resolution model to an effective single Gaussian model with the same dilution. The single Gaussian scale factor $s_{\sigma_{\text{t}}}$ can hence be determined, by requiring

$$\frac{1}{N_{\text{ev}}} \sum_{j}^{N_{\text{ev}}} \exp\left(\frac{-\Delta m_{\text{s}}^2 \cdot (s_{\sigma_{\text{t}}} \sigma_{\text{t},j})^2}{2}\right) = \frac{1}{N_{\text{ev}}} \sum_{j}^{N_{\text{ev}}} \sum_{i=1}^{2} f_i \exp\left(\frac{-\Delta m_{\text{s}}^2 \cdot (s_{\sigma_{\text{t}},i}\, \sigma_{\text{t},j})^2}{2}\right). \tag{7.8}$$

For the model obtained from simulated signal events one obtains an effective single Gaussian scale factor $s_{\sigma_{\text{t}}} = 1.262 \pm 0.021$ and for simulated prompt background events $s_{\sigma_{\text{t}}} = 1.214 \pm 0.048$. The small difference between the individual scale factors represents the difference in the dilutions from the resolution models of the two event types. Although the single Gaussian scale factors themselves agree within their statistical uncertainties, a small difference in the order of ~ 0.05 is possible.
As a conclusion, the prompt background events can be used to determine the resolution model for signal $B_s^0 \to J/\psi\phi$ candidates in data. A possible bias of ~ 0.05 in the scale factor of the estimated decay time uncertainty must, however, be considered in the determination of ϕ_{s}.

7.3 Time resolution in data

The scale factor $s_{\sigma_{\text{t}}}$ of the estimated decay time uncertainty is determined on data by fitting a resolution model to the decay time distribution of B_s^0 background candidates reconstructed from prompt J/ψ. The true decay time of these candidates is known to be zero. The decay time distribution of all selected B_s^0 candidates, shown in Figure 7.2, however contains also contributions from background candidates without a true $J/\psi \to \mu^+\mu^-$ decay. These non-J/ψ background candidates have to be subtracted before fitting the resolution model. The subtraction is done on a statistical basis by assigning weights to each B_s^0 candidate. The weights are calculated, using the sWeight technique, [66] as follows:

- First a fit to the J/ψ mass distribution of all selected B_s^0 candidates is performed, shown in Figure 7.4. The shape of the J/ψ mass peak is determined by the detector resolution and the radiative tails of the resonance and can be described by a Crystal-Ball function [60]. The non-J/ψ background component is modeled with an exponential function.

- For each candidate an *sWeight* is calculated, using the relative fraction of the fitted signal and background functions at the candidates reconstructed J/ψ mass[1]. These weights are constructed such that a candidate which is more likely to be signal gets a larger weight and events that are likely to be background a smaller or even negative weight.

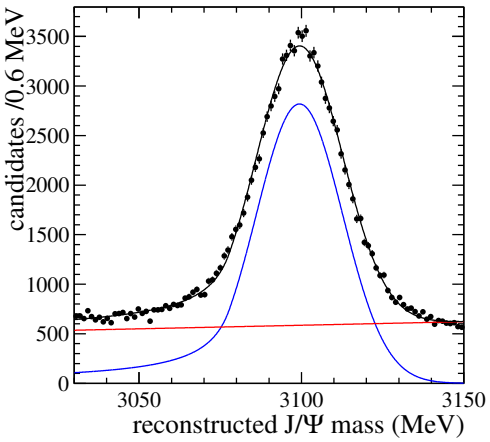

Figure 7.4: Invariant J/ψ mass distribution of selected $B_s^0 \to J/\psi\phi$ candidates. The distribution is fitted by a Crystal-Ball function for the signal component (blue) and a linear function for the background component (red).

[1]For a candidate with mass m the weight is given by

$$w(m) = \frac{V_{s,s} f_s(m) + V_{s,b} f_b(m)}{N_s f_s(m) + N_b f_b(m)}, \tag{7.9}$$

where f_s, f_b is the value of the fitted signal and background function evaluated at mass m and N_s, N_b are the number of signal and background candidates determined in the mass fit. $V_{s,s}$ and $V_{s,b}$ are covariance matrix elements, given by

$$V_{s,s}^{-1} = \sum_{i=1}^{N} \frac{f_s(m) f_s(m)}{(N_s f_s(m) + N_b f_b(m))^2}, \quad V_{s,b}^{-1} = \sum_{i=1}^{N} \frac{f_s(m) f_b(m)}{(N_s f_s(m) + N_b f_b(m))^2} \tag{7.10}$$

where N is the number of signal plus background candidates.

The decay time distribution after subtracting the non-J/ψ background candidates is shown in Figure 7.5 and contains only B_s^0 candidates reconstructed from true J/ψ. It consists of candidates reconstructed from prompt J/ψ from the primary vertex, long-living background candidates containing a true J/ψ and signal $B_s^0 \to J/\psi\phi$ candidates.

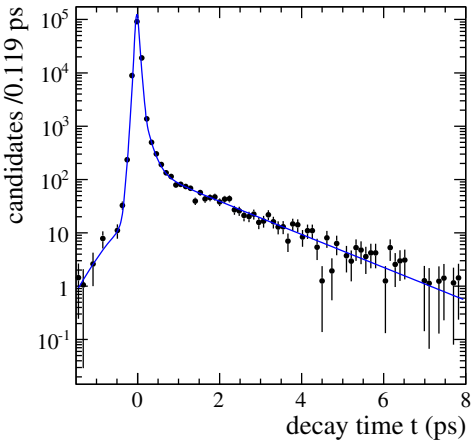

Figure 7.5: Decay time distribution of background candidates containing a true J/ψ, overlaid with a fitted function to extract the time resolution (Equation 7.12).

The physical decay time distribution of the prompt candidates is given by a delta-function at $t = 0$. The distribution of long-living $B_s^0 \to J/\psi\phi$ signal and background candidates can be effectively modeled with a sum of two exponential functions $L(t|f_{\mathrm{LL}}, \tau_{\mathrm{LL},1}, \tau_{\mathrm{LL},2})$ with slopes $\tau_{\mathrm{LL},1}$ $\tau_{\mathrm{LL},2}$ and relative fraction f_{LL}. Both components are convoluted with an event-dependent resolution model. The description of the long tail to negative decay times in Figure 7.5 requires a resolution model consisting of a sum of three Gaussian functions $G(t - t', \sigma_{\mathrm{t}}|s_{\sigma_{\mathrm{t}},i}, \mu)$ with

$$G(t - t', \sigma_{\mathrm{t}}|s_{\sigma_{\mathrm{t}},i}, \mu) = \frac{1}{\sqrt{2\pi} s_{\sigma_{\mathrm{t}},i}\, \sigma_{\mathrm{t}}} \exp \frac{-(t - t' - \mu)}{2(s_{\sigma_{\mathrm{t}},i}\, \sigma_{\mathrm{t}})^2}\,, \tag{7.11}$$

and scale factors $s_{\sigma_{\mathrm{t}},i}$ for the estimated decay time uncertainty σ_{t} and common mean μ. The model to describe the decay time distribution of the B_s^0 candidates, reconstructed from true J/ψ (Figure 7.5), is then given by

$$\begin{aligned} p(t, \sigma_{\mathrm{t}}|s_{\sigma_{\mathrm{t}},i}) =& f_{\mathrm{pr}} \cdot \delta(t) \otimes \left(\sum_{i=1}^{3} f_i G(t, \sigma_{\mathrm{t}}|s_{\sigma_{\mathrm{t}},i}, \mu) \right) \\ &+ (1 - f_{\mathrm{pr}}) \cdot L(t|f_{\mathrm{LL}}, \tau_{\mathrm{LL},1}, \tau_{\mathrm{LL},2}) \otimes \left(\sum_{i=1}^{3} f_i G(t, \sigma_{\mathrm{t}}|s_{\sigma_{\mathrm{t}},i}, \mu) \right), \end{aligned} \tag{7.12}$$

where the f_i are the absolute fraction of the Gaussian functions and $f_{\rm pr}$ is the relative fraction between prompt and long-living candidates. The parameters obtained from the fit are listed in Table 7.2.

parameter	fit result
$f_{\rm pr}$	0.946 ± 0.003
$f_{\rm LL}$	0.490 ± 0.027
$\tau_{\rm LL,1}(ps)$	0.154 ± 0.021
$\tau_{\rm LL,2}(ps)$	1.425 ± 0.060
$\mu(ps)$	-0.0041 ± 0.0003
f_1	0.788 ± 0.039
f_2	0.208 ± 0.038
s_1	1.257 ± 0.024
s_2	2.179 ± 0.106
s_3	8.82 ± 1.10

Table 7.2: Results of fit to decay time distribution of B_s^0 background candidates containing a true J/ψ, using Equation 7.12.

Similar to the study with simulated events one can compute the dilution of the CP asymmetry introduced by this resolution model and it is found to be 0.714 ± 0.015. The scale factor $s_{\sigma_{\rm t}}$ for a corresponding effective single Gaussian resolution model with the same dilution can be calculated analog to Equation 7.8 and is found to be $s_{\sigma_{\rm t}} = 1.467 \pm 0.048$. In addition, it can be observed that there is a small bias of the measured decay time, represented by the deviation of the Gaussian mean from zero. Such a shift is expected to have only a small effect on the measurement of the CP violation parameters and it will be considered in the systematic uncertainties.

For the measurement of $\phi_{\rm s}$, the effective single Gaussian model is used to describe the decay time resolution effects. As discussed in the previous section it was verified that this simplification does not lead to a bias in the measured physics parameters. The observed difference between simulated prompt background and signal candidates will be considered as uncertainty on the scale factor $s_{\sigma_{\rm t}}$.
From the scaled decay time uncertainties ($s_{\sigma_{\rm t}} \cdot \sigma_{\rm t}$) of the selected $B_s^0 \to J/\psi\phi$ signal candidates, an effective average decay time resolution $\sigma_t^{\rm av}$ can be calculated

$$\sigma_t^{\rm av} = \frac{1}{N_{\rm ev}} \sum_j s_{\sigma_{\rm t}} \cdot \sigma_{{\rm t}j} \,. \tag{7.13}$$

It is determined to be $\sigma_t^{\rm av} = 46.4 \pm 1.6\,{\rm fs}$.

CHAPTER 8

Detector acceptances

The physics parameters measured in this analysis are extracted from the decay time and angular distributions of $B_s^0 \to J/\psi\phi$ decays. These distributions can be distorted by detector, reconstruction and selection effects. In order to get the correct results, it is important to understand and correct for these effects, which can be expressed by so called acceptance functions. The following chapter will address the studies that were performed to determine and understand the acceptance corrections for the reconstructed decay time and angles.

8.1 Angular acceptance

The angular acceptance describes the effect of the detector geometry, the trigger, reconstruction and offline selection on the measured angular distributions of $B_s^0 \to J/\psi\phi$ decays. It is given by the ratio between selected and originally produced B_s^0 candidates

$$\varepsilon(\Omega) = \frac{\text{number of selected } B_s^0(\Omega)}{\text{number of produced } B_s^0(\Omega)} \,. \tag{8.1}$$

Here, $\varepsilon(\Omega) = \varepsilon(\cos\theta_\mathrm{k}, \cos\theta_\mu, \varphi_\mathrm{h})$ denotes the angular acceptance as a function of the helicity angles. It is necessary to use a three-dimensional description of the acceptance, as the decay angles are highly correlated. Figure 8.1 shows two-dimensional correlation plots of the helicity angles for simulated $B_s^0 \to J/\psi\phi$ decays where clear structures are visible.

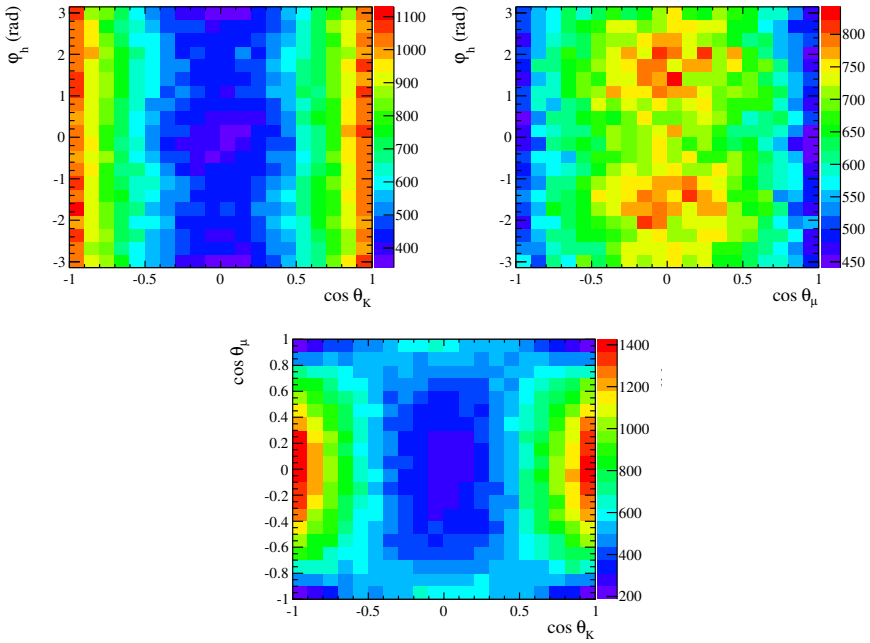

Figure 8.1: Two-dimensional correlation plots of the helicity angles for simulated $B_s^0 \to J/\psi\phi$ decays.

There is no way to determine the angular acceptance directly with measured events as the real angular distributions of the produced $B_s^0 \to J/\psi\phi$ decays is not known. In fact the polarisation amplitudes that determine this distribution are supposed to be measured in this analysis. Therefore one has to completely rely on the simulation to correctly describe the angular acceptance shape. In first order a correct description of the polarisation amplitudes in the simulation is not necessary, as the angular acceptance is determined differentially in the three helicity angles.
The simulated $B_s^0 \to J/\psi\phi$ event sample which was introduced in Chapter 5 has already geometric cuts applied in the generation of the events which would bias the denominator of Equation 8.1. Instead, the theoretical distribution used in the generation of the events is used, to normalise the selected events:

$$\varepsilon(\Omega_i) = \frac{\text{number of selected } B_s^0(\Omega_i)}{N \int \mathrm{d}t \int\limits_{\Omega_i} \mathrm{d}\Omega \; s(t, \Omega|\vec{\lambda}_{\text{phys}})} \,. \tag{8.2}$$

N is the total number of selected events and $s(t, \Omega|\vec{\lambda}_{\text{phys}})$ is the theoretical decay distribution, that is defined by the differential decay rates of produced B_s^0 and produced $\overline{B}_s^0$ as introduced in Chapter 2:

$$s(t, \Omega|\vec{\lambda}_{\text{phys}}) = \frac{1}{2}\frac{\mathrm{d}\Gamma(B_s^0 \to J/\psi\phi)}{\mathrm{d}t\mathrm{d}\Omega} + \frac{1}{2} \cdot \frac{\mathrm{d}\Gamma(\overline{B}_s^0 \to J/\psi\phi)}{\mathrm{d}t\mathrm{d}\Omega} \,. \tag{8.3}$$

$\vec{\lambda}_{\rm phys}$ denotes all decay parameters given in Table 3.1. In order to get the number of produced B_s^0 in bin i, $s(t, \Omega|\vec{\lambda}_{\rm phys})$ is integrated over the decay time and the corresponding Ω_i range.
Figure 8.2 shows the one-dimensional projections of the three-dimensional acceptance histogram $\varepsilon(\Omega_{\rm i})$ on the decay angles $\varphi_{\rm h}$, $\cos\theta_\mu$, $\cos\theta_{\rm k}$. The projections are normalised to the number of selected $B_s^0 \to J/\psi\phi$ candidates[1]. A completely flat histogram would mean that the measured decay angle distribution is identical to the real distribution and there would be no need to apply any correction. The largest deviation from a flat acceptance is $10 - 15\%$ and can be seen in the $\cos\theta_\mu$ dimension. In the $\varphi_{\rm h}$ dimension on the other hand there seem to be only very small acceptance corrections necessary. The effects that cause this specific shape of the angular acceptance will be discussed in the next section.

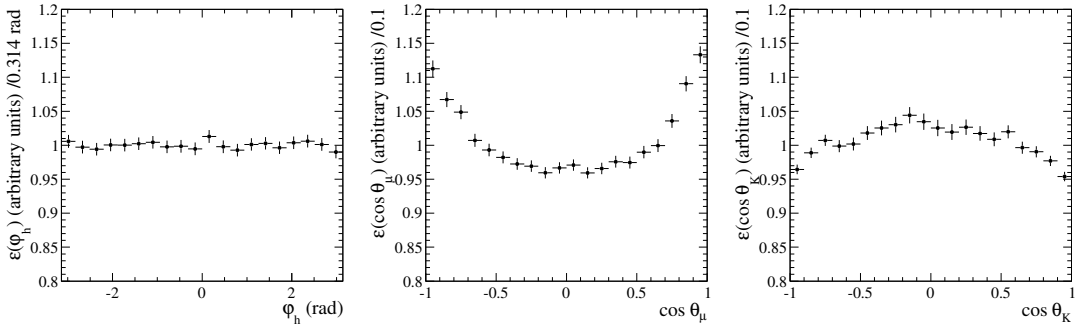

Figure 8.2: One-dimensional projections of the three-dimensional angular acceptance histogram, determined with simulated $B_s^0 \to J/\psi\phi$ events according to Equation 8.2.

8.1.1 Origin of the angular acceptance shape

A priori it is not clear how well the simulation reproduces the acceptance effects in data. In order to verify this, one first has to understand which effects are responsible for the existing acceptance loss. This can be done in the simulation by studying step-by-step each cut that is introduced in the reconstruction process.

The fully simulated $B_s^0 \to J/\psi\phi$ event sample, available to calculate the acceptance correction, has already several cuts applied that could influence the angular distributions. Therefore it is necessary to produce a new simulated event sample without any geometry or selection cuts on the signal decay. In order to save CPU time the complete detector simulation was switched off and only the physical processes were generated.

[1]The absolute scale of the acceptance, given by the ratio between all selected and generated $B_s^0 \to J/\psi\phi$ candidates, is $\varepsilon = 1.6\%$.

In the following this simulated $B_s^0 \to J/\psi\phi$ event sample will be denoted as *generator level simulation*. By definition the acceptance histogram calculated with this sample (according to Equation 8.2) should then be exactly flat in all three decay angles. This cross-check is shown in Figure 8.3 compared to the acceptance obtained with the fully simulated events.

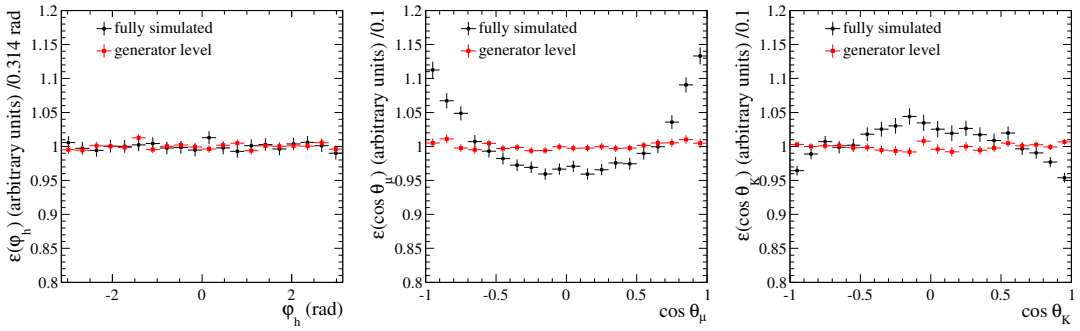

Figure 8.3: Angular acceptance projections of generator level events (red) compared to fully simulated events after the full selection (black).

In the following the generator level sample is used to reproduce the effects of the reconstruction and selection process on the $B_s^0 \to J/\psi\phi$ signal decay:

- The stable decay products of the $B_s^0 \to J/\psi\phi$ decay, the kaons and muons, need to be produced inside the geometrical acceptance of the LHCb detector in order to be measured. Therefore the first obvious constraint is a requirement on the polar angle Θ of the muon and kaons from the $B_s^0 \to J/\psi\phi$ signal decays of $10\,\text{mrad} < \Theta < 400\,\text{mrad}$. Figure 8.4 shows the resulting acceptance projection. They are compared to the histogram determined from fully simulated events after the full selection (as shown also in Figure 8.2). It can be seen that already the specific geometrical shape of the detector is responsible for a large part of the final acceptance corrections in the $\cos\theta_\mu$ dimension. On contrast the acceptance in the other two angle dimensions is hardly influenced by the detector geometry.

- The second effect originates from the fact that charged particles, in order to be reconstructed, must have a minimum momentum to pass the magnetic field in the detector and reach the tracking stations. Figure 8.5 shows the momentum distributions of kaons from generator level and fully simulated $B_s^0 \to J/\psi\phi$ decays, that pass the full reconstruction and selection. The purely physical momentum spectrum of the generator level events starts at lower values than the one of the fully simulated reconstructed kaons. In fact, the threshold introduced by the magnetic field is not at a sharp momentum value but modifies smoothly the shape of the spectrum in the low momentum region. It is therefore not easy to place a simple

momentum cut on the generator level simulation to reproduce this effect. In order to determine the effect, the generator level $B_s^0 \to J/\psi\phi$ decays were weighted such that they reproduce the kaon and muon momentum distribution of the fully simulated and selected particles. This procedure does not only account for the magnetic field threshold but also for trigger or selection requirements that implicitly influence the momentum distribution (e.g. the $\Delta \ln \mathcal{L}_{K\pi}$). A new angular acceptance histogram is calculated from the weighted events, still applying the polar angle cut introduced before. The projections are shown in Figure 8.6, again compared to the nominal acceptance correction from the fully simulated selected events. The acceptance shape in all three dimensions is now nicely reproduced by the generator level decays.

In summary, this means that only the geometrical form of the detector, the momentum threshold in the reconstruction and selection cuts that influence the momentum distribution of the $B_s^0 \to J/\psi\phi$ final state particles are responsible for the existing acceptance corrections. Impacts of other trigger or selection criteria have been studied and found to be negligible.

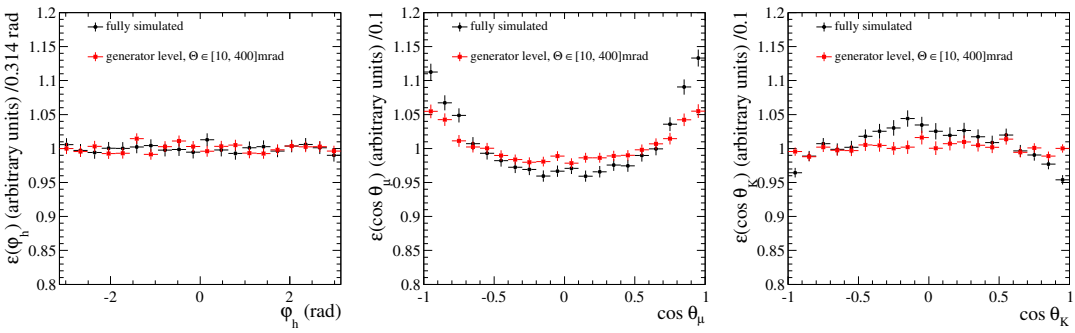

Figure 8.4: Angular acceptance projections of generator level events with polar angle cut (red) compared to fully simulated events after the full selection (black).

8.1.2 Verification of acceptance determination

In the last section it was shown that the specific shape of the angular acceptance is determined by the geometry of the detector and implicit momentum requirements on the final state particles. To be able to use the simulated acceptance in the analysis, one has to make sure that both, the detector geometry and the effects on the momentum, are properly described in the simulation. This can be done by comparing the polar angle and momentum distribution of kaons and muons from simulated $B_s^0 \to J/\psi\phi$ decays and measured signal decays. The corresponding histograms are shown in Figure 8.7 for the positively charged muons and kaons in the decay. It was verified that the

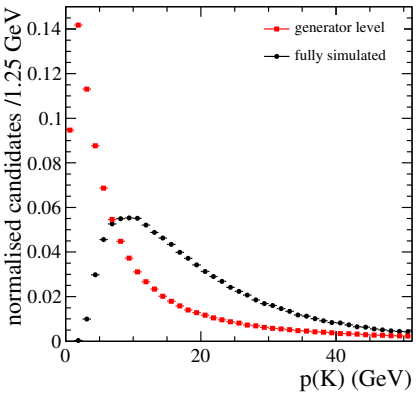

Figure 8.5: Momentum distributions of kaons from generator level events (red) compared to fully simulated events after the full selection (black).

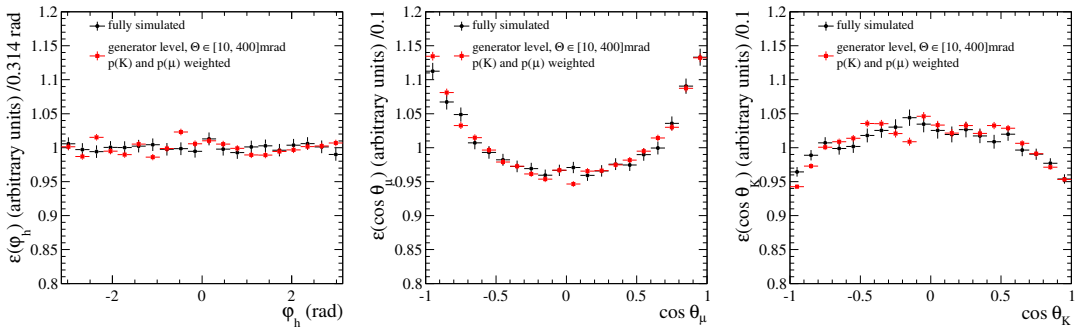

Figure 8.6: Angular acceptance projections of weighted generator level events with polar angle cut (red) compared to fully simulated events after the full selection (black).

negatively charged particles show an identical behaviour. From the histograms one can see that the shapes of both the muon and kaon spectra are different in the simulation. To estimate the effect of the differences on the acceptance corrections, the polar angle and momentum spectra of the simulated kaons and muons are reweighted to reproduce the data distributions. The momentum spectra of μ^- and μ^+, as well as of K^- and K^+, are correlated as their kinematics are determined from the J/ψ and ϕ, respectively. Therefore the weighting is done in two dimensions for μ^-, μ^+ and K^-, K^+. From the reweighted simulation, new acceptance corrections are calculated and the corresponding histograms can be seen in Figure 8.8. The correction of the kaon momenta distribution has by far the largest impact on the angular acceptance. The muon momenta and the polar angle differences have only little effect.
The obtained differences in the spectra between data and simulated events can be

caused either by a different angular acceptance or by different physics parameters in the simulation. The kaon momentum for example is correlated with the decay angle $\cos\theta_k$. Figure 8.9 shows $\cos\theta_k$ as a function of the K^+ and K^- momenta. A clear dependence of the momentum distribution on the decay angle is visible which is different for positively and negatively charged kaons. As the decay angle distribution is determined by the polarisation amplitudes, the kaon momentum distribution can vary for different values of the polarisation amplitudes. This means that the disagreement of the kaon momentum spectra can partially be due to different polarisation amplitudes in data and simulation.
Without disentangling the effect of different polarisation amplitudes from true differences in the angular acceptance of data and simulation, the reweighted acceptance can not be used in the analysis. Instead the nominal acceptance is used and systematic uncertainties are assigned to the measured parameters, depending on the observed differences. The exact procedure of this will be discussed in Chapter 12.

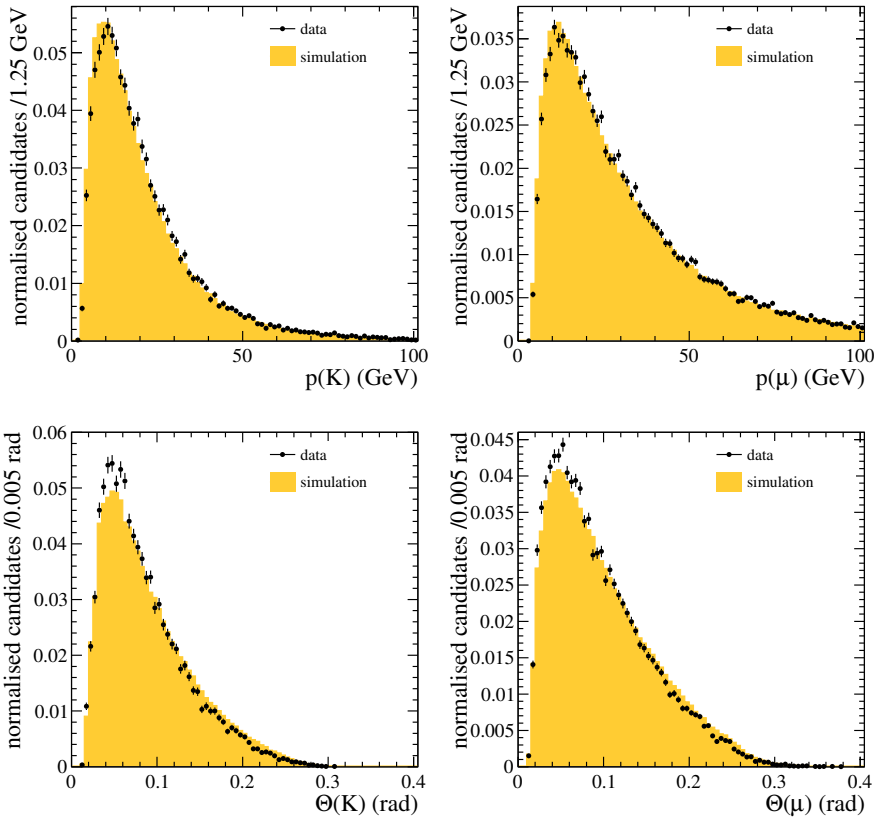

Figure 8.7: Polar angle and momentum distributions for muons and kaons from measured (black) and simulated (yellow) $B_s^0 \to J/\psi\phi$ decays. The data is background subtracted.

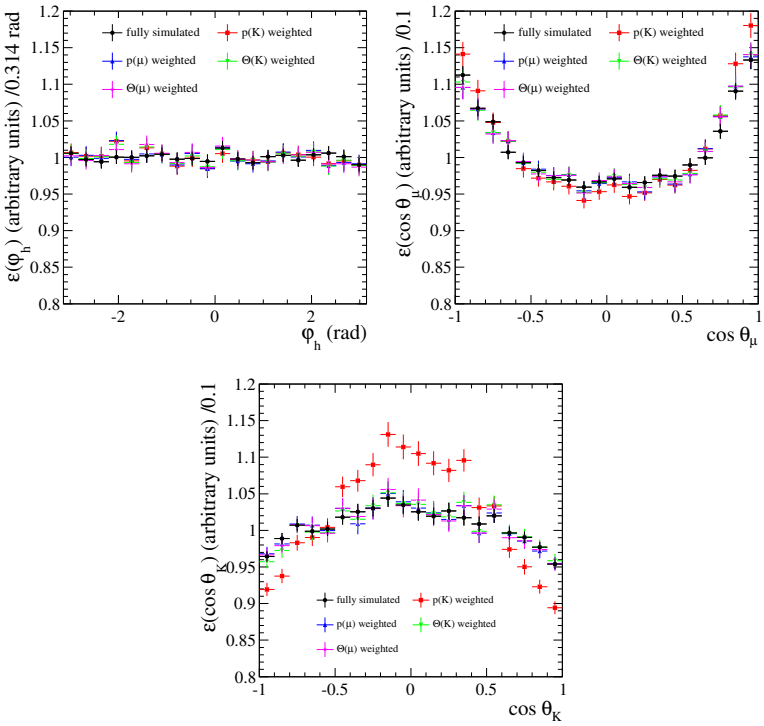

Figure 8.8: Angular acceptance projections of fully simulated events after reweighting the momentum distributions of kaons ($p(K)$), the momentum distributions of muons ($p(\mu)$), the polar angle distributions of kaons ($\Theta(K)$) and the polar angle distribution of muons ($\Theta(\mu)$) to match the distributions in data.

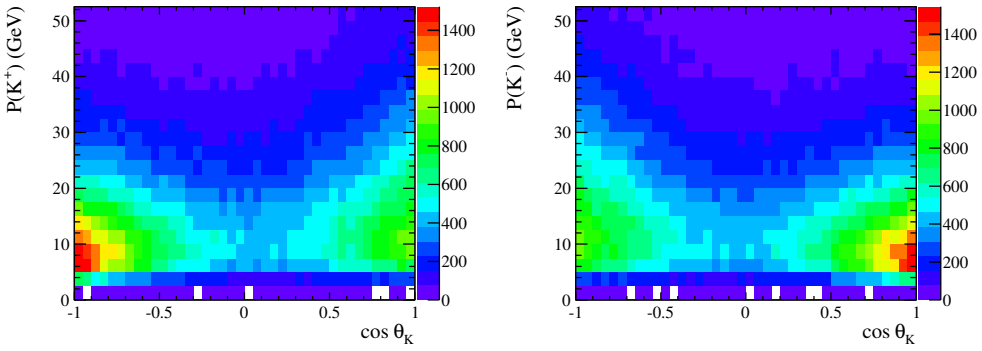

Figure 8.9: Correlation of $\cos\theta_k$ and momentum p for positively (left) and negatively (right) charged kaons from simulated selected $B_s^0 \to J/\psi\phi$ decays.

8.2 Decay time acceptance

A decay time acceptance function is needed to correct the observed decay time distribution for effects introduced by trigger, reconstruction and selection requirements. Similar to the angular acceptance function, the decay time acceptance is given as the ratio of selected to produced $B_s^0 \to J/\psi\phi$ decays for a certain decay time t:

$$\varepsilon(t) = \frac{\text{number of selected } B_s^0(t)}{\text{number of produced } B_s^0(t)} \,. \tag{8.4}$$

In principle it is possible to determine $\varepsilon(t)$ from simulated events using Equation 8.4, similar to the angular acceptance. In the case of the decay time acceptance, one can however extract the corrections partially from the measured data with the advantage that there is no need to worry about the reliability of the simulation.
The main acceptance effect is introduced by the selection requirements applied in the HLT software trigger. These lead to inefficiencies in the selection of events with small decay times. All additional, time dependent acceptance effects in reconstruction and selection can be put into a single correction factor which has to be derived using both measured and simulated events. The two different methods will be discussed in the following sections and the corresponding acceptance corrections will be determined.

8.2.1 Decay time acceptance introduced by the trigger selections

The main distortion of the measured decay time distribution is introduced by requirements in the trigger selection. As was already indicated in Section 5.1, the whole data sample can be split in two subsamples: one with a decay time dependent selection in the first stage of the software trigger (HLT1-biased) and one without decay time dependent selection requirements (HLT1-unbiased). In the second stage of the software trigger (HLT2), however, the selection requirements influence the decay time distribution of both subsamples.
The acceptances are calculated separately for the two subsamples, rather than being split in a part describing the HLT1 and a part describing the HLT2 effects. The acceptances for both subsamples can be determined directly with measured data and the exact procedure will be discussed in the following.

Decay time acceptance for the HLT1-unbiased event sample

The HLT1-unbiased subsample consists of events that are triggered in the first software trigger stage by the *HLT1unbiased* line and in the second stage by the *HLT2biased* trigger line (see Section 5.1). The HLT1 selection does not introduce any distortion in the decay time distribution. The *HLT2biased* trigger line however requires a minimum decay length significance $\mathrm{DL}/\sigma_{\mathrm{DL}}$ of the online reconstructed J/ψ with respect to the primary vertex. Due to this, it is more likely to select B_s^0 candidates with a long decay time than candidates with a short decay time. In order to determine this effect

and to calculate the corresponding time acceptance corrections, one needs a sample of $B_s^0 \to J/\psi\phi$ decays that are selected without the requirement on the decay length significance.
In fact, there is a HLT2 trigger line (*HLT2unbiased*) available that introduces no acceptance effects in the decay time distribution of the selected events. It uses exactly the same selection requirements as the *HLT2biased* line, except for the requirement on the decay length significance. However, due to its high rate it was strongly prescaled during parts of the 2011 data taking period and is not taken into account in the default trigger strategy of this analysis.
The decay time acceptance introduced by the *HLT2biased* selection can be determined by dividing the decay time distribution of candidates that are triggered by both, *HLT2biased* and *HLT2unbiased*, by the decay time distribution of all candidates that are triggered by the *HLT2unbiased* line:

$$\varepsilon_{\text{HLT}}(t) = \frac{\textit{HLT1unbiased}\ \text{AND}\ \left(\textit{HLT2biased}\ \text{AND}\ \textit{HLT2unbiased}\right)}{\textit{HLT1unbiased}\ \text{AND}\ \left(\textit{HLT2unbiased}\right)}\,.$$

The resulting acceptance histogram is plotted in Figure 8.10(a). A small acceptance drop at low decay times is visible, introduced by the flight distance significance requirement. There is an additional drop at about 2 ps which results from a simplified primary vertex reconstruction in the trigger leading to an inefficiency for B_s^0 candidates with short decay time. Besides these two effects the time acceptance for the HLT2-unbiased event sample is basically flat.

Decay time acceptance for the HLT1-biased event sample

Events in the HLT1-biased subsample are triggered by one of the two decay time dependent lines *HLT1biasedA* or *HLT1biasedB* and subsequently in the second trigger stage by the *HLT2biased* trigger line. To avoid overlap with the HLT1-unbiased sample, it is required that the events are explicitly not triggered by the decay time independent line *HLT1unbiased*.
To accept an event, the selection in the HLT1 requires one track from the B_s^0 decay to have a minimum χ^2_{IP} with respect to the primary vertex. This means B_s^0 candidates with long decay times are preferred, as the resulting tracks have in general a larger distance to the primary vertex than tracks from B_s^0 decaying close to the interaction point.
The acceptance effects introduced by the *HLT2biased* line were already determined in the previous section. The resulting corrections could also be applied to this subsample. However, it is possible to directly model the combined decay time acceptance for events in this subsample by dividing their decay time distribution by the decay time distribution of candidates that pass a fully decay time independent trigger selection:

$$\varepsilon_{\text{HLT}}(t) = \frac{\left(\left[\textit{HLT1biasedA}\ \text{OR}\ \textit{HLT1biasedB}\right]\ \text{AND NOT}\ \textit{HLT1unbiased}\ \text{AND}\ \textit{HLT2biased}\right)}{\left(\textit{HLT1unbiased}\ \text{AND}\ \textit{HLT2unbiased}\right)}\,.$$

The corresponding histogram is shown in Figure 8.10(b). A significant smooth acceptance drop for low decay time is visible, reflecting the effects of the χ^2_{IP} requirement in the trigger selection.

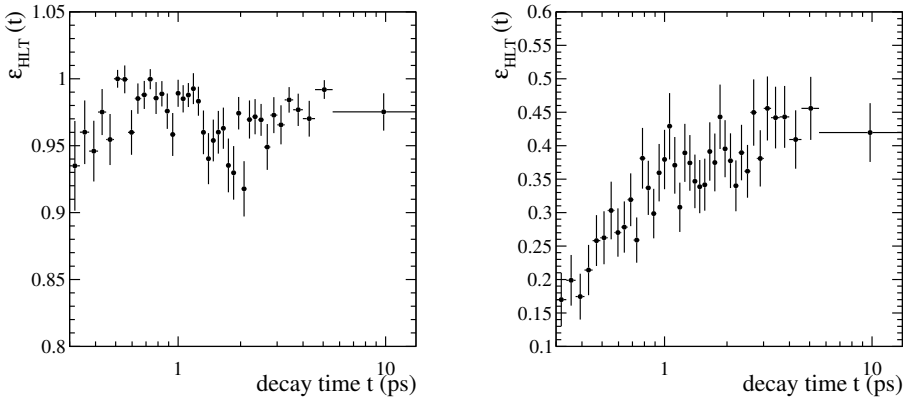

(a) HLT1-unbiased acceptance (b) HLT1-biased acceptance

Figure 8.10: Decay time acceptance for the (a) HLT1-unbiased and (b) HLT1-biased event sample. The x-axis is shown in a logarithmic scale.

Decay time acceptance for simulated events

The decay time acceptance for simulated $B^0_s \to J/\psi\phi$ candidates can be determined using the same method as in data. The resulting acceptance histograms for the simulated HLT1-unbiased and HLT1-biased subsamples are shown in Figure 8.11. Their shape is similar to the acceptance histograms determined with the measured event sample. The simulated acceptance histograms can be used to test the reliability of the method that is used to determine the acceptances in data. Fitting the decay time distribution of simulated $B^0_s \to J/\psi\phi$ candidates while taking into account the acceptance histograms in Figure 8.11 should give a lifetime that is identical to the generated lifetime of the events. This study will be done in Chapter 9.

8.2.2 Upper decay time acceptance

In addition to the trigger selection cuts, which mainly influence the decay time distribution at lower values, there is an additional acceptance drop at large decay times [67]. Figure 8.12 shows the ratio of selected to generated B^0_s signal decays as a function of the decay time. Only B^0_s candidates that are triggered by a decay time independent trigger line are used for the ratio. A linear efficiency drop is visible that can be parameterised by an acceptance function of the form

$$\varepsilon(t) = 1 + \beta t\,, \tag{8.5}$$

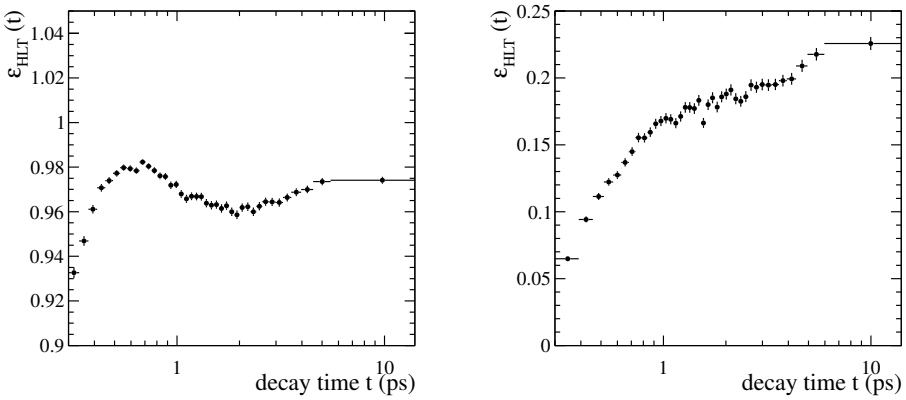

(a) HLT1-unbiased acceptance (b) HLT1-biased acceptance

Figure 8.11: Decay time acceptance for the (a) HLT1-unbiased and (b) HLT1-biased simulated event sample. The x-axis is shown in a logarithmic scale.

with the slope correction factor β. The observed acceptance drop is caused by a combination of several effects:

- The geometrical acceptance of the vertex detector leads to a dependence of the detection efficiency on the position of the B_s^0 production vertex and the kinematics of the decay products.
- The efficiency of the track reconstruction in the vertex detector depends on the transverse distance to the interaction point. Tracks originating from a long-living particle decay have in general a higher distance and therefore a lower reconstruction efficiency.
- The simplified track reconstruction in the trigger leads to a different trigger efficiency for long- and short living B_s^0 candidates. This effect is not yet included in the lower decay time acceptance discussed the section before.
- Several requirements in the offline selection introduce biases in the decay time distribution.

The exact value of the correction factor β can be determined partially on data and partially using simulated events. It was determined to be $\beta = (-8.3 \pm 4.0)10^{-3}\,\mathrm{ps}^{-1}$ for $B_s^0 \to J/\psi\phi$ decays. The effect is with $\sim 1\%$ small compared to the acceptance losses introduced in the trigger. A more detailed description of the upper decay time acceptance and the determination of β can be found in [67].

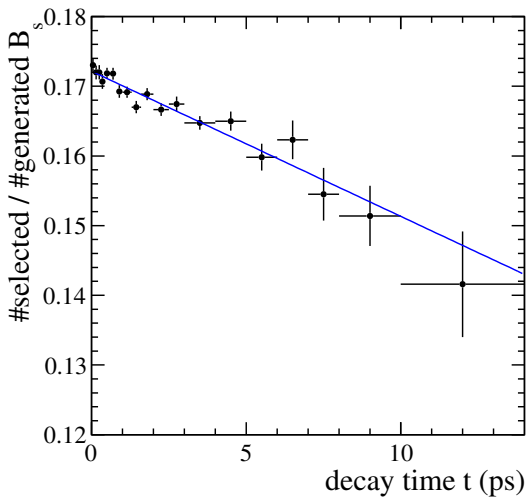

Figure 8.12: Ratio of selected to generated $B_s^0 \to J/\psi\phi$ signal candidates as a function of the decay time. The linear acceptance drop is parameterised with a function $\varepsilon(t) \propto (1 + \beta t)$.

CHAPTER 9

Determination of the physics observables

The physics parameters are extracted from a four-dimensional maximum likelihood fit to the measured decay time and angular distributions. This requires the modeling of the distributions with theoretical functions that need to be corrected for acceptance and resolution effects. The basic concepts of a maximum likelihood estimation and the specific implementation for this analysis will be explained in the following chapter. Two different fitting techniques, distinguished by the treatment of the background component, will be discussed.

9.1 The Maximum Likelihood Estimation

The maximum likelihood method is a technique to estimate a set of parameters $\vec{\lambda}$ from a given datasample $\vec{x}_1, ...\vec{x}_N$ with N number of events. In general each event $\vec{x}_i$ itself is a set of several measured quantities.
Assuming the data is described by a theoretical function $p(\vec{x}|\vec{\lambda})$ depending on $\vec{\lambda}$, one can construct a probability density function (PDF) by requiring the normalisation condition

$$\int_D p(\vec{x}|\vec{\lambda})\mathrm{d}\vec{x} = 1\,, \tag{9.1}$$

where D denotes the domain of $\vec{x}$. Then, $p(\vec{x}|\vec{\lambda})$ gives for each parameter value the probability of a measurement in the interval $[\vec{x} + \mathrm{d}\vec{x}]$.

The likelihood function is defined as the product of the probability densities for all events in the datasample

$$\mathcal{L}(\vec{\lambda}) = \prod_{i}^{N} p(\vec{x}_i|\vec{\lambda}) \tag{9.2}$$

and corresponds to the probability that the datasample $\vec{x}_1, ...\vec{x}_N$ is produced, given the parameters $\vec{\lambda}$. Maximising the likelihood function by varying the values of $\vec{\lambda}$ maximises this probability. More details of the maximum likelihood principle can be found in [68].
In practice one usually minimises the negative logarithm of the likelihood to avoid huge likelihood values:

$$-\ln \mathcal{L}(\vec{\lambda}) = -\sum_{i}^{N} \ln p(\vec{x}_i|\vec{\lambda})\,. \tag{9.3}$$

The minimisation process in this analysis is technically done with the program MINUIT [69]. The basic implementation of the fitting algorithm was developed for a previous analysis [53] and is adopted and extended for the here presented measurement.

9.1.1 Properties of the maximum likelihood fit

Several techniques are used in this analysis:

Conditional probability

The probability density function used to describe the datasample can depend conditionally on several event quantities $\vec{\sigma}$:

$$p(\vec{x}|\vec{\lambda};\vec{\sigma})\ . \tag{9.4}$$

In order to get a non-conditional probability the likelihood must include the probability density function for $\vec{\sigma}$ [70]:

$$\mathcal{L}(\vec{\lambda}) = \prod_{i}^{N} p(\vec{x}_i;\vec{\sigma}_i|\vec{\lambda}) = \prod_{i}^{N} p(\vec{x}_i|\vec{\lambda};\vec{\sigma}_i)\cdot p(\vec{\sigma}_i|\vec{\lambda})\,. \tag{9.5}$$

Examples for conditional event quantities are the decay time resolution or the mistag probability.

Constraining parameters

In some cases a previous measurement of a parameter λ_j exists, constraining its true value to an interval $\pm\sigma$ around a central value μ. Assuming the probability to measure

a value of λ_j is Gaussian distributed around the central value, one can transfer this constraint to the likelihood function

$$\mathcal{L}(\vec{\lambda}) = \prod_i^N p(\vec{x}_i|\vec{\lambda}) \cdot p(\lambda_j)\,, \tag{9.6}$$

where $p(\lambda_j) = \frac{1}{\sqrt{2\pi}\sigma} e^{-\frac{(\lambda_i-\mu)^2}{2\sigma^2}}$. This is called a Gaussian constraint and will be used for example for the calibration parameters of the mistag probability. In case of a simultaneous constraint of n parameters $\vec{\lambda}_j$, and taking into account their relative correlations, a multivariate Gaussian function is needed:

$$p(\vec{\lambda}_j) = \frac{1}{(2\pi)^{n/2}|\Sigma|^{1/2}} e^{-\frac{1}{2}(\vec{\lambda}_j-\vec{\mu})^T\Sigma^{-1}(\vec{\lambda}_j-\vec{\mu})}\,. \tag{9.7}$$

$\vec{\mu}$ is the vector of central values and Σ the covariance matrix defined as $\Sigma_{kl} = \rho_{kl}\sigma_k\sigma_l$ with relative parameter correlations ρ_{kl}.

Parameter errors

For large number of events the maximum likelihood estimation is unbiased, meaning that the expectation value of the parameters is equal to their true value. The probability distribution of the estimated parameters is Gaussian. Then the error of a parameter λ_j is given by

$$\sigma_j = \sqrt{-\left(\frac{\mathrm{d}^2 \ln \mathcal{L}}{\mathrm{d}\lambda_j^2}\right)^{-1}}\,. \tag{9.8}$$

where the second derivative is taken at the value of λ_j that maximises the likelihood function.

Likelihood ratio method

The likelihood ratio method can be used to obtain confidence intervals for a set of parameters. According to the central limit theorem every likelihood function becomes Gaussian for large statistics and well behaved probability density functions [71]. For a likelihood function depending on a single parameter λ_j this leads to

$$-\ln \mathcal{L}(\lambda_j) = \frac{(x-\lambda_j)^2}{2\sigma^2} + const.\,, \tag{9.9}$$

with standard deviation σ and mean x of the Gaussian distribution. $-\ln\mathcal{L}$ is minimised when $\lambda_j = \lambda_{\max} = x$. Building the likelihood ratio (difference of $\ln\mathcal{L}$)

$$-2\Delta\ln\mathcal{L}(\lambda_j) = -2(\ln\mathcal{L}(\lambda_{\max}) - \ln\mathcal{L}(\lambda_j)) \tag{9.10}$$

and requiring $-2\Delta\ln\mathcal{L}(\lambda_j) = 1$ gives the solutions $\lambda_j^{\pm} = \lambda_{\max} \pm \sigma$ and thus the 68.3% confidence interval for λ_j. The 95.4% and 99.7% confidence intervals are defined by

$-2\Delta \ln \mathcal{L}(\lambda_j) = 4$ and $-2\Delta \ln \mathcal{L}(\lambda_j) = 9$, respectively.
In practice the likelihood ratio method is performed by determining $-2\Delta \ln \mathcal{L}(\lambda_j)$ for a grid of fixed λ_j values (likelihood scan). In case the likelihood function depends on additional parameters $\vec{\lambda}$, the ratio $-2\Delta \ln \mathcal{L}(\lambda_j, \vec{\lambda})$ is determined at each grid point of λ_j by minimising the likelihood function with respect to all other parameters $\vec{\lambda}$.
Similar, two-dimensional confidence intervals of parameters λ_i, λ_j can be derived by determining the likelihood ratio $-2\Delta \ln \mathcal{L}(\lambda_i, \lambda_j)$ in a two-dimensional grid. The two-dimensional 68.3%, 90.0% and 95.0% confidence intervals correspond to likelihood ratio values of 2.3, 4.61 and 5.99.

9.2 The PDF for $B_s^0 \to J/\psi\phi$

The aim of the maximum likelihood fit is the determination of the physics observables in the differential decay rate of B_s^0 decays. The parameters $\vec{\lambda}$ occurring in the PDF for $B_s^0 \to J/\psi\phi$ can be separated in $\vec{\lambda} = \{\vec{\lambda}_{\text{phys}}, \vec{\lambda}_{\text{nuis}}\}$, where $\vec{\lambda}_{\text{phys}}$ denotes the parameters that describe the physics observables and $\vec{\lambda}_{\text{nuis}}$ represents all additional parameters (*nuisance* parameters) that arise for example in the description of resolution effects or background contributions.

The dataset used to measure $\vec{\lambda}_{\text{phys}}$ is divided into several subsamples. They are distinguished by their trigger selection (HLT1-unbiased and HLT1-biased) and their tagging category (OST only, SST only, OST and SST). Most of the parameters extracted in the maximum likelihood fit, in particular $\vec{\lambda}_{\text{phys}}$ are the same for all subsamples and can be fitted simultaneously exploiting the full statistical power of the dataset. However some properties of the subsamples are different and have to be described by separate parameters that are only determined by the corresponding events.

A dataset composed of signal and background events is generally described by a PDF consisting of a signal part $S(\vec{x}; \vec{\lambda})$ and a background part $B(\vec{x}; \vec{\lambda})$:

$$p(\vec{x}|\vec{\lambda}) = f_{\text{sig}} \cdot S(\vec{x}|\vec{\lambda}) + (1 - f_{\text{sig}}) \cdot B(\vec{x}|\vec{\lambda}), \tag{9.11}$$

where f_{sig} is the relative fraction between signal and background and is different for the unbiased $f_{\text{sig}} = f_{\text{sig}}^{\text{ub}}$ and biased $f_{\text{sig}} = f_{\text{sig}}^{\text{b}}$ subsamples.
Both signal and background component depend on five measured observables $\vec{x}$: The decay time t, three decay angles $\Omega = \{\varphi_{\text{h}}, \cos\theta_{\text{k}}, \cos\theta_{\mu}\}$ and the reconstructed mass of the B_s^0-candidate m which is used to separate the signal and background components. In addition they depend conditionally on the estimated uncertainty of the decay time σ_{t}, the tagging decision q and calibrated mistag probability ω_{C} of each event.
According to the tagging strategy discussed in Section 6.3 the events are divided into three tagging categories that are fitted simultaneously: q and ω_{C} are either taken from the opposite side tagger (OST), the same side tagger (SST) or are a combination of both (OST+SST). For untagged events q is zero, for all other events q and ω_{C} are

defined as follows

$$\begin{array}{lll} q = q^{\mathrm{OST}}, & \omega_{\mathrm{C}} = \omega_c^{\mathrm{OST}} & \text{for } q^{\mathrm{OST}} = \pm 1 \text{ and } q^{\mathrm{SST}} = 0\,, \\ q = q^{\mathrm{SST}}, & \omega_{\mathrm{C}} = \omega_c^{\mathrm{SST}} & \text{for } q^{\mathrm{SST}} = \pm 1 \text{ and } q^{\mathrm{OST}} = 0\,, \\ q = q^{\mathrm{OST+SST}}, & \omega_{\mathrm{C}} = \omega_c^{\mathrm{OST+SST}} & \text{for } q^{\mathrm{OST}} = \pm 1 \text{ and } q^{\mathrm{SST}} = \pm 1\,, \\ q = 0, & \omega_{\mathrm{C}} = 0.0 & \text{for } q^{\mathrm{OST}} = 0 \text{ and } q^{\mathrm{SST}} = 0\,. \end{array} \tag{9.12}$$

In the following sections the implementation of the signal and background components will be discussed in detail.

9.2.1 Description of the signal decay

The reconstructed B_s^0 mass is uncorrelated to the decay time and angular distribution. Therefore the signal PDF used to determine the physics parameters can be factorised in a term describing the reconstructed mass distribution S_{M} and a term describing the time and angular dependent decay rate S_{t}. As $S_{\mathrm{t}} = S_{\mathrm{t}}(t, \sigma_{\mathrm{t}}, \Omega, \omega_{\mathrm{C}}, q|\vec{\lambda})$ depends conditionally on the quantities σ_{t}, ω_{C} and q, the signal PDF needs to contain as well the probability density functions of the estimated decay time uncertainty $S_{\sigma_{\mathrm{t}}}$ and the calibrated mistag probability S_{D}:

$$S(\vec{x}|\vec{\lambda}) = S_{\mathrm{M}}(m|\vec{\lambda}_{\mathrm{nuis}}) \cdot S_{\mathrm{t}}(t, \sigma_{\mathrm{t}}, \Omega, \omega_{\mathrm{C}}, q|\vec{\lambda}_{\mathrm{phys}}, \vec{\lambda}_{\mathrm{nuis}}) \cdot S_{\sigma_{\mathrm{t}}}(\sigma_{\mathrm{t}}) \cdot S_{\mathrm{D}}(\omega_{\mathrm{C}}) \cdot S_q\,. \tag{9.13}$$

$S_{\sigma_{\mathrm{t}}}$ and S_{D} are represented in the fit by histograms shown in Figures 7.1 and 6.2. $S_q = S_q^{\mathrm{OST}} \cdot S_q^{\mathrm{SST}} \cdot S_q^{\mathrm{OST+SST}}$ is defined by the tagging efficiencies of the three categories with

$$S_q^{\mathrm{OST}} = \begin{cases} \frac{\varepsilon_{\mathrm{sig}}^{\mathrm{OST}}}{2} & \text{for } q^{\mathrm{OST}} = \pm 1 \\ (1 - \varepsilon_{\mathrm{sig}}^{\mathrm{OST}}) & \text{for } q^{\mathrm{OST}} = 0 \end{cases}\,, \tag{9.14}$$

and similar expressions for S_q^{SST} and $S_q^{\mathrm{OST+SST}}$. The three tagging efficiencies for the signal decays can be determined directly in the minimisation and are free parameters in the fit. The remaining parts of the signal PDF are detailed in the following sections.

The mass distribution

The mass shape of the B_s^0 is in principle described by a Breit-Wigner function. However, the width of the B_s^0 resonance is much smaller than the actual mass resolution of the detector. The effect of the detector resolution results in a B_s^0 mass distribution that is found to be modeled best with a sum of two Gaussian functions:

$$S_{\mathrm{M}}(m|\vec{\lambda}_{\mathrm{nuis}}) = f_{\mathrm{m}} \frac{1}{\sqrt{2\pi}\sigma_{\mathrm{m}}} e^{-\frac{(m - M_{\mathrm{B_s^0}})^2}{2\sigma_{\mathrm{m}}^2}} + (1 - f_{\mathrm{m}}) \frac{1}{\sqrt{2\pi} s_{\mathrm{m}} \sigma_{\mathrm{m}}} e^{-\frac{(m - M_{\mathrm{B_s^0}})^2}{2(s_{\mathrm{m}}\sigma_{\mathrm{m}})^2}}\,. \tag{9.15}$$

The parameters to be estimated in the likelihood fit are the mean of the B_s^0 mass distribution $M_{\mathrm{B_s^0}}$, the width of the first Gaussian σ_{m} and the fraction of the two Gaussian functions f_{m}. The width of the second Gaussian is given by σ_{m} multiplied with a scaling factor s_{m} which is also varied in the fitting procedure. This parameterisation is chosen in order to minimise the correlation between the two Gaussian functions.

The time and angular distributions

The signal distribution of the decay time and the decay angles $s(t, \Omega, \omega_C, q|\vec{\lambda})$ is the main part of the PDF containing all physics observables of interest. It is build from the differential decay rates for produced B_s^0 and $\overline{B}_s^0$ mesons as given in Equation 2.51 and 2.52, with $P_{B_s^0}(t, \Omega|\vec{\lambda}_{\text{phys}}) = \frac{d\Gamma(B_s^0 \to J/\psi\phi)}{dt d\Omega}$ and $P_{\overline{B}_s^0}(t, \Omega|\vec{\lambda}_{\text{phys}}) = \frac{d\Gamma(\overline{B}_s^0 \to J/\psi\phi)}{dt d\Omega}$:

$$s(t, \Omega, \omega_C, q|\vec{\lambda}) = \frac{1 + qD_{\text{tag}}}{2} P_{B_s^0}(t, \Omega|\vec{\lambda}_{\text{phys}}) + \frac{1 - q\bar{D}_{\text{tag}}}{2} P_{\overline{B}_s^0}(t, \Omega|\vec{\lambda}_{\text{phys}}), \tag{9.16}$$

where q is the tagging decision and $\overset{(-)}{D}_{\text{tag}} = (1 - 2\overset{(-)}{\omega}_{\text{tag}})$ the tagging dilution with the mistag probability $\overset{(-)}{\omega}_{\text{tag}}$ of produced B_s^0 and $\overline{B}_s^0$, respectively. The physics parameters are $\vec{\lambda}_{\text{phys}} = \{\phi_s, \Delta\Gamma_s, \Gamma_s, |\lambda_{CP}|, \Delta m_s, |A_0|^2, |A_\perp|^2, F_s, \delta_\perp, \delta_\parallel, \delta_{s,\perp}\}$. The differential decay rate is normalised in a way that the P-wave amplitudes satisfy the condition $|A_\perp|^2 + |A_0|^2 + |A_\parallel|^2 = 1$. Therefore only two of them are free parameters in the fit. As only phase differences are measurable quantities, the value of one strong phase can be fixed. The convention $\delta_0 = 0$ is chosen. The S-wave fraction is parameterised such that $F_s = 1/(|A_\perp|^2 + |A_0|^2 + |A_\parallel|^2 + |A_s|^2)$. Instead of fitting for δ_s, the parameterisation $\delta_{s,\perp} = \delta_s - \delta_\perp$ is chosen which turned out to decrease correlations between δ_s and $\delta_\perp$ in the fit. All physics parameters $\vec{\lambda}_{\text{phys}}$ are varied in the fit, except Δm_s which will be constrained to the value $\Delta m_s = 17.63 \pm 0.11\,\text{ps}^{-1}$, measured in a previous analysis [25].

As discussed in Section 2.4, ignoring the dependence of the polarisation amplitudes on the K^+K^- mass requires an additional correction factor $C_{sp}e^{-i\delta_{sp}}$ for the P-wave and S-wave interference terms. The phase $e^{-i\delta_{sp}}$ is absorbed in the definition of $\delta_{s,\perp}$. The factor C_{sp} for a given $m_{K^+K^-}$ interval $[m^1_{K^+K^-}, m^2_{K^+K^-}]$ can be calculated following Equation 2.56. The ϕ resonance shape of the P-wave amplitudes is described by a Breit-Wigner function

$$g(m_{K^+K^-}) \propto \frac{1}{m_{K^+K^-} - m^\phi_{K^+K^-} + i\Gamma_\phi/2}, \tag{9.17}$$

where $m^\phi_{K^+K^-}$ is the ϕ mass (1020 MeV), Γ_ϕ is the ϕ width (4.26 MeV). The $m_{K^+K^-}$ dependence of the S-wave amplitude is not known in detail. It can either be due a non-resonant K^+K^- component having a flat linear-shape or partially due to an intermediate $f_0(980)$ resonance, described by a Flatté function[1]. In this analysis a flat $m_{K^+K^-}$ dependence of the S-wave amplitude is assumed, $v(m_{K^+K^-}) \propto 1$. For a $m_{K^+K^-}$ mass range of [1008 MeV, 1032 MeV] the correction factor is calculated to be $C_{sp} = 0.498$.

For the three possible tagging decisions $q = \pm 1, 0$, Equation 9.16 can be written as

$$\begin{aligned}
s(t, \Omega, \omega_C, q = -1|\vec{\lambda}) &= \omega_{\text{tag}} \cdot P_{B_s^0}(t, \Omega|\vec{\lambda}_{\text{phys}}) + (1 - \overline{\omega}_{\text{tag}}) \cdot P_{\overline{B}_s^0}(t, \Omega|\vec{\lambda}_{\text{phys}}), \\
s(t, \Omega, \omega_C, q = +1|\vec{\lambda}) &= (1 - \omega_{\text{tag}}) \cdot P_{B_s^0}(t, \Omega|\vec{\lambda}_{\text{phys}}) + \overline{\omega}_{\text{tag}} \cdot P_{\overline{B}_s^0}(t, \Omega|\vec{\lambda}_{\text{phys}}), \\
s(t, \Omega, \omega_C, q = 0|\vec{\lambda}) &= \frac{1}{2} \cdot P_{B_s^0}(t, \Omega|\vec{\lambda}_{\text{phys}}) + \frac{1}{2} \cdot P_{\overline{B}_s^0}(t, \Omega|\vec{\lambda}_{\text{phys}}),
\end{aligned} \tag{9.18}$$

This shows clearly that an imperfect knowledge of the B_s^0 production flavour ($\overset{(-)}{\omega}_{\text{tag}} \neq 0$) leads to a mixture of the B_s^0 and $\overline{B}_s^0$ differential decay rates in the PDF.
As described in Section 6.3, $\overset{(-)}{\omega}_{\text{tag}}$ itself depends on calibration parameters and the calibrated mistag probability ω_{C}. Depending on the tagging category, different calibration parameters appear in the PDF: p_0^{OST}, p_1^{OST}, $\langle\omega_{\text{C}}\rangle^{\text{OST}}$, Δ^{OST} for events with only an OST decision, p_0^{SST}, p_1^{SST}, $\langle\omega_{\text{C}}\rangle^{\text{SST}}$, Δ^{SST} for events tagged only with SST and $p_0^{\text{OST+SST}}$, $p_1^{\text{OST+SST}}$, $\langle\omega_{\text{C}}\rangle^{\text{OST+SST}}$, $\Delta^{\text{OST+SST}}$ for events that have tagging decisions from both taggers. All these calibration parameters are varied in the fit inside their uncertainties using Gaussian constraints. Their measured values and uncertainties are given in Table 6.1.

Acceptance and resolution effects

Equation 9.16 describes the distribution of decay time and angles ignoring any detector or resolution effects. Taking these into account and normalising $s(t, \Omega, \omega_{\text{C}}, q|\vec{\lambda})$ according to Equation 9.1 leads to

$$S_{\text{t}}(t, \sigma_{\text{t}}, \Omega, \omega_{\text{C}}, q|\vec{\lambda}) = \frac{\varepsilon(t, \Omega) \cdot s(t, \Omega, \omega_{\text{C}}, q|\vec{\lambda}) \otimes G(t, \sigma_{\text{t}}|s_{\sigma_{\text{t}}})}{\int \varepsilon(t, \Omega) \cdot s(t, \Omega, \omega_{\text{C}}, q|\vec{\lambda}) \otimes G(t, \sigma_{\text{t}}|s_{\sigma_{\text{t}}}) \text{d}t\text{d}\Omega}\,, \tag{9.19}$$

where $\varepsilon(t, \Omega)$ is the detector acceptance including trigger, reconstruction and selection inefficiencies. $\varepsilon(t, \Omega)$ has in principle to be described in four dimensions, as the distributions of the decay time and the three angles can be correlated. The effect of neglecting this correlation is much smaller than the statistical precision of this analysis. Therefore $\varepsilon(t, \Omega) = \varepsilon(t) \cdot \varepsilon(\Omega)$ is used. $s(t, \Omega, \omega_{\text{C}}, q|\vec{\lambda})$ is for each event convoluted with a Gaussian resolution function $G(t - t', \sigma_{\text{t}}|s_{\sigma_{\text{t}}})$ with mean zero and width $s_{\sigma_{\text{t}}} \cdot \sigma_{\text{t}}$ to account for the limited decay time resolution of the detector. Possible resolution effects of the decay angles are neglected in this analysis as earlier studies proved them to be negligible.

The description of the decay time resolution was discussed in Chapter 7. The scale factor $s_{\sigma_{\text{t}}}$ is determined with prompt J/ψ background candidates. To account for differences in the resolution between simulated signal and prompt background events, the

[1] The Flatté amplitude [72] is used when a second decay channel opens close to a resonance. For $f_0(980)$ it is parameterised by

$$F(m_{\pi\pi}) = \frac{1}{m_{f_0(980)}^2 - m_{\pi\pi}^2 - i(\rho_{\pi\pi} g_{\pi\pi}^2 + \rho_{KK} g_{KK}^2)}\,,$$

where $g_{\pi\pi}$ and g_{KK} are the $f_0(980)$ coupling constants to $\pi^+\pi^-$ and K^+K^-, respectively. The phase space factors $\rho_{\pi\pi/KK}$ are defined as

$$\rho_{\pi\pi} = \frac{2}{3}\sqrt{1 - \frac{4m_{\pi^+}^2}{m^2(K^+K^-)}} + \frac{1}{3}\sqrt{1 - \frac{4m_{\pi^0}^2}{m^2(K^+K^-)}}\,, \quad \rho_{KK} = \frac{1}{2}\sqrt{1 - \frac{4m_{K^+}^2}{m^2(\pi^+\pi^-)}} + \frac{1}{2}\sqrt{1 - \frac{4m_{K^0}^2}{m^2(\pi^+\pi^-)}}\,.$$

scale factor is varied in the fit, constraint to $s_{\sigma_t} = 1.47 \pm 0.05$. A possible bias from a non-zero mean of the resolution model will be discussed in the systematic uncertainties.
The time acceptance $\varepsilon(t)$ was determined in Section 8.2 and is different for the unbiased and biased subsample. Only the acceptance introduced by the trigger selections are modeled in the fit. It is included in the PDF as one dimensional histograms given in Figure 8.10. The upper decay time acceptance, parameterised in Equation 8.5 is not described in the fit. The measured value of Γ_s will be corrected after the fit by adding the factor $\beta = -8.3\,\mathrm{ps}^{-1}$ (see Section 8.2.2). Other parameters are not affected by this correction.
The angular acceptance $\varepsilon(\Omega)$ is calculated using simulated events and given by a three dimensional histogram, described in Section 8.1. The one-dimensional projections of this histogram are shown in Figure 8.2, corresponding to 20 bins in each of the decay angles.

Also the denominator of $S_t(t, \sigma_t, \Omega, \omega_C, q|\vec{\lambda})$ depends on the time and angular acceptance. Using Equation 2.51 one can transform the normalisation such that the integral factorises in a integral over Ω an an integral over t:

$$\int \varepsilon(t) \cdot \varepsilon(\Omega) \cdot P^{(-)}_{B^0_s}(t, \Omega|\vec{\lambda}_{\mathrm{phys}})\mathrm{d}t\mathrm{d}\Omega \rightarrow \sum_{k=1}^{10} \int \varepsilon(\Omega) f_k(\Omega)\mathrm{d}\Omega \cdot \int \varepsilon(t)\overset{(-)}{h}_k(t)\mathrm{d}t \qquad (9.20)$$

The ten normalisation weights $\xi_k = \int \varepsilon(\Omega) f_k(\Omega)\mathrm{d}\Omega$ are independent of any parameter in the minimisation process and can therefore be determined once before the fit. This is not possible for the time integral which must be calculated numerically for each event. The ξ_k can be calculated by using either the three-dimensional histogram $\varepsilon(\Omega)$ or, in an unbinned way, by summing over all simulated events N [73]

$$\xi_k = \sum_{i=0}^{N} \frac{f_k(\Omega_i)}{s(t_i, \Omega_i, \omega_{Ci}, q_i|\vec{\lambda})} \qquad (9.21)$$

The normalisation weights calculated like this will be used in the fit and are given in Table 9.1. In addition the normalisation weight calculated from the acceptance histogram are shown for comparison. They are in very good agreement. Their absolute value show that the necessary acceptance corrections are rather small. A completely flat angular acceptance would lead to $\xi_1 = \xi_2 = \xi_3 = \xi_7 = 1$, $\xi_4 = \xi_5 = \xi_6 = \xi_8 = \xi_9 = \xi_{10} = 0$.

9.2.2 Description of the background

Similar to the signal description the background PDF $B(\vec{x}|\vec{\lambda}_{\mathrm{nuis}})$ is a product of a mass term B_M, a component describing the decay time and angular distribution B_t and the

k	Normalisation weights ξ_k	
	unbinned	from histogram
1	0.980 ± 0.001	0.980 ± 0.002
2	1.029 ± 0.002	1.028 ± 0.002
3	1.029 ± 0.002	1.028 ± 0.002
4	-0.001 ± 0.003	-0.001 ± 0.001
5	0.000 ± 0.001	0.000 ± 0.001
6	0.000 ± 0.001	0.000 ± 0.001
7	0.992 ± 0.002	0.991 ± 0.002
8	0.001 ± 0.002	0.001 ± 0.001
9	0.001 ± 0.001	0.001 ± 0.001
10	-0.007 ± 0.003	-0.007 ± 0.003

Table 9.1: Normalisation weights ξ_i calculated according to Equation 9.21 and calculated using the three dimensional acceptance histogram (last column). Both methods agree very well.

distributions of the conditional per-event variables for background events, B_{σ_t}, B_D and B_q:

$$B(\vec{x}|\vec{\lambda}_{\text{nuis}}) = B_M(m|\vec{\lambda}_{\text{nuis}}) \cdot B_t(t, \sigma_t, \Omega|\vec{\lambda}_{\text{nuis}}) \cdot B_{\sigma_t}(\sigma_t) \cdot B_D(\omega_C) \cdot B_q \tag{9.22}$$

The background in this analysis shows no correlation between decay time and decay angles, therefore one can factorise $B_t(t, \sigma_t, \Omega|\vec{\lambda}_{\text{nuis}}) = B_t(t, \sigma_t|\vec{\lambda}_{\text{nuis}}) \cdot B_\Omega(\Omega)$. Similar to the signal PDF B_{σ_t} and B_D are represented by histograms determined from candidates in the B_s^0 mass sidebands and shown in Figure 7.1 and 6.2. $B_q = B_q^{\text{OST}} \cdot B_q^{\text{SST}} \cdot B_q^{\text{OST+SST}}$ takes into account the conditional dependence of B on the tagging decision q and is defined analogously to the signal PDF as

$$B_q^{\text{OST}} = \begin{cases} \frac{\varepsilon_{\text{bkg}}^{\text{OST}}}{2} & \text{for } q^{\text{OST}} = \pm 1 \\ (1 - \varepsilon_{\text{bkg}}^{\text{OST}}) & \text{for } q^{\text{OST}} = 0 \end{cases}, \tag{9.23}$$

with similar expressions for the SST and OST+SST categories. All three background tagging parameters are varied in the fit.

The mass distribution

The probability density function describing the mass shape of the combinatorial background events is empirically given by a normalised exponential function

$$B_M(m|\vec{\lambda}_{\text{nuis}}) = \frac{e^{-\alpha_m \cdot m}}{\int_{min}^{max} e^{-\alpha_m \cdot m} \mathrm{d}m} \tag{9.24}$$

where the slope parameter α_m is estimated in the fit. The integral in the normalisation is calculated from the lower (*min*) to the upper (*max*) edge of the fitted mass region.

The decay time distribution

Figure 9.1(a) shows the decay time distributions of background candidates from the HLT1-biased and HLT1-unbiased subsample. They have a reconstructed B_s^0 mass in the sideband intervals [5200 MeV, 5320 MeV] and [5420 MeV, 5550 MeV]. Both distributions look very similar and a common parameterisation is chosen for the subsamples. The PDF describing best the shape of the background is found to be a sum of three exponential functions with relative fractions f^1_{bkg} and f^2_{bkg},

$$B_{\text{t}}(t, \sigma_{\text{t}}|\vec{\lambda}_{\text{nuis}}) = \frac{1}{N}\Big(f^1_{\text{bkg}} \cdot e^{-\frac{t}{\tau^1_{\text{bkg}}}} + (1 - f^1_{\text{bkg}}) f^2_{\text{bkg}} \cdot e^{-\frac{t}{\tau^2_{\text{bkg}}}} + (1 - f^1_{\text{bkg}})(1 - f^2_{\text{bkg}}) \cdot e^{-\frac{t}{\tau^3_{\text{bkg}}}} \Big), \tag{9.25}$$

where τ^1_{bkg} τ^2_{bkg} and τ^3_{bkg} are the three lifetimes of the exponential functions. $N = \int B_{\text{t}}(t, \sigma_{\text{t}}|\vec{\lambda}_{\text{nuis}})\text{d}t$ is the normalisation integrated over the fitted decay time range. The choice of the parameterisation has no physical motivation but is purely driven by observations. Figure 9.1(b) shows the decay time distribution of background events for both subsamples overlaid with the fitted function. The distribution is well described by this parameterisation. The parameters of the fit are given in Table 9.2. The parameterisation is used in the full likelihood fit with free fractions and lifetimes to describe the decay time background component.

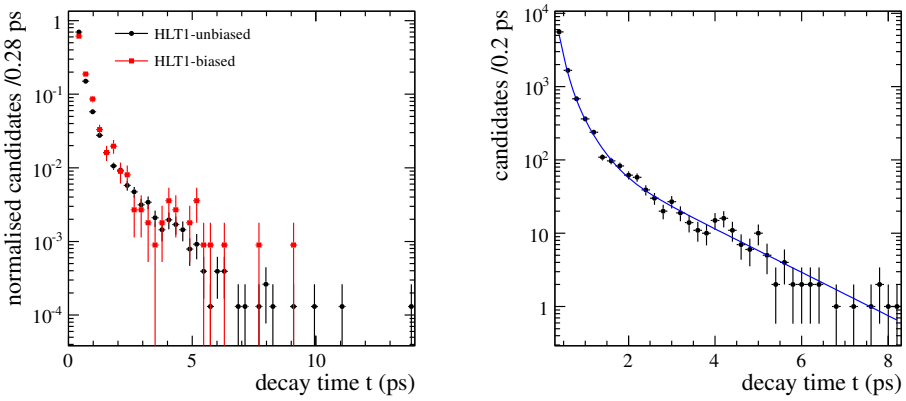

(a) HLT1-unbiased and HLT1-biased (b) all B_s^0 background candidates

Figure 9.1: Decay time distribution of background candidates from (a) the two differently triggered subsamples and (b) of all background candidates, overlaid with the fitted PDF (Equation 9.25).

parameter	fit result
f^1_{bkg}	0.518 ± 0.062
f^2_{bkg}	0.236 ± 0.026
τ^1_{bkg}[ps]	0.114 ± 0.008
τ^2_{bkg}[ps]	1.467 ± 0.100
τ^3_{bkg}[ps]	0.334 ± 0.041

Table 9.2: Results from fit to decay time distribution of B^0_s background candidates using the function defined in Equation 9.25.

The decay angle distribution

To address possible correlations between the decay angles $\Omega = \{\cos\theta_{\text{k}}, \cos\theta_\mu, \varphi_{\text{h}}\}$, a three-dimensional histogram is used to describe the background angular distributions in the maximum likelihood fit. It can be determined with background events from the B^0_s mass sidebands [5205 MeV, 5325 MeV] and [5400 MeV, 5520 MeV]. Figure 9.2 shows two-dimensional projections of this histogram. While the background distribution in the $\cos\theta_\mu$ and φ_{h} dimension is rather smooth, there are clear spikes at the edges of the $\cos\theta_{\text{k}}$ distribution. This feature makes it nearly impossible to find a precise parameterisation of the three-dimensional histogram. Therefore the normalised histogram itself is used as probability density function in the fit. The binning is chosen such that the number of bins is maximised, while keeping in average 10 events per bin.

9.3 The classical fitting technique

Two different fitting methods will be used as complementary approaches to determine the physics parameters in this analysis. One technique, in the following called *classical* fit, minimises the probability density function given in Equation 9.11. Both signal and background distributions of the measured observables are modeled in the fit by the PDFs introduced in the last section. The mass is fitted simultaneously with the decay time and angular distributions to separate the background component. In summary this means for the classical fit that in total about 40 different parameters have to be determined simultaneously. As an overview they are summarised in Table 9.3.

9.4 The sFit technique

The so called *sFit* technique [74] is a method to perform a maximum likelihood fit without explicitly modeling the background component $B(\vec{x}; \vec{\lambda}_{\text{nuis}})$. In a first step the B^0_s mass distribution is fitted using the probability density functions defined in 9.15 and 9.24. The fitted PDF is used to assign a weight (*sWeight*) $w(m_i)$ to each candidate

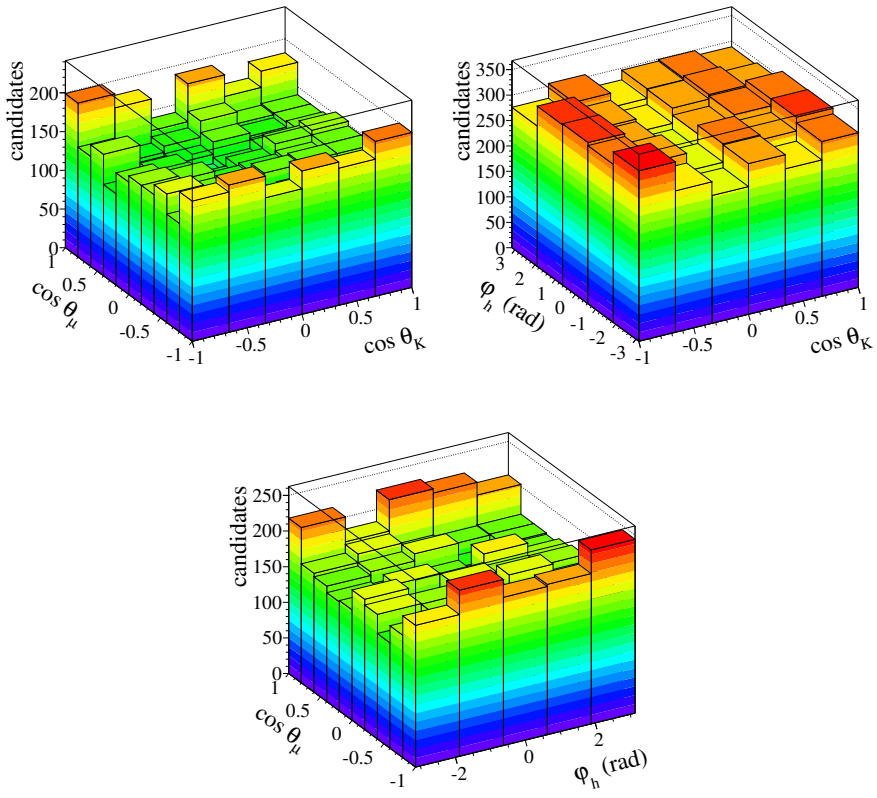

Figure 9.2: Two-dimensional helicity angle distributions for selected B_s^0 background candidates in the B_s^0 mass sidebands [5205 MeV, 5325 MeV] and [5400 MeV, 5520 MeV].

depending on its reconstructed B_s^0 mass (see also Section 7.3). The exact procedure is documented in [66]. By defining the likelihood function as

$$\mathcal{L}(\vec{\lambda}) = -\alpha \sum_i^N \left[w(m_i) \cdot \ln S'(t_i, \sigma_{\mathrm{t}i}, \Omega_i, \omega_{\mathrm{C}i}, q_i|\vec{\lambda}) \right] , \tag{9.26}$$

the background component cancels on a statistical basis. $\alpha = \sum_i^N w(m_i) / \sum_i^N w^2(m_i)$ is a factor due to the reweighting, to ensure a correct error estimation of the fit.
$S'(t, \sigma_{\mathrm{t}}, \Omega, \omega_{\mathrm{C}}, q|\vec{\lambda})$ is the probability density function describing the signal distributions of the decay time and angles and is, following Equation 9.16, given as

$$S'_{\mathrm{t}}(t, \sigma_{\mathrm{t}}, \Omega, \omega_{\mathrm{C}}, q|\vec{\lambda}) = \frac{s(t, \Omega, \omega_{\mathrm{C}}, q|\vec{\lambda}) \otimes G(t, \sigma_{\mathrm{t}}|s_{\sigma_{\mathrm{t}}})}{\int \varepsilon(t, \Omega) \cdot s(t, \Omega, \omega_{\mathrm{C}}, q|\vec{\lambda}) \otimes G(t, \sigma_{\mathrm{t}}|s_{\sigma_{\mathrm{t}}}) \mathrm{d}t \mathrm{d}\Omega} . \tag{9.27}$$

Additional terms like the acceptance correction histogram in the numerator of Equation 9.16 or the PDFs for the conditional variables σ_{t}, ω_{C} and q do not have to be

	signal parameter	background parameter	treatment in fit
signal fraction	$f_{\mathrm{sig}}^{\mathrm{ub}}$, $f_{\mathrm{sig}}^{\mathrm{b}}$		varied
mass	$M_{\mathrm{B_s^0}}$, f_{m}, σ_{m}, s_{m}	α_{m}	varied
decay rate	Γ_{s}, $\Delta\Gamma_{\mathrm{s}}$, $\lvert\lambda_{\mathrm{CP}}\rvert$, ϕ_{s}	f_{bkg}^1, f_{bkg}^2	varied
	$\lvert A_0\rvert^2$, $\lvert A_\perp\rvert^2$, F_{s}, $\delta_\parallel$, $\delta_\perp$, $\delta_{\mathrm{s},\perp}$	τ_{bkg}^1, τ_{bkg}^2, τ_{bkg}^3	varied
	Δm_{s}, $s_{\sigma_{\mathrm{t}}}$		constrained
	C_{sp}		fixed
tagging	$\varepsilon_{\mathrm{sig}}^{\mathrm{OST}}$, $\varepsilon_{\mathrm{sig}}^{\mathrm{SST}}$, $\varepsilon_{\mathrm{sig}}^{\mathrm{OST+SST}}$	$\varepsilon_{\mathrm{bkg}}^{\mathrm{OST}}$, $\varepsilon_{\mathrm{bkg}}^{\mathrm{SST}}$, $\varepsilon_{\mathrm{bkg}}^{\mathrm{OST+SST}}$	varied
	$\langle\omega_{\mathrm{C}}\rangle^{\mathrm{OST}}$,$\langle\omega_{\mathrm{C}}\rangle^{\mathrm{SST}}$,$\langle\omega_{\mathrm{C}}\rangle^{\mathrm{OST+SST}}$		fixed
	p_0^{OST}, p_1^{OST}, Δ^{OST}		constrained
	p_0^{SST}, p_1^{SST}, Δ^{SST}		constrained
	$p_0^{\mathrm{OST+SST}}$, $p_1^{\mathrm{OST+SST}}$, $\Delta^{\mathrm{OST+SST}}$		constrained

Table 9.3: Physics and nuisance parameters in the classical fitting technique.

included in this PDF. In the absence of a background model these terms separate in the minimisation of the logarithmic likelihood and lead only to an additional constant offset.

9.5 Validation of fitting procedure

It is essential to ensure that the implementation of the probability density functions, especially their normalisation is correct. A mistake there could lead to a bias in the estimated parameters or the associated errors. To validate the fit method a set of pseudo-experiments is performed as follows:
100000 events $\vec{x}_i$ are generated according to the probability density functions described in the previous section. For the generation, fixed parameter $\vec{\lambda}$ are used. The maximum likelihood fit is then performed on this dataset, varying the parameters according to Table 9.3. This procedure is repeated 700 times.
In case of a correct implementation of the PDFs, the distribution of the 700 fitted parameter sets should be centered around the value used for the generation of the event samples. The mean of the central value distribution are given in Table 9.4 for the physics parameters together with the values used in the generation of the datasamples. No bias can be observed. The pull-distributions, showing the difference between generated and fitted parameter value divided by the fit uncertainty are shown in Figure 9.3. All distributions can be nicely described by a Gaussian function with a mean consistent with 0 and a width consistent with 1, showing the correct error estimate of the fit.

parameter	generated value	mean of fitted values
ϕ_s[rad]	0.10	0.099 ± 0.002
$\lvert\lambda_{CP}\rvert$	0.950	0.9499 ± 0.0005
$\Delta\Gamma_s$[ps^{-1}]	0.08	0.0794 ± 0.0003
Γ_s[ps^{-1}]	0.671	0.6711 ± 0.0001
$\lvert A_\perp\rvert^2$	0.250	0.2502 ± 0.0002
$\lvert A_0\rvert^2$	0.520	0.5199 ± 0.0001
F_s	0.100	0.0999 ± 0.0002
$\delta_\parallel$[rad]	2.00	2.0014 ± 0.0006
$\delta_\perp$[rad]	2.50	2.493 ± 0.004
$\delta_{s,\perp}$[rad]	2.50	2.500 ± 0.002

Table 9.4: Mean of fitted parameter value distribution of 700 pseudo-experiments with 200000 events each, compared to the values used in the generation of the events.

9.6 Validation with fully simulated events

In order to further test the implementation of the maximum likelihood fit and the determination of the detector acceptances, the fit procedure is performed using fully simulated $B_s^0 \to J/\psi\phi$ signal events. Therefore no background description in the fit is necessary. Only the decay time and angular distributions are fitted. The decay time acceptances for simulated events are given in Figure 8.11, the angular acceptance is introduced in Chapter 8. The decay time resolution is described by a single Gaussian model with the fixed scaling factor $s_{\sigma_t} = 1.26$, derived in Chapter 7 for simulated $B_s^0 \to J/\psi\phi$ signal decays. Flavour tagging is performed using only the opposite side tagger decisions with an average mistag probability for all candidates. The B_s^0-$\overline{B}_s^0$ mixing frequency Δm_s is fixed to the simulated value $\Delta m_s = 17.8\,\text{ps}^{-1}$. No S-wave or direct CP violation is generated in the simulation, therefore the corresponding parameters are fixed in the fit to $F_s = 0.0$ and $|\lambda_{CP}| = 1.0$.
The fit was performed separately for the HLT1-unbiased and the HLT1-biased event samples and simultaneously for both. The extracted parameter values and their fit uncertainties can be found in Table 9.5 compared to the values used in the generation of the decays. The one dimensional projection of the fitted probability density function for the combined event samples can be seen in Figure 9.4. The decay time and angular distributions are well described by the projected PDF. All extracted parameter values agree within 2 standard deviation with the generated values. The values of Γ_s in Table 9.5 are already corrected for the upper decay time acceptance (Section 8.2.2). The corresponding correction factor for simulated events is $\beta = -0.011\,\text{ps}^{-1}$.

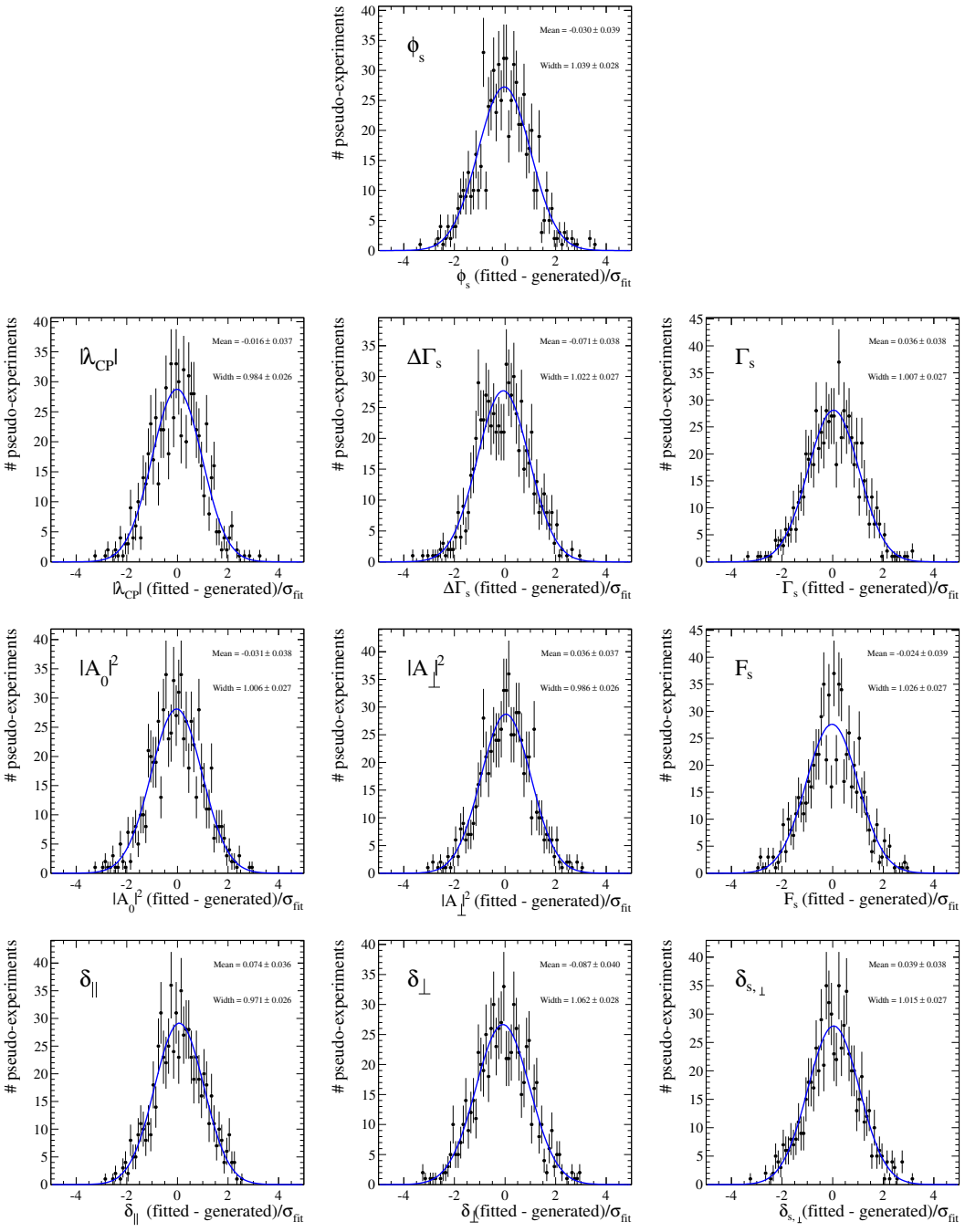

Figure 9.3: Pull-distributions of physics parameters obtained from 700 pseudo-experiments with 100000 generated events each.

parameter	HLT1-unbiased	HLT1-biased	full sample	generated value
ϕ_s[rad]	-0.049 ± 0.026	-0.095 ± 0.064	-0.055 ± 0.024	-0.04
$\Delta\Gamma_s$[ps^{-1}]	0.051 ± 0.005	0.039 ± 0.013	0.050 ± 0.005	0.06
Γ_s[ps^{-1}]	0.679 ± 0.002	0.683 ± 0.005	0.680 ± 0.001	0.679
$\lvert A_\perp \rvert^2$	0.162 ± 0.002	0.163 ± 0.005	0.162 ± 0.002	0.16
$\lvert A_0 \rvert^2$	0.598 ± 0.001	0.601 ± 0.004	0.598 ± 0.001	0.6
$\delta_\parallel$[rad]	2.505 ± 0.012	2.466 ± 0.027	2.500 ± 0.011	2.5
$\delta_\perp$[rad]	$-0.2.04 \pm 0.068$	-0.439 ± 0.174	-0.235 ± 0.064	-0.17

Table 9.5: Parameter values obtained from a fit to fully simulated $B_s^0 \to J/\psi\phi$ events. The fit was done separately for the HLT1-unbiased, the HLT1-biased subsample and the sum of both. The result is compared to the parameter values used in the generation of the simulated event sample.

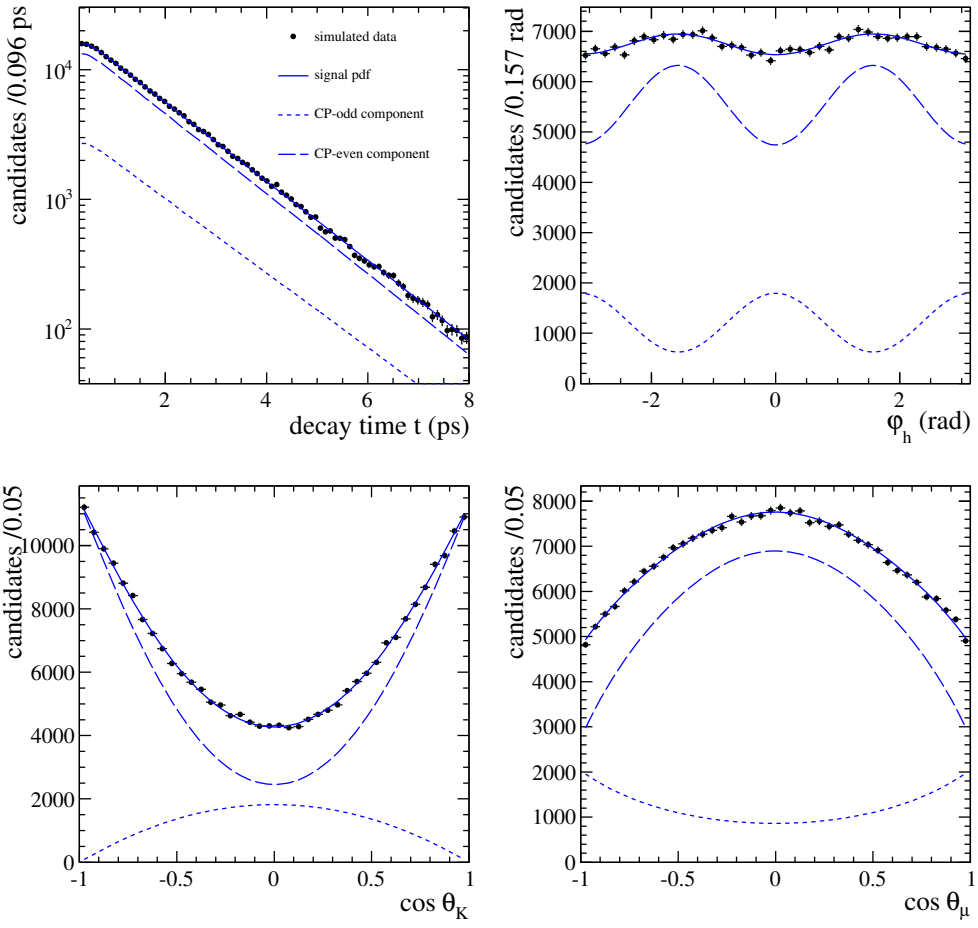

Figure 9.4: One-dimensional fit projections of classical maximum likelihood fit to fully simulated $B_s^0 \to J/\psi\phi$ signal decays.

CHAPTER 10

Fit in small K^+K^- mass interval

The fitting procedure introduced in the last chapter is used to extract the physics parameters from the selected $B_s^0 \to J/\psi\phi$ decays. The ϕ_s-$\Delta\Gamma_s$ ambiguity in the differential decay rate can only be resolved by measuring the dependence of the strong phases on the K^+K^- mass (Section 2.4). Therefore an enlarged $m_{K^+K^-}$ mass window in the $B_s^0 \to J/\psi\phi$ selection and a more complicated fit with separate parameters for different $m_{K^+K^-}$ intervals is necessary. Before discussing this fit in the next chapter, the performance of the fitting procedure is tested in a single, small [1008, 1032] MeV K^+K^- mass interval. The two-fold ambiguity can not be resolved by this simplified fit. Central values and statistical uncertainties of the physics parameters are determined, using the classical fitting technique as well as the sFit technique. The results are presented together with a detailed discussion of the error estimates.

10.1 Results of maximum likelihood fit

The extraction of the physics parameters in the $B_s^0 \to J/\psi\phi$ decay is done using all 37361 B_s^0 candidates that remain after the full selection in the B_s^0 mass range of [5200 MeV, 5550 MeV]. Two separate fits are performed: First the classical fitting technique, describing simultaneously the B_s^0 mass, the decay time and the three decay angles for signal and background events and secondly, the sFit method using a separate B_s^0 mass fit to determine event weights with which a statistical subtraction of the background is possible.

The fit results for the B_s^0 mass description, as well as the signal fractions obtained with both methods, are given in Table 10.1. The parameter values are slightly different for the two techniques which reflects the difference between performing a separate mass fit (sFit) and fitting the mass simultaneously with the decay times and angles (classical fit). Figure 10.1 shows the fitted mass PDF, used for the sFit technique and projected on the measured B_s^0 mass distribution.

parameter	classical fit	sFit
$M_{\mathrm{B_s^0}}$	5368.24 ± 0.05	5368.23 ± 0.05
f_{m}	0.827 ± 0.017	0.786 ± 0.027
σ_{m}	6.332 ± 0.090	6.175 ± 0.114
s_{m}	2.413 ± 0.097	2.202 ± 0.103
α_{m}	0.0016 ± 0.0001	0.0016 ± 0.0001
$f_{\mathrm{sig}}^{\mathrm{ub}}$	0.667 ± 0.003	0.665 ± 0.003
$f_{\mathrm{sig}}^{\mathrm{b}}$	0.708 ± 0.007	0.702 ± 0.007

Table 10.1: B_s^0 mass parameters and signal fractions obtained from the classical fit and the sFit technique.

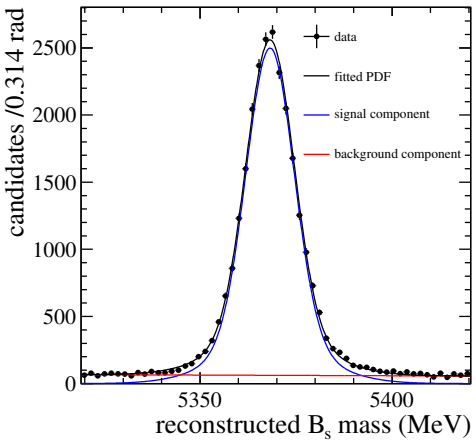

Figure 10.1: B_s^0 mass distribution overlaid with the fitted mass PDF from the sFit technique. The plotted range is restricted to [5320 MeV, 5420 MeV].

For both fit techniques, the results for the physics parameters, determined in the time and angular dependent fit, are given in Table 10.2. The quoted errors are the uncertainties from the fit and contain beside a statistical component also the uncertainties

related to the constrained parameters of the decay time resolution, the tagging calibration and the oscillation frequency. Their contribution to the fit error is < 3% and the fit uncertainties will in the following also be denoted as statistical uncertainties.
The uncertainties and central values of the physics parameters are in very good agreement between the two fit methods. The difference for most of the parameters is in the order of 10 − 15% of the fit uncertainties. For the polarisation amplitudes the difference is larger due to the limited precision of the background angular description in the classical fit (see Section 9.2).

parameter	classical fit	sFit
ϕ_s (rad)	0.017 ± 0.096	0.004 ± 0.099
$\lvert\lambda_{CP}\rvert$	0.927 ± 0.043	0.928 ± 0.043
$\Delta\Gamma_s$ (ps^{-1})	0.093 ± 0.017	0.095 ± 0.017
Γ_s (ps^{-1})	0.6729 ± 0.0050	0.6725 ± 0.0051
$\lvert A_\perp\rvert^2$	0.253 ± 0.009	0.251 ± 0.009
$\lvert A_0\rvert^2$	0.517 ± 0.006	0.520 ± 0.006
F_s	0.023 ± 0.009	0.027 ± 0.010
$\delta_\parallel$ (rad)	3.296 ± 0.197	3.312 ± 0.184
$\delta_\perp$ (rad)	3.019 ± 0.237	2.966 ± 0.254
$\delta_{s,\perp}$ (rad)	-0.012 ± 0.169	0.006 ± 0.160
Δm_s (ps^{-1}) ⋆	17.660 ± 0.082	17.652 ± 0.084

Table 10.2: Central values and fit uncertainties of the physics parameters extracted from selected $B_s^0 \to J/\psi\phi$ candidates using the classical fit and the sFit technique. Parameters marked with ⋆ are constrained in the fit to external measurements.

The correlations between the physics parameters are listed in Table 10.3. The largest correlations can be observed between $\Delta\Gamma_s$ and the polarisation amplitudes $|A_0|^2$ and $|A_\perp|^2$. The CP violation parameter ϕ_s and $|\lambda_{CP}|$ on the other hand are hardly correlated to any other parameter. In particular it was checked that there is no large correlation between the physics parameters and the remaining nuisance parameters of the background description or the tagging part. For completeness, the fit results for the nuisance parameters are given in Table 10.4.
The one-dimensional projections of the fitted PDF for decay time and angular distributions, obtained from the sFit technique, are shown in Figure 10.2. In the projections, the data is very well described by the fitted PDF.
The presented result corresponds only to one possible solution of the fit. The differential $B_s^0 \to J/\psi\phi$ decay rate allows for an ambiguous solution ($\pi - \phi_s, -\Delta\Gamma_s, -\delta_\parallel, \pi -$

$\delta_\perp, -\pi - \delta_{s,\perp}$). The determination of the true physical result using the dependence of the strong phases on the K^+K^- mass will be discussed in the next chapter.

	Γ_s	$\Delta\Gamma_s$	$\lvert\lambda_{CP}\rvert$	ϕ_s	$\lvert A_0\rvert^2$	$\lvert A_\perp\rvert^2$	F_s	$\delta_\parallel$	$\delta_\perp$	$\delta_{s,\perp}$	Δm_s
Γ_s	1.00	-0.43	-0.01	0.02	-0.30	0.40	0.16	-0.10	-0.04	-	-0.01
$\Delta\Gamma_s$		1.00	-	-0.02	**0.65**	**-0.69**	-0.02	0.03	0.02	0.01	0.02
$\lvert\lambda_{CP}\rvert$			1.00	0.04	0.02	-0.05	0.12	0.10	-0.37	0.04	-0.33
ϕ_s				1.00	-0.02	0.04	0.01	-0.01	0.21	-0.02	0.11
$\lvert A_0\rvert^2$					1.00	**-0.58**	0.07	-0.03	-0.03	0.01	-
$\lvert A_\perp\rvert^2$						1.00	0.03	-0.31	-0.11	0.01	-
F_s							1.00	-0.25	-0.19	0.04	-0.05
$\delta_\parallel$								1.00	0.39	-0.07	-0.01
$\delta_\perp$									1.00	-0.11	**0.55**
$\delta_{s,\perp}$										1.00	-
Δm_s											1.00

Table 10.3: Correlations of physics parameters in the classical fit. Correlations larger than 0.5 are highlighted.

10.2 Sensitivity study

The parameter uncertainties from the fit contain beside a statistical component also the uncertainties related the decay time resolution, tagging calibration and the mixing frequency. In order to test the reliability of the parameter error estimates, a set of pseudo experiments is done. 950 datasets are generated, each of them containing 37361 events, corresponding to the selected number of $B_s^0 \to J/\psi\phi$ candidates used in the fit to data. Their mass, decay time and angular distributions are generated according to the probability density functions and parameter values obtained from the classical fit.
Each of the 950 datasets is fitted with the classical fit method, extracting the central values and estimated fit uncertainties of the parameters. The distribution of the fit uncertainties for the physics parameters are shown in Figure 10.3. Table 10.5 gives the mean of the error distributions, corresponding to the expected parameter sensitivity with the available number of B_s^0 candidates. For comparison the parameter errors obtained from the data fit are shown as well. The parameter uncertainties of the data fit agree well with the expected sensitivity.

parameter	classical fit	sFit
f^1_{bkg}	0.446 ± 0.071	-
f^2_{bkg}	0.235 ± 0.024	-
τ^1_{bkg} (ps)	0.105 ± 0.009	-
τ^2_{bkg} (ps)	1.386 ± 0.081	-
τ^3_{bkg} (ps)	0.290 ± 0.033	-
$s_{\sigma_t}\star$	1.470 ± 0.049	1.470 ± 0.050
$p_0^{\text{OST}}\star$	0.394 ± 0.008	0.394 ± 0.008
$p_1^{\text{OST}}\star$	1.001 ± 0.023	1.001 ± 0.023
$\Delta^{\text{OST}}\star$	0.011 ± 0.003	0.011 ± 0.003
$p_0^{\text{SST}}\star$	0.352 ± 0.016	0.351 ± 0.016
$p_1^{\text{SST}}\star$	1.031 ± 0.157	1.028 ± 0.158
$\Delta^{\text{SST}}\star$	-0.019 ± 0.005	-0.019 ± 0.005
$p_0^{\text{OST+SST}}\star$	0.002 ± 0.024	0.005 ± 0.025
$p_1^{\text{OST+SST}}\star$		-
$\Delta^{\text{OST+SST}}\star$	-0.011 ± 0.004	-0.011 ± 0.004
$\varepsilon^{\text{OST}}_{\text{sig}}$	0.276 ± 0.008	-
$\varepsilon^{\text{SST}}_{\text{sig}}$	0.068 ± 0.004	-
$\varepsilon^{\text{OST+SST}}_{\text{sig}}$	0.041 ± 0.003	-
$\varepsilon^{\text{OST}}_{\text{bkg}}$	0.335 ± 0.013	-
$\varepsilon^{\text{SST}}_{\text{bkg}}$	0.056 ± 0.006	-
$\varepsilon^{\text{OST+SST}}_{\text{bkg}}$	0.035 ± 0.005	-

Table 10.4: Central values and fit uncertainties of the nuisance parameters extracted from selected $B^0_s \to J/\psi\phi$ candidates using the classical fit and the sFit technique. Parameters marked with $\star$ are constrained in the fit.

10.3 Profile likelihood scans

As already discussed in Chapter 9, the error estimation of the maximum likelihood fit assumes a likelihood function which is Gaussian and thus derives symmetric parameter uncertainties. This is justified only for large number of events and has to be checked for the size of the available dataset. Therefore, likelihood ratio scans are performed for each of the physics parameters to obtain their confidence intervals.
For each parameter λ the likelihood ratio $-2\Delta \ln \mathcal{L} = -2(\ln \mathcal{L}(\lambda_{\text{max}}) - \ln \mathcal{L}(\lambda))$ is determined at fixed values of λ in a certain range around the result from the data fit λ_{max}. At each λ value the likelihood is minimised with respect to all other parameters. Figure

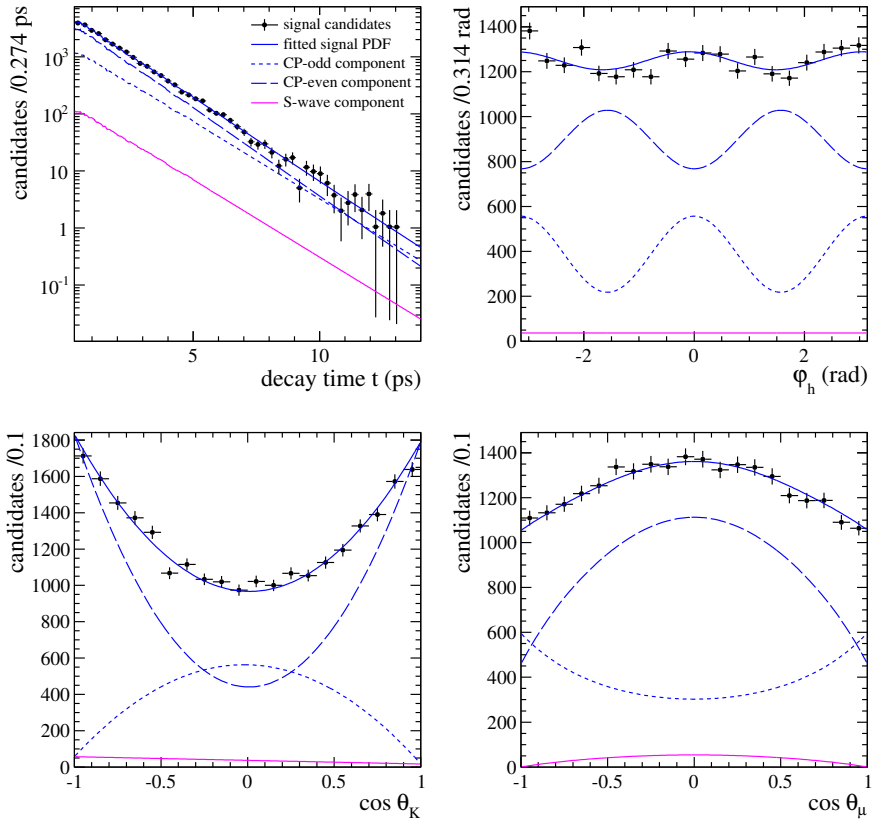

Figure 10.2: Decay time and angular distributions of background subtracted B_s^0 signal candidates, overlaid with the fitted PDF from the sFit technique.

10.4 shows the obtained likelihood ratio curves. For most of the parameters they are nicely parabolic around the minimum reflecting the Gaussian behaviour of the likelihood function. Their 68.3% confidence interval are defined at the parameter values where $-2\Delta \ln \mathcal{L} = 1$ and agree with the error estimates from the fit. Only $\delta_\parallel$ has an asymmetric likelihood ratio which leads to a 68.3% confidence interval of $[2.98, 3.45]$.

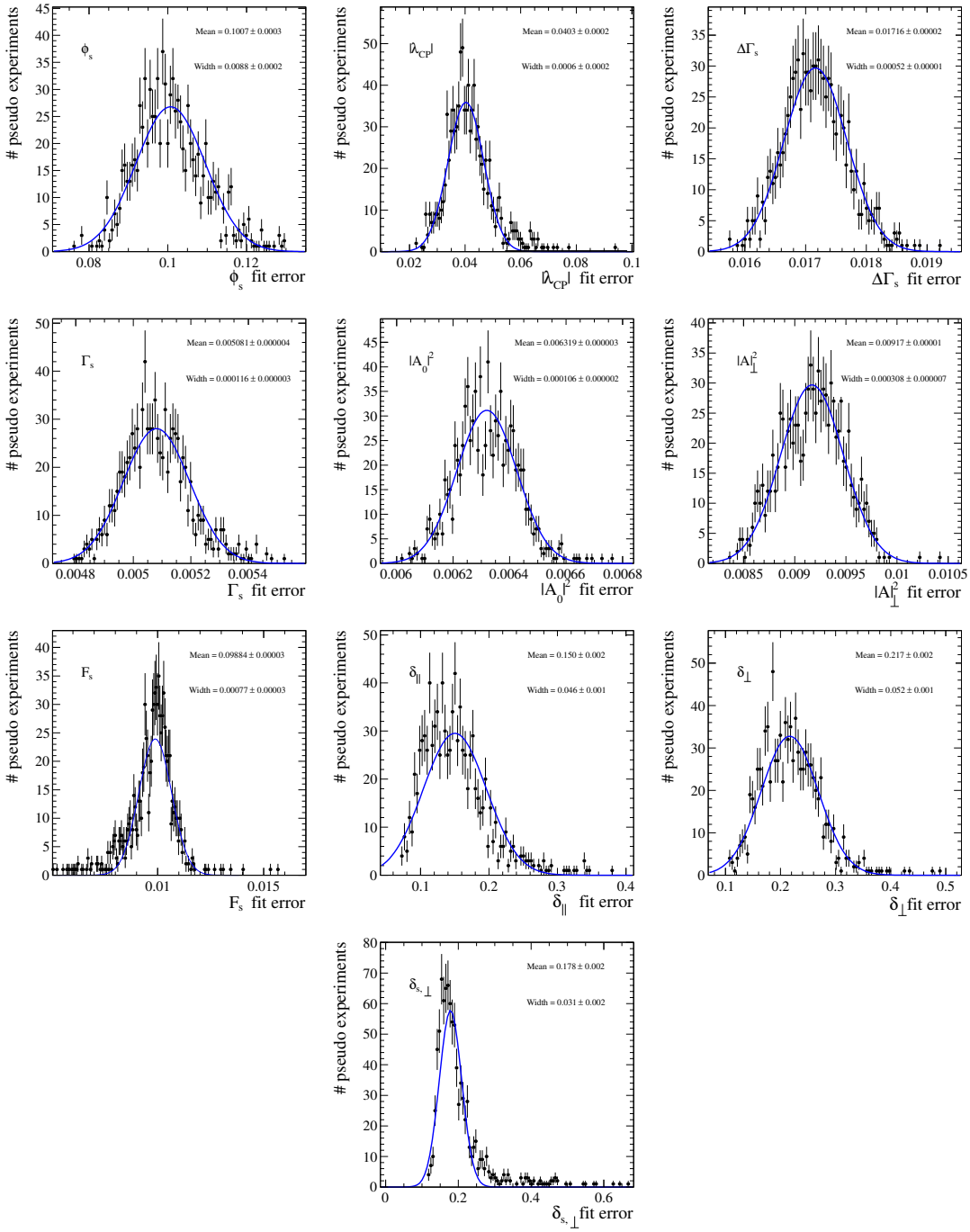

Figure 10.3: Distributions of fit errors of all physics parameters, obtained from 950 pseudo experiments. Each generated dataset contains 37361 events, corresponding to the number of selected $B_s^0 \to J/\psi\phi$ candidates in data. The distributions are fitted with a Gaussian function.

parameter	expected sensitivity	observed sensitivity
ϕ_s[rad]	0.101	0.096
$\lvert\lambda_{CP}\rvert$	0.040	0.043
$\Delta\Gamma_s$[ps^{-1}]	0.017	0.017
Γ_s[ps^{-1}]	0.0051	0.0050
$\lvert A_\perp\rvert^2$	0.009	0.009
$\lvert A_0\rvert^2$	0.006	0.006
F_s	0.010	0.009
$\delta_\parallel$[rad]	0.150	0.197
$\delta_\perp$[rad]	0.217	0.237
$\delta_{s,\perp}$ rad]	0.178	0.169

Table 10.5: Expected and observed fit uncertainties of the physics parameters. The expected sensitivity is determined from 950 pseudo experiments.

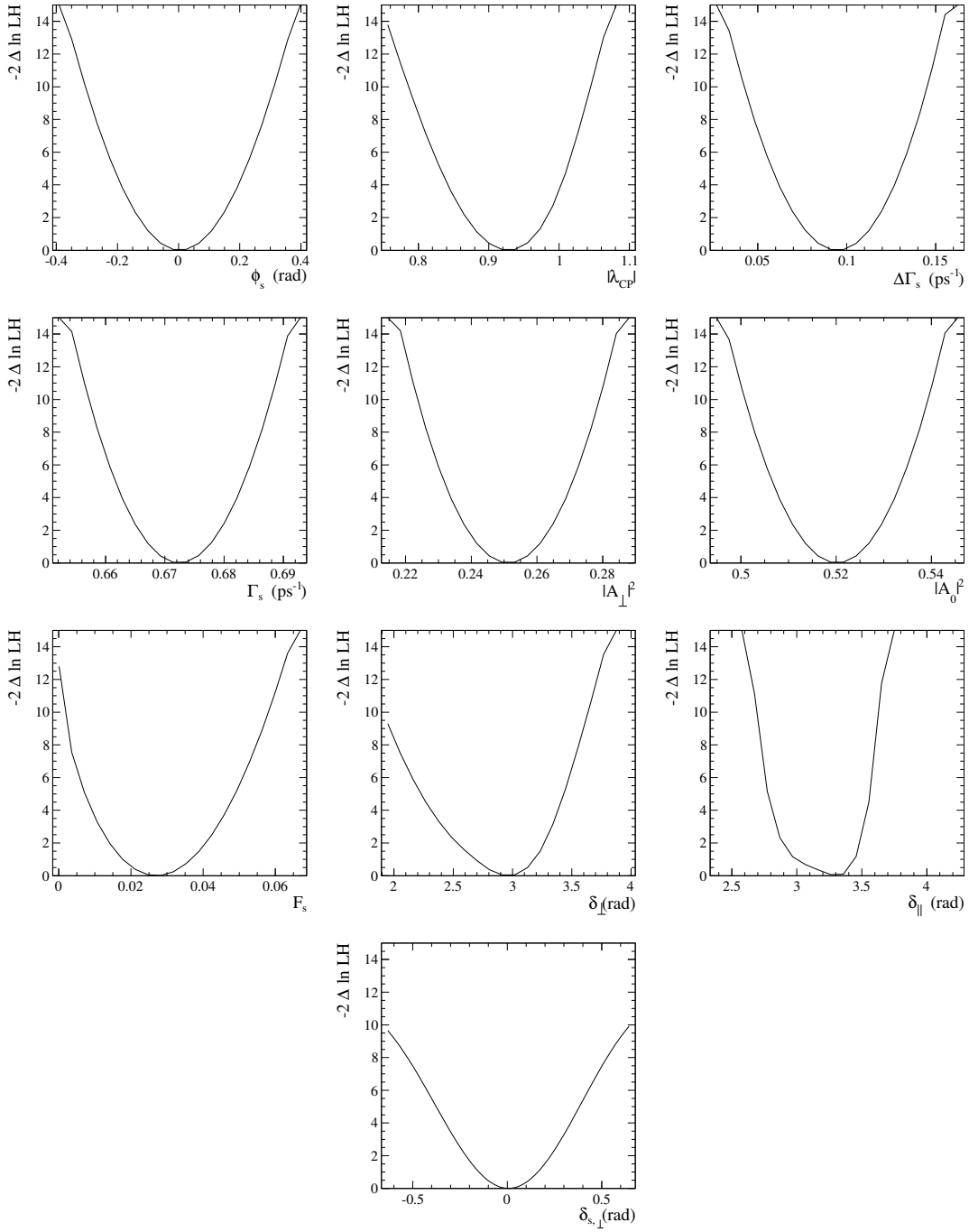

Figure 10.4: Likelihood ratio $-2\Delta \ln \mathcal{L}$ of the physics parameters, as a function of the paramter value.

CHAPTER 11

Fit results resolving the ϕ_s-$\Delta\Gamma_s$ ambiguity

The differential decay rate describing the $B_s^0 \to J/\psi\phi$ decay is invariant under a transformation of $(\phi_s, \Delta\Gamma_s, \delta_\parallel, \delta_\perp, \delta_s, \delta_0)$ to $(\pi - \phi_s, -\Delta\Gamma_s, -\delta_\parallel, \pi - \delta_\perp, -\delta_s, -\delta_0)$, in the following referred to as solution 1 ($\Delta\Gamma_s > 0.0\,\mathrm{ps}^{-1}$) and solution 2 ($\Delta\Gamma_s < 0.0\,\mathrm{ps}^{-1}$). The solution with $\Delta\Gamma_s > 0.0\,\mathrm{ps}^{-1}$, as obtained in the last chapter, is compatible with the Standard Model predictions of the CP-violating phase ϕ_s, while the ambiguous solution is not. To test the Standard Model hypothesis it is mandatory to resolve this ambiguity and find the correct parameter set. This can be done by fitting the relative P-and S-wave phases as a function of the invariant K^+K^- mass. The principle idea of this method and the fit implementation as well as the final results will be presented in the following chapter.

11.1 Method of resolving the ambiguity

The ambiguity in the differential $B_s^0 \to J/\psi\phi$ decay rate can be resolved by measuring the strong phase difference between the P- and S-wave amplitudes as a function of the reconstructed K^+K^- mass $m_{K^+K^-}$. The dependence of the resonant P-wave amplitudes on $m_{K^+K^-}$ can be described by a non-relativistic Breit-Wigner function

$$g(m_{K^+K^-}) \propto \frac{1}{m_{K^+K^-} - m^{\phi}_{K^+K^-} + i\Gamma_\phi/2}\,, \tag{11.1}$$

where $m^{\phi}_{K^+K^-}$ is the ϕ mass (1020 MeV), Γ_ϕ is the ϕ width (4.26 MeV). The phase of this Breit-Wigner amplitude rises rapidly through the ϕ mass region. The S-wave amplitude can either be described by a flat function $v(m_{K^+K^-}) \propto 1$, representing a non-resonant $B^0_s \to J/\psi K^+K^-$ contribution or by a Flatté function [72], representing an intermediate $f_0(980)$ resonance. In both cases the phase of the S-wave amplitude is expected to vary slowly as a function of $m_{K^+K^-}$. Figure 11.1 shows the dependence of a Breit-Wigner phase and a flat model phase on $m_{K^+K^-}$.
Following Equation 2.54 the $m_{K^+K^-}$ dependence of the strong phases $\delta_\perp$, $\delta_\parallel$ and δ_0 is described by the Breit-Wigner phase and the dependence of δ_s is described by the flat model phase. As a consequence the phase difference between P- and S-wave amplitudes, e.g. $\delta_{s,\perp} = \delta_s - \delta_\perp$, should decrease with $m_{K^+K^-}$. This expected behaviour can be used to single out the physically correct phase set. The correct solution of the differential decay rate shows the expected $m_{K^+K^-}$ behaviour, while for the unphysical solution the phase difference should rise as a function of $m_{K^+K^-}$. More details can be found in [75].
As all P-wave phases have the same $m_{K^+K^-}$ dependence, any of the P- and S-wave phase differences $\delta_s - \delta_i$ with $i = \{0, \parallel, \perp\}$ could be used to determine the physically correct solution. For this analysis the phase difference $\delta_{s,\perp}$ is chosen. The measured $B^0_s \to J/\psi\phi$ dataset is split in intervals of $m_{K^+K^-}$ and both fitting techniques, introduced in the previous chapters, are used to determine $\delta_{s,\perp}$ in each $m_{K^+K^-}$ interval.

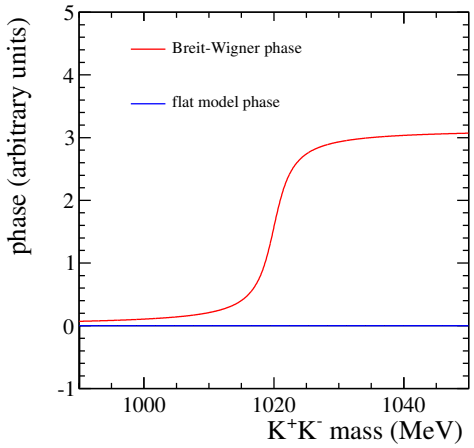

Figure 11.1: Phase dependence of Breit-Wigner amplitude $g(m_{K^+K^-})$ and flat amplitude $v(m_{K^+K^-})$ on the K^+K^- mass.

11.2 Extracting the physics parameters in bins of $m_{K^+K^-}$

In order to perform the parameter determination as a function of $m_{K^+K^-}$ over a large $m_{K^+K^-}$ region, the considered K^+K^- mass window is enlarged to [990 MeV, 1050 MeV].

The total number of selected events after enlarging the mass window is $N = 54762$. Figure 11.2 shows the reconstructed B_s^0 mass distribution of all selected events. The distribution is fitted with a sum of two Gaussian functions describing the signal and a linear function describing the background component. The number of signal events increases slightly by 12% to $N_{\text{sig}} = 27897 \pm 203$, while the number of background events increases by a factor 2.2. This is not surprising as a widening of the $m_{K^+K^-}$ window also increases the amount of combinatorial background. The signal to background level in a B_s^0 mass interval of [5320 MeV, 5420 MeV] stays with $\frac{S}{B} = 3.62$ nevertheless high. However, the description of the background component in the classical maximum likelihood fit becomes more critical than for the analysis of the previous chapter.

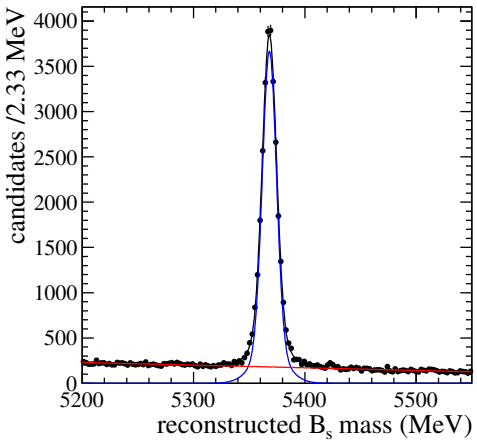

Figure 11.2: B_s^0 mass distribution of selected $B_s^0 \to J/\psi\phi$ candidates in a K^+K^- mass interval [990 MeV, 1050 MeV]. The distribution is fitted with two Gaussian functions, describing the signal component and a linear function, describing the background component.

11.2.1 The fitting conditions

The datasample is split in six subsamples depending on the reconstructed K^+K^- mass. The $m_{K^+K^-}$ intervals are given in Table 11.1 with the corresponding number of B_s^0 candidates for each interval. The K^+K^- mass distribution is shown in Figure 11.3 with indicated bins.

A simultaneous fit is performed, using one common likelihood function for all six subsamples. For each of the subsamples a separate S-wave fraction F_s and phase difference $\delta_{s,\perp}$ is extracted. The other physics parameters have no dependence on $m_{K^+K^-}$ and are common for each mass interval. This is in particular true for the P-wave amplitudes

bin	$m_{K^+K^-}$ interval (MeV)	number of B_s^0 candidates
1	990 - 1008	5231
2	1008 - 1016	6121
3	1016 - 1020	12634
4	1020 - 1024	10936
5	1024 - 1032	7645
6	1032 - 1050	12187

Table 11.1: K^+K^- mass intervals used to divide the selected B_s^0 candidates in six $m_{K^+K^-}$ bins.

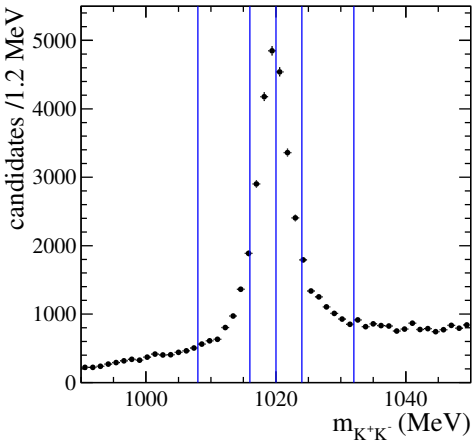

Figure 11.3: K^+K^- mass distribution for all selected B_s^0 candidates with 30 MeV $m_{K^+K^-}$ mass window.

$|A_\perp|^2$ and $|A_0|^2$ which fulfill, following Section 9.2, in each interval the normalisation condition $|A_\perp|^2 + |A_0|^2 + |A_\parallel|^2 = 1$. The $m_{K^+K^-}$ dependence of the strong P-wave phases is identical for the three polarisations. By parameterising the P-and S-wave phase difference with $\delta_{s,\perp} = \delta_s - \delta_\perp$ and using the convention $\delta_0 = 0$ in each $m_{K^+K^-}$ interval, the remaining P-wave phase parameters $\delta_\perp$ and $\delta_\parallel$ are as well simultaneously fitted all mass intervals.
Both, the classical fitting technique as well as the sFit technique are applied, using the same treatment of acceptances, decay time resolution and tagging as in the previous chapter. For the PDFs several changes are introduced:

- The factor C_{sp} that corrects the differential decay rate for the different $m_{K^+K^-}$ dependence of P- and S-Wave amplitudes in a certain mass interval, is calculated separately for each $m_{K^+K^-}$ bin. The values are shown in Table 11.2. The smaller mass intervals compared to the single bin fit in the last chapter lead to corrections factors that are are closer to 1.

$m_{K^+K^-}$ bin (MeV)	$C_{\rm sp}$
990 - 1008	0.966
1008 - 1016	0.956
1016 - 10020	0.926
1020 - 1024	0.926
1024 - 1032	0.956
1032 - 1050	0.966

Table 11.2: P- and S-wave coupling correction factors $C_{\rm sp}$ for the six $m_{K^+K^-}$ intervals. They are calculated assuming a Breit-Wigner shape of the P-wave amplitudes and a flat shape of the S-wave amplitudes.

- The parameters of the mass PDFs describing the signal distributions are common to all six subsamples. The background mass parameter $\alpha_{\rm m}$ and the signal fractions $f_{\rm sig}^{\rm b}$ and $f_{\rm sig}^{\rm ub}$ are fitted separately for the different $m_{K^+K^-}$ bins.

- The histograms, that are used in the classical fit as probability density functions for the conditional variables $\sigma_{\rm t}$ and $\omega_{\rm C}$, are updated with the full statistics in the [990 MeV, 1050 MeV] $m_{K^+K^-}$ interval. The same histograms are used for all six subsamples.

- The histogram describing the background angular distribution is remade for the datasample with the enlarged $m_{K^+K^-}$ mass interval. Due to the larger amount of background it is possible to increase the number of bins in the three-dimensional histogram. The corresponding two dimensional distributions are shown in Figure 11.4. There is no obvious difference compared to the histogram determined in the smaller $m_{K^+K^-}$ mass range, shown in Figure 9.2.
  In principle the decay time and angular distribution of the background candidates can depend on the K^+K^- mass. They are shown in Figure 11.5 for background candidates from the B_s^0 mass sidebands separately for different $m_{K^+K^-}$ bins. The background shapes look very similar for different K^+K^- masses although a definite statement is due to the low background statistics not possible. In the classical fit, the PDF describing the decay time and angular background will be used simultaneously for all $m_{K^+K^-}$ bins.

11.2.2 Fit results

Both classical fit and sFit are used to determine the physics parameters for the two possible minima of the differential decay rate ($\phi_{\rm s}, \Delta\Gamma_{\rm s}, \delta_{\parallel}, \delta_{\perp}, \delta_{\rm s}, \delta_0$) and ($\pi-\phi_{\rm s}, -\Delta\Gamma_{\rm s}, -\delta_{\parallel}, \pi-\delta_{\perp}, -\delta_{\rm s}, -\delta_0$). The results of the physics parameters that are fitted simultaneously in all $m_{K^+K^-}$ intervals are shown in Table 11.3. Considering the 12% gain in signal yield the extracted parameter values are compatible with the results obtained in the previous

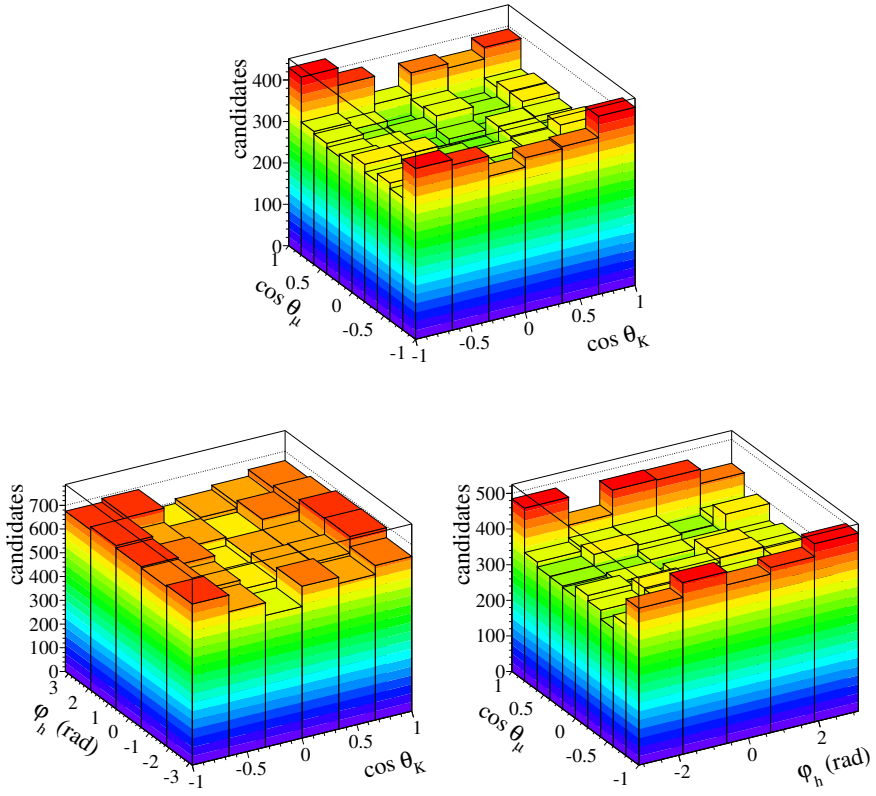

Figure 11.4: Two-dimensional helicity angle distributions of $B_s^0 \to J/\psi\phi$ background candidates in the B_s^0 mass sidebands [5205 MeV, 5325 MeV] and [5400 MeV, 5520 MeV].

chapter (see Table 10.2).
The results for the S-wave fraction F_s and the phase difference $\delta_{s,\perp}$ for the six $m_{K^+K^-}$ intervals are shown in Table 11.4 for the solution with $\Delta\Gamma_s > 0\,\text{ps}^{-1}$ and in Table 11.5 for the solution with $\Delta\Gamma_s < 0\,\text{ps}^{-1}$. For both classical fit and sFit a clear trend of decreasing $\delta_{s,\perp}$ is visible for the first solution while for the second solution $\delta_{s,\perp}$ is increasing as function of $m_{K^+K^-}$.
The error estimate of the fit was tested by doing likelihood ratio scans for all physics parameters. Especially the likelihood ratios of the phase parameters $\delta_{s,\perp}$ and the S-wave fractions F_s for the six bins, shown in Figure 11.6, have asymmetric shapes and are therefore used to assign the 68.3% confidence intervals.
The projections of the fitted signal PDFs on the decay time and angular distributions using the sFit technique are shown in Figure 11.7. The plotted distributions are background subtracted and are well described by the fitted signal PDF.

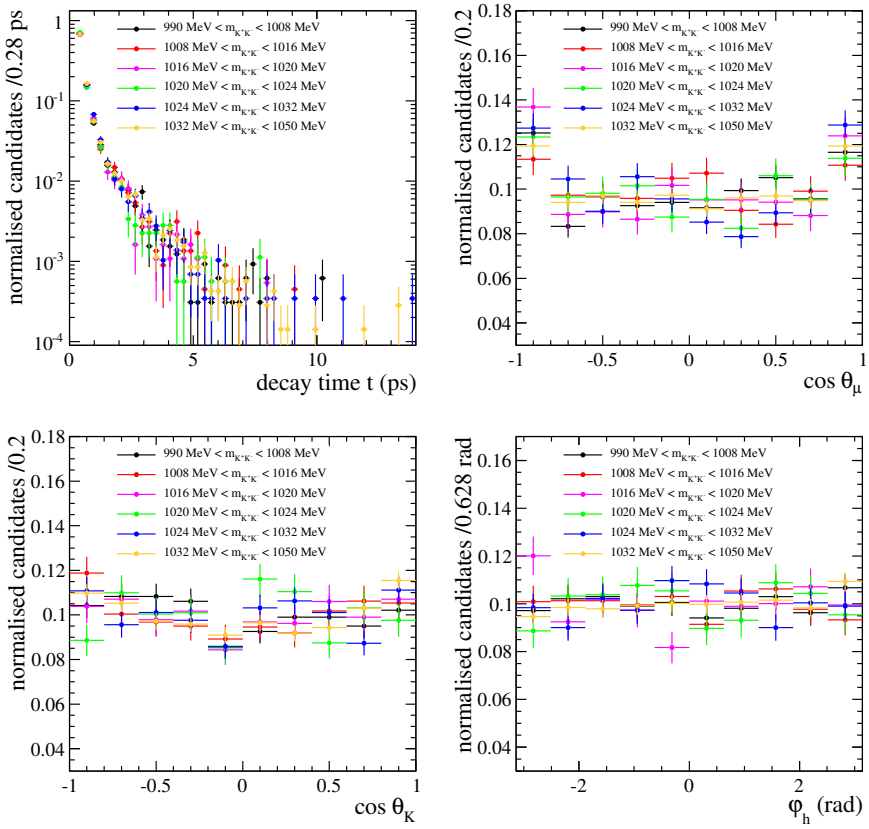

Figure 11.5: Decay time and angular distributions of $B_s^0 \to J/\psi\phi$ background candidates for different $m_{K^+K^-}$ intervals.

The agreement between the classical fitting technique and the sFit is comparable to the results in the smaller $m_{K^+K^-}$ range. For most of the physics parameters the differences are much smaller than the statistical uncertainty. Only for the S-wave parameters in the lowest and highest $m_{K^+K^-}$ bin the difference is in the order of the statistical error. Due to the higher number of simultaneously fitted parameters, the classical fit is more time-consuming and unstable than the sFit when treating the six $m_{K^+K^-}$ intervals separately. This could result in problems when performing the necessary systematic studies and cross-checks. Therefore the sFit technique will be used for the systematic studies. The sFit results from the fit of the six $m_{K^+K^-}$ intervals will be used when quoting a final result.

Figure 11.8 shows the $\delta_{s,\perp}$ results of the sFit for both solutions of the B_s^0 decay rate as a function of $m_{K^+K^-}$. The decreasing trend of $\delta_{s,\perp}$ is the physical solution and corresponds to solution 1 in Table 11.3.

Figure 11.9 shows the corresponding two-dimensional ϕ_s-$\Delta\Gamma_s$ confidence intervals. They are obtained by a likelihood ratio scan in two dimensions. At each fixed ϕ_s-$\Delta\Gamma_s$ grid point the likelihood function is minimised with respect to all other parameters

in the fit (see Section 9.1). The resulting confidence intervals include only the fit uncertainties. The obtained results are within the 68% confidence interval in agreement with the Standard Model expectation for ϕ_s and $\Delta\Gamma_s$. The systematic uncertainties of this analysis procedure will be evaluated in the next chapter.

	solution 1		solution 2	
parameter	classical fit	sFit	classical fit	sFit
ϕ_s[rad]	0.068 ± 0.090	0.069 ± 0.091	3.074 ± 0.090	3.072 ± 0.091
$\lvert\lambda_{CP}\rvert$	0.949 ± 0.028	0.944 ± 0.030	0.949 ± 0.028	0.944 ± 0.030
$\Delta\Gamma_s$[ps^{-1}]	0.095 ± 0.016	0.100 ± 0.016	-0.095 ± 0.016	-0.100 ± 0.016
Γ_s[ps^{-1}]	0.6752 ± 0.0047	0.6726 ± 0.0048	0.6752 ± 0.0047	0.6726 ± 0.0048
$\lvert A_\perp\rvert^2$	0.251 ± 0.009	0.249 ± 0.009	0.251 ± 0.009	0.249 ± 0.009
$\lvert A_0\rvert^2$	0.517 ± 0.006	0.521 ± 0.006	0.517 ± 0.006	0.521 ± 0.006
$\delta_\parallel$[rad]	$3.288^{+0.133}_{-0.214}$	$3.308^{+0.128}_{-0.213}$	$-3.287^{+0.133}_{-0.214}$	$-3.308^{+0.128}_{-0.213}$
$\delta_\perp$[rad]	3.065 ± 0.221	3.069 ± 0.219	0.079 ± 0.221	0.073 ± 0.219
Δm_s[ps^{-1}] $\star$	17.659 ± 0.077	17.667 ± 0.077	17.659 ± 0.077	17.667 ± 0.077

Table 11.3: Central values and fit uncertainties of the physics parameters extracted from selected $B_s^0 \to J/\psi\phi$ candidates using the classical fit and the sFit technique. Parameters marked with $\star$ are constrained in the fit.

$m_{K^+K^-}$ bin (MeV)	parameter	classical fit	sFit
990 - 1008	F_s	$0.339^{+0.085}_{-0.082}$	$0.227^{+0.082}_{-0.073}$
	$\delta_{s,\perp}$ [rad]	$0.900^{+0.437}_{-0.293}$	$1.310^{+0.787}_{-0.493}$
1008 - 1016	F_s	$0.072^{+0.029}_{-0.027}$	$0.067^{+0.030}_{-0.027}$
	$\delta_{s,\perp}$ [rad]	$0.678^{+0.301}_{-0.203}$	$0.769^{+0.389}_{-0.233}$
1016 - 1020	F_s	$0.008^{+0.013}_{-0.007}$	$0.008^{+0.014}_{-0.007}$
	$\delta_{s,\perp}$ [rad]	$0.522^{+1.180}_{-0.302}$	$0.482^{+1.320}_{-0.291}$
1020 - 1024	F_s	$0.015^{+0.012}_{-0.009}$	$0.016^{+0.012}_{-0.009}$
	$\delta_{s,\perp}$ [rad]	$-0.537^{+0.222}_{-0.373}$	$-0.512^{+0.215}_{-0.356}$
1024 - 1032	F_s	$0.043^{+0.026}_{-0.023}$	$0.056^{+0.027}_{-0.025}$
	$\delta_{s,\perp}$ [rad]	$-0.545^{+0.216}_{-0.368}$	$-0.451^{+0.183}_{-0.255}$
1032 - 1050	F_s	$0.185^{+0.040}_{-0.038}$	$0.168^{+0.043}_{-0.042}$
	$\delta_{s,\perp}$ [rad]	$-0.564^{+0.153}_{-0.176}$	$-0.653^{+0.183}_{-0.225}$

Table 11.4: Central values and fit uncertainties of the S-wave parameters for solution 1, extracted from selected $B^0_s \to J/\psi\phi$ candidates using the classical fit and the sFit technique.

$m_{K^+K^-}$ bin (MeV)	parameter	classical fit	sFit
990 - 1008	F_s	$0.339^{+0.085}_{-0.082}$	$0.227^{+0.081}_{-0.073}$
	$\delta_{s,\perp}$ [rad]	$2.242^{+0.293}_{-0.438}$	$1.832^{+0.494}_{-0.787}$
1008 - 1016	F_s	$0.072^{+0.029}_{-0.027}$	$0.067^{+0.030}_{-0.027}$
	$\delta_{s,\perp}$ [rad]	$2.463^{+0.203}_{-0.300}$	$2.373^{+0.233}_{-0.389}$
1016 - 1020	F_s	$0.008^{+0.013}_{-0.007}$	$0.008^{+0.014}_{-0.007}$
	$\delta_{s,\perp}$ [rad]	$2.620^{+0.301}_{-1.180}$	$2.660^{+0.291}_{-1.319}$
1020 - 1024	F_s	$0.015^{+0.012}_{-0.009}$	$0.016^{+0.012}_{-0.009}$
	$\delta_{s,\perp}$ [rad]	$3.678^{+0.373}_{-0.222}$	$3.653^{+0.358}_{-0.215}$
1024 - 1032	F_s	$0.043^{+0.026}_{-0.023}$	$0.056^{+0.027}_{-0.025}$
	$\delta_{s,\perp}$ [rad]	$3.686^{+0.368}_{-0.215}$	$3.592^{+0.255}_{-0.183}$
1032 - 1050	F_s	$0.185^{+0.040}_{-0.038}$	$0.168^{+0.043}_{-0.042}$
	$\delta_{s,\perp}$ [rad]	$3.706^{+0.176}_{-0.153}$	$3.794^{+0.225}_{-0.183}$

Table 11.5: Central values and fit uncertainties of the S-wave parameters for solution 2, extracted from selected $B^0_s \to J/\psi\phi$ candidates using the classical fit and the sFit technique.

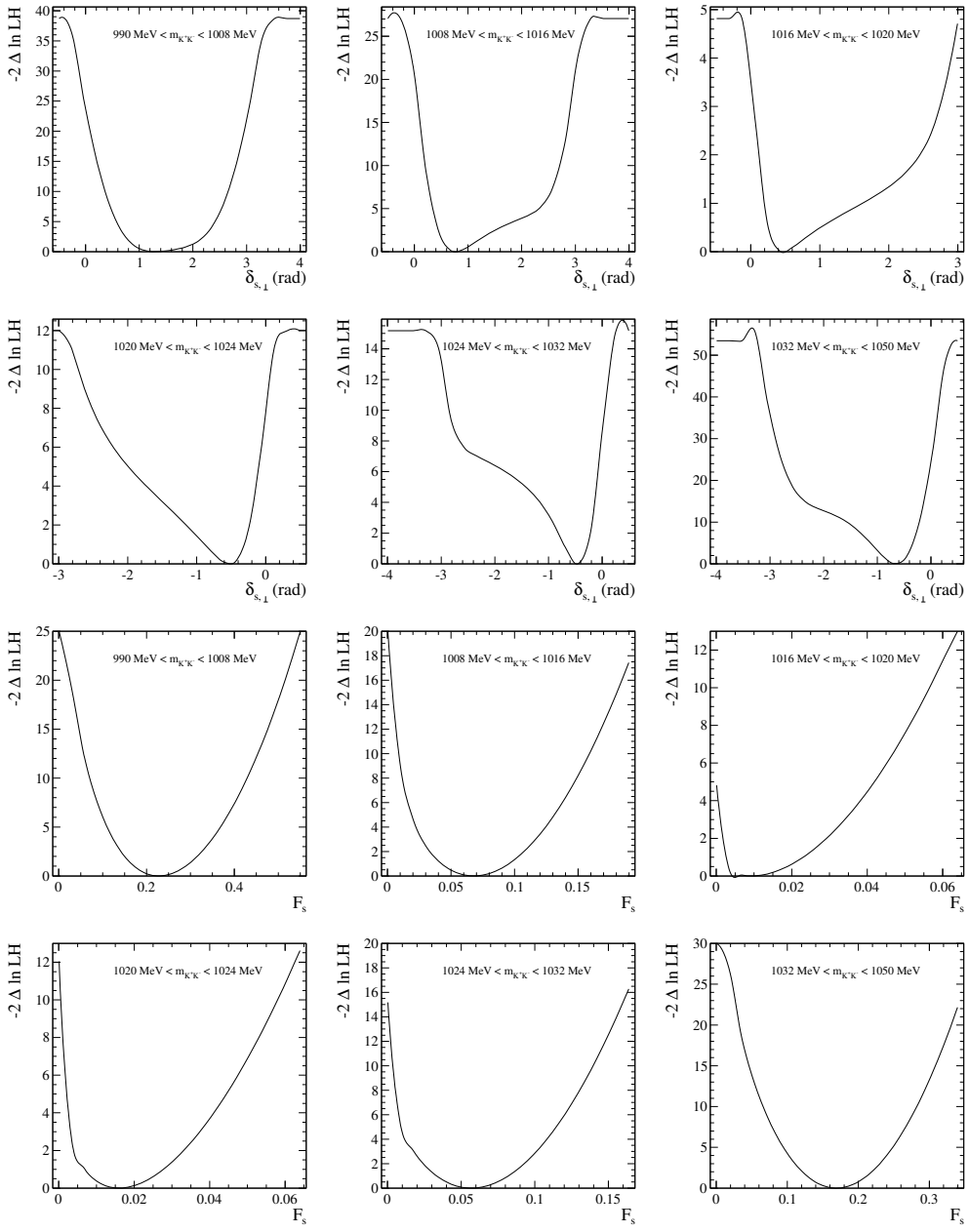

Figure 11.6: Likelihood ratio scans of the phase difference $\delta_{s,\perp}$ and the S-wave fraction F_s for the six $m_{K^+K^-}$ intervals.

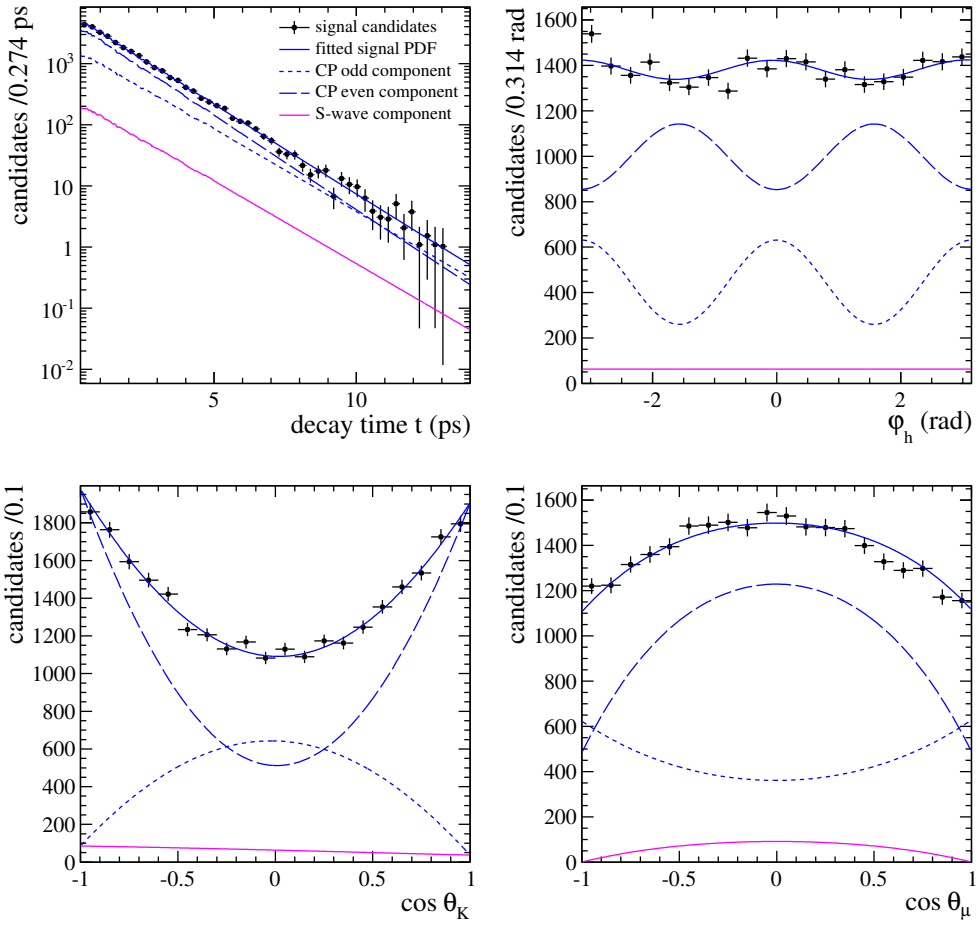

Figure 11.7: Decay time and angular distributions of background subtracted $B_s^0 \to J/\psi\phi$ signal candidates, overlaid with the fitted PDF from the sFit technique.

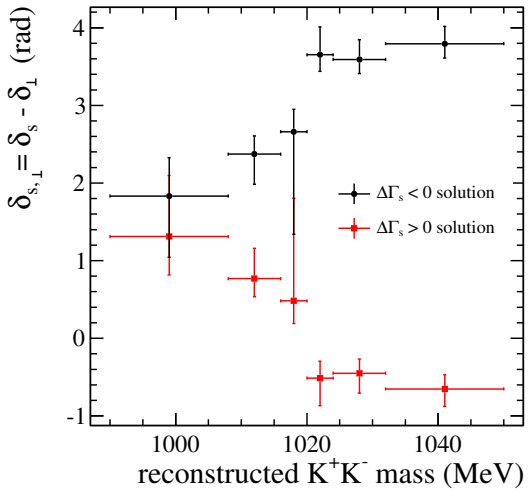

Figure 11.8: Measured K^+K^- mass trend of the phase difference of P-wave and S-wave amplitudes, $\delta_{s,\perp} = \delta_s - \delta_\perp$, for the two possible solutions of the differential $B_s^0 \to J/\psi\phi$ decay rate. The error bars include only the uncertainties of the fit.

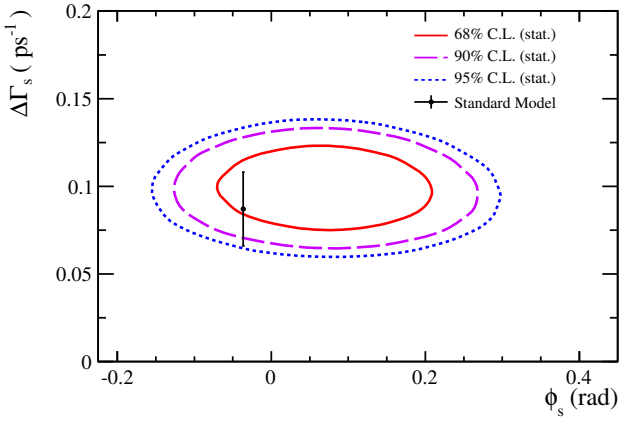

Figure 11.9: Two-dimensional ϕ_s-$\Delta\Gamma_s$ confidence intervals determined from a likelihood ratio scan using the sFit technique. The black point shows the Standard Model expectation.

CHAPTER 12

Systematic uncertainties

Several possible sources of systematic uncertainties have to be investigated in this analysis. Some of them are already taken into account in the errors of the fitted parameters. Other possible uncertainties occur for example from the background description or the decay time and angular acceptances. The systematic errors will be evaluated in the following chapter for all physics parameters including the S-wave parameter in the six bins of K^+K^- mass.

12.1 Decay time resolution, tagging calibration, mixing frequency

Systematic effects from the decay time resolution, the tagging calibration and the mixing frequency are already accounted for by the fit uncertainties. The decay time resolution model is determined from J/ψ decays produced directly in the proton-proton interaction. The scaling factor for the estimated event-dependent resolution is floated in the fit, constrained to $s_{\sigma_t} = 1.47 \pm 0.05$, where the error represents the statistical uncertainty of the scale factor and the uncertainty related to differences in the resolution between signal and prompt background candidates.
The parameters of the tagging calibration, given in Table 6.1, are floated in the fit constrained to their statistical and systematic uncertainties from the calibration method. In addition a possible difference in the tagging performance for produced B_s^0 and $\overline{B}_s^0$ mesons is allowed in the tagging parameterisation.

The uncertainty of the mixing frequency is taken into account by constraining Δm_s in the fit to the value from a previous measurement, $\Delta m_s = 17.63 \pm 0.11\,\mathrm{ps}^{-1}$.
The overall contribution of the uncertainties from time resolution, tagging calibration and mixing frequency on the ϕ_s fit uncertainty is $< 3\%$.

12.2 Mass model

In the sFit technique a fit to the B_s^0 mass distribution is used to determine the sWeights and separate the signal and background fractions. To estimate a possible systematic effect due to the choice of the mass model, the fit is repeated using an alternative mass PDF. A modified symmetric Crystal-Ball function [60] (see also Section 5.4), with tails on both sides of the distribution, is used to model the signal component and a linear function to model the background. The difference of the fit results to the nominal values are given in Table 12.1. They are assigned as systematic errors to the physics parameters. For all parameters, the effect of a different mass model is negligible compared to the fit uncertainties.

parameter		shift in fit result
ϕ_s (rad)		0.001
$\lvert\lambda_{CP}\rvert$		-
$\Delta\Gamma_s$ (ps^{-1})		-
Γ_s (ps^{-1})		0.0008
$\lvert A_\perp\rvert^2$		0.001
$\lvert A_0\rvert^2$		0.001
$\delta_\parallel$ (rad)		0.006
$\delta_\perp$ (rad)		0.003
$m_{K^+K^-}$ bin 1	F_s	0.003
	$\delta_{s,\perp}$ (rad)	0.012
$m_{K^+K^-}$ bin 2	F_s	-
	$\delta_{s,\perp}$ (rad)	0.002
$m_{K^+K^-}$ bin 3	F_s	-
	$\delta_{s,\perp}$ (rad)	0.002
$m_{K^+K^-}$ bin 4	F_s	-
	$\delta_{s,\perp}$ (rad)	0.003
$m_{K^+K^-}$ bin 5	F_s	-
	$\delta_{s,\perp}$ (rad)	-
$m_{K^+K^-}$ bin 6	F_s	0.001
	$\delta_{s,\perp}$ (rad)	0.003

Table 12.1: Absolute shift in the fit results when changing the mass model in the determination of the sWeight to a modified Crystal-ball function for the signal and a linear function for the background description. "-" indicates no shift is observed.

12.3 Background description

The background description in this analysis leads to two possible sources of systematic uncertainties: The statistical subtraction of the combinatorial background component in the sFit technique and a possible contribution of true $B_d^0 \to J/\psi K^{*0}$ decays. Both will be evaluated in the following.

12.3.1 Background treatment

The sFit technique requires the invariant B_s^0 mass to be uncorrelated to the decay time and angular distributions. It relies on a single fit of the B_s^0 mass distribution to determine the weights for each candidate, independent of its measured decay time and helicity angles.
To estimate the reliability of this method, the full dataset is divided in three bins of decay time and decay angles, in total 3×4 bins. The bins are listed in Table 12.2. They are chosen to contain approximately the same number of B_s^0 candidates. The mass distribution of the candidates in each of the 12 bins is fitted separately, leading to different mass parameters depending on the decay time or helicity angle bin. The mass parameters are used to calculate 12 different sets of sWeights for the full dataset. For each set of weights the full maximum likelihood fit is repeated and the shift of the parameter results with respect to the nominal fit result evaluated. The maximal shifts in the t, $\cos\theta_{\rm k}$, $\cos\theta_\mu$ and $\varphi_{\rm h}$ bins are given in Table 12.3. Their quadratic sum is assigned as systematic uncertainty to the physics parameters. This largest uncertainty is introduced for $\Gamma_{\rm s}$, where the evaluated systematic error is $\sim 77\%$ of the statistical uncertainty. Also $\phi_{\rm s}$ and $\Delta\Gamma_{\rm s}$ are affected by $\sim 7\%$ and $\sim 20\%$ of their statistical uncertainties. The shift of the phase difference $\delta_{\rm s,\perp}$ is in average $\sim 10\%$ of the statistical errors.

bins	t (ps)	$\cos\theta_{\rm k}$	$\cos\theta_\mu$	$\varphi_{\rm h}$ rad
1	$[0.3, 1.5]$	$[-1.0, -0.5]$	$[-1.0, -0.5]$	$[-\pi, -\frac{1}{3}\pi]$
2	$[1.5, 2.5]$	$[-0.5, 0.5]$	$[-0.5, 0.5]$	$[-\frac{1}{3}\pi, \frac{1}{3}\pi]$
3	$[2.5, 14.0]$	$[0.5, 1.0]$	$[0.5, 1.0]$	$[\frac{1}{3}\pi, \pi]$

Table 12.2: Decay time and angles bins used to determine separate sets of mass parameters and sWeights.

12.3.2 Peaking background

The amount of wrongly reconstructed $B_d^0 \to J/\psi K^{*0}$ decays in the $m_{K^+K^-}$ mass range is estimated following the procedure described in Section 5.4. The fraction of $B_d^0 \to J/\psi K^{*0}$ background candidates is found to be $\sim 1.5\%$ relative to the signal events. This was not taken into account in the fit and could lead to a bias of the extracted parameter

parameter		shift due to sWeigths calculated in bins of t	$\cos\theta_k$	$\cos\theta_\mu$	φ_h	quadratic sum
ϕ_s (rad)		0.007	0.001	0.001	0.001	0.007
$\lvert\lambda_{CP}\rvert$		0.001	0.001	-	0.001	0.002
$\Delta\Gamma_s$ (ps^{-1})		0.002	-	0.001	0.001	0.003
Γ_s (ps^{-1})		0.0017	0.0008	0.0031	0.0005	0.0037
$\lvert A_\perp\rvert^2$		0.002	-	0.002	-	0.003
$\lvert A_0\rvert^2$		0.002	0.001	0.003	0.001	0.004
$\delta_\parallel$ (rad)		0.004	0.007	0.030	0.004	0.031
$\delta_\perp$ (rad)		0.013	0.007	0.016	0.004	0.022
$m_{K^+K^-}$ bin 1	F_s	0.025	0.003	0.010	-	0.027
	$\delta_{s,\perp}$ (rad)	0.110	0.022	0.017	0.001	0.113
$m_{K^+K^-}$ bin 2	F_s	0.001	0.001	-	0.001	0.002
	$\delta_{s,\perp}$ (rad)	0.011	0.008	0.010	0.010	0.020
$m_{K^+K^-}$ bin 3	F_s	-	-	0.001	-	0.001
	$\delta_{s,\perp}$ (rad)	0.012	0.010	0.012	0.014	0.024
$m_{K^+K^-}$ bin 4	F_s	-	-	0.001	-	0.001
	$\delta_{s,\perp}$ (rad)	0.006	0.002	0.022	0.008	0.024
$m_{K^+K^-}$ bin 5	F_s	-	0.001	0.004	-	0.004
	$\delta_{s,\perp}$ (rad)	0.004	0.001	0.001	0.001	0.004
$m_{K^+K^-}$ bin 6	F_s	-	0.002	0.005	0.001	0.006
	$\delta_{s,\perp}$ (rad)	0.008	0.002	0.009	0.003	0.013

Table 12.3: Shift in fit results when using sWeights determined from events in different bins of decay time t and decay angles $\cos\theta_k$, $\cos\theta_\mu$ and φ_h. Each column gives the maximum shift of results from three bins, indicated in Table 12.2.

values. In order to evaluate a systematic uncertainty, simulated $B_d^0 \to J/\psi K^{*0}$ candidates are added to the $B_s^0 \to J/\psi\phi$ datasample corresponding to the estimated fractions. They are randomly chosen from the simulated $B_d^0 \to J/\psi K^{*0}$ sample and reflect the decay time and angular distributions shown in Figure 5.7. The candidates are added with negative weight and thus by repeating the sFit on the combined dataset statistically subtracted. The shifts of the parameter values relative to the nominal fit result are given in Table 12.4 and are assigned as systematic uncertainty. The effect is for all parameters small compared to the statistical uncertainties. For ϕ_s, the systematic error due to the peaking background component is $\sim 8\%$ of the statistical uncertainties. For the other parameters the effect is even smaller.

parameter		shift in fit result
ϕ_s (rad)		0.007
$\lvert\lambda_{CP}\rvert$		0.001
$\Delta\Gamma_s$ (ps^{-1})		0.0008
Γ_s (ps^{-1})		0.0002
$\lvert A_\perp\rvert^2$		-
$\lvert A_0\rvert^2$		-
$\delta_\parallel$ (rad)		0.001
$\delta_\perp$ (rad)		0.010
$m_{K^+K^-}$ bin 1	F_s	-
	$\delta_{s,\perp}$ (rad)	0.002
$m_{K^+K^-}$ bin 2	F_s	0.002
	$\delta_{s,\perp}$ (rad)	0.029
$m_{K^+K^-}$ bin 3	F_s	-
	$\delta_{s,\perp}$ (rad)	0.004
$m_{K^+K^-}$ bin 4	F_s	0.001
	$\delta_{s,\perp}$ (rad)	0.011
$m_{K^+K^-}$ bin 5	F_s	0.001
	$\delta_{s,\perp}$ (rad)	0.004
$m_{K^+K^-}$ bin 6	F_s	0.008
	$\delta_{s,\perp}$ (rad)	-

Table 12.4: Absolute shift in fit results when adding a 1.5% contribution of simulated $B_d^0 \to J/\psi K^{*0}$ background to the fitted datasample and subtracting them with negative weight.

12.4 Angular acceptance

The angular acceptance correction used in the fitting procedure is determined with fully simulated $B_s^0 \to J/\psi\phi$ candidates. Differences between simulation and data can lead to systematic biases. In addition statistical uncertainties in the acceptance determination need to be taken into account.

12.4.1 Differences between data and simulation

As discussed in Section 8.1 the angular acceptance correction is mainly determined by the detector acceptance and implicit momentum cuts on the final state particles. The polar angle and momentum distributions of these particles however show significant discrepancies between data and simulation. Partially these discrepancies can be explained by different polarisation amplitudes in data and simulation, partially this could be an improper simulation of the detector response. A possible systematic bias introduced by this on the angular acceptance must be evaluated.
The two possible sources of the discrepancies are not disentangled here. As a con-

servative approach the full differences in the polar angle and momentum spectra are used to estimate a systematic uncertainty (see Figure 8.7). The simulated events are reweighted to match the data distributions. This is done separately for the polar angle and momentum distributions of muons and kaons, resulting in four reweighted acceptances. They are shown in Figure 8.8 for the different weightings. The exact procedure is discussed in Section 8.1. For each of the four recalculated acceptances a set of 600 pseudo-experiments is performed: Corresponding to the observed signal yield and the PDFs introduced in Chapter 9, datasets are generated using the parameter values measured in the previous chapter as input. The reweighted angular acceptance is used to model the detector effects in the generation of the events. Each dataset is fitted with the sFit technique using the nominal, uncorrected acceptance in the PDF.
The mean shift of the 600 fit results with respect to the generated values is listed in Table 12.5 for all physics parameters. The shift is estimated separately for the polar angle and momentum distributions of the final state muons and kaons. The quadratic sum of the biases is assigned as systematic error to the final parameter values.
The P- and S-wave amplitudes and strong phases are most sensitive to the angular acceptance and thus strongly affected by this systematic uncertainty. The largest effect is visible for the P-wave amplitudes: the systematic errors for $|A_\perp|^2$ and $|A_0|^2$ are 1.6× and 5× larger than the statistical uncertainties. Also the phase difference $\delta_{s,\perp}$ is affected by up to 50% of the statistical uncertainties, depending on the $m_{K^+K^-}$ interval. In addition $|\lambda_{CP}|$ is significantly influenced by ∼40% of the statistical error.

12.4.2 Statistical uncertainty of angular acceptance

The angular acceptance histogram as well as the normalisation weights of the signal PDF in the maximum likelihood fit are determined from a simulated $B_s^0 \to J/\psi\phi$ sample and have statistical uncertainties depending on the size of the sample. These are not taken into account in the fitting procedure and their effect on the measured physics parameter values has to be investigated.
The values and statistical uncertainties of the normalisation weights are given in Table 9.1. To estimate a systematic uncertainty the normalisation weights are randomly fluctuated inside their statistical errors. The correlation between the different normalisation weights are taken into account. This is done 100 times and each set of fluctuated normalisation weights is used to refit the dataset. The width of the distribution of the estimated parameter values is given in Table 12.6 for all physics parameters and is assigned as systematic uncertainty.
For most of the parameters this systematic error is much smaller than the error due to the differences in data and simulation. It however is one of the largest contributions to the systematic errors of ϕ_s and $|\lambda_{CP}|$ with ∼ 8% and ∼ 20% of the statistical uncertainties.

		shift as result of modified acceptance				
parameter		$\Theta(K)$	$p(K)$	$\Theta(\mu)$	$p(\mu)$	quadratic sum
ϕ_s (rad)		0.003	0.003	0.001	0.004	0.006
$\lvert\lambda_{CP}\rvert$		0.008	0.009	0.008	0.003	0.013
$\Delta\Gamma_s$(ps^{-1})		-	0.0004	0.0002	0.0001	0.0005
Γ_s(ps^{-1})		-	0.0012	-	0.0001	0.0012
$\lvert A_\perp\rvert^2$		0.001	0.015	-	0.001	0.015
$\lvert A_0\rvert^2$		0.001	0.030	-	0.001	0.030
$\delta_\parallel$(rad)		0.018	0.049	0.012	0.002	0.055
$\delta_\perp$(rad)		0.011	0.017	0.001	0.013	0.020
bin 1	F_s	0.001	0.014	0.001	0.001	0.014
	$\delta_{s,\perp}$(rad)	0.024	0.013	0.037	0.014	0.048
bin 2	F_s	-	0.008	0.001	0.001	0.008
	$\delta_{s,\perp}$(rad)	-	0.067	0.003	0.008	0.068
bin 3	F_s	-	0.003	0.001	-	0.003
	$\delta_{s,\perp}$(rad)	0.053	0.117	0.039	0.015	0.135
bin 4	F_s	-	0.004	0.001	0.001	0.004
	$\delta_{s,\perp}$(rad)	0.035	0.108	0.012	0.010	0.115
bin 5	F_s	0.001	0.008	0.001	0.001	0.008
	$\delta_{s,\perp}$(rad)	0.006	0.037	0.003	0.001	0.038
bin 6	F_s	0.001	0.014	0.001	0.001	0.014
	$\delta_{s,\perp}$(rad)	0.002	0.030	-	0.001	0.030

Table 12.5: Absolute shift of the physics parameters when using the nominal acceptance corrections in the fit and the reweighted acceptance corrections (Figure 8.8) in the generation of the datasets. The reweighting is performed separately using the polar angle distributions of kaons ($\Theta(K)$), of muons ($\Theta(\mu)$) and the momentum distributions of kaons ($p(K)$) and muons ($p(\mu)$). The last column is the quadratic sum of the effects of the individual reweightings.

12.5 Decay time acceptance

The decay time acceptance used in the fit is modeled by histograms determined directly with measured $B_s^0 \to J/\psi\phi$ candidates. No systematic uncertainty is expected to be introduced by the determination of the acceptance. The histograms however have statistical uncertainties which are not propagated to the fit. The possible uncertainties on the physics parameters introduced by this are determined by fluctuating the decay time acceptance histograms randomly inside their statistical errors. Each histogram bin is changed by a random number, thrown following a Gaussian distribution with width corresponding to the statistical error of the bin. The maximum likelihood fit is repeated 200 times using different fluctuated time acceptance histograms. The spread of the fitted parameter values is given in Table 12.7 for all physics parameters and is

parameter		spread in fit results
ϕ_s (rad)		0.007
$\lvert\lambda_{CP}\rvert$		0.006
$\Delta\Gamma_s$ (ps^{-1})		0.0002
Γ_s (ps^{-1})		0.0002
$\lvert A_\perp\rvert^2$		0.002
$\lvert A_0\rvert^2$		0.001
$\delta_\parallel$ (rad)		0.032
$\delta_\perp$ (rad)		0.037
$m_{K^+K^-}$ bin 1	F_s	0.003
	$\delta_{s,\perp}$ (rad)	0.033
$m_{K^+K^-}$ bin 2	F_s	0.003
	$\delta_{s,\perp}$ (rad)	0.023
$m_{K^+K^-}$ bin 3	F_s	0.002
	$\delta_{s,\perp}$ (rad)	0.067
$m_{K^+K^-}$ bin 4	F_s	0.001
	$\delta_{s,\perp}$ (rad)	0.036
$m_{K^+K^-}$ bin 5	F_s	0.003
	$\delta_{s,\perp}$ (rad)	0.019
$m_{K^+K^-}$ bin 6	F_s	0.004
	$\delta_{s,\perp}$ (rad)	0.015

Table 12.6: Spread of fit results when fluctuating the angular acceptance corrections inside their statistical uncertainties.

taken as systematic uncertainty. The decay time acceptance influences only Γ_s (20% of the fit error) and $\Delta\Gamma_s$(6% of the statistical error). In some of the $m_{K^+K^-}$ bins also the phase difference $\delta_{s,\perp}$ is slightly affected.

12.6 Bias of decay time

In Chapter 7 it was observed that the measured decay time is biased by about −0.004 ps. This shift has not been taken into account in the decay time resolution model of the maximum likelihood fit. A possible bias is evaluated by shifting the decay time of each B_s^0 candidate and repeating the maximum likelihood fit. The difference of the fit results to the nominal results are shown in Table 12.8 for all physics parameters and are assigned as systematic uncertainties.
The resulting systematic errors are for most of the parameters small compared to other systematic uncertainties. For $\Delta\Gamma_s$ it corresponds to $\sim$ 12% of the statistical uncertainty.

parameter		spread in fit result
ϕ_s (rad)		-
$\lvert\lambda_{CP}\rvert$		-
$\Delta\Gamma_s$ (ps^{-1})		0.001
Γ_s (ps^{-1})		0.001
$\lvert A_\perp\rvert^2$		-
$\lvert A_0\rvert^2$		-
$\delta_\parallel$ (rad)		-
$\delta_\perp$ (rad)		-
$m_{K^+K^-}$ bin 1	F_s	0.001
	$\delta_{s,\perp}$ (rad)	0.002
$m_{K^+K^-}$ bin 2	F_s	-
	$\delta_{s,\perp}$ (rad)	0.003
$m_{K^+K^-}$ bin 3	F_s	-
	$\delta_{s,\perp}$ (rad)	0.006
$m_{K^+K^-}$ bin 4	F_s	-
	$\delta_{s,\perp}$ (rad)	0.003
$m_{K^+K^-}$ bin 5	F_s	-
	$\delta_{s,\perp}$ (rad)	0.002
$m_{K^+K^-}$ bin 6	F_s	0.001
	$\delta_{s,\perp}$ (rad)	0.001

Table 12.7: Spread in fit results when fluctuating the decay time acceptance histograms inside their statistical errors.

12.7 Nuisance asymmetries

The measurement of the CP-violating phase ϕ_s in the interference of B_s^0 mixing and decay relies on the measurement of an asymmetry between the B_s^0 and the $\overline{B}_s^0$ decay rates. It can be affected by direct CP violation in decay, production asymmetry or tagging asymmetry. Direct CP violation in decay is already modeled in the analysis by fitting for $|\lambda_{CP}|$.
Tagging asymmetries can be either due to a different mistag probability or due to a different tagging efficiency for produced B_s^0 and $\overline{B}_s^0$ mesons. The separate tagging calibration parameters in the PDF already account for differences in the mistag probability. Pseudo experiments are done to estimate the effect of production and tagging efficiency asymmetries. The production asymmetry was measured at LHCb for $B_d^0 \to J/\psi K^{*0}$ decays and found to be $A_p = 0.010 \pm 0.013$ [76]. The tagging efficiency asymmetry is estimated in the calibration of the taggers to be $< 0.3\%$ (see Section 6.3). As a conservative approach, a production asymmetry of 2% and a tagging efficiency asymmetry of 0.6% is considered in the pseudo experiments:
1000 datasets are generated according to the PDFs used in the default fitting procedure with the measured physics parameters as input. In the generation of these datasets

parameter		shift in fit result
ϕ_s (rad)		0.003
$\lvert\lambda_{CP}\rvert$		0.002
$\Delta\Gamma_s$ (ps^{-1})		0.002
Γ_s (ps^{-1})		0.0002
$\lvert A_\perp\rvert^2$		0.002
$\lvert A_0\rvert^2$		0.001
$\delta_\parallel$ (rad)		0.006
$\delta_\perp$ (rad)		0.046
$m_{K^+K^-}$ bin 1	F_s	0.001
	$\delta_{s,\perp}$ (rad)	0.038
$m_{K^+K^-}$ bin 2	F_s	-
	$\delta_{s,\perp}$ (rad)	0.015
$m_{K^+K^-}$ bin 3	F_s	-
	$\delta_{s,\perp}$ (rad)	0.016
$m_{K^+K^-}$ bin 4	F_s	-
	$\delta_{s,\perp}$ (rad)	0.003
$m_{K^+K^-}$ bin 5	F_s	0.002
	$\delta_{s,\perp}$ (rad)	0.004
$m_{K^+K^-}$ bin 6	F_s	-
	$\delta_{s,\perp}$ (rad)	0.017

Table 12.8: Absolute shift of fit result when changing the estimated decay time of each candidate by -0.004 ps.

the production asymmetry is introduced. The datasets are fitted with the default fitting conditions. The same procedure is repeated for the tagging efficiency asymmetry in the generation of the events. The mean shift of the parameter results, relative to the generated values, is given in Table 12.9. Although the asymmetries in the pseudo experiments are upper limits of the true asymmetries, the shifts are small for all parameters, compared to other systematic uncertainties. The quadratic sum of the shifts due to production and tagging asymmetry is assigned as systematic error to the parameter results.

12.8 Fitter bias

As discussed in Section 9.1 the maximum likelihood estimation is unbiased for a very large number of events. This has not to be the case for the size of the data sample available in this analysis. The bias in the fit procedure is determined by a set of 850 pseudo experiments. Datasets are generated according to the physics parameters measured in data with the same number of signal and background candidates. The datasets are fitted with the default fitting procedure. Figure 12.1 and 12.2 show the distributions of the fitted central values overlaid with a fitted Gaussian function. For the parameters

parameter		shift as result of		quadratic sum
		prod.asym	tag.asym	
ϕ_s (rad)		0.002	0.003	0.004
$\lvert\lambda_{CP}\rvert$		0.001	0.001	0.001
$\Delta\Gamma_s$(ps^{-1})		-	-	-
Γ_s(ps^{-1})		-	-	-
$\lvert A_\perp\rvert^2$		-	-	-
$\lvert A_0\rvert^2$		0.001	-	0.001
$\delta_\parallel$		0.005	0.011	0.012
$\delta_\perp$		0.002	0.002	0.003
$m_{K^+K^-}$ bin 1	F_s	-	-	-
	$\delta_{s,\perp}$	0.007	0.002	0.007
$m_{K^+K^-}$ bin 2	F_s	0.001	-	0.001
	$\delta_{s,\perp}$	-	0.002	0.002
$m_{K^+K^-}$ bin 3	F_s	-	-	-
	$\delta_{s,\perp}$	0.004	0.007	0.008
$m_{K^+K^-}$ bin 4	F_s	-	-	-
	$\delta_{s,\perp}$	0.016	0.005	0.017
$m_{K^+K^-}$ bin 5	F_s	-	0.001	0.001
	$\delta_{s,\perp}$	0.005	0.004	0.006
$m_{K^+K^-}$ bin 6	F_s	0.001	0.001	0.001
	$\delta_{s,\perp}$	0.003	0.002	0.004

Table 12.9: Absolute shift of the physics parameters when introducing nuisance asymmetries in the generation of pseudo experiments and neglecting them in the fit. A production asymmetry of 2% and a relative tagging efficiency of 0.6% was chosen. The last column shows the quadratic sum of the measured biases.

that are fitted simultaneously in all six $m_{K^+K^-}$ intervals, the distribution of the fitted values are well described by the Gaussian function. For the separate S-wave parameters, especially the phase $\delta_{s,\perp}$, the distributions have large tails, reflecting the problems of the likelihood fit with low statistics. The difference between fitted mean value of the distributions and generated values is given in Table 12.10 for all physics parameters. It is assigned as systematic error to the measured results accounting for a fit bias due to limited statistics.

For most of the parameters that are fitted simultaneously in all $m_{K^+K^-}$ bins the systematic error is negligible or even zero. The assigned error on $|\lambda_{CP}|$ and $\delta_\parallel$ are $\sim 16\%$ and $\sim 30\%$ of the statistical uncertainties. For the S-wave parameters, especially in the outer $m_{K^+K^-}$ bins with low statistics, the fit bias is one of the larger systematic uncertainties.

parameter		fit bias
ϕ_s (rad)		-
$\lvert\lambda_{CP}\rvert$		0.005
$\Delta\Gamma_s$ (ps^{-1})		-
Γ_s (ps^{-1})		-
$\lvert A_\perp\rvert^2$		0.001
$\lvert A_0\rvert^2$		-
$\delta_\parallel$ (rad)		0.045
$\delta_\perp$ (rad)		-
$m_{K^+K^-}$ bin 1	F_s	0.016
	$\delta_{s,\perp}$ (rad)	0.114
$m_{K^+K^-}$ bin 2	F_s	-
	$\delta_{s,\perp}$ (rad)	-
$m_{K^+K^-}$ bin 3	F_s	-
	$\delta_{s,\perp}$ (rad)	0.037
$m_{K^+K^-}$ bin 4	F_s	-
	$\delta_{s,\perp}$ (rad)	-
$m_{K^+K^-}$ bin 5	F_s	0.002
	$\delta_{s,\perp}$ (rad)	0.022
$m_{K^+K^-}$ bin 6	F_s	-
	$\delta_{s,\perp}$ (rad)	0.015

Table 12.10: Absolute bias of the parameter introduced by the maximum likelihood procedure due to the limited statistics of the available data sample. The fit bias is determined as the mean shift of fit results obtained from 850 pseudo-experiments.

12.9 C_{sp} coupling factor

The C_{sp} factors used in the maximum likelihood fit are calculated assuming a Breit-Wigner amplitude of the P-wave component and a non-resonant amplitude of the S-wave component (see Section 9.2). The S-wave component however can also be partially due to a $f_0(980)$ contribution which can be described by a Flatté-function. Table 12.11 shows the C_{sp} factors calculated for a Flatté shape according to Equation 2.56. The fit is repeated with these coupling factors and the difference in the results, given in Table 12.12, are assigned as systematic errors.
Compared to other systematic uncertainties, the error due to the C_{sp} factors are negligible. They are only different from zero for the strong phases $\delta_\perp$, $\delta_\parallel$ and for the phase difference $\delta_{s,\perp}$ in the six $m_{K^+K^-}$ intervals.

$m_{K^+K^-}$ bin (MeV)	$C_{\rm sp}$
990 - 1008	0.949
1008 - 1016	0.950
1016 - 10020	0.922
1020 - 1024	0.926
1024 - 1032	0.960
1032 - 1050	0.973

Table 12.11: P- and S-wave coupling correction factors $C_{\rm sp}$ for the six $m_{K^+K^-}$ intervals, assuming a Flatté S-wave shape and a Breit-Wigner P-wave shape.

parameter		shift in result
$\phi_{\rm s}$ (rad)		-
$\lvert\lambda_{\rm CP}\rvert$		-
$\Delta\Gamma_{\rm s}$ (ps^{-1})		-
$\Gamma_{\rm s}$ (ps^{-1})		-
$\lvert A_\perp\rvert^2$		-
$\lvert A_0\rvert^2$		-
$\delta_\parallel$ (rad)		0.001
$\delta_\perp$ (rad)		0.003
$m_{K^+K^-}$ bin 1	$F_{\rm s}$	0.002
	$\delta_{\rm s,\perp}$ (rad)	0.025
$m_{K^+K^-}$ bin 2	$F_{\rm s}$	-
	$\delta_{\rm s,\perp}$ (rad)	0.004
$m_{K^+K^-}$ bin 3	$F_{\rm s}$	-
	$\delta_{\rm s,\perp}$ (rad)	0.003
$m_{K^+K^-}$ bin 4	$F_{\rm s}$	-
	$\delta_{\rm s,\perp}$ (rad)	0.001
$m_{K^+K^-}$ bin 5	$F_{\rm s}$	-
	$\delta_{\rm s,\perp}$ (rad)	0.002
$m_{K^+K^-}$ bin 6	$F_{\rm s}$	-
	$\delta_{\rm s,\perp}$ (rad)	0.005

Table 12.12: Absolute shift in the fit results when using $C_{\rm sp}$ coupling factors calculated with a Flatté shape for the S-wave amplitude.

12.10 Momentum and z-scale

The B_s^0 decay time is, as shown in Equation 7.5, determined from the flight distance $\vec{d}$ and the momentum p of the B_s^0. Uncertainties on $\Gamma_{\rm s}$ and $\Delta\Gamma_{\rm s}$ arise from the accuracy of the absolute scale of flight distance and momentum. The flight distance uncertainty is determined by the z-position uncertainty of the VELO modules. It is estimated to be

$\frac{\delta z}{z} < 0.1\%$. This leads directly to an uncertainty of 0.1% on Γ_s and $\Delta\Gamma_s$. The absolute momentum scale is estimated to be $\frac{\delta p}{p} < 0.15\%$. Both the B_s^0 momentum as well as the B_s^0 mass in Equation 7.5 are affected by this. The uncertainty on Γ_s and $\Delta\Gamma_s$ is 0.02% and thus negligible compared to other systematic errors.

12.11 Upper decay time acceptance

The upper decay time acceptance as discussed in Section 8.2.2 is not modeled in the fit. The measured value of Γ_s is corrected afterwards by the factor $\beta = (-8.26 \pm 4.0)10^{-3}$ [67]. The uncertainty of β is fully assigned as systematic error on Γ_s. All other parameters are not affected by the upper decay time acceptance and thus no systematic uncertainty is necessary.

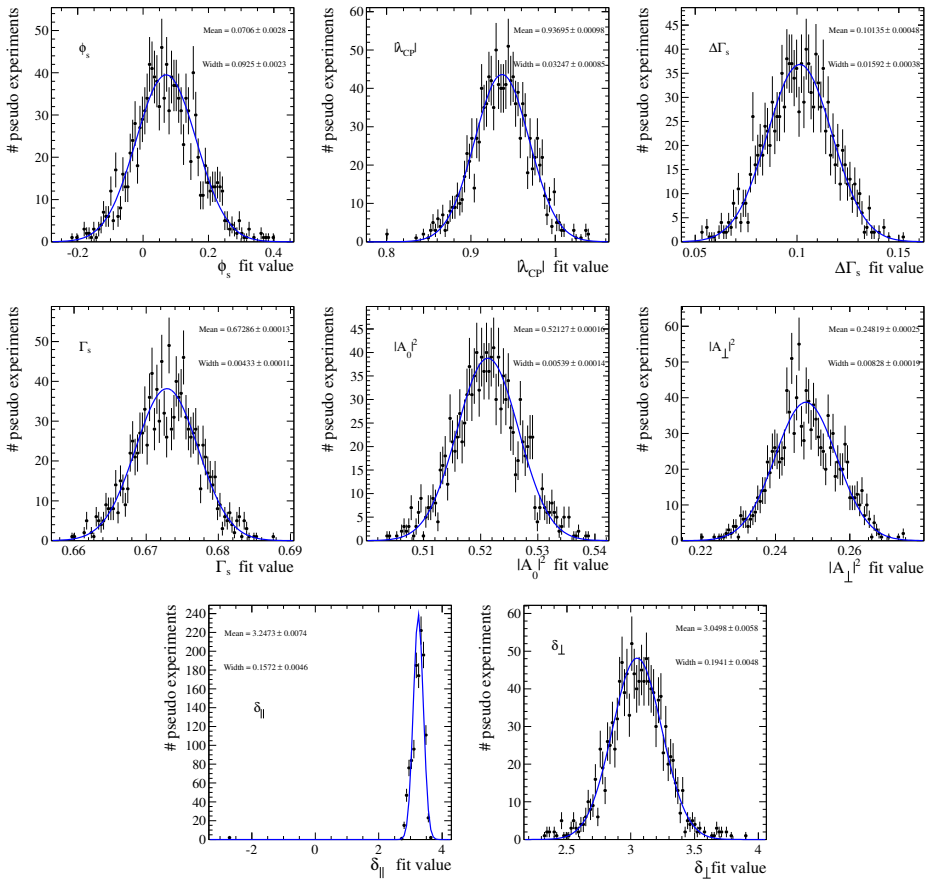

Figure 12.1: Distributions of fit results for simultaneously fitted physics parameters, obtained from 850 pseudo-experiments. The size of the generated datasamples corresponds to the measured number of signal and background candidates.

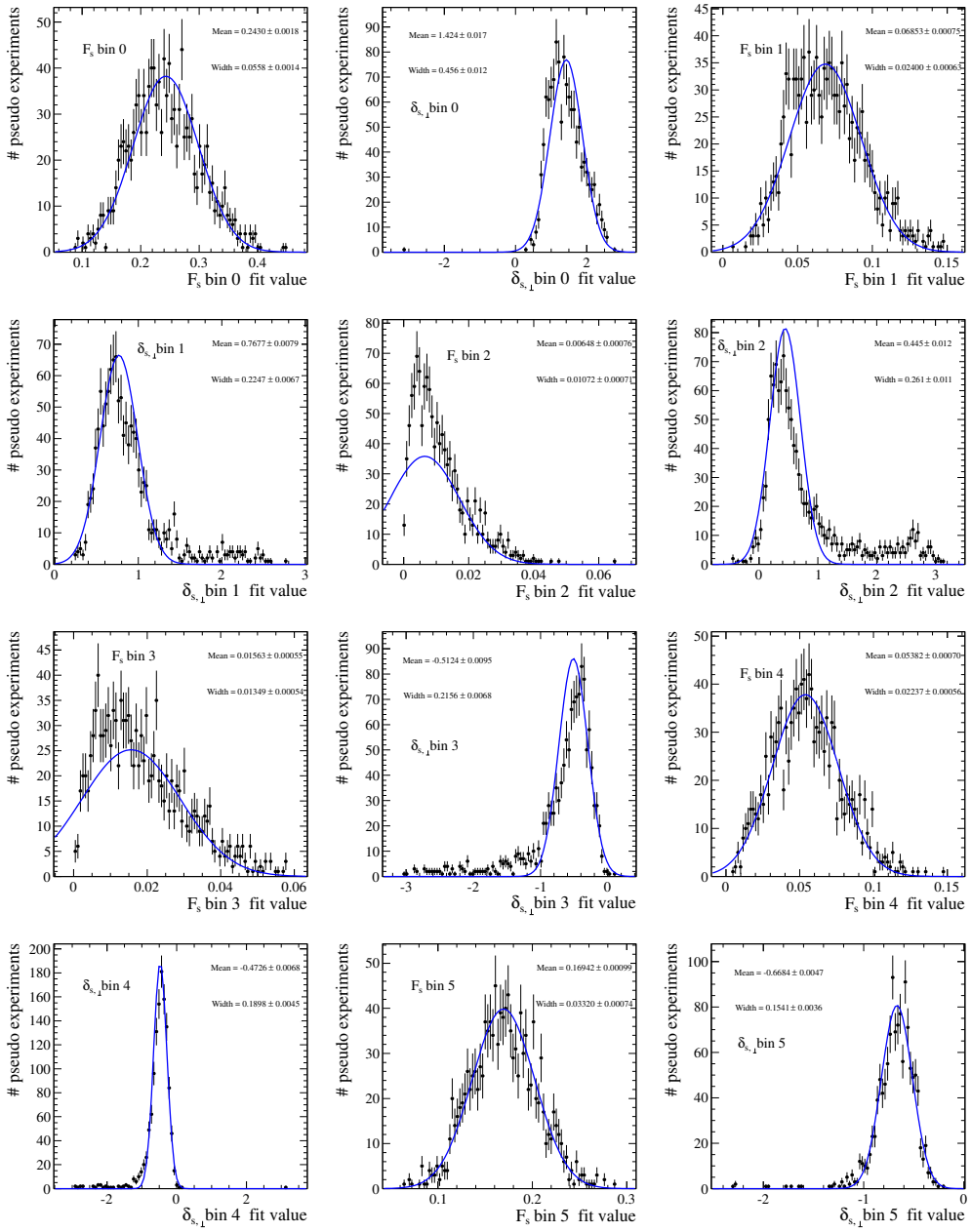

Figure 12.2: Distributions of fit results for S-wave parameters, obtained from 850 pseudo-experiments. The size of the generated datasamples corresponds to the measured number of signal and background candidates.

12.12 Summary of systematic uncertainties and $B_s^0 \to J/\psi\phi$ results

A summary of the systematic uncertainties evaluated in the last sections is given in the Table 12.13 for the parameters fitted simultaneously in all $m_{K^+K^-}$ bins and in the Tables 12.14, 12.15 for the S-wave parameters. The statistical uncertainties obtained from the fit are shown for comparisons. Except for Γ_s and the polarisation amplitudes $|A_\perp|^2$ and $|A_0|^2$, the statistical uncertainties are dominant for all physics parameters. For the CP violation parameters ϕ_s and $|\lambda_{CP}|$ the main contribution to the systematic uncertainties comes from the background modeling and the angular acceptance. The systematic uncertainty of the lifetime parameters $\Delta\Gamma_s$ and Γ_s is dominated by the background treatment and the correction for the upper decay time acceptance. The sensitivity of the polarisation amplitudes is limited by the description of the angular acceptance in the simulation. The largest systematic on the S-wave parameters is introduced by the background description and the angular acceptances.

source	ϕ_s (rad)	$\lvert\lambda_{CP}\rvert$	$\Delta\Gamma_s$ (ps^{-1})	Γ_s (ps^{-1})	$\lvert A_\perp\rvert^2$	$\lvert A_0\rvert^2$	$\delta_\parallel$ (rad)	$\delta_\perp$ (rad)
stat. uncertainty	0.091	0.030	0.016	0.0048	0.009	0.006	$^{+0.128}_{-0.213}$	0.219
mass model	0.001	-	-	0.0008	0.001	0.001	0.006	0.003
background treatment	0.007	0.002	0.003	0.0037	0.003	0.004	0.031	0.022
$B_d^0 \to J/\psi K^{*0}$ background	0.007	0.001	0.001	0.0002	-	-	0.001	0.010
angular acc. reweighting	0.006	0.013	0.001	0.0012	0.015	0.030	0.055	0.020
angular acc. statistics	0.007	0.006	-	0.0002	0.002	0.001	0.032	0.037
time acc. statistics	-	-	0.001	0.001	-	-	-	-
decay time bias	0.003	0.002	0.002	0.0002	0.002	0.001	0.006	0.046
nuisance asym.	0.004	0.001	-	-	-	0.001	0.012	0.003
time acc. corr. β	-	-	-	0.004	-	-	-	-
z + p scale	-	-	-	0.0009	-	-	-	-
fit bias	-	0.005	-	-	0.001	-	0.045	-
C_{sp} factor	-	-	-	-	-	-	0.001	0.003
quad. sum of syst.	0.014	0.016	0.004	0.0058	0.016	0.030	0.085	0.067

Table 12.13: Summary of systematic uncertainties for physics parameters that are fitted simultaneously in all $m_{K^+K^-}$ intervals.

Figure 12.3 shows the measured phase values for the six bins of $m_{K^+K^-}$ and the two possible solutions, including the statistical uncertainties from the fit and the systematic uncertainties evaluated in the last sections. The physically correct parameter set corresponds to the decreasing trend of $\delta_{s,\perp}$. The measured physics parameter of the correct solution are summarised in Table 12.16, together with the statistical uncertainties from the fit and the systematic uncertainties. The value of Γ_s, determined in the maximum likelihood fit, is corrected for the upper decay time acceptance by subtracting the β-factor as given in Section 8.2.2.
The measured values of ϕ_s and $\Delta\Gamma_s$ are compatible with the Standard Model predictions of $\phi_s = -0.0364 \pm 0.0016$ rad [8] and $\Delta\Gamma_s = 0.087 \pm 0.021$ ps^{-1} [77].

	$m_{K^+K^-}$ bin 1		$m_{K^+K^-}$ bin 2		$m_{K^+K^-}$ bin 3	
source	F_s	$\delta_{s,\perp}$(rad)	F_s	$\delta_{s,\perp}$(rad)	F_s	$\delta_{s,\perp}$(rad)
stat. uncertainty	$^{+0.082}_{-0.073}$	$^{+0.787}_{-0.493}$	$^{+0.030}_{-0.027}$	$^{+0.389}_{-0.233}$	$^{+0.014}_{-0.007}$	$^{+1.320}_{-0.291}$
mass model	0.003	0.012	-	0.002	-	0.002
background treatment	0.027	0.113	0.002	0.020	0.001	0.024
$B_d^0 \to J/\psi K^{*0}$ background	-	0.002	0.002	0.029	-	0.004
angular acc. reweighting	0.014	0.048	0.008	0.068	0.003	0.135
angular acc. statistics	0.003	0.033	0.003	0.023	0.002	0.067
time acc. statistics	0.001	0.002	-	0.003	-	0.006
decay time bias	0.001	0.038	-	0.015	-	0.016
nuisance asym.	-	0.007	0.001	0.002	-	0.008
time acc. corr. β	-	-	-	-	-	-
z + p scale	-	-	-	-	-	-
fit bias	0.016	0.114	-	-	-	0.037
C_{sp} factor	0.002	0.025	-	0.004	-	0.003
quad. sum of syst.	0.035	0.177	0.010	0.082	0.004	0.158

Table 12.14: Summary of systematic uncertainties for S-wave parameters fitted in the first three $m_{K^+K^-}$ intervals.

	$m_{K^+K^-}$ bin 4		$m_{K^+K^-}$ bin 5		$m_{K^+K^-}$ bin 6	
source	F_s	$\delta_{s,\perp}$(rad)	F_s	$\delta_{s,\perp}$(rad)	F_s	$\delta_{s,\perp}$(rad)
stat. uncertainty	$^{+0.012}_{-0.009}$	$^{+0.215}_{-0.356}$	$^{+0.027}_{-0.025}$	$^{+0.183}_{-0.255}$	$^{+0.043}_{-0.042}$	$^{+0.183}_{-0.225}$
mass model	-	0.003	-	-	0.001	0.003
background treatment	0.001	0.024	0.004	0.004	0.006	0.013
$B_d^0 \to J/\psi K^{*0}$ background	0.001	0.011	0.001	0.004	0.008	-
angular acc. reweighting	0.004	0.115	0.008	0.038	0.014	0.030
angular acc. statistics	0.001	0.036	0.003	0.019	0.004	0.015
time acc. statistics	-	0.003	-	0.002	0.001	0.001
decay time bias	-	0.003	0.002	0.004	-	0.017
nuisance asym.	-	0.017	0.001	0.006	0.001	0.004
time acc. corr. β	-	-	-	-	-	-
z + p scale	-	-	-	-	-	-
fit bias	-	-	0.002	0.022	-	0.015
C_{sp} factor	-	0.001	-	0.002	-	0.005
quad. sum of syst.	0.007	0.125	0.010	0.049	0.018	0.043

Table 12.15: Summary of systematic uncertainties for S-wave parameters fitted in the last three $m_{K^+K^-}$ intervals.

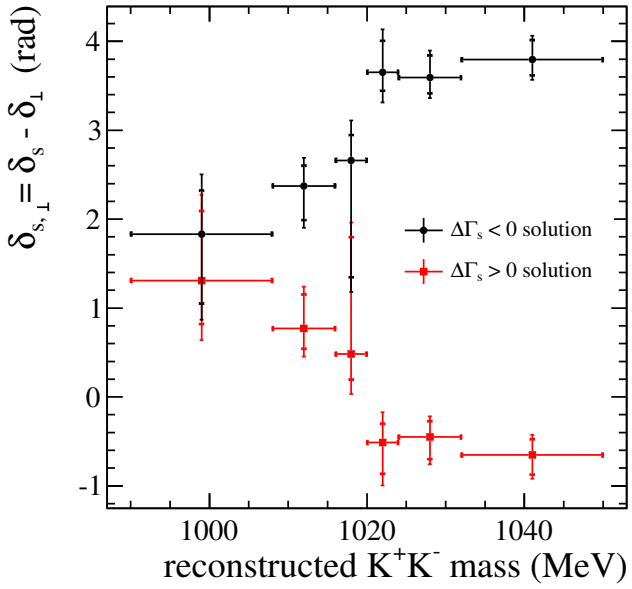

Figure 12.3: Measured values of $\delta_{s,\perp}$ as a function of $m_{K^+K^-}$. The error bars include statistical and systematic uncertainties.

parameter	value	stat. error	syst. error
ϕ_s(rad)	0.069	0.091	0.014
$\lvert\lambda_{CP}\rvert$	0.944	0.030	0.016
$\Delta\Gamma_s$(ps^{-1})	0.100	0.016	0.004
Γ_s(ps^{-1})	0.6643	0.0048	0.0058
$\lvert A_\perp\rvert^2$	0.249	0.009	0.016
$\lvert A_0\rvert^2$	0.521	0.006	0.030
$\delta_\parallel$(rad)	3.308	$^{+0.128}_{-0.213}$	0.085
$\delta_\perp$(rad)	3.069	0.219	0.067

Table 12.16: Central values and statistical and systematic uncertainties for the physics parameters measured with $B_s^0 \to J/\psi\phi$ decays.

CHAPTER 13

Combined fit to $B_s^0 \to J/\psi\phi$ and $B_s^0 \to J/\psi\pi^+\pi^-$

An additional approach of measuring the CP violating phase ϕ_s is using $B_s^0 \to J/\psi\pi^+\pi^-$ events. This decay is a pure CP eigenstate and has the advantage that no angular analysis is necessary to separate the CP components. Due to the lower branching ratio the sensitivity on ϕ_s is smaller than with $B_s^0 \to J/\psi\phi$ decays. In the following chapter the results of a common fit will be presented, using the $B_s^0 \to J/\psi\phi$ as well as the $B_s^0 \to J/\psi\pi^+\pi^-$ data as input. The $B_s^0 \to J/\psi\pi^+\pi^-$ datasample and analysis techniques are taken from a previous analysis, given in Reference [54]. They will only be discussed briefly here.

13.1 The $B_s^0 \to J/\psi\pi^+\pi^-$ decay and dataset

The decay of $B_s^0 \to J/\psi[\to \mu^+\mu^-]\pi^+\pi^-$ was firstly used to measure the CP-violating phase ϕ_s at LHCb by requiring an intermediate $f_0(980)$ resonance with $f_0(980) \to \pi^+\pi^-$ [78]. As the $f_0(980)$ resonance, and a possible non-resonant contribution, have zero spin, the final state is a pure CP-odd eigenstate. By extending the invariant $\pi^+\pi^-$ mass range to the interval $\pi^+\pi^- \in [775\,\text{MeV}, 1550\,\text{MeV}]$ more intermediate resonances with different spin states can contribute to this final state. Figure 13.1 shows the reconstructed invariant $\pi^+\pi^-$ mass of $B_s^0 \to J/\psi\pi^+\pi^-$ decays. The large peak at 980 MeV is from $f_0(980) \to \pi^+\pi^-$ decays. The full resonance substructure in the indicated $\pi^+\pi^-$

mass interval was resolved by a Dalitz plot analysis [26]. The contributing components are given in Table 13.1. The CP-odd fraction of $B_s^0 \to J/\psi\pi^+\pi^-$ decays in this $\pi^+\pi^-$ mass range was estimated to be $> 97.7\%$ at 95%CL [26].

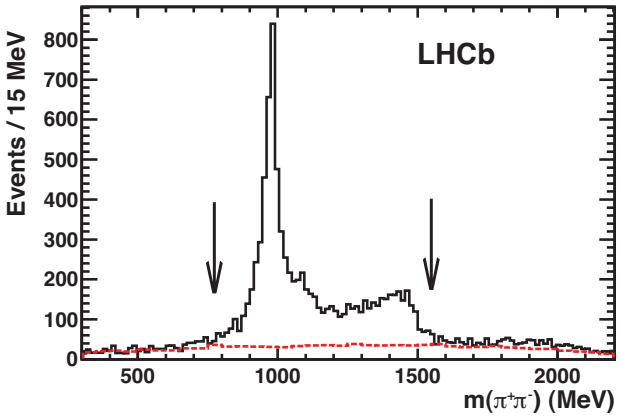

Figure 13.1: Invariant $\pi^+\pi^-$ mass distribution of selected $B_s^0 \to J/\psi\pi^+\pi^-$ in a signal region of ± 20 MeV around the true B_s^0 mass. The red histogram represents the combinatorial background contribution. The arrows indicate the considered [775 MeV, 1550 MeV] $m_{K^+K^-}$ mass interval. The figure is taken from [79].

state	fraction in $\pi^+\pi^- \in$ [775 MeV, 1550 MeV]
$f_0(980)$	$(69.7 \pm 2.3)\%$
$f_0(1370)$	$(21.2 \pm 2.7)\%$
non-resonant	$(8.4 \pm 1.5)\%$
$f_2(1270)$	$(0.49 \pm 0.16)\%$

Table 13.1: Normalised fractions of resonant and non-resonant contributions to the $B_s^0 \to J/\psi\pi^+\pi^-$ decay in the $\pi^+\pi^-$ mass range [775 MeV, 1550 MeV], [26].

13.1.1 Reconstruction of $B_s^0 \to J/\psi\pi^+\pi^-$

The trigger requirement to select $B_s^0 \to J/\psi\pi^+\pi^-$ candidates is based on the reconstruction of a single muon or a di-muon pair in the event and on decay time related quantities. The specific trigger lines are to large part identical to those used in the $B_s^0 \to J/\psi\phi$ analysis. In the first stage of the software trigger, only candidates are selected that pass either the *HLT1unbiased*, *HLT1biasedA* or *HLT1biasedB* trigger lines.

Their specific selection cuts are given in Table 5.1.
In the second stage of the software trigger, candidates are selected that pass the *HLT2biased* line, described in Table 5.2. Compared to the $B_s^0 \to J/\psi\phi$ trigger strategy, two additional lines are used, requiring a reconstructed J/ψ candidate in the event with a minimum momentum.
The offline selection of $B_s^0 \to J/\psi\pi^+\pi^-$ decays follows the selection used in [78] optimised for $B_s^0 \to J/\psi f_0(980)$ decays. Some specific selections criteria are modified to allow for a wider $\pi^+\pi^-$ mass range. The detailed requirements can be found in Table 13.2.

The J/ψ reconstruction

Two muon track candidates with a minimum track fit $\chi^2_{\text{track}}/\text{ndf}$ and a positive muon probability $\Delta \ln \mathcal{L}_{\mu\pi}$ are combined to form a common J/ψ vertex with a good vertex quality, $\chi^2_{\text{vtx}}/\text{ndf}(J/\psi)$. A minimum transverse momentum of the muon candidates is required. The reconstructed invariant mass of the combined J/ψ candidate has to be in a narrow interval around the true J/ψ mass.

The $\pi^+\pi^-$ reconstruction

Two tracks with a good track fit $\chi^2_{\text{track}}/\text{ndf}$ are combined to a common vertex, requiring a good vertex fit $\chi^2_{\text{vtx}}/\text{ndf}(J/\psi)$. The tracks have to have a larger probability to be pions than kaons. A minimum sum of their transverse momentum p_{T} is required. A requirement on their minimum impact parameter χ^2_{IP} rejects tracks originating from the primary proton-proton interaction. The invariant mass of the two pion candidates is required to be in a given interval.

The B_s^0 reconstruction

The B_s^0 candidates are combined from the reconstructed J/ψ candidate and the combined $\pi^+\pi^-$ system. A good vertex fit $\chi^2_{\text{vtx}}/\text{ndf}(B_s^0)$ and a maximum $\chi^2_{\text{IP}}(B_s^0)$ of the B_s^0 candidate is required. In order to reject wrong combinations from the primary vertex several selection requirements on decay time related quantities are applied: A minimum flight distance as well as a minimum decay time of the B_s^0 candidate is required. In addition, the B_s^0 candidate has to fulfill a requirement on the cosine of the pointing angle Θ_{P}, defined as the angle between the flight distance vector and the momentum vector of the B_s^0. For correctly reconstructed B_s^0 candidates this angle has to be small.

13.1.2 Signal composition

After the selection a total number of 34942 $B_s^0 \to J/\psi\pi^+\pi^-$ candidates remain. There invariant mass distribution is plotted in Figure 13.2. On top of a combinatorial background component a clear peak around the nominal B_s^0 mass is observed. The addi-

Decay mode	Cut parameter	Final selection
all tracks	$\chi^2_{\text{track}}/\text{ndf}$	< 4
$J/\psi \to \mu^+\mu^-$	$\Delta \ln \mathcal{L}_{\mu\pi}$	> 0
	$min(p_T(\mu^+), p_T(\mu^-))$	$> 0.5\,\text{GeV}$
	$\chi^2_{\text{vtx}}/\text{ndf}(J/\psi)$	< 11
	$\lvert m(\mu^+\mu^-) - M(J/\psi)\rvert$	$\in [3048.92, 3139.92]\,\text{MeV}$
$\pi^+\pi^-$	$\Delta \ln \mathcal{L}_{K\pi}$	> -10
	$(p_T(\pi^+) + p_T(\pi^-))$	$> 0.9\,\text{GeV}$
	$m(\pi^+\pi^-)$	$\in [775, 1550]\,\text{MeV}$
	$\chi^2_{\text{vtx}}/\text{ndf}(\pi^+\pi^-)$	< 10
	$\chi^2_{\text{IP}}(\pi)$	> 9
$B_s^0 \to J/\psi\pi^+\pi^-$	$m(B_s^0)$	$\in [5200, 5550]\,\text{MeV}$
	$\chi^2_{\text{vtx}}/\text{ndf}(B_s^0)$	< 5
	$\chi^2_{\text{IP}}(B_s^0)$	< 25
	flight distance(B_s^0)	$> 1.5\,\text{mm}$
	$\cos\theta_P(B_s^0)$	> 0.99993
	t	$> 0.3\,\text{ps}$

Table 13.2: Selection requirements for the $B_s^0 \to J/\psi\pi^+\pi^-$ decay, taken from [78] and slightly modified.

tional structures at invariant masses below $\sim 5300\,\text{MeV}$ are due to several physical background components passing the selection process [54]:

- The peak at an invariant mass of $5280\,\text{MeV}$ represents correctly reconstructed $B_d^0 \to J/\psi\pi^+\pi^-$ decays.
- The peaking structure around $5520\,\text{MeV}$ results from wrongly reconstructed $B_d^0 \to J/\psi K^{*0}$ decays where the kaon is misreconstructed as a pion. Due to the lower mass hypothesis these candidates have a reconstructed invariant mass smaller than the nominal B_d^0 mass.
- An additional small background component of wrongly reconstructed $B_s^0 \to J/\psi\eta'$ with $\eta' \to \rho\gamma$ decays is found in a mass range from $\sim 5200\,\text{MeV}$ to about $\sim 5400\,\text{MeV}$ and is polluting the peak region of the B_s^0 signal decays. The amount of this background however is estimated to be very small relative to the signal and combinatorial background component and is neglected in this analysis.

13.2 The $B_s^0 \to J/\psi\pi^+\pi^-$ fit

In a first step, a separate fit is performed using only the $B_s^0 \to J/\psi\pi^+\pi^-$ data as input. For simplicity only the sFit technique is used in this study. To reject the physics background contributions at lower B_s^0 masses, only B_s^0 candidates with invariant mass in the

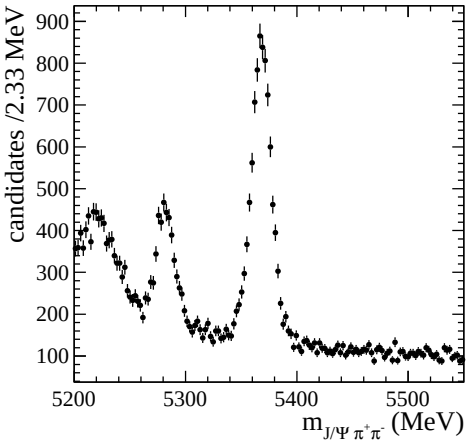

Figure 13.2: Invariant $J/\psi\pi^+\pi^-$ mass distribution of all selected events. The B_s^0 signal peak is around 5370 MeV. The peak at $\sim$ 5280 MeV represents correctly reconstructed $B_d^0 \to J/\psi\pi^+\pi^-$ decays, the peak at $\sim$5520 MeV results from wrongly reconstructed $B_d^0 \to J/\psi K^{*0}$ decays.

interval [5320 MeV, 5600 MeV] are used (in total 20832 candidates). In the following the PDFs describing the $B_s^0 \to J/\psi\pi^+\pi^-$ decay rate as well as the results of this fit will be discussed.

13.2.1 Signal description

The differential decay rate describing the $B_s^0 \to J/\psi\pi^+\pi^-$ decay is much simpler than the one for $B_s^0 \to J/\psi\phi$ as the final state is a pure CP-eigenstate. No separation between polarisation amplitudes is necessary. The physical observables are $\lambda_{\text{phys}} = \{\phi_s, \Delta\Gamma_s, \Gamma_s, |\lambda_{CP}|, \Delta m_s\}$.
The PDF used in the sFit to describe the signal decay time distribution is given following Equation 9.27 by

$$S'_t(t, \sigma_t, \omega_C, q|\vec{\lambda}) = \frac{s(t, \omega_C, q|\vec{\lambda}) \otimes R(t, \sigma_t|\vec{\lambda}_{\text{nuis}})}{\int \varepsilon(t) \cdot s(t, \omega_C, q|\vec{\lambda}) \otimes R(t, \sigma_t|\vec{\lambda}_{\text{nuis}}) \mathrm{d}t}\,, \tag{13.1}$$

with $s(t, \omega_C, q|\vec{\lambda})$ given by

$$s(t, \omega_C, q|\vec{\lambda}) = \frac{1 + qD_{\text{tag}}}{2} P_{B_s^0}(t|\vec{\lambda}_{\text{phys}}) + \frac{1 - q\bar{D}_{\text{tag}}}{2} P_{\overline{B}_s^0}(t|\vec{\lambda}_{\text{phys}})\,. \tag{13.2}$$

The differential decay rates of initially produced B_s^0 and $\overline{B}_s^0$ mesons in CP eigenstates are $P_{B_s^0}(t|\vec{\lambda}_{\text{phys}}) = \frac{\mathrm{d}\Gamma(B_s^0 \to f_{CP})}{\mathrm{d}t}$ and $P_{\overline{B}_s^0}(t|\vec{\lambda}_{\text{phys}}) = \frac{\mathrm{d}\Gamma(\overline{B}_s^0 \to f_{CP})}{\mathrm{d}t}$, as introduced in Equation 2.44

and 2.45. The tagging decision q and tagging dilution $\overset{(-)}{D}_{\rm tag} = (1 - 2\overset{(-)}{\omega}_{\rm tag})$ are defined as for the $B_s^0 \to J/\psi\phi$ fit. The same tagging strategy is used separating the sample in three categories: OST only, SST only and OST+SST tagged events. The tagging calibration parameters are varied with Gaussian constraints in the fit and are given in Table 6.1.

The event-dependent decay time resolution model is parameterised by a sum of three Gaussian functions as

$$R(t - t', \sigma_{\rm t}|\vec{\lambda}_{\rm nuis}) = \sum_{i=1}^{3} f_i G(t - t', \sigma_{\rm t}|s_{\sigma_{\rm t},i}, \mu) \tag{13.3}$$

with three absolute fractions f_i, mean μ and scaling factors $s_{\sigma_{\rm t},i}$ of the estimated decay time uncertainty. The parameters of the resolution model are determined using prompt J/ψ decays produced in the primary interaction [54]. They are fixed in the fit to the central values given in Table 13.3.

parameter	value in fit
$\mu(ps)$	0.0
f_1	0.818
f_2	0.177
f_3	0.005
$s_{\sigma_{\rm t},1}$	1.2951
$s_{\sigma_{\rm t},2}$	2.601
$s_{\sigma_{\rm t},3}$	13.61

Table 13.3: Parameter values used to the describe the decay time resolution in the maximum likelihood fit for $B_s^0 \to J/\psi\pi^+\pi^-$ candidates.

The decay time acceptance $\varepsilon(t)$ is determined with the kinematic similar decay channel $B_d^0 \to J/\psi K^{*0}$. The $B_d^0 \to J/\psi K^{*0}$ candidates are selected following the same trigger and selection requirements as for $B_s^0 \to J/\psi\pi^+\pi^-$. The precise world average value of the B_d^0 lifetime, $\tau_{\rm d} = 1.525 \pm 0.009\,{\rm ps}$, [9] allows to extract the decay time acceptance from a fit to the decay time distribution of $B_d^0 \to J/\psi K^{*0}$ signal candidates. The decay time is parameterised with a single exponential function with fixed $\tau_{\rm d}$ multiplied by an acceptance function

$$\varepsilon(t) = \frac{a[(t - t_0)]^n}{1 + [a(t - t_0)]^n} \tag{13.4}$$

The extracted acceptance parameter values are $a = 1.91$, $n = 1.84$ and $t_0 = 0.135$. The above parameterisation of the decay time acceptance $\varepsilon(t)$ would result in a complicated normalisation of the signal PDF in the maximum likelihood fit for $\phi_{\rm s}$. Therefore $\varepsilon(t)$ will be represented by a histogram in the $B_s^0 \to J/\psi\pi^+\pi^-$ fit instead of using the analytical description in Equation 13.4. The corresponding histogram is shown in Figure 13.3.

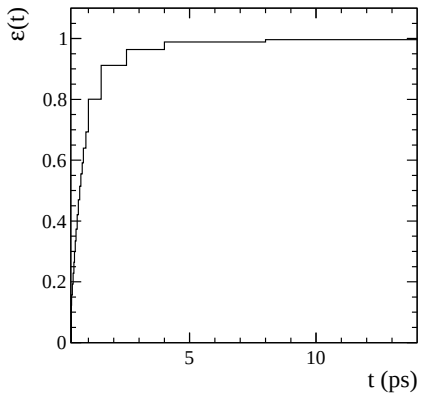

Figure 13.3: Decay time acceptance for $B_s^0 \to J/\psi\pi^+\pi^-$ decays. The histogram is obtained from the parameterisation given in Equation 13.4.

13.2.2 Results of $B_s^0 \to J/\psi\pi^+\pi^-$ fit

The maximum likelihood is performed using in total 20832 $B_s^0 \to J/\psi\pi^+\pi^-$ candidates in the invariant B_s^0 mass interval of [5320 MeV, 5600 MeV]. The sWeight for the statistical subtraction of the background component in the sFit technique are determined by a fit of the B_s^0 mass distribution. The signal component is modeled with a double Gaussian function and the background component with an exponential function. The exact parameterisations were introduced in Equations 9.15 and 9.24. The B_s^0 mass distribution, overlaid with the fitted PDF, is shown in Figure 13.4. The data is well described by the fitted function.

In the time-dependent maximum likelihood fit for ϕ_s, additional constraints on Γ_s and $\Delta\Gamma_s$ are necessary: For small values of ϕ_s (exact for $\phi_s = 0$), the differential decay rate for CP-odd eigenstates consists mainly of terms that are proportional to

$$e^{-\Gamma_s t} \cdot e^{\Delta\Gamma_s t} \propto e^{-\Gamma_H t} . \tag{13.5}$$

The $B_s^0 \to J/\psi\pi^+\pi^-$ decay is therefore effectively only sensitive to Γ_H and a determination of both $\Delta\Gamma_s$ and Γ_s is not possible. To account for this Γ_s and $\Delta\Gamma_s$ are constrained in the fit to the central values and uncertainties derived from the $B_s^0 \to J/\psi\phi$ fit in the previous chapter. A two-dimensional constraint is applied to propagate also their correlations to the fit.

The resulting central values and fit uncertainties of the physics parameters from $B_s^0 \to J/\psi\pi^+\pi^-$ decays are given in Table 13.4. The quoted uncertainties contain a statistical component as well as components from the tagging calibration and the uncertainties of $\Delta\Gamma_s$, Γ_s, and Δm_s. The parameter values are compatible with the results obtained in [54] and with the results from the $B_s^0 \to J/\psi\phi$ fit. The background subtracted decay time distribution is plotted in Figure 13.5 with the fitted PDF.

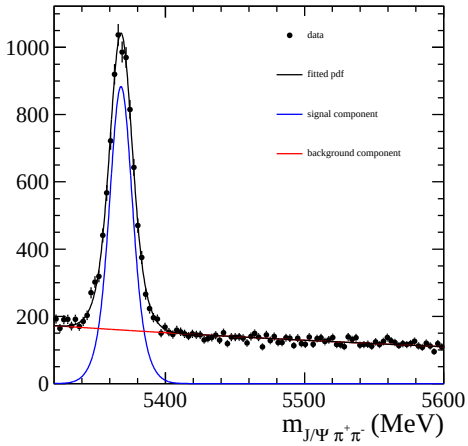

Figure 13.4: Mass distributions of $B_s^0 \to J/\psi\pi^+\pi^-$ candidates in [5320 MeV, 5600 MeV], overlaid with the fitted PDF used to determine the sWeights.

parameter	fit results
ϕ_s[rad]	-0.008 ± 0.154
$\lvert\lambda_{CP}\rvert$	0.856 ± 0.110
$\Delta\Gamma_s$[ps^{-1}] $\star$	0.111 ± 0.011
Γ_s[ps^{-1}] $\star$	0.6617 ± 0.0039
Δm_s[ps^{-1}] $\star$	17.630 ± 0.111

Table 13.4: Central values and fit uncertainties of the physics parameters extracted from selected $B_s^0 \to J/\psi\pi^+\pi^-$ candidates using the sFit technique. Parameters marked with $\star$ are constrained in the fit to the results of external measurements.

13.3 Combined fit of $B_s^0 \to J/\psi\phi$ and $B_s^0 \to J/\psi\pi^+\pi^-$

A simultaneous maximum likelihood fit is performed using both $B_s^0 \to J/\psi\phi$ and $B_s^0 \to J/\psi\pi^+\pi^-$ candidates. A joint likelihood function is minimised with common parameters ϕ_s, $|\lambda_{CP}|$, $\Delta\Gamma_s$, Γ_s, Δm_s and the tagging calibration parameters. The fitting conditions for the $B_s^0 \to J/\psi\phi$ sample are identical to those used for the results in Chapter 11. This especially means separate S-wave parameters in six intervals of the K^+K^- mass. For the $B_s^0 \to J/\psi\pi^+\pi^-$ sample, the fitting conditions were discussed in the previous section. Due to the simultaneous fit with $B_s^0 \to J/\psi\phi$ candidates there is no need to constrain $\Delta\Gamma_s$ and Γ_s.
The results of the physics parameters from the simultaneous fit are given in Table 13.5.

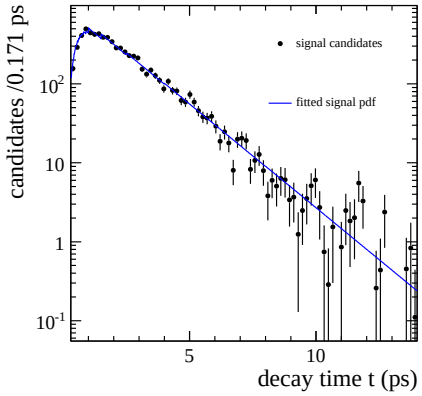

Figure 13.5: Decay time distributions of $B_s^0 \to J/\psi\pi^+\pi^-$ candidates, overlaid with the fitted PDF from the sFit technique.

They are in agreement with the results from the individual fits. The fit uncertainties on the parameters decrease as expected with the additional statistics. The correlation matrix of the physics parameters is given in Table 13.6. Especially the correlation between $\Delta\Gamma_s$ and Γ_s is smaller compared to the fit using $B_s^0 \to J/\psi\phi$ decays due to the additional information from $B_s^0 \to J/\psi\pi^+\pi^-$ on the decay width Γ_H of the CP-odd component. The systematic errors of this measurement are dominated by the systematic uncertainties determined in the analysis of $B_s^0 \to J/\psi\phi$ decays. They are fully assigned as errors to the values from the combined fit.

parameter	fit results	stat. error	syst. error
ϕ_s[rad]	0.043	0.076	0.014
$\lvert\lambda_{CP}\rvert$	0.940	0.030	0.016
$\Delta\Gamma_s$[ps^{-1}]	0.109	0.011	0.004
Γ_s[ps^{-1}]	0.6604	0.0039	0.0058
$\lvert A_\perp\rvert^2$	0.245	0.007	0.016
$\lvert A_0\rvert^2$	0.524	0.005	0.030
$\delta_\parallel$[rad]	3.32	0.154	0.085
$\delta_\perp$[rad]	3.05	0.210	0.067

Table 13.5: Central values and statistical uncertainties of the physics parameters determined from a combined fit to $B_s^0 \to J/\psi\phi$ and $B_s^0 \to J/\psi\pi^+\pi^-$ candidates. The S-wave parameters are not listed here. The systematic uncertainties are taken from the $B_s^0 \to J/\psi\phi$ analysis.

	Γ_s	$\Delta\Gamma_s$	$\lvert\lambda_{CP}\rvert$	ϕ_s	$\lvert A_0\rvert^2$	$\lvert A_\perp\rvert^2$	$\delta_\parallel$	$\delta_\perp$
Γ_s	1.00	0.06	0.03	0.02	0.01	0.10	-0.08	-0.03
$\Delta\Gamma_s$		1.00	0.01	-	0.48	**-0.51**	-	0.01
$\lvert\lambda_{CP}\rvert$			1.00	0.05	0.03	-0.05	0.05	-0.04
ϕ_s				1.00	-0.01	0.04	-0.02	0.23
$\lvert A_0\rvert^2$					1.00	-0.42	-0.05	-0.03
$\lvert A_\perp\rvert^2$						1.00	-0.33	-0.11
$\delta_\parallel$							1.00	-0.22
$\delta_\perp$								1.00

Table 13.6: Parameter correlations in the simultaneous fit of $B_s^0 \to J/\psi\phi$ and $B_s^0 \to J/\psi\pi^+\pi^-$ decays. Correlations larger than 0.5 are highlighted.

13.4 Interpretation of results

The presented measurement of ϕ_s and $\Delta\Gamma_s$ is the most precise determination of these quantities up to now. Figure 13.6 shows the current experimental status of ϕ_s and $\Delta\Gamma_s$ in a two-dimensional plane. The most recent results from CDF, D0, ATLAS and LHCb are combined to a common two-dimensional confidence interval. The result presented in this thesis can roughly be compared with the preliminary LHCb measurement [80]. Both measurements use the same 1 fb^{-1} data sample but the precision of the presented analysis is slightly better due to improved trigger strategies and systematic uncertainties. For comparison the ϕ_s result of the LHCb measurement using $B_s^0 \to J/\psi\phi$ decays is $\phi_s = -0.001 \pm 0.101 \pm 0.017$ rad and combined with $B_s^0 \to J/\psi\pi^+\pi^-$ decays $\phi_s = -0.002 \pm 0.083 \pm 0.027$ rad. The combined confidence interval of all single measurements in Figure 13.6 is well compatible with the Standard Model predictions for ϕ_s and $\Delta\Gamma_s$.

The precise measurement of ϕ_s puts also new constraints on possible physics contributions beyond the Standard Model. Figure 13.7 shows the impact of the recent ϕ_s measurements on the model independent New Physics parameter Δ_s, introduced in Section 2.5. After the solution of the ϕ_s-$\Delta\Gamma_s$ ambiguity, the 68% confidence interval of Δ_s is reduced from two (Figure 2.9) to only one area, which is very well compatible with the Standard Model prediction $\Im\Delta_s = 0$, $\Re\Delta_s = 1$. Although the possible values for Δ_s are significantly reduced by the ϕ_s measurement, there is still room for New Physics contributions.

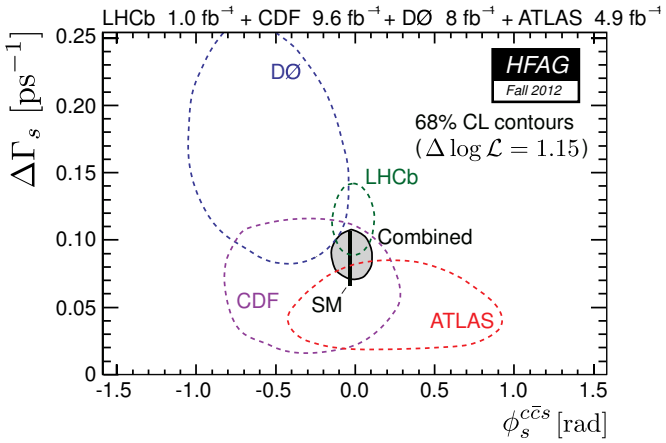

Figure 13.6: Current experimental status of ϕ_s and $\Delta\Gamma_s$. The 68% confidence contours are shown for measurements of D0 [36], LHCb [80], CDF [81], ATLAS [82], and for a combination of them (grey). The black bar indicates the Standard Model expectation. The figure is taken from [83].

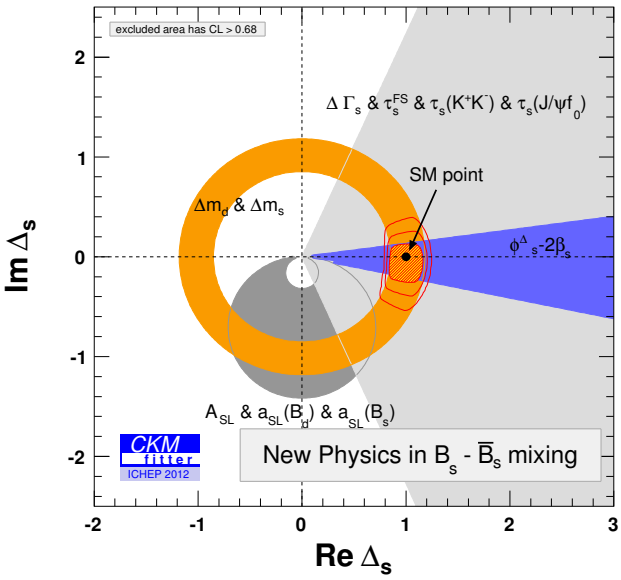

Figure 13.7: Constraints on the model independent New Physics parameter Δ_s. Results from ϕ_s, $\Delta\Gamma_s$, τ_s and the semileptonic CP asymmetry are used. The blue area shows the constraints from ϕ_s measurements. The red region indicates the combined 68% confidence contour. The figure is taken from [18].

CHAPTER 14

Summary and Outlook

This thesis presented a measurement of the CP-violating phase ϕ_s arising in the interference of B_s^0-$\overline{B}_s^0$ mixing and decay amplitudes. Within the Standard Model, ϕ_s is precisely predicted. It is an excellent observable to search for contributions of New Physics beyond the Standard Model. The measurement is performed using the decay channels $B_s^0 \to J/\psi\phi$, reconstructed and selected at the LHCb experiment. The analysis principle relies on a maximum likelihood estimation, fitting the theoretical differential decay rates of the $B_s^0 \to J/\psi\phi$ decay to the experimentally measured decay time and angular distributions.

Using the data taken in the full 2011 running period of the LHC with an recorded integrated luminosity of $\mathcal{L} \approx 1.0\,\text{fb}^{-1}$ a set of ≈ 28000 $B_s^0 \to J/\psi\phi$ signal candidates is selected. The background pollution of the sample is small ($\sim 20\%$ in the B_s^0 signal region).

For the flavour tagging to determine the B_s^0 production flavour, two different types of tagging algorithms are used, exploiting the properties of the signal B_s^0 decay or the properties of the second produced B-hadron in the event. Combining all informations of the tagging algorithms the tagging efficiency is $\varepsilon_{\text{tag}} = 39.4\%$ and the mistag probability $\omega_{\text{tag}} = 35.9\%$. The overall tagging power is determined to be $\varepsilon_{\text{eff}} = 3.13\%$ representing the statistical reduction of the data sample due to imperfect determination of the B_s^0 production flavour.

The decay time resolution determines the capability of resolving the fast B_s^0 oscillation. It is measured using B_s^0 background candidates reconstructed from J/ψ produced in the primary pp-interaction, combined with two additional random tracks. The effective

average decay time resolution is determined to be $\sigma_t^{\text{av}} \approx 46\,\text{fs}$.
The detector acceptances influencing the measured angular distributions are determined with simulated events and investigated in detail. The acceptance distortions are caused by the geometry of the detector and implicit momentum cuts in reconstruction and selection of the $B_s^0 \to J/\psi\phi$ candidates. Differences in related kinematic distributions of measured and simulated candidates are observed and used to estimate uncertainties in the measurement of the physics parameters. The acceptance losses for the decay time distributions are mainly caused by requirements in the software trigger and are determined using a lifetime-unbiased sample of $B_s^0 \to J/\psi\phi$ candidates.
The technical implementation of the maximum likelihood estimation is tested with high statistics pseudo-experiments and on a large simulated $B_s^0 \to J/\psi\phi$ event sample. Two different fitting techniques are used to determine the physics observables from the decay time and angular distributions of selected $B_s^0 \to J/\psi\phi$ decays, taking into account the tagging performance, the decay time resolution and the acceptance corrections. Separate S-wave parameters for different K^+K^- mass regions allow to resolve the twofold ambiguity in the differential decay rate. The measured results for the B_s^0-$\overline{B}_s^0$ mixing parameters using $B_s^0 \to J/\psi\phi$ decays are:

$$\begin{aligned}
\phi_\text{s} &= 0.069 \pm 0.091\,(\text{stat.}) \pm 0.014\,(\text{syst.})\,\text{rad}\,,\\
\Delta\Gamma_\text{s} &= 0.100 \pm 0.016\,(\text{stat.}) \pm 0.004\,(\text{syst.})\,\text{ps}^{-1}\,,\\
\Gamma_\text{s} &= 0.6643 \pm 0.0048\,(\text{stat.}) \pm 0.0058\,(\text{syst.})\,\text{ps}^{-1}\,,
\end{aligned}$$

where the first uncertainty is statistical and the second systematic. The measured values are in agreement with the prediction from the Standard Model for the CP-violating phase $2\beta_\text{s} = 0.0364 \pm 0.0016\,\text{rad}$ [8] the decay width difference $\Delta\Gamma_\text{s} = 0.087 \pm 0.021\,\text{ps}^{-1}$ [77]. No evidence for new physics affecting the B_s^0-$\overline{B}_s^0$ mixing phase is found.
In addition a measurement of the B_s^0 mixing parameters is made combining the information of $B_s^0 \to J/\psi\phi$ and $B_s^0 \to J/\psi\pi^+\pi^-$ datasets. The increase in statistical power leads to the results

$$\begin{aligned}
\phi_\text{s} &= 0.043 \pm 0.076\,(\text{stat.}) \pm 0.014\,(\text{syst.})\,\text{rad}\,,\\
\Delta\Gamma_\text{s} &= 0.109 \pm 0.011\,(\text{stat.}) \pm 0.004\,(\text{syst.})\,\text{ps}^{-1}\,,\\
\Gamma_\text{s} &= 0.6604 \pm 0.0039\,(\text{stat.}) \pm 0.0058\,(\text{syst.})\,\text{ps}^{-1}\,.
\end{aligned}$$

It is the most precise determination of these quantities up to know. Especially for the CP-violating phase ϕ_s the limiting factor in precision is the available statistics.
In the near future the statistical precision will be improved by analysing the LHCb dataset collected in 2012 with an integrated luminosity of $2.2\,\text{fb}^{-1}$. Extrapolating the number of selected $B_s^0 \to J/\psi\phi$ and $B_s^0 \to J/\psi\pi^+\pi^-$ signal candidates in the analysed $1.0\,\text{fb}^{-1}$ dataset to the combined $3.2\,\text{fb}^{-1}$ dataset (2011 + 2012), without taking into possible improvements in selection and trigger efficiency, the expected statistical uncertainty of ϕ_s is $\sim 0.04\,\text{rad}$.
With the planned upgrade of the LHCb detector [84] and the expected integrated luminosity of $\mathcal{L} \approx 50\,\text{fb}^{-1}$ the statistical precision of ϕ_s is extrapolated to be $\sim 0.007\,\text{rad}$

[85]. The already very small systematic uncertainties are currently dominated by the background description and the angular acceptances. With more data available and intensive studies, they are expected to decrease further.
When achieving this precision it will be important to understand the contribution of the suppressed Standard Model penguin diagrams to the $B_s^0 \to J/\psi\phi$ decay amplitude (see figure 2.5). They contribute to the measured value of ϕ_s and could be misinterpreted as New Physics effects. A reliable theoretical prediction of the effect on ϕ_s is not possible, effects of up to ~ -0.1 rad can not be excluded [27]. The contribution of the penguin amplitudes can, however, be experimentally measured by exploiting flavour SU(3) symmetry of the strong interaction and analysing the decay $B_s^0 \to J/\psi K^{*0}$, where the penguin diagrams are not suppressed compared to the tree-level process. A first analysis of $B_s^0 \to J/\psi K^{*0}$ decays was already performed at LHCb [86]. Studies for the decay $B_d^0 \to J/\psi K_S^0$, that is topological similar to $B_s^0 \to J/\psi\phi$, showed that effects in the order of ~ -0.01 rad are realistic [87].
In summary, the aspired precision of ϕ_s will allow to either measure a significant deviation from the Standard Model prediction or put very strong constraints on New Physics scenarios.

List of Figures

(lof)

List of Tables

(lof)

Bibliography

[1] S. L. Glashow, *Partial Symmetries of Weak Interactions*, Nucl. Phys. 22, 579 (1961).

[2] A. Salam, J. Ward, *Electromagnetic and Weak Interactions*, Phys. Lett. 13, 168 (1964).

[3] S. Weinberg, *A Model of Leptons*, Phys. Rev. Lett. 19, 1264 (1967).

[4] G. Bertone, D. Hopper, J. Silk, *Particle Dark Matter: Evidence, Candidates and Constraints*, Phys.Rept. 405:279-390, 2005.

[5] J. Frieman, M. Turner, D. Huterer, *Dark Energy and the Accelerating Universe*, Ann.Rev.Astron.Astrophys. 46:385-432, 2008.

[6] A. D. Sakharov, *Violation of CP Invariance, c Asymmetry, and Baryon Asymmetry of the Universe*, Pisma Zh.Eksp.Teor.Fiz. 5 (1967) 32-35.

[7] P. Huet, E. Sather, *Electroweak Baryogenesis and Standard Model CP Violation*, Phys. Rev. D 51, 379 (1995).

[8] J. Charles et al., *Predictions of selected flavour observables within the Standard Model*, Phys. Rev. D84 (2011) 033005, arXiv:1106.4041 with updated results and plots available at http://ckmfitter.in2p3.fr

[9] K. Nakamura et al (Particle data Group), Journal of Physics G 37 075021 (2010).

[10] G. Altarelli, *The Standard Model of Particle Physics*, arXiv:hep-ph/0510281v1.

[11] O. Nachtmann, *Phänomene und Konzepte der Elemntarteilchenphysik*, Friedr. Vieweg & Sohn (1986).

[12] The Atlas Collaboration, *Observation of a new particle in the search for the Standard Model Higgs boson with the Atlas detector at the LHC*, Phys.Lett. B716 (2012) 1-29.

[13] The CMS Collaboration, *Observation of a new boson at a mass of 125* GeV*with the CMS experiment at the LHC*, Phys. Lett. B716 (2012) 30.

[14] I. Brock, T. Schörner-Sadenius, *Physics at the Terascale*, WILEY-VCH Verlag (2011).

[15] M. Kobayashi und T. Maskawa, *CP Violation In The Renormalizable Theory Of Weak Interaction*, Prog. Theor. Phys. 49 652 (1973).

[16] L. Wolfenstein, *Parametrization of the Kobayashi-Maskawa-Matrix*, Phys. Rev. Lett. 51, 1945 (1983).

[17] J. Van Tilburg, *Track simulation and reconstruction in LHCb*, CERN-THESIS-2005-020, (2005).

[18] CKMfitter Group (J. Charles et al.), Eur. Phys. J. C41, 1-131 (2005) [hep-ph/0406184], updated results and plots available at: http://ckmfitter.in2p3.fr

[19] K Anikeev et al., B physics wt the Tevatron: Run II and beyond, Fermilab-Pub-01/197, 2002. arXiv:hep-ph/01201071.

[20] The Babar Collaboration, *The BABAR Physics Book: Physics at an Asymmetric B Factory*, SLCAC Report SLAC-R-504.

[21] I. Dunietz, R. Fleischer, U. Nierste, *In Pursuit of New Physics with B_s^0 decays*, Phys.Rev. D63 (2001) 114015.

[22] R. Aaij et al. *Measurement of CP-violation and the B_s^0-meson decay width difference with $B_s^0 \to J/\psi K^+K^-$ and $B_s^0 \to J/\psi\pi^+\pi^-$ decays*, LHCb-PAPER-2013-002.

[23] ARGUS Collaboration, *Observation of B_d^0-$\overline{B}^0$ mixing*, Phys. Lett. B192 245, (1987).

[24] CDF Collaboration, *Observation of B_s^0-$\overline{B}_s^0$ oscillations*, Phys. Rev. Lett. 97, 242003.

[25] R. Aaij et al. *Measurement of the B_s^0-$\overline{B}_s^0$ oscillation frequency Δm_s in $B_s^0 \to D_s(3)\pi$ decays*, Phys. Lett. B709 (2012) 177-184.

[26] R. Aaij et al. *Analysis of the resonant components in $B_s^0 \to J/\psi\pi^+\pi^-$*, Phys. Rev. D 86, 052006 (2012).

[27] S. Faller, R. Fleischer, T. Mannel, *Precision physics with $B_s^0 \to J/\psi\phi$ at the LHC: the quest for new physics*, Phys. Rev. D79 (2009) 014005.

[28] R. Fleischer, R. Knegjens, G. Ricciardi, *Anatomy of $B_s^0 \to J/\psi f_0(980)$*, Eur.Phys.J. C71 (2011) 1832.

[29] A. S. Dighe, I. Dunietz, H. J. Lipkin, J. L. Rosner, *Angular distributions and lifetime differences in $B_s^0 \to J/\psi\phi$ decays*, Phys. Lett. B369 (1996) 144.

[30] Y. Xie, P. Clarke, G. Cowan, F. Muheim *Determination of $2\beta_s$ in $B_s^0 \to J/\psi K^+K^-$ decays in the presence of a K^+K^- S-wave contribution*, JHEP 09 (2009) 074.

[31] F. Azfar et al. *Formulae for the Analysis of the Flavor-Tagged Decay $B_s^0 \to J/\psi\phi$*, JHEP11 (2010) 158.

[32] Y. Xie, *Some physics and technical issues in analysis of the decay $B_s^0 \to J/\psi K^+K^-$*, LHCb-INT-2012-017.

[33] A. Lenz, *Theoretical status of B_s^0-mixing and lifetimes of heavy hadrons*, Int.J.Mod.Phys. A23 (2008) 3321-3328.

[34] A. Lenz, U. Nierste, *Theoretical update of B_s^0-$\overline{B}_s^0$ mixing*, JHEP 0706 (2007) 072.

[35] T. Aaltonen et al., *Measurement of the CP-Violating phase β_s in $B_s^0 \to J/\psi\phi$ decays with the CDF II Detector*, Phys.Rev. D85 (2012) 072002.

[36] V. M. Abazov et al., *Measurement of the CP-violating phase $\phi_s^{J/\psi\phi}$ using the flavor-tagges decay $B_s^0 \to J/\psi\phi$ in 8 fb^{-1} of $p\overline{p}$ collisions*, Phys. Rev. D85 (2012) 032006.

[37] R. Aaij et al., *Measurement of the CP-violating phase ϕ_s in the decay $B_s^0 \to J/\psi\phi$*, Phys. Rev. Lett. 108 (2012) 101803.

[38] J. Beringer et al. (Particle Data Group), Phys. Rev. D86, 010001 (2012).

[39] L. Evans, P. Bryant, *LHC Machine*, 2008 JINST, 3 S08001.

[40] CERN document server, https://cds.cern.ch/record/40525.

[41] R. Aaij et al., *Measurement of J/ψ production in pp collisions at $\sqrt{s} = 7$ TeV*, Eur. Phys. J. C 71 (2011) 1645.

[42] J. Nardulli, *Reconstruction of tow-body B decays in LHCb*, CERN-THESIS-2007-063.

[43] The LHCb Collaboration, *LHCb Technical design Report, Reoptimized Detector Design and Performance*, CERN-LHCC-2003-030.

[44] http://lhcb.web.cern.ch/lhcb/speakersbureau/excel/default.html

[45] The LHCb Collaboration, *The LHCb Detector at the LHC*, 2008 JINST, 3 S08005.

[46] LHCb Silicon Tracker Website, http://lhcb.physik.uzh.ch/ST/public/material/index.php.

[47] R. E. Kalman, *A new approach to linear filtering and prediction problems*, Trans. ASME J. Bas. Eng. D82 (1960) 35.

[48] M. Adinolfi et al., *Performance of the LHCb RICH detector at the LHC*, arXiv:1211.6759v1 [physics.ins-det] (2012).

[49] R. Aaij, *The LHCb Trigger and its Performance*, arXiv:1211.3055v1 [hep-ex] (2012).

[50] T. Sjöstrand, *S. Mrenna, P.Skands, PYTHIA 6.4 Physics and manual*, JHEP 05 (2006) 026.

[51] D. J. Lange, *The EvtGen particle decay simulation package*, Nucl. Instrum. Meth. A462 (2001) 152.

[52] GEANT4 collaboration, J. Allison et al., *Geant4 developments and applications*, IEEE Trans. Nucl. Sci. 53 (2006) 270.

[53] C. Langenbruch, *Measurement of the B_s^0 mixing phase in the decay $B_s^0 \to J/\psi\phi$ with the LHCb experiment*, CERN-THESIS-2011-161.

[54] M. Neuner, *Measurment of the CP-violating phase ϕ_s in $B_s^0 \to J/\psi\pi^+\pi^-$ decays at the LHCb experiment*, diploma thesis.

[55] LHCb public webpage, http://lhcb-public.web.cern.ch/lhcb-public/

[56] R. Aaij et al. *Selections and lifetime measurements for exclusive $b \to J/\psi X$ decays with $J/\psi \to \mu^+\mu^-$ with 2010 data*, LHCb-ANA-2011-001.

[57] M. Needham, *Clone Track Identification using the Kullback-Liebler Distance*, LHCb 2008 002.

[58] W. Hulsbergen, *Decay Chain Fitting with a Kalman Filter*, arXiv:physics/0503191 [physics.comp-ph].

[59] R. Aaij et al. *Tagged time-dependent angular analysis of $B_s^0 \to J/\psi\phi$ decays with $\approx 337\,\mathrm{pb}^{-1}$*, LHCb-ANA-2010-036.

[60] T. Swarnicki, *A study of the radiative cascade transistions between the Upsilon-Prime and Upsilon resonances*, DESY-F31-86-02.

[61] LHCb MonteCarlo generator statistics, http://lhcb-release-area.web.cern.ch/LHCb-release-area/DOC/STATISTICS/MC11STAT/B2Charm-WG/Generation_Beam3500GeV-md100-MC11-nu2.html#11144001

[62] M. Calvi et al. *Flavour tagging algorithms and Performances in LHCb*, LHCb-2007-058.

[63] R. Aaij et al. *Opposite-side flavour tagging of B mesons at the LHCb experiment* , Eur. Phys. J. C 72 (2012) 2022.

[64] M. Calvi et al. *Optimization and calibration of the Same Side Kaon tagging algorithm using hadronic B_s^0 decays in 2011 data* , LHCb-ANA-2011-103.

[65] R. Aaij at al., *Tagged time-dependent angular analysis of $B_s^0 \to J/\psi\phi$ decays with* $1.03\,\text{fb}^{-1}$, LHCb-ANA-2012-004.

[66] M. Pivk, F.R. Le Diberder, *sPlot: a statistical toolto unfold data distributions*, Nucl.Instrum.Meth.A555:356-369,2005.

[67] Y. Amhis et al. *Understanding decay time acceptances in $B_s^0 \to J/\psi\phi$ decays*, LHCb-ANA-2013-008.

[68] R. J. Barlow, *Statistics - A Guide to the Use of Statistical Methods in the Physical Sciences*, WILEY-VCH Verlag (1989).

[69] Minuit Manual, http://wwwasdoc.web.cern.ch/wwwasdoc/minuit/minmain.html

[70] Giavanni Punzi, *Comments on Likelihood fits with variable resolution*, arXiv:physics/0401045 [physics.data-an].

[71] F. Porter, *Interval Estimation using the Likelohood Function*, Nucl. Inst. Meth., A368:993-803, 1996.

[72] S. M. Flatté, *On the nature of 0+ Mesons*, Phys. Lett B63 (1976) 228.

[73] T. du Pree, *Search for a Strange Phase in Beautiful Oscillations*, CERN-THESIS-2010-124 (2010).

[74] Y. Xie, *sFit: a method for background subtraction in maximum likelihood fit*, arXiv:0905.0724 [physics.data-an].

[75] P.Clarke et al. *First ambiguity-free measurement of ϕ_s and $\Delta\Gamma_s$ in $B_s^0 \to J/\psi K^+K^-$ decays*, LHCb-ANA-2011-083.

[76] R.Aaij et al., *First evidence of direct CP violation in charmless two-body decays of B_s^0 mesons*, Phys. Rev. Lett. 108 (2012) 201601.

[77] A. Lenz, U. Nierste, *Numerical update of lifetime and mixing parameters of B mesons*, arXiv 1102.4274v1.

[78] R. Aaij et al. *Measurement of the CP violating phase ϕ_s in $B_s^0 \to J/\psi f_0(980)$*, Phys. Lett. B 707 (2012) 497âĂŞ505.

[79] R.Aaij et al. *Measurement of the CP-violating phass ϕ_s in $B_s^0 \to J/\psi\pi^+\pi^-$ decays*, Phys. Lett. B 713 (2012) 378-386.

[80] R. Aaij et. al., *Tagged time-dependent angular analysis of $B_s^0 \to J/\psi\phi$ decays*, LHCb-CONF-2012-002.

[81] T. Aaltonen et al., *Measurement of the Bottom-Strange Meson Mixing Phase in the Full CDF Data Set*, Phys. Rev. Lett 109 (2012) 171802.

[82] G. Aad et al., *Time-dependent angular analyis of the decay $B_s^0 \to J/\psi\phi$ and extraction of $\Delta\Gamma_s$ and the CP-violating phase $\phi_s$by ATLAS*, arXiv:1208.0572.

[83] Y. Amhis et al., (Heavy Flavor Averaging Group), *Averages of b-hadron, c-hadron, and tau-lepton properties as of early 2012*, arXiv:1207.1158 [hep-ex] and online update at http://www.slac.stanford.edu/xorg/hfag

[84] R. Aij et al. *Letter of Intent for the LHCb Upgrade*, CERN-LHCC-2011-001.

[85] R. Aij et al. *Implications of LHCb measurements and future prospects*, arXiv:1208.3355 [hep-ex].

[86] R. Aaij et al., *Measurement of $B_s^0 \to J/\psi K^{*0}$ branching fraction and angular amplitudes*, Phys. Rev. D86 (2012) 071102(R).

[87] R. Fleischer, *Theory Issues of Precision B Physics in the LHC Era*, slides at B-Physics Workshop, Neckarzimmern 2013.